Spring 2018

Behavior of Piled Raft Foundation in Partially Saturated Soils

Salman Alrubaye
Old Dominion University

Behavior of Piled Raft Foundation in Partially Saturated Soils

By

Salman Alrubaye

B.S. July 2001, University of Technology, Baghdad, Iraq
M.E. July 2007, University of Technology, Baghdad, Iraq

A Dissertation Submitted to the Faculty of
Old Dominion University in Partial Fulfillment of the
Requirements for the Degree of

DOCTOR OF PHILOSOPHY

CIVIL AND ENVIROMENTAL ENGINEERING

OLD DOMINION UNIVERSITY
May 2018

Approved by:

_____
Isao Ishibashi (Committee Chair)

_____
Duc Nguyen (Member)

_____
Julie Z. Hao (Member)

Abstract

Behavior of Piled Raft Foundation in Partially Saturated Soils

Salman Rubaye
Old Dominion University, 2018
Director: Dr. Isao Ishibashi

Current foundation design practice considers conventional pile group foundation when simpler and rather economical raft foundations do not meet one of the design criteria. However, design requirements could be met by incorporating a reduced number of piles with the raft. Piled Raft foundation (PRF) is a composite foundation in which, the piles and the raft contribute to the total resistance of the foundation.

The objective of this dissertation is to study the behavior of PRF in fully and partially saturated soils. The primary purpose of this study is to develop models capable of estimating the resistance of different types of foundations in fully and partially saturated soils. In this investigation, an experimental program was first proposed to characterize the shear strength of partially saturated soils. Interaction factors between the raft and the piles at different suctions were explored. The effect of the suction on skin friction and end bearing resistances was also studied.

The outputs of the experimental program were discussed and analyzed. The analysis results produced models for predicting the capacity of single pile and 3x3 group foundations in soils at different suctions.

In addition, three-dimensional finite element models were developed using Abaqus software. Numerical analyses simulating the performance of different types of foundations in various

suctions were conducted. Load-settlement curves and distribution of the suction resulted from these analyses were and verified against the experimental models.

The numerical model was also utilized to study the effect of some key parameters on the behavior of PRF. The influence of raft thickness, settlement amount, pile spacing, and pile length to diameter ratios were examined. The outputs of the study were analyzed statistically and numerical models for predicting the capacity of PRF in different suctions were developed.

In this study, it was found that the shear strength was increased when the suction in the soil went up. The increment reached the peak at the Air Entry Value (AEV, 105 kPa) and then leveled off at 600 kPa suctions. The resistance of the single pile increased with suction. The increment in Skin Friction Resistance (SFR) attained the maximum while the increment in End Bearing Resistance (EBR) extended to 2AEV suction and then leveled off.

As expected, Piled Raft Foundation (PRF) showed higher resistance than Pile Group Foundation (PGF) due to the contribution of the raft in PRF. However, PRF resistance was less than the resistance of PGF and Unpiled Raft Foundation (URF) combined due to the interaction between the foundation components. The raft contribution increased with suction from 12 % for zero suction to 45 % at 600 kPa suction. In PGF and PRF, SFR was highly influenced by interaction effects while those effects were negligible in EBR.

It has shown that when piles with large spacing (7d) were added to 24x24 m raft, the resistance of PRF was doubled in comparison with raft foundation only. PRF resistance increased linearly with increasing L/d ratio of the piles. Selected raft thickness ranged from 0.8 to 1.6 m and had insignificant effect on PRF capacity.

This dissertation is dedicated to

my wife

Kawther Magsoosi

and my son

Ali

Acknowledgement

I would like to express my gratitude to my advisor Dr. Isao Ishibashi, professor in the civil and environmental department, for supervising my research work.

I would like to show my appreciation and gratitude to Prof. Dr. Mohammed Y. Fattah from the University of Technology in Baghdad, Iraq for allowing me to work on his research proposal as well as for his support and information during the research.

NOMENCLATURE

AEV	Air Entry Value
B	raft width
c	cohesion in Mohr-Coulomb model
Cu	undrained cohesion
CU	consolidated undrained triaxial test
CWU	consolidated undrained water phase
e_o	Initial void ratio
E_s	modulus of elasticity for soil
E_p	modulus of elasticity for piles
E_r	modulus of elasticity for raft
EBR	end bearing resistance
G	elastic shear modulus of soil
K	shape parameter of yield surface for Drucker-Prager-Cap model
K_p	stiffness of piles
K_c	stiffness of the cap
K_{pc}	stiffness of pile-cup
K_{rs}	stiffness of raft-soil
L	pile length
n	number of piles
p	equivalent normal stress
p_a	evolution factor
P_b	yield stress in Drucker-Prager-Cap model

PRF piled raft foundation

PGF pile group foundation

Q applid load

Q_r raft resistance

Q_p pile resistance

Q_b end bearing resistance

q Von Mises equivalent stress

R cap eccentricity

R^2 Pearson' s coefficient of determination

S_p pile spacing

SPF single pile foundation

SFR skin friction resistance

S_r degree of saturation (%)

SWCC soil water characteristic curve

t_r raft thickness

t deviator stress

TFR total foundation resistance

TPR total pile resistance

URF unpiled raft foundation

U_w Suction

$(u_w - u_a)$ Suction in soil

V_o initial volume of soil

z depth of soil (m)

Greek Symbols

ε_{vol}^{pl}	volumetric plastic strain
ε_{vol}^{el}	volumetric elastic strain
α	friction factor
δ	settlement
$\alpha_{P\text{-}R}$	pile-raft interaction factor
$\alpha_{R\text{-}P}$	raft-pile interaction factor
τ	shear strength
λ	slope of normal consolidation loading line
ν	Poisson ratio
κ	slope of normal consolidation reloading line
η	group efficiency factor
β	friction angle in Drucker-Prager-Cap model
φ	friction angle in Mohr-Coulomb model
φ^b	angle related to change of sher strength with suction
$d_{D\text{-}P}$	cohesion in Drucker-Prager-Cap model
θ	volumetric water content
χ	soil parameter related to degree of saturation
σ_n	normal stress
$(\sigma_n - u_a)$	net normal stress in partially saturated soil
Ψ	soil suction
ρ	density of soil
ρ_o	initial density of soil

TABLE OF CONTENTS

List of Tables

List of Figures

CHAPTER 1

INTRODUCTION

1.1 Introduction

Well-designed foundation transmits loads from superstructure to the soil in a safe, reliable, and cost-effective way. It is known in foundation design that shallow foundations (raft) should be the first option to consider for supporting structure. However, in many cases, the allowable settlements may exceed in these foundations even when they do provide adequate bearing resistance. Conventionally once the decision is made to go for deep foundations, a design approach based on Pile Group Foundation (PGF) is considered in these situations.

1.2 Research Problem

Usually, raft foundation is in direct contact with the soil underneath and works as a basement in most structures. On the other hand, piled foundation ignores the load resisted by the raft component, and assumes that the load is supported by the piles only. This assumption results in over conservative foundation design. Thus, a design that considers a combination of shallow and pile foundations provides an optimized solution. Such a foundation is called Piled Raft Foundation (PRF).

It is evident that both shallow and deep foundations interact with the soil. In addition, strength parameters in the soil and capacities of shallow and deep foundations are formulated considering the assumption that the soil is fully saturated. However, in numerous situations and particularly in arid areas where the water table is at great depth, the soil above the water level is

partially saturated. The differentiation between fully and partially saturated soils is needed particularly for cohesive soils. The variation in the performance of the fully and partially saturated soils is related to the essential differences in their nature and engineering behavior (for example, Fredlund et al., 2011). The influences of strength behavior of partially saturated on the resistance of Single Pile Foundation (SPF) and Piled Raft Foundation (PRF) are investigated in this study.

1.3 Research Procedure

The purpose of this study primarily consists of two correlated parts. In the first one, a model for defining shear strength in partially saturated soils is proposed based on experimental results of shear strength tests.

In the second part, total bearing capacities of different types of pile foundations are estimated based on extensive pile model experiments. The program includes laboratory tests for Single Pile Foundation (SPF), Piled Raft Foundation (PRF), Pile Group Foundation (PGF), and Unpiled Raft Foundation (URF) models in fully and partially saturated soils. Based on the results of these tests, a model for computing the resistance of single pile based on skin friction and end bearing components is suggested. Another model for determining the total bearing capacity of PRF and PGF is presented as well. The model determines the total resistance of 3x3 PRF and 3x3 PGF based on the capacity of single pile and interaction factors between the components of the foundations.

The percentage of load carried by the raft in PRF in fully and partially saturated soils is explored in this study. The distribution of the load between the piles based on their locations in the group (at center, at side, and at corner) is also investigated.

Three dimensional finite element models of pile groups of different configurations are developed to capture the effect of several parameters on the total capacity of PRF. Numerical

models for estimating the total resistance of any PRF is proposed based on the results of the parametric study.

1.4 Organization of the Dissertation

Previous research findings related to properties of partially saturated soils are explored in Chapter Two. The available literatures for studying the behavior of PRF in fully saturated soil are reviewed. The literatures for capturing the behavior of single pile in partially saturated soil are studied as well in this chapter.

An experimental program for characterizing the behavior of partially saturated soil is presented in Chapter Three. Test setup for single piles, group piles, and other tests are proposed in this chapter. Results of all conducted tests are discussed in Chapter Three as well.

Development of numerical models of different configurations is displayed in Chapter Four. Validation of the numerical models with experimental ones is presented in this chapter. A parametric study is performed to capture the behavior of PRF in fully and partially saturated soils.

The analytical models for predicting the shear strength behavior of partially saturated soils is developed in Chapter Five. Models for predicting the total foundation resistance for SPF, PGF, and PRF are also suggested in this chapter. Parametric study data obtained from Abaqus outputs are analyzed in Chapter Five as well. Multi regression analyses are conducted, and analytical models for predicting *TFR* of PRF are presented in this chapter. These models are validated against other models available in the literatures.

The main findings and conclusions of this study are summarized in Chapter Six and recommendations are suggested for future researchers.

CHAPTER 2

LITERATURE REVIEW

2.1 Introduction

A practical foundation design approach must adequately satisfy strength and serviceability requirements and provide safe and economic design. Investigations that consider optimizing foundation performance based on design requirements and soil profile are getting continuing attention.

Polous (2001) stated that a conventional approach of Capacity Based Design (CBD) is usually followed whenever shallow foundation does not meet settlement criteria. In this approach, superstructure loads are carried entirely by the piles in the group, even in cases where the raft still meets the bearing capacity requirement. Such design that ignores the raft-soil contact will lead to unnecessarily overdesigned foundation.

Negative pore pressure substantially influences strength and stiffness properties of partially saturated soils for short piles which are embedded in soils of arid and semi-arid zones. Accordingly, the behavior of foundations interacting with these soils is also influenced.

The following literature review is divided into three sections; the first summarizes design philosophies, design issues, and classification of analysis methods. The second section discusses available techniques for determining and quantifying shear strength parameters, state variables, and the proposed equations describing shear strength function of unsaturated soils. The third section highlights modeling aspects and reviews available literature for determining shallow and deep foundation bearing capacities based on the shear strength of unsaturated soils.

2.2 Piled Raft Foundation (PRF)

Briand et al. (2005) defined PRF as a geotechnical assembly that unlike conventional pile group foundation, considers the bearing effects of both piles as well as raft soil contact. It takes into account the interaction between the foundation components. Figure 2.1(a) shows schematic concept for PRF and Figure 2.1(b) shows major interactions between PRF elements, where P-R is the interaction of piles on the raft, R-P is the interaction of raft on the piles, P-P is pile-pile interaction, Q represents superstructure load. Q_r is the raft resistance, Q_p is the skin friction resistance of the piles and Q_b is the end bearing resistance of the piles.

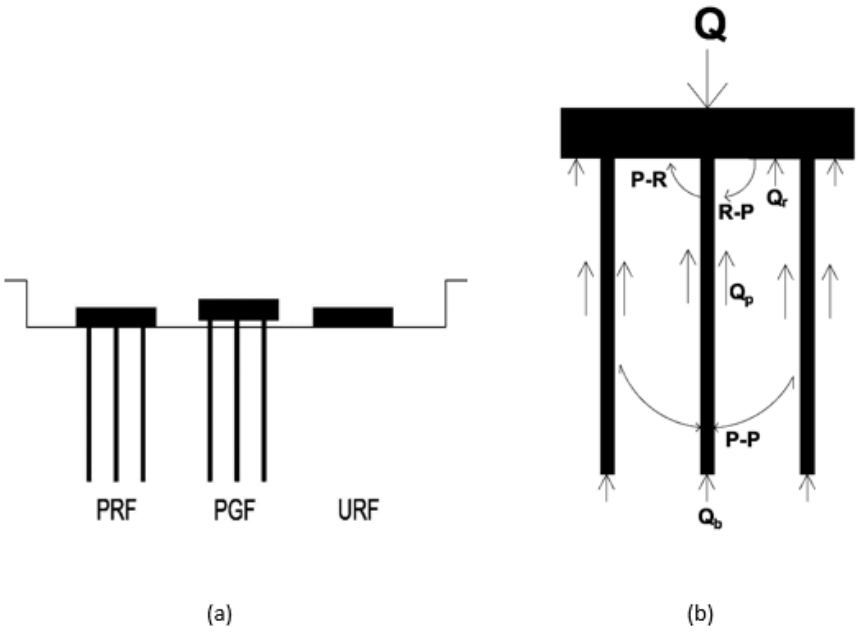

Figure 2.1 (a) Piled Raft Foundation, Pile Group Foundation, Unpiled Raft Foundation (b) major interactions in piled raft foundation

The subsequent section reviews the most recognized methods of piled raft foundation design, in addition to the issues that must be considered when designing PRF. Soil conditions in which

adoption of PRF is appropriate, are included in this section also. Different analysis methods of piled raft foundation are highlighted, as well as the advantages and drawbacks of each method.

2.3 Design of Piled Raft Foundations

2.3.1 Design Considerations

The following considerations must be addressed to establish a functioning piled raft design:

1- Ultimate foundation resistance value that PRF can provide under vertical, lateral and moment loadings.

2- Load sharing mechanism between the raft and the piles and the piles themselves based on their locations in the group (at center, at side, at corner).

3- Maximum predicted total average settlement.

4- Maximum differential settlement.

5- Ultimate moment and shear in the raft and piles for structural design.

The following factors must be taken into account to reach a realistic bearing capacity estimation of piled raft foundations:

1- Considering interaction factors between PRF elements. Ignoring the interactions produces a foundation design with unreasonable results.

2- Nature of applied loads, whether the loads were concentrated or uniformly distributed, symmetric or unsymmetric, the rate of applied load and the intensity of the current load compared to the maximum resistance.

3- Piles characteristics represented by number, layout, length, spacing, and the stiffness of the piles.

4- Soil characteristics which include soil properties, soil stratification, and the hydraulic conditions of the soil.

2.3.2 Design Philosophies

Three different design philosophies were specified by Randolph (1994). Those are:

1- The conventional approach, in which the piles in the group are still carrying significant portion of the loads with minor share taken by the raft.

2- Creep piling, in which the function of the piles minimizes average total settlement by reducing raft-soil contact to below the pre-consolidation pressure of the soil. The piles in this group are designed to work at about 70-80 % at their ultimate resistance, where considerable creep starts to take place.

3- Differential settlement control piles, in which piles are strategically positioned to decrease differential settlement rather than the average total settlement.

Other major groups of piled raft foundation had been identified by De Sanctis et al. (2001); and Viggiani (2001) and those are:

1- Small piled rafts, where the fundamental purpose for considering the pile is to increase the factor of safety of the raft against the ultimate bearing capacity. Usually, in such PRF, the depth of the pile (L) is less than the width of the raft (B).

2- Large piled rafts, where this concept is adopted when the raft provides an adequate factor of safety, and the pile's function is to minimize total and differential settlements. The width of the raft is larger than the length of the piles in this group.

Apparently, large piled rafts by DeSanctis at al. are similar to the second and third design philosophies identified by Randolph, while the small piled rafts by DeSanctis et al. are equivalent

to the first design philosophy by Randolph. Figure 2.2 graphically presents the load-settlement curves of piled raft foundation based on each design philosophy.

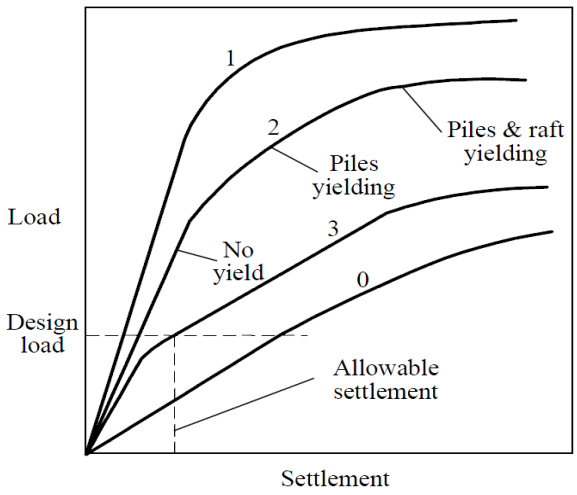

Figure 2.2 Load settlement curves for PRF based on various design philosophies, (Poulos, 2001)

In the figure, Curve 0 illustrates the performance of Unpiled Raft Foundation (URF). It can be noticed that the settlement corresponding to design load is quite beyond the allowable settlement. Curve 1 shows the behavior of conventional piled raft, in which the piles carry the main loads. The load-settlement curve of the foundation designed by this approach may be linear at the design loads. Curve 2 exhibits the situation where creeping piles are used. Considerable load is carried by the raft and piles are at a high level of their capacities. Creeping pile approach enhances the bearing capacity of the raft and reduces the average overall settlement. Curve 3 indicates the philosophy of using piles as settlement reducers and employs the ultimate pile resistance at the design load. Accordingly, the load-settlement curve may be nonlinear at the design load. However, the corresponding settlement is within the allowable settlement. Settlements in Curves 1, 2, and 3

have satisfied the settlement design criteria, but the design characterized by Curve 3 would be the most optimum one.

2.3.3 Applicable and Inapplicable Situations

Poulos (1991) investigated several favorable conditions for considering piled raft foundation. He indicated that soil profile with relatively stiff clay or dense sand is the most appropriate case to take PRF into account.

Accordingly, it may not be favorable to consider PRF when one or more of the following cases exist:

1- The existence of very soft to soft clay or loose sand near the ground surface.

2- Soil profiles with highly compressible soil such as organic soils at a relatively shallow depth.

3- Soil layers that are expected to undergo swelling movement due to environmental causes.

Briand et al. (2005) stated that PRF should not be used in soil layers of relatively low stiffness which are situated closely beneath the raft. In general, PRF shall not be adopted with soil's stiffness ratio of 1 to 10 between the upper and lower layers of the soil profile, that is,

$$\frac{E_s,uper}{E_s,lower} \leq \frac{1}{10}$$

as well as situations where the pile raft coefficient $\alpha_{pr} > 0.9$ where

$$\alpha_{pr} = \frac{\sum_{j=1}^{m} R_{pile}}{R_{tot,k}}$$

where R_{pile} is the total resistance of the piles in PRF and $R_{tot,k}$ is total resistance of PRF.

2.3.4 Design Process

The process of logical pile raft foundation design primarily includes two main stages. In the first stage, the feasibility of adopting PRF is examined, the necessity of piles is assessed, and an approximate number of piles is proposed at this stage also.

Once the use of PRF is justified, the second stage generally requires the use of appropriate computer software that considers the interaction between the foundation components. In this step, the optimum number of piles is determined as well as the location and configuration of piles. Average and differential settlements to be predicted in addition to the distribution of shear forces and bending moment for the structural design of the raft and piles. The second stage also includes conducting geotechnical numerical simulations and other reliability analysis.

2.4 Research on Piled Raft Foundation Behavior

2.4.1 Introduction

Researchers have proposed various methods of analysis to predict the behavior of piled raft foundations. Broadly, the analysis methods are divided into three main categories. Simplified analysis, approximated numerical method, and more rigorous numerical methods. Capabilities and limitations of some of the analysis approaches utilizing each method are discussed below.

2.4.2 Simplified Analysis Methods

(A) Butterfield and Banerjee Approach

Butterfield and Banerjee (1971) were the first who presented elastic analysis concerning the load-displacement behavior of rigid PRF of any shape of foundations. The analysis was formulated based on Mindlin's equation for a point load applied in a semi-infinite ideal elastic

half-space medium. In this method, by distributing a point load over the cap, piles shafts, and the piles base, an integral expression can be obtained to solve the vertical displacement at all points in the soil in terms of fictitious stress intensities as shown in Figure 2.3. In this figure, φ_c is the fictitious normal direct stress on an element in the effective cap area, and φ_s is fictitious shear and direct stress acting on the pile-soil interface of the pile shaft element and pile tip area. The point load is distributed over the cap area. Equation 2.2 was developed for the vertical displacement of all points in the medium.

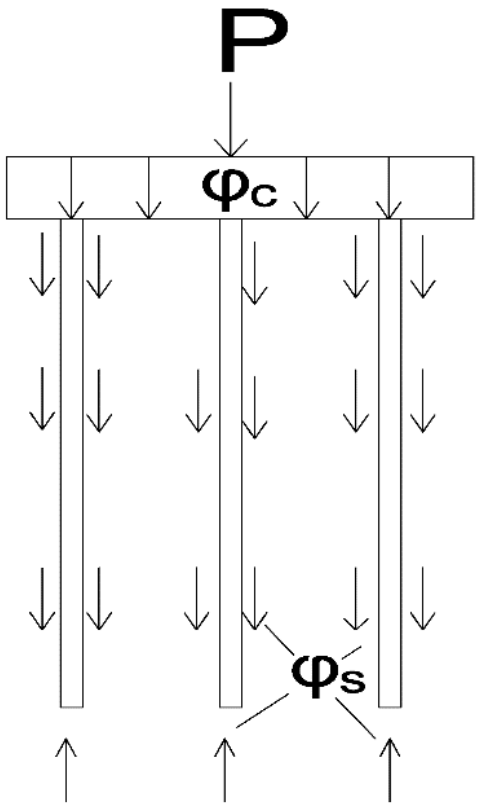

Figure 2.3 Schematic representation of PRF (after Butterfield and Banerjee, 1971)

$$\omega_{(p)} = \int_{c} \phi_c K(p_c, , Q_C) dc + \int_{s} \phi_s K(P_c, Q_S) ds \quad 2.1$$

The first term of the right side of Equation 2.1 is the vertical displacement resulted from the cap, while the second term is the vertical displacement of the piles. The terms $K(p_c, , Q_c)$ and $K(P_c, Q_S)$ can be obtained from Mindlin's equation (Mindlin 1936).

(B) Randolph Approach

Randolph (1983) proposed the most straightforward analytical approach for a single pile cap unit and verified its applicability for a 3x3 piled raft foundation. The analysis was conducted on a unit of rigid pile, which is connected to a rigid circular cap and the soil was taken as an elastic semi-infinite medium. The analytical results were in good agreement with Butterfield and Banerjee (1971).

Two pile cap interaction factors were suggested based on the relationship between displacement (ω_o) of pile shaft and locally induced shear stress (τ_o, where, $\tau_o = G_{wo}/\zeta_{ro}$) as follows:

$$\text{Cap-pile interaction factor, } \alpha_{cp} = 1 - \frac{\ln(r_c/r_0)}{\zeta} \quad 2.2$$

$$\text{Pile- cap interaction factor, } \alpha_{pc} = \frac{k}{4L}\left[\left(1 - \frac{1}{2(1-v)} + \left(2 + \frac{1}{(1-v)}\right) \cdot \sinh^{-1}(L/r_c)\right)\right] \quad 2.3$$

where, the parameter ζ contains the influence of pile geometry and relative homogeneity of the soil. Randolph and Wroth (1978) expressed the parameter as $\zeta = ln(r_m/r_o)$, where, r_m is the maximum radius of influence of pile, which is related to the pile length (L) as $r_m = 2 \cdot 5\rho(1-v)L$ and to the degree of homogeneity (ρ) of the soil and r_o is the pile radius.

The two above interaction factors were then used to correlate the stiffness (k) to settlement (w) and load (p) taken by pile and cap is obtained below:

$$\begin{bmatrix} 1/K_p & \alpha_{pc}/K_c \\ \alpha_{cp}/K_p & 1/k_c \end{bmatrix} \begin{bmatrix} p_p \\ p_c \end{bmatrix} = \begin{bmatrix} w_p \\ w_c \end{bmatrix} \quad 2.4$$

where K_p and K_c are the stiffness of piles and cap, respectively.

$w_p=w_c=w_{cp}$ for the combined unit, since the analysis was for a rigid pile-cap unit. To satisfy the reciprocal theorem the above matrix is expected to be symmetric (i.e., $\alpha_{cp}/K_p = \alpha_{pc}/K_c$). Flexibility matrix 2.4 can be solved for the overall stiffness and load sharing considering the symmetry approximation as follows:

$$K_{pc} = \frac{K_P+(1-2\alpha_{cp})K_c}{1-\alpha_{cp}^2 K_c/K_p} \quad 2.5$$

and $$\frac{p_c}{p_c+p_p} = \frac{(1-\alpha_{cp})K_c}{K_p+(1-2\alpha_{cp}/K_c)} \quad 2.6$$

Only the total settlement of a single pile cap unit can be computed by adopting elastic analysis with direct estimation of load, carried by each component of the foundation. However, Randoph (1983) stated that the relations above for stiffness which is settlement, and load are calculated from the raft area associated with each pile.

The validity of this analytical approach was examined by Clancy and Randolph (1993) utilizing numerical Finite Element Method (FEM) and they found an excellent agreement with a single pile cap unit. For larger pile group, the numerical analysis indicated that the value of α_{rp} increased as the size of pile group increased, but lead to a constant value of $\alpha_{rp} = 0.8$, which was independent of slenderness ratio, stiffness ratio, and spacing of pile.

An elaborated research was conducted by Clancy and Randolph (1996) on the raft-pile interaction factor (α_{rp}) convergence with increased pile group size. A rectangular plate bending finite element numerical approach similar to that used in their 1993 study was adopted with a larger number of piles and the results are shown in Figure 2.4.

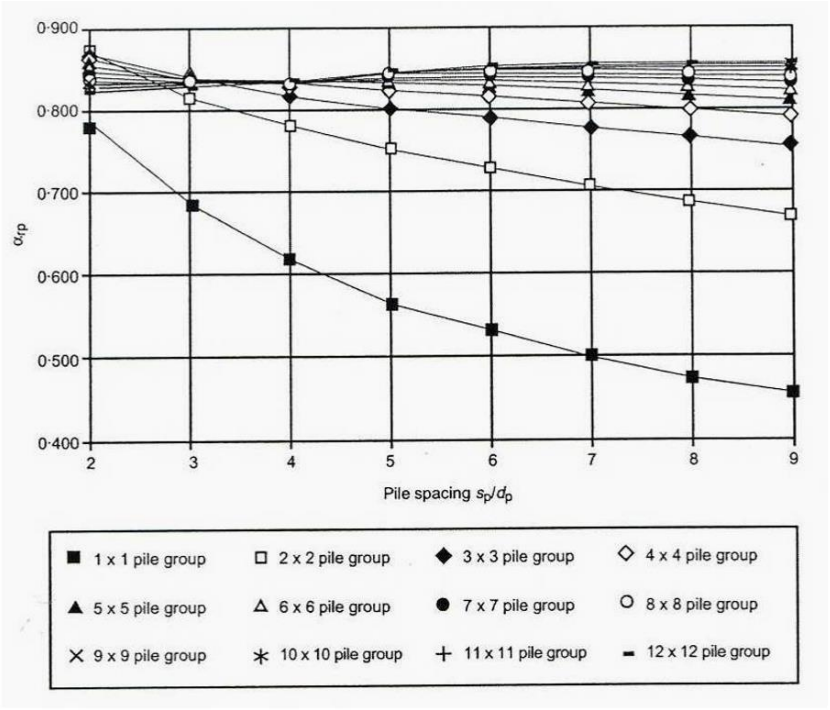

Figure 2.4 Values of interaction factor α_{rp} for various size with Lp/dp = 25, K_{ps} = 1000 kPa and K_{rs} = 10 kPa (Clancy and Randolph, 1996)

The results of the analysis recommended α_{rp} of 0.85 for large numbers of piles in the group (> 6x6 pile group) instead of 0.80 (1993). They also presented Equations 2.6 and 2.7 in their study.

$$K_{pr} = \frac{1-0.7K_r/K_p}{1-0.7K_r/K_p}\ K_p \qquad 2.6$$

$$\frac{P_r}{P_r+P_p} = \frac{0.15K_r/K_p}{1-0.7K_r/K_p} \qquad 2.7$$

The above straightforward analytical method is well recognized due to its straightforwardness and explicit expressions of load sharing and stiffness of the foundation elements. The implementation of one interaction factor (α_{rp}), which is not difficult to be computed, extends the more straightforward application of this approach. However, the method can only compute the total settlement like the Davis and Poulos method (1980). It is based on a single cap unit, and therefore, the restriction related to its implementation for the whole pile raft foundation is still under question. Although Clancy and Randolph tried to verify its implementation for larger pile raft using numerical applications as illustrated above, the extensive investigation is required to find a generic interaction factor for larger scale piled raft foundations.

In summary, the simplified method in this section was considered as cases in a semi-infinite elastic medium, and a point load was applied on rigid pile and rigid cap. The load influence was calculated utilizing Mindlin's or both of Mindlin's and Boussinesq's equations.

Butterfield and Banerjee's approach was for the total settlement and for any size of pile group. However, only single point load was considered in the analysis. Davis-Poulos and

Randolph methods considered a unit composed of rigid circular cap that is connected to a rigid pile. The single pile-cap unit behavior (interaction and load-settlement) is not the same as those of a piled raft foundation. The analysis based on single pile cap unit does not involve the influence of structural integrity, especially, the stresses (both flexural and shear) around the cap periphery within the raft material. Also, all these methods compute total settlement only.

2.4.3 Approximated Methods

Approximated numerical methods such as those presented by Poulos (1994), Russo (1998), Horikoshi (1998), and Nguyen et al. (2013) are more sophisticated than simplified methods and less expensive to run than rigorous numerical methods. In these methods, the foundation behavior is examined by modeling the piled raft foundation as strip or plate with loaded springs. These approaches simplify the rigorous numerical computational cost by incorporating analytical solutions with certain approximations. Accordingly, these methods demand fewer equations to solve than the finite element numerical method.

(A) Strip on Springs Approach (GASP code)

Poulos (1991) developed an analytical approach in which the raft is modeled as a strip resting on piles that are modeled by springs. As shown in Figure 2.5, some approximations were made in the four interaction factors (raft-raft elements, pile-pile, raft-pile, pile-raft), and the influence of the exterior parts of the raft which are located outside of the analyzed strip sections are considered by calculating the free-field soil settlements. The computed settlements are then added to the analysis, and the strip is analyzed to compute the settlements and moments due to the imposed loading on that strip section.

A computer program GASP (Geotechnical Analysis of Strip with Piles) was used to perform the analysis, and the resulted settlement was in fair agreement with more comprehensive methods of analysis. However, this method has major drawbacks as it cannot take into account torsional moments in the raft, and it does not give unique settlements at a point in the strip when strips were analyzed in two different directions.

The non-linearity in the soil was taken into account approximately by specifying the strip-soil contact pressures not to go beyond the compression bearing capacity or the tension capacity. The pile loads as well are specified not to be higher than the compressive and uplift resistances of the piles. The maximum pile load resistance must be known, and it is mostly taken to be the one for single piles. When conducting a nonlinear analysis where the strips are analyzed in two orthogonal directions, it has been noticed that it would be more convenient to consider nonlinearity in the longer raft direction and to treat the shorter raft direction to be linear. Such approach minimizes unreasonable yielding of the soil underneath the strip and accordingly overpredicts settlement.

(B) Plate on Springs Approach

In this analysis, the raft is modeled as an elastic plate, the soil is treated as an elastic medium, and the piles are represented by interacting springs as seen in Figure 2.6. Clancy (1993) proposed an approach for piled raft analysis, named (HyPR), based on a hybrid approach presented by Chow (1986). HyPR was used to model flexible piled raft foundation on a homogenous soil of finite depth. Pile groups and the interaction between the piles and the raft were approached using Mindlin' s solution, Randolph and Worth (1978)'s load transfer model

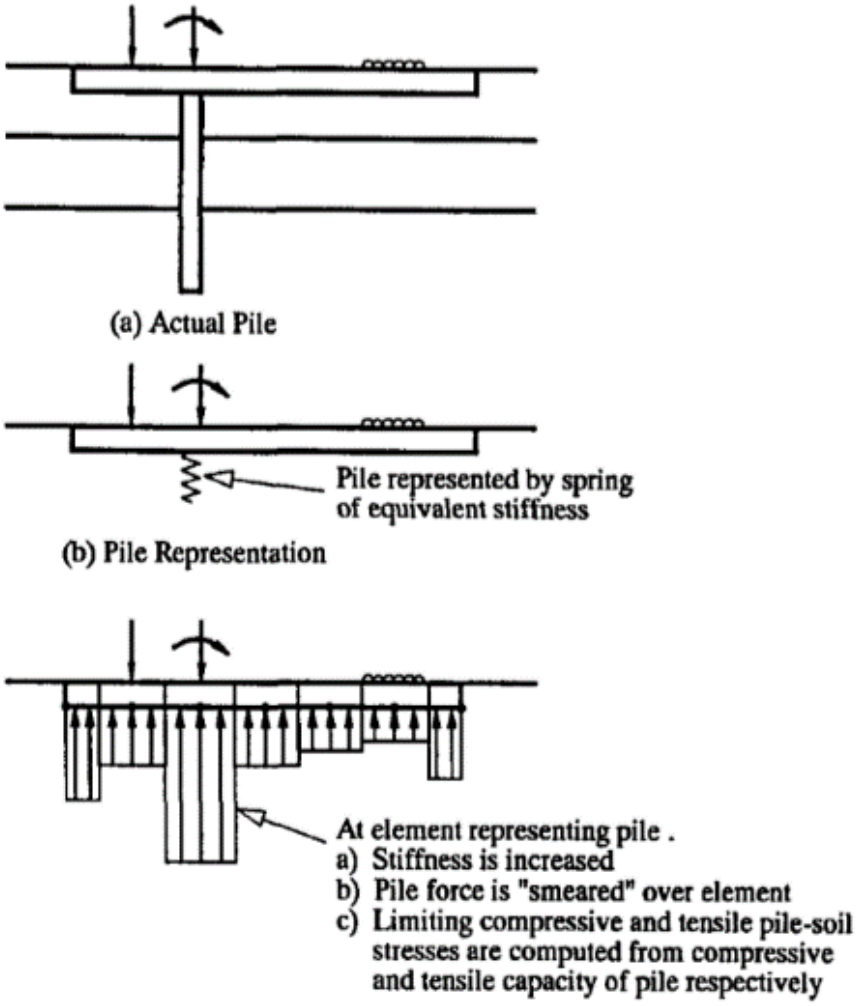

Figure 2.5 Schematic representation of piled strip foundation analysis (Poulos, 1991)

were used for each single pile behavior. The plate-bending finite element was used to model the flexible raft response. The method can efficiently predict the complicated piled raft performance considering the interaction between the foundation elements. The major drawback in the Clancy method is the restriction to homogenous soil layer.

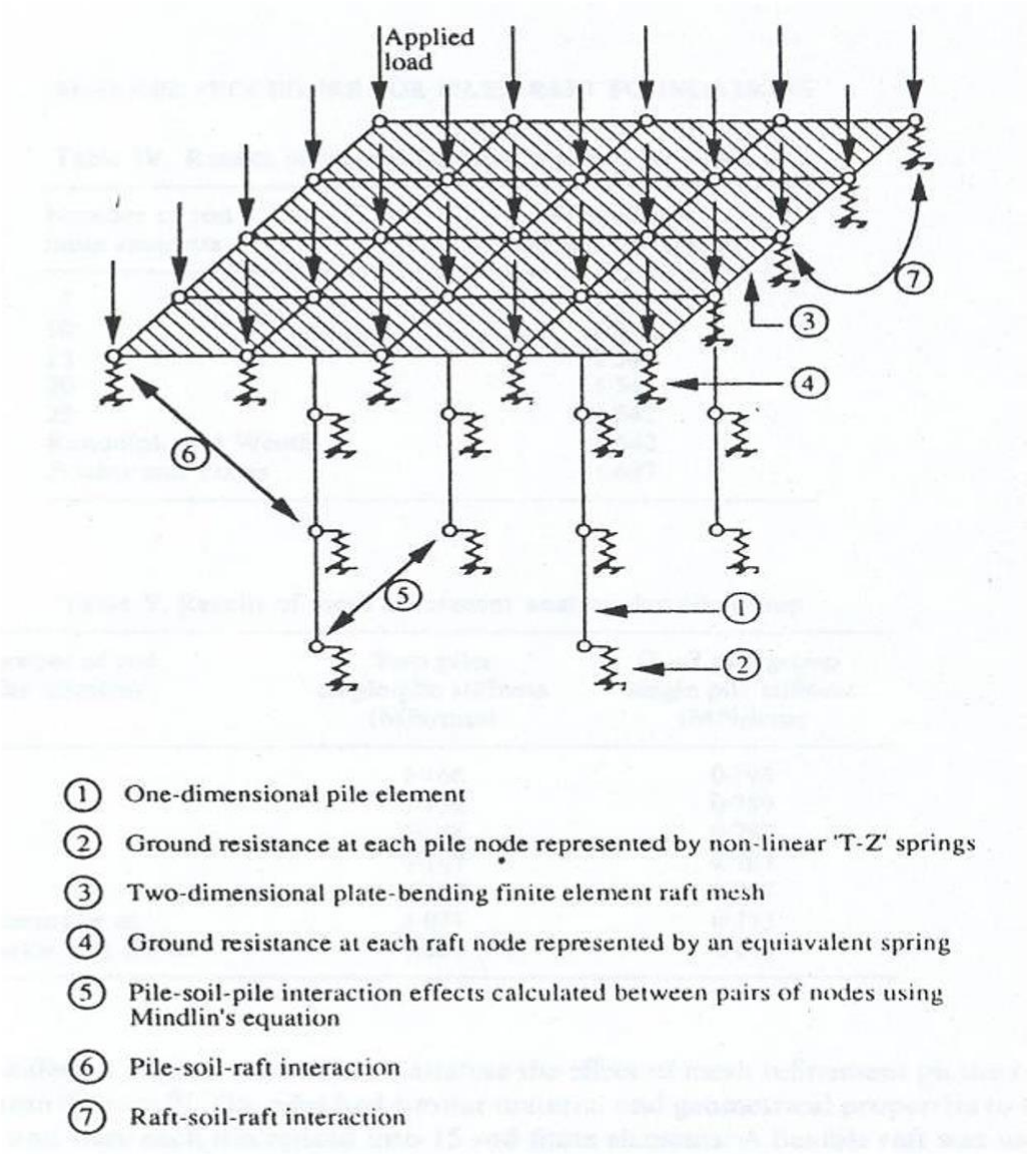

Figure 2.6 Numerical modeling of PRF (Calncy, 1993)

Horikoshi and Randolph (1998) conducted a parametric study on piled raft foundation using the piles as settlement reducers as shown in Figure 2.7. The hybrid approach presented by Clancy was utilized to verify the results against centrifuge model tests. It was concluded that zero differential settlement could be obtained by designing pile raft foundation incorporating the ratio of the cross-sectional area of piles to the area of the raft to be 16-25 % and piles are

concentrated at the area at the center of the raft. These results were obtained when the pile group stiffness is approximately equal to the stiffness of the raft alone. It was recommended that the total pile's resistance must be 40-70% of superstructure loads.

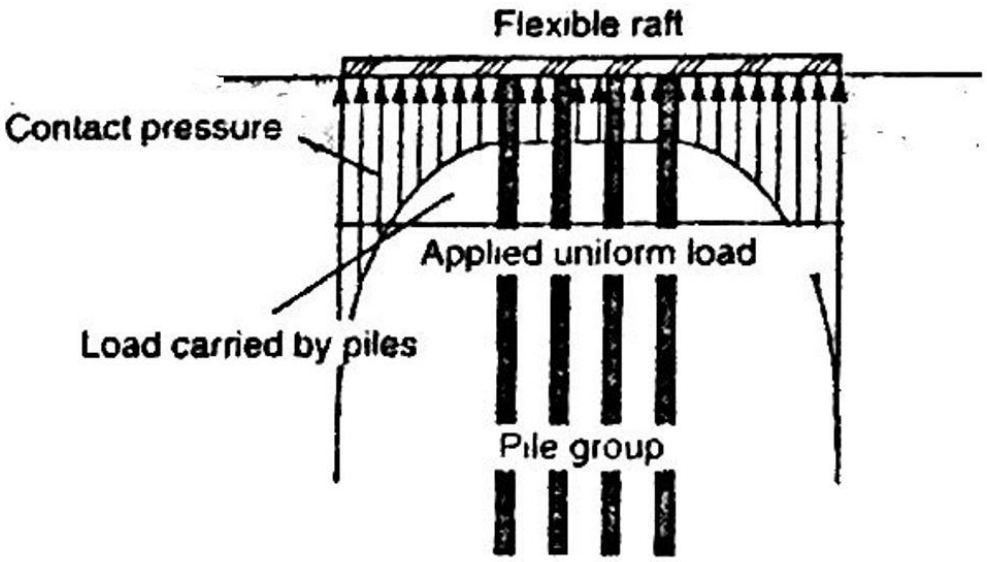

Figure 2.7 Principle of using piles as settlement reducers (Horikoshi and Randolph, 1998)

Nguyen et al. (2013) suggested a design method which takes into account interaction effects for PRF. The raft was modeled as a plate supported by a group of piles and soil as seen in Figure 2.9, the maximum load resistance of the pile group is considered in computing the settlement when the vertical load was applied. A step by step approach was developed in the method for calculating the settlement and for determining the distribution of bending moment in the raft. Piled raft analysis using Plaxis 3D software was performed. The results were verified

against the experimental results of 4x4 and 3x3 piled raft models of different length embedded in homogenous silica sand using a centrifuge accelerator. Good agreement was obtained when both experimental and numerical results were approved.

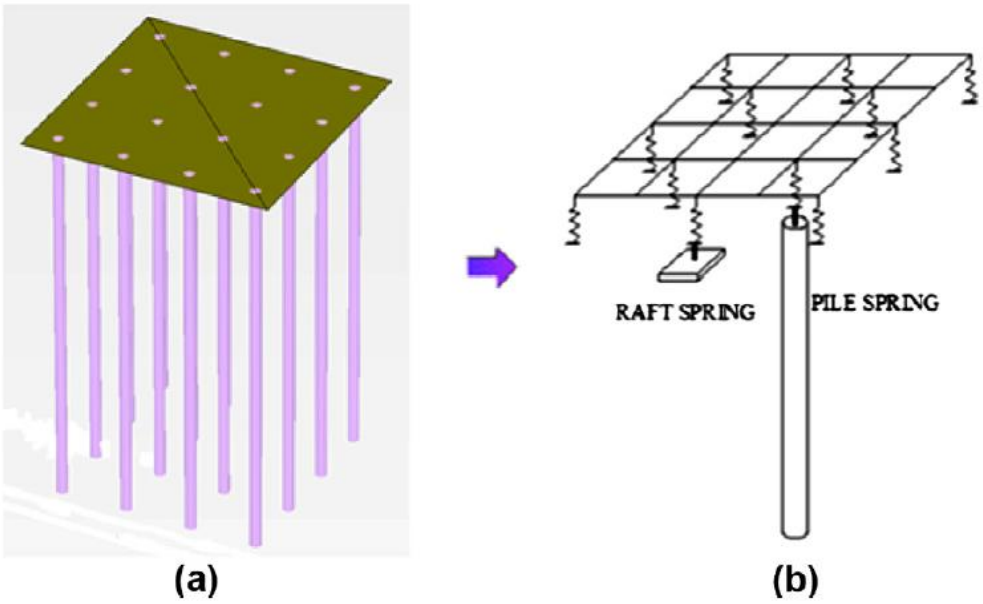

Figure 2.8 Model of piled raft foundation. (a) A piled raft foundation (b) Modelling for proposed design method (Nguyen et al., 2013)

2.4.4 Numerical Methods

Multi-dimensional analysis of a piled raft foundation system can be implemented using different numerical methods such as Finite Element Method, Finite Difference Method, Boundary Element Method and Finite Layer Method. The implementation of three-dimensional analysis utilizing these techniques eliminates the necessity to include various assumptions and approximations involved in the methods discussed previously. Complete numerical analyses are

capable of modeling complicated cases and sizeable models that cannot be addressed experimentally. In addition, simulating the nonlinear behavior of piled raft foundation and conducting nonlinear analysis have become less cumbersome with the substantial advancement in the computational resources. However, a reliable technique is required to model contact zones between the elements of the foundation themselves and between the foundation and the soil.

Moreover, discretization of the domain involved in these analyses necessitates bigger memories and faster processors. Computer software such as Abaqus and Plaxis, FLAC, and Dyana can be used to conduct such analyses. Being the most powerful numerical method and followed in this study, only Finite Element Method (FEM) is discussed in the following review.

(A) Two-Dimensional Finite Element Methods

Two-dimensional finite element analysis was used to model the piled raft foundation as an axi-symmetric or two-dimensional plane strain problem. Substantial approximations were made in both situations. The first finite element analysis was performed by Hooper (1973). The piled raft foundation of Hyde Park Cavalry Barracks on London clay was analyzed. The analysis was linear elastic axi-symmetric and linear increment was assumed in soil modulus of elasticity with Poisson's ratio of 0.5 for undrained and 0.1 for drained situations. Reasonable agreement was found between the analysis results and the field measurements obtained at six years after the construction. However, the analysis considered dry soil only with limited loading types. Hassen et al. (2006) presented a 2D plane strain elasto-plastic multiphase model to simulate the performance of piled raft foundation system with combined horizontal and vertical loading. The soil medium and pile reinforced zone were modeled using six nodded triangular finite element as shown in Figure 2.9. The problem was numerically simulated by superposing two matrix

phases (soil mass and piles). No separation between the soil, raft, and the piles were assumed. No experimental or field measurements data supported the outputs of the presented methods.

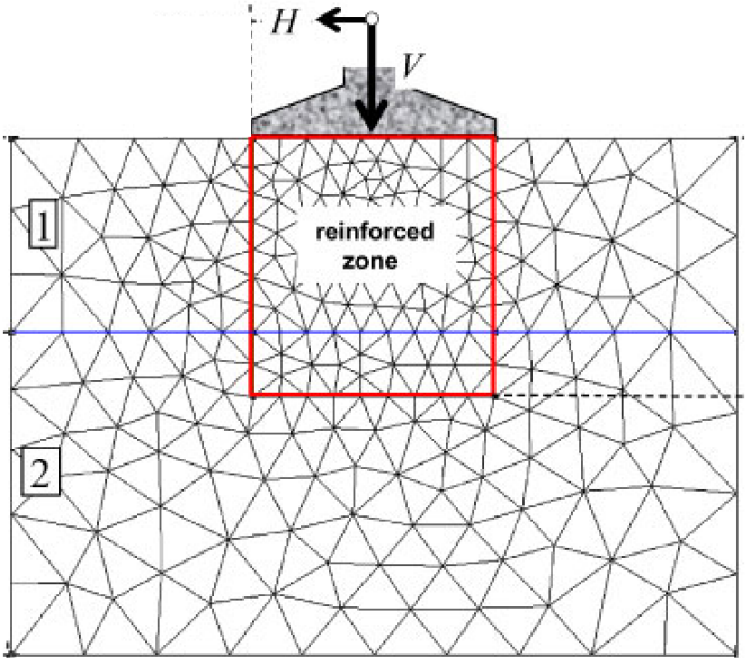

Figure 2.9 Finite element model of piled raft foundation (Hassen et al., 2006)

(B) Three-Dimensional Finite Element Methods

Poulos et al. (1997) reported that Ottaviani (1975) was the first who conducted a three-dimensional analysis of piled raft foundation. The analysis aimed to observe load transfer mechanism, distribution of load, and settlement of piled raft foundations. The analysis incorporated some simplification such as considering the soil as an elastic homogenous medium. Three-dimensional finite element analysis was later conducted by Katzenbach et al. (1997a). The soil was simulated as elasto-plastic meduim using Drucker Prager model. Resulting load-settlement curves were verified against a static load test from Sony Center, Berlin, Germany as

shown in Figure 2.10. In the figure, R_l = Lower band of computed load settlement curve, R_u = Upper band of computed load-settlement curve and R_{Test} = Load settlement curve of static load test.

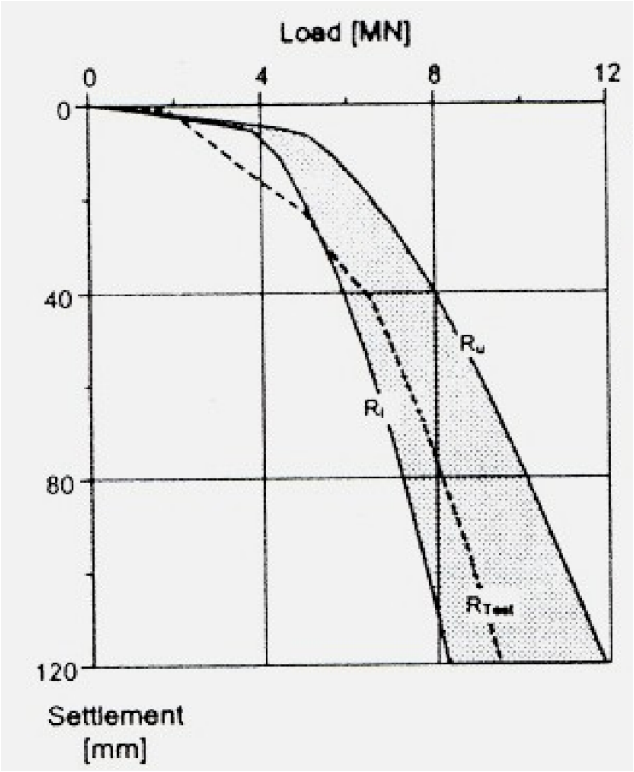

Figure 2.10 Verification of Katzenbach analysis against static load test

Reul (2004) examined the bearing behavior of piled raft foundation in overconsolidated clay (Figure 2.11) to understand the influence of the interaction factors. Abaqus software was used to model the soil and the piles as a brick element and wedge shape, respectively. The raft was modeled by a first-order shell element. Special thin solid continuum elements were used to model the contact zones instead of special interface elements. It was stated that the analysis results were dominated by the stiffness of the soil rather than its strength. The soil was modeled as an elasto-plastic Cap model. The analysis

outputs were verified against the results obtained from back analysis of static load tests and measured bearing behavior of the three piled raft foundations in Frankfurt, Germany as shown in Figure 2.12. The study indicated that the resistance of the pile in the group is significantly affected by the location of the pile, loading level, or induced settlement. It is noticed that choosing the right thickness of the contact zones in modeling is not an easy task in such analysis.

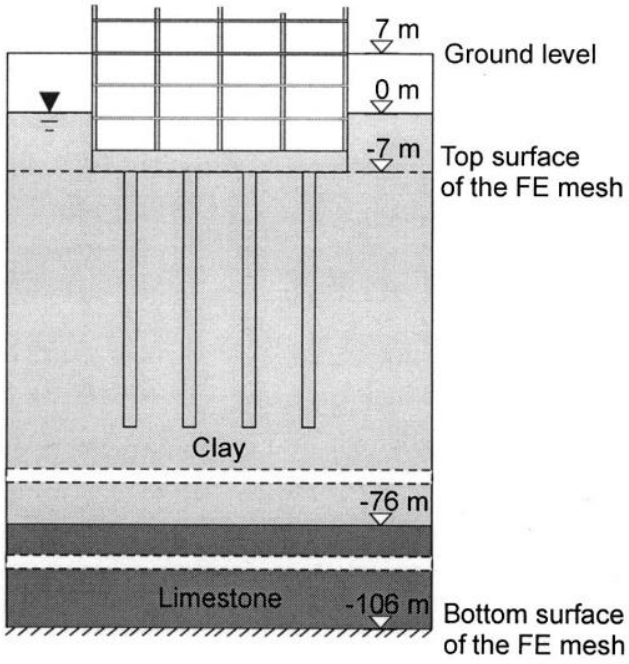

Figure 2.11 Model condition in the numerical model (Ruel, 2004)

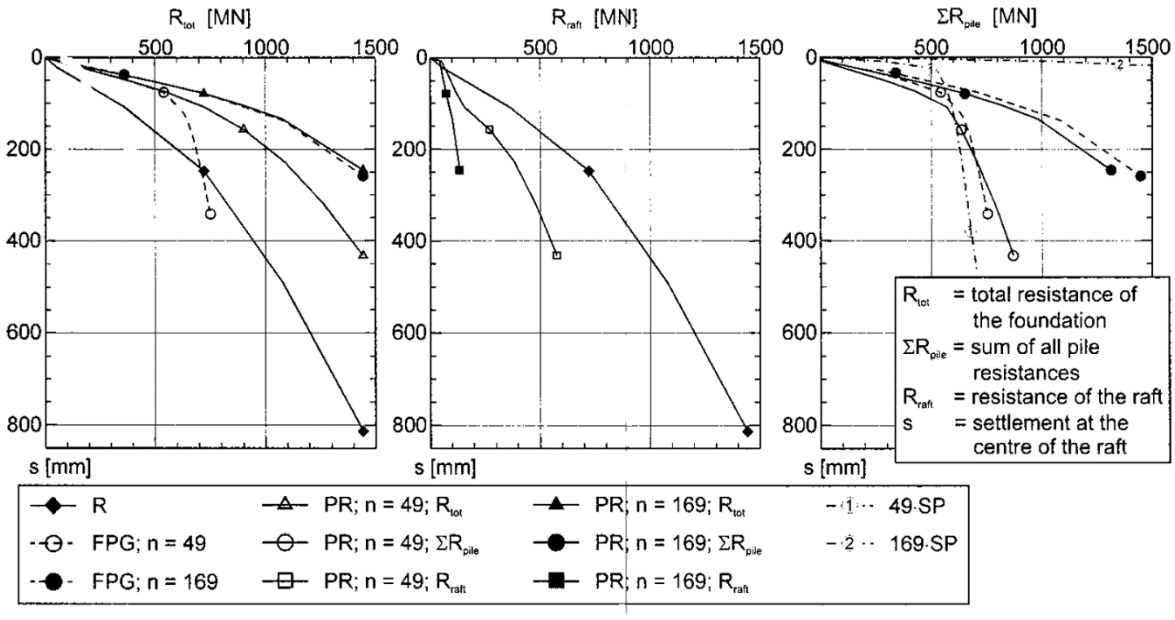

n = number of piles in the group

Figure 2.12 Resistance-settlement curves of Raft (R), Foundation of Pile Group (FPG), And Piled Raft (PR) (Ruel, 2004)

DeSanctis (2006) evaluated the factor of safety of piled raft foundation (Figure 2.13) by computing the ultimate capacity of the foundation as a function of the resistance of each component in that foundation. Parametric study was conducted on three dimensional finite element analysis. For single pile, thin soil element of 0.1 d thickness (d = pile diameter) was used to model the contact zone. The raft was assumed to be rigid and displacement control loading was applied. Coupled deformation pore pressure analysis was performed. Mohr-Coulomb model was adopted and stratification of soil profile was accounted by assigning various soil properties for each layer. Zero dilation angle was followed for undrained soil condition. De Sanctis found that the portion of the load taken by the pile underneath the raft at

failure is constant and approximately equal to the resistance of single pile. The ratio of the load taken by the raft is less than unity and depends on the number and layout of the piles underneath. α_{UR} was defined as ration of the load carried by the raft in PRF to the ultimate load of unpiled foundation (R_{PRF}/URF). A relationship between the factor (α_{UR}) and dimensionless factor defined as (A_G/A)/(s/d), was also established as shown in Figure 2.14 and Equation 2.8.

$$\alpha_{UR} = 1\text{-}3[A_G/A/(s/d)] \qquad 2.8$$

where A_G is the summation of the cross-sectional area of the piles in the group; A is the raft area, s is pile spacing, d is pile diameter, A_G/A =0 corresponds to unpiled raft foundation that yields to α_{UR}= 1 in Equation 2.8.

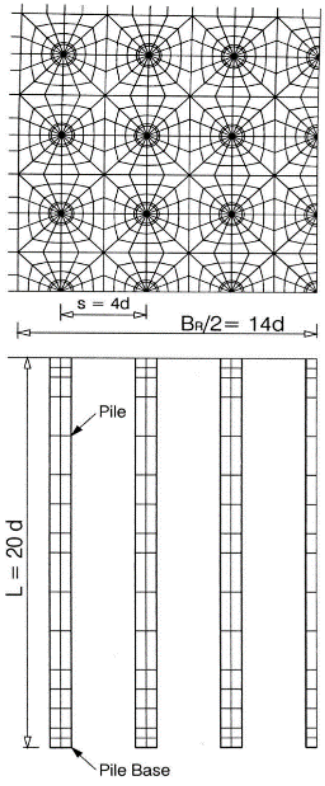

Figure 2.13 Plan view and cross-section of FE mesh (DeSanctis, 2006)

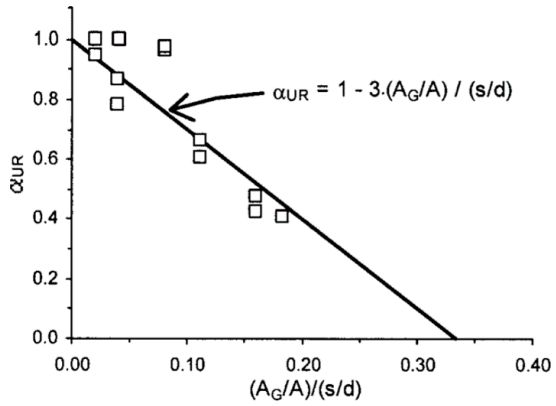

Figure 2.14 Relationship between α_{UR} and (AG/A)/(s/d), (DeSanctis, 2006)

In DeSanctis study, the presentation and the flow of experimental and numerical work are straightforward. However, his finding that the capacity of an individual pile in the PRF foundation is equal to the capacity of single free-standing pile underestimates the effect of interaction between the components of the foundation and seems to be unrealistic.

Small and Poulos (2007) conducted three-dimensional finite element analysis to investigate the effect of pile-soil slip on the bearing behavior of a vertically loaded piled raft on soft clay. Different pile configurations were used in the analysis. Load sharing between the piled raft components was also studied. Mohr-Coulomb model was adopted to present the elsto-plastic behavior of the soil. Slip element of zero thickness was used to simulate the pile-soil interface utilizing Abaqus software. Infinite elements were used to model the soil away from the foundation (Figure 2.15). The outputs of the numerical analysis were verified against the centrifuge experimental results conducted by Horikoshi (1998). Small and Poulos found that the development of settlement and loads in the foundation depends on the slippage of the pile-soil

interface. He also concluded that the portion of the load taken by the raft does not depend much on the configuration of the piles underneath. The soil was also modeled as fully saturated only, in their study.

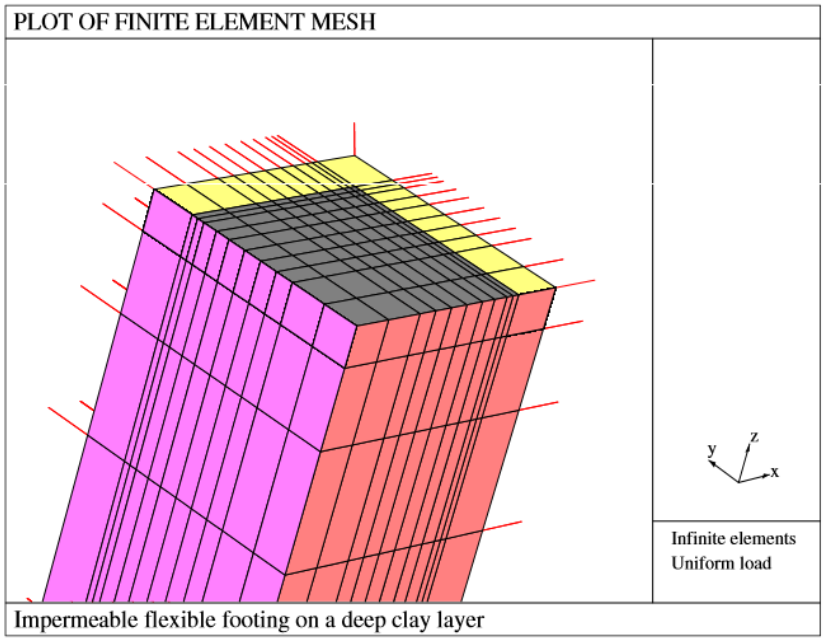

Figure 2.15 Finite element mesh of quarter model and infinite elements (Small, 2007)

Sinha (2013) conducted finite element analysis on a three-dimensional model to study interaction factors, total settlement, and differential settlement in piled raft foundations. A parametric study was performed on a piled raft and pile group foundations with various configurations. Using Abaqus software, the soil was modeled as a single phase elastoplastic material using modified Drucker Prager Cap model. The raft and piles were modeled as an elastic material. First order brick elements with eight nodes were used in the model. Soil piles contact was simulated using the master slave technique. Material properties used in the analysis were adopted from Katchebach (2000). The results of the analysis were verified against the

outputs of the model reported in American Society of Civil Engineers (ASCE) Technical Committee – 18 (TC -18) in 2001**.** Sinha performed multi-regression analysis utilizing statistical software called Minitab and presented analytical models for computing raft pile interaction factor and piled raft interaction factor as shown in Equations 2.9 and 2.10

$$\alpha_{rp} = \frac{K_p}{P_p}(\omega_{pr} - \frac{P_r}{K_r}) \quad 2.9$$

$$\alpha_{pr} = \frac{K_r}{P_r}(\omega_{pr} - \frac{P_p}{K_p}) \quad 2.10$$

where ω_{pr} is settlement of PRF, K_p *and* K_r are the stiffness of the piles and the raft. P_p *and* P_r are the forces carried by the piles and the raft, respectively.

Another two models were suggested by Sinha for computing total (ω_t) and differential settlement (ω_d) as shown in Equations 2.11 and 2.12, respectively.

$$\omega_t = - 0.0316 + 4.9*10\text{-}7*W + 0.0126*S - 4.79*10\text{-}4*L - 3*10\text{-}5*D - 1.48*10\text{-}4*t + 2.5*10\text{-}4*\varphi + 4*10\text{-}7*c \quad 2.11$$

$$\omega_d = 0.0003t^{-3}x\,(x + 6) - 0.085S^{0.76}\,t^{0.18} \quad 2.12$$

Where, W = Applied load, S = pile spacing, L = pile length, D = pile diameter, t = raft thickness, x = distance from raft center, and φ and c are the angle of internal friction and cohesion in the soil, respectively.

In the study conducted by Sinha, the soil was modeled as a dry sand only and pore water pressure effect was neglected. This dry soil approximation would question the application of the output to real world problems.

2.4.5 Experimental Research

Park (2014) conducted experimental comparative analysis to investigate load response and interaction effects of piled raft foundations in sands with various relative densities using centrifuge model test (Figure 2.16). Tests on single piles, unpiled raft, pile group, and piled raft foundations were performed. The load-settlement curves of the piled raft were similar to those of group piles at the initial settlement stage and became similar to those of rafts as the settlement increased. The pile-raft and raft-pile interaction factors showed dependency on the state of soil, configuration of the test, and nonlinear variations with the settlement. Both pile-raft and raft-pile interaction factors decreased within the initial settlement stage and increased with increasing settlement. The range of pile-raft interaction factor values was much larger than the range of values of the raft-pile interaction factor. The load response and the mechanism of load transfer relationship of piles in PRF were not the same as those of single piles, showing that the effect of raft-pile interaction was more dominant within the upper soil zone.

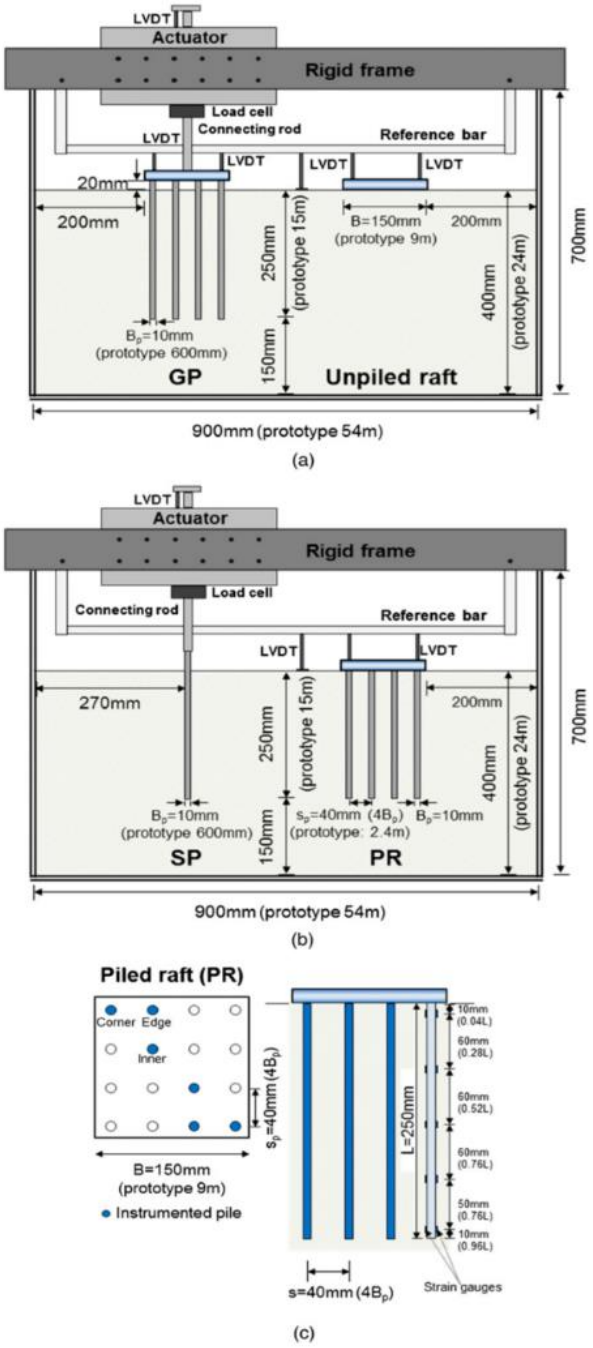

Fig. 2.16 Centrifugal sets of model foundations for (a) GP and UR, (b) SP and PR, and (c) configuration of instrumented (Park, 2014)

2.5 Multi-Phase Soils

2.5.1 Introduction

Soil could be treated with two phase materials with solid and void phases such as completely dry or fully saturated. Those, however, are often three-phase materials; that is, solid phase and void phase with air or water. There are many situations where soil behavior is not consistent with that classically described as two-phase materials in soil mechanic text books and literature.

The voids in the soil above the water table are filled partially with water, and the rest are occupied with air. Partially and fully saturated soil have different constituents, and accordingly, their engineering behavior is different also (Fredlund et al., 2011). Soils above the water table, which in many situations interacting with foundations, retaining walls, utility pipes, and transportation structures are partially saturated. These soils are subjected to atmospheric changes that produce negative pore water pressure distribution and reduced the degree of saturation as shown in Figure 2.17.

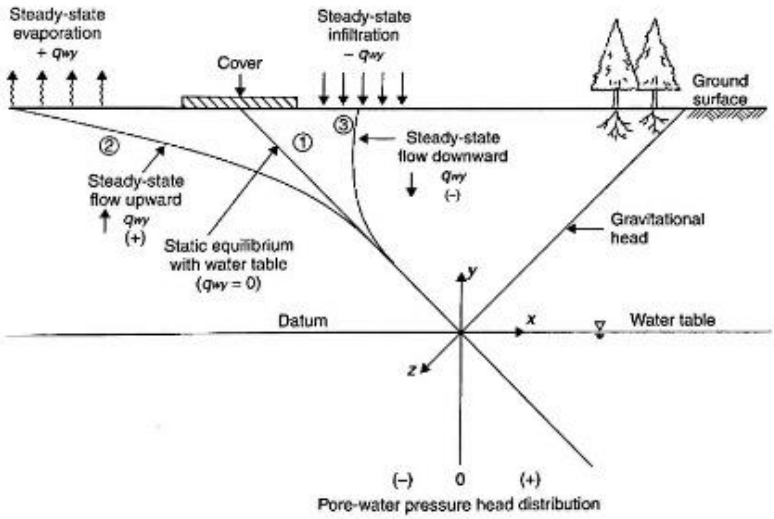

Figure 2.17 Distribution of total stress, pore air pressure, and pore water pressure in partially saturated soils (Fredlund et al., 2011)

The relation between suction in the soil and the corresponding degree of saturation is called Soil Water Characteristic Curve (SWCC). In fully saturated soils, flow, shear strength and volume change parameters are constant, while in partially saturated soils these parameters vary in nonlinear functions. These functions depend on the evolution of suction and degree of saturation. In other words, the parameters given above in fully saturated soils are the special values of those in partially saturated soils. These functions can be formulated using the properties of fully saturated soil and SWCC of that soil.

The subsequent sections briefly review fundamental methods and techniques for measuring suction in the soils. Then, procedures for constructing SWCC are highlighted. Advantages and limitations of each method for measuring the suction and constructing SWCC are reviewed. Finally, well establised equations that describe shear strength functions of partially saturated soil are discussed.

2.5.2 Suction in Soils

In simple words, suction is the pressure that attracts, holds on and derives the water movement in the soil. It also shows the energy that must be exerted to pull the water out of the soil sample. The drier the soil is, the higher suction is. Two components majorly contribute to the suction in the soil. Those are osmotic and matric suctions. Osmotic suction can be defined as the pressure driven by the difference in salt concentration of soil-water in two mediums separated by a semi-permeable membrane. Matric suction is the pressure exerted by a dry soil on the surrounding soils to balance the water content in the overall block of soil. Only matric suction is reviewed in this study.

Matric suction is usually correlated with the capillary phenomenon originated from the surface tension of water. The capillary forces have negative pore water pressure and they bring

soil water up through the pores in the soil. The matric or capillary suction is inversely proportional to the diameter of the pores as shown in Figure 2.18 and to the Relative Humidity (RH) of the soil water in the pores. Relative Humidity can be defined as the relative vapor pressure in the air immediately adjacent to the water ($\frac{u'_v}{u'_{vo}}$). The relation between RH and matric suction (ψ) is expressed in Equation 2.13.

$$\psi = \frac{R\,T_k}{v_{wo}\omega_v}\ln\left(\frac{u'_v}{u'_{vo}}\right) \qquad 2.13$$

where

ψ = soil suction or total suction, kPa,

R = universal (molar) gas constant [i.e., 8.31432 J/(mol K)]

T_K = absolute temperature

$\boldsymbol{v}_{wo}$ = specific volume of water or the inverse of the density of water, m^3/kg,

ρ_w = density of water (i.e., 998 kg/m^3 at temperature T = 20 C^0),

ω_v = molecular mass of water vapor (i.e., 18.016 kg/kmol),

$u`_v$= partial pressure of pore-water vapor, kPa,

$u`_{vo}$= saturation pressure of water vapor over a flat surface of pure water at the same temperature, kPa.

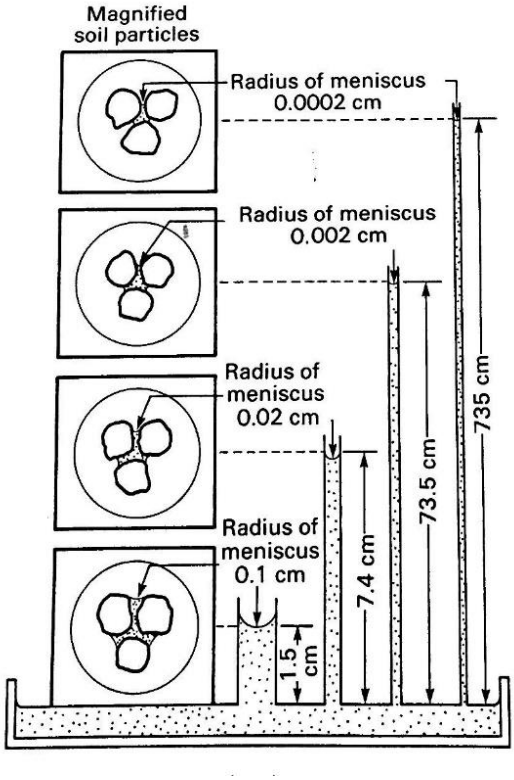

Figure 2.18 Capillary tubes showing air-water interfaces at varying heights for different radii of curvature (Jansen and Dempsey, 1980)

2.5.3 Measurements of Suction

The pore pressure in the soil above the water table is negative, which makes the soil partially saturated with water. Partially saturated soil has different engineering behavior than fully saturated soil. Therefore, it is important to measure the negative pore pressure or suction in the soil. Primarily, suction is quantified either directly using a high air entry ceramic tip as an interface with surrounding soil or indirectly by measuring another property which relates to the suction in the soil**.** Advantages and shortcomings of each method are discussed in the subsequent sections.

2.5.3.1 Direct Measurement of Suction Using Tensiometers

Direct methods are based on the fluid equilibrium of water phase between a porous ceramic tip and the surrounding soil. The ceramic tip is connected to a suction gauge or transducer through the coaxial plastic tubing as shown in Figure 2.19. The tensiometers should be prepared by flushing water through the coaxial tubing to get rid of any air bubbles in the tensiometer. The existence of air bubbles cause cavitation in the water and consequently inaccurate suction measurements. The small size of the ceramic tip and the flexible tubing makes this type of tensiometers convenient for measuring suction in small areas with the least disturbance to the soil. Figure 2.20 shows typical time response to reach equilibrium condition between the small tip tensiometer and surrounding soil.

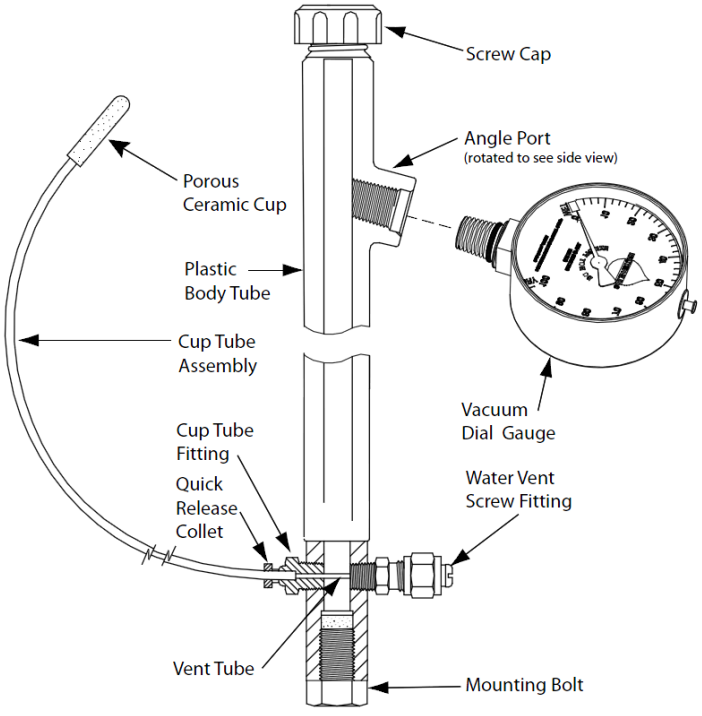

Figure 2.19 Small tensiometer tip (Soil Moisture Inc.)

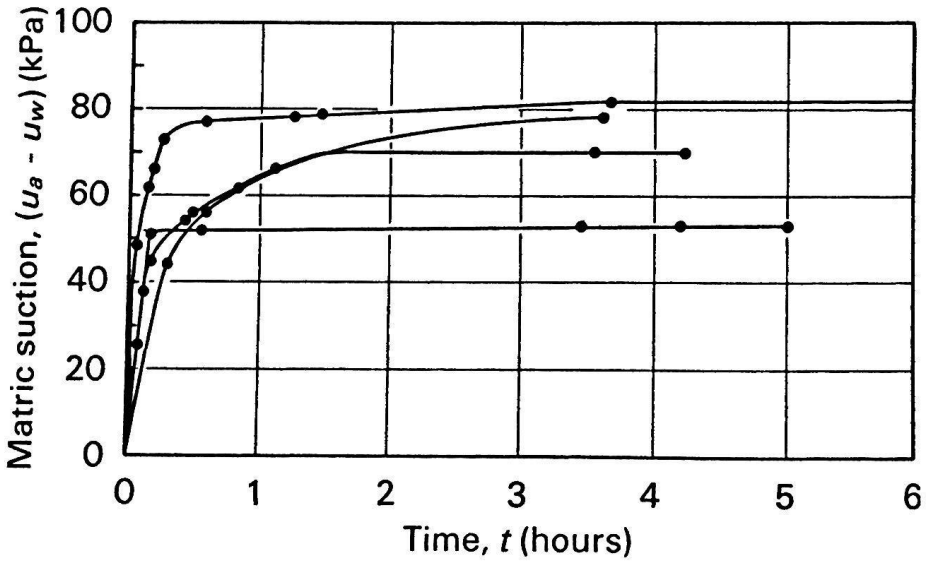

Figure 2.20 Typical time response of small tip tensiometer placed in decomposed volcanic soil (after Sweeny, 1982)

Small tip tensiometer does not require any calibration and it measures suction accurately if the tip is in good contact with the soil. However, the tensiometer must be prepared properly before each usage and every two days if it is used for an extended period (Sweeny, 1982). The capacity of this type of tensiometers is limited to 90 kPa. Beyond this suction, water starts to cavitate and measured suction drops sharply.

Another type of tensiometers is called High Suction Tensiometer (HST). HST, supposedly measures suction higher than 90 kPa, was developed by Guan and Fredland (1997), Meilani et al. (2002), Li (2013), and others. HST consists of a thin ceramic disk of 1-2 mm thickness attached to a pressure transducer with 0.1-0.5 mm gap which works as a water compartment as shown in Figure 2.21. HST is based on the same principle followed in small tip tensiometer in which water equilibrium is reached between the ceramic tip and surrounding soil. HST requires a lengthy process of conditioning by which the water inside the water compartment is highly pressurized to

dissolve all free air. The pressurizing process is considered an essential step in the conditioning process according to Fredlund et al. (2011). Trials were performed in this study to manufacture high suction tensiometers following the procedures recommended in the literature. Measured suction lasts for periods much less than those reported in the literature due to the cavitation of water in the compartment. None of those tensiometers reported in the literature was used in a big scale test or in a test setup in open box. Fredlund et al. stated that HST is impractical for industrial or field measurements usage for their lengthy maintenance requirements. It is worth to note here that HST is not standardized nor commercialized yet.

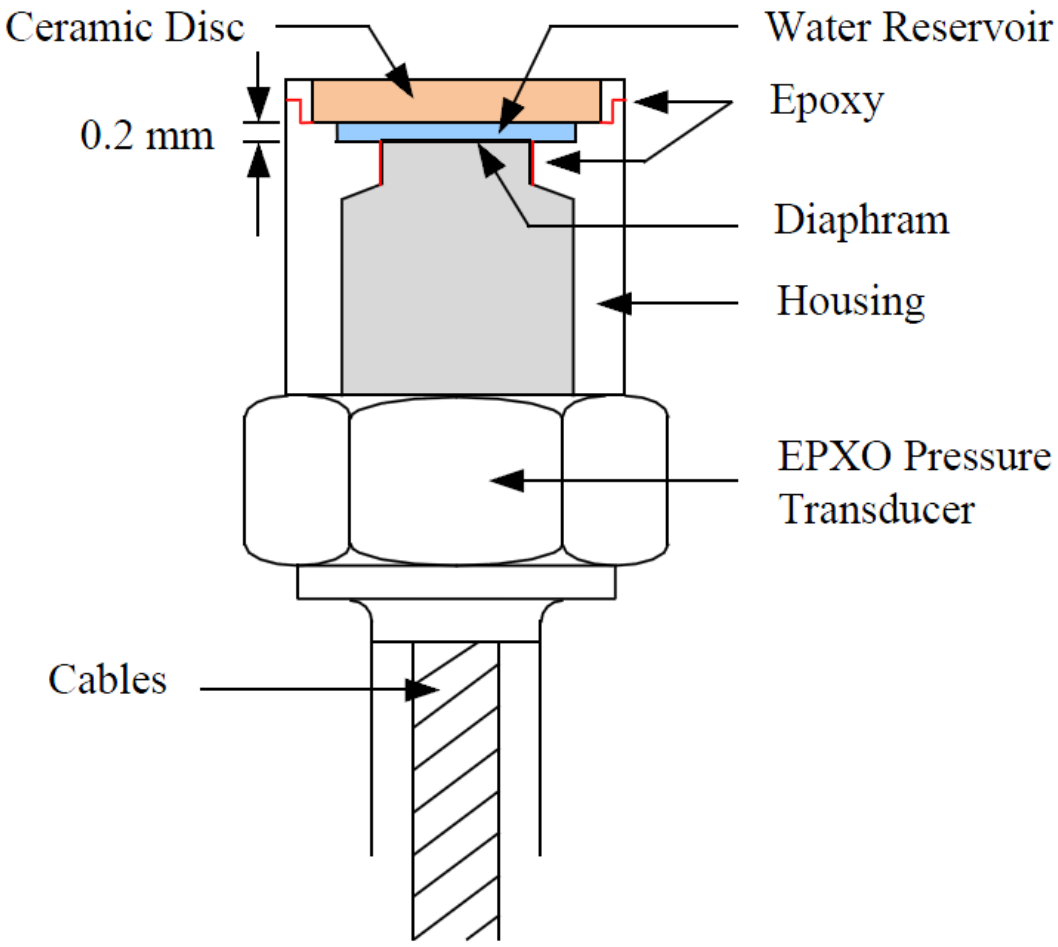

Figure 2.21 High suction tensiometer (Li, 2013)

It was shown that cavitation of water impeded the measurement of suction beyond 90 kPa. Null type axis translation device shown in Figure 2.22 was first proposed by Hilf (1956) and then used by Olsen and Langefelder (1965) and Fredlund (1989c). The concept of this technique is countering the measured suction by increasing the air pressure in the chamber. The increase in air pressure generates positive pore water pressure. The matric suction is then taken to be the difference between the air pressure in the chamber and the measured water pressure at equilibrium.

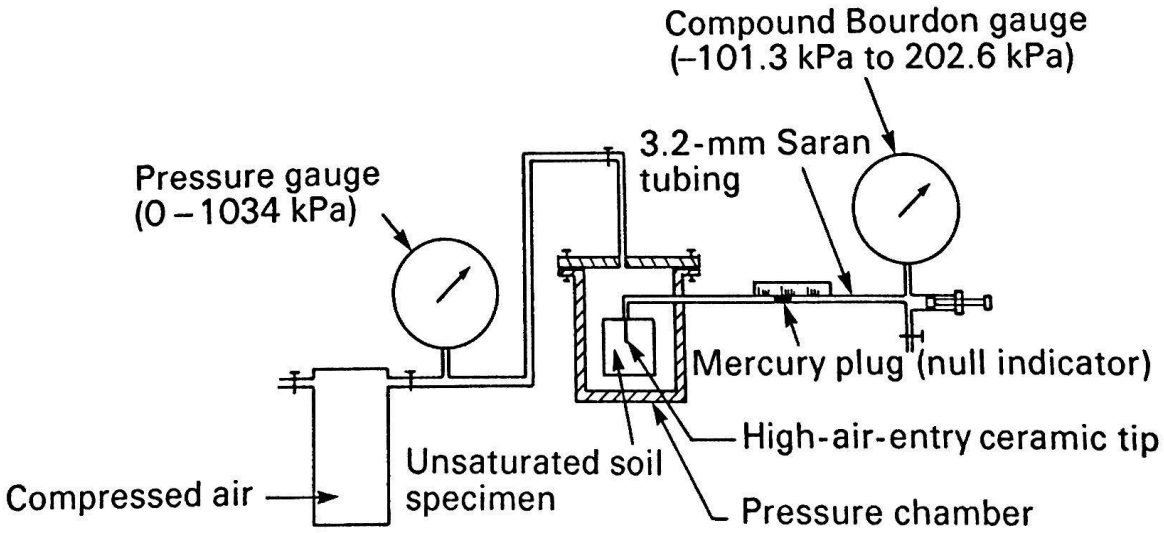

Figure 2.22 Axis translation device used to measure suction in soil (Hilf, 1956)

The axis translation technique basically shifts the origin of reference for the pore water pressure from standard atmospheric condition to the applied air pressure in the chamber (Figure 2.23). Axis translation technique prevents the problem of water cavitation when measuring suction above 90 kPa. However, its usage is limited to laboratory tests in a closed chamber. Axis translation technique is considered an inappropriate mean to apply or measure suction when testing

soil specimens with the percentage of fines higher than 50%. The issues associated with using the axis translation technique for measuring suction in cohesive soils are discussed later in this chapter.

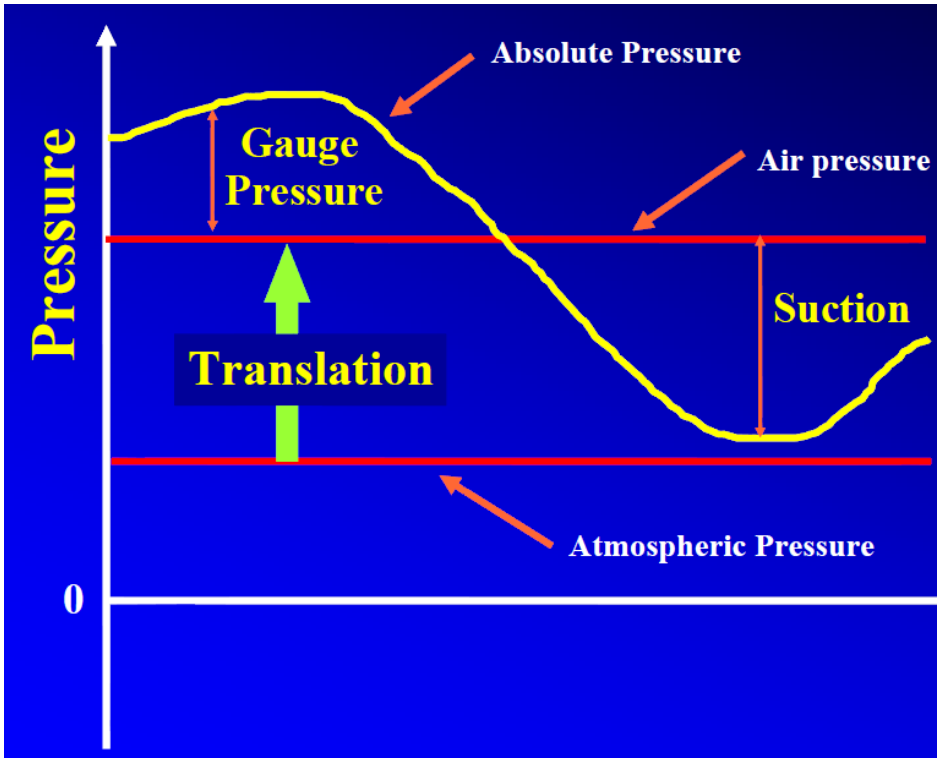

Figure 2.23 Concept of Axis translation technique, (Vanapalli et al. 2005)

2.5.3.2 Indirect Measurement of Suction

Practically, there is no efficient approach to measure the suction directly beyond 90 kPa while suction values in the cohesive soil could be well beyond 90 kPa. There is a need to develop indirect measurements of suction in the field and in open box test setup. In these methods, properties such as electrical resistance, thermal conductivity, water content, relative humidity, etc are measured in the soil. These properties are related to the suction in that soil. The efficiency of each method depends on how well that property is calibrated to the suction as well as on whether the measured property is sensitive to other factors in that soil. Fixed matrix porous ceramic disk

sensor is an indirect suction sensor that measures dielectric permittivity in the ceramic disk. Dielectric permittivity depends on the water content in the disk. Thus, the suction is quantified using predetermined soil water characteristic curve of the ceramic disk. When an equilibrium state is reached, the suction in the soil is considered same as the suction in the ceramic disk if there is a good contact between them. Figure 2.24 shows MPS-6 sensor commercially produced by Decagon Devices as an example of such suction sensors. The range of the MPS-6 sensor is 9 to 100 000 kPa which covers a wide range of suction values in geotechnical applications. Decagon claimed that the MPS-6 sensor could calibrate to have an accuracy of ± 10%. Tripathy et al. (2016) used the MPS-6 sensor to measure the suction in white kaolin and in MX 80 bentonite soils. The measurements of suctions were compared to suction readings obtained from identical samples using chilled mirror potentiometer. The results of the study indicated that the time to reach equilibrium between the sensor and the soil depends on the magnitude of suction in the soil and on the initial state of the sensor (dry or wet). Measurements of suction showed better agreement in white kaolin specimens than MX 80 bentonite specimens when MPS-6 measurements are compared with the results from the other devices as indicated in Figure 2.25.

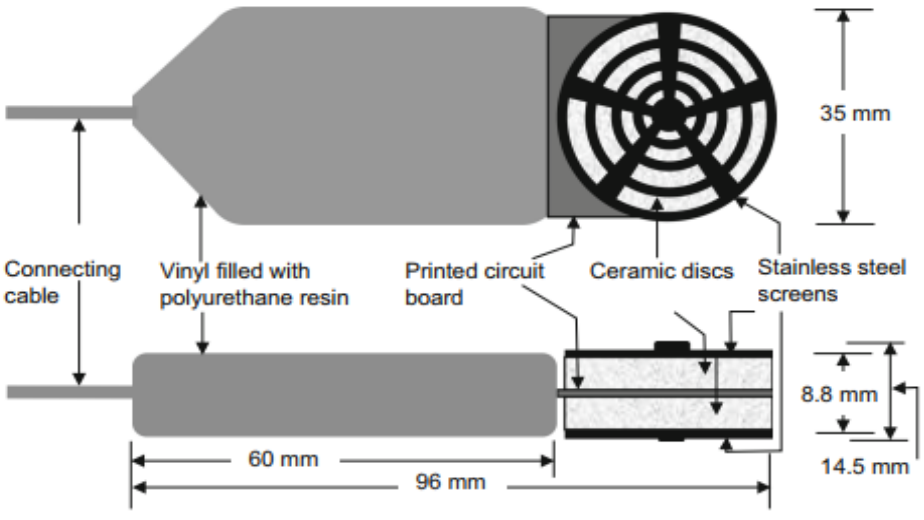

Figure 2.24 MPS-6 suction sensor (Tripathy et al., 2016)

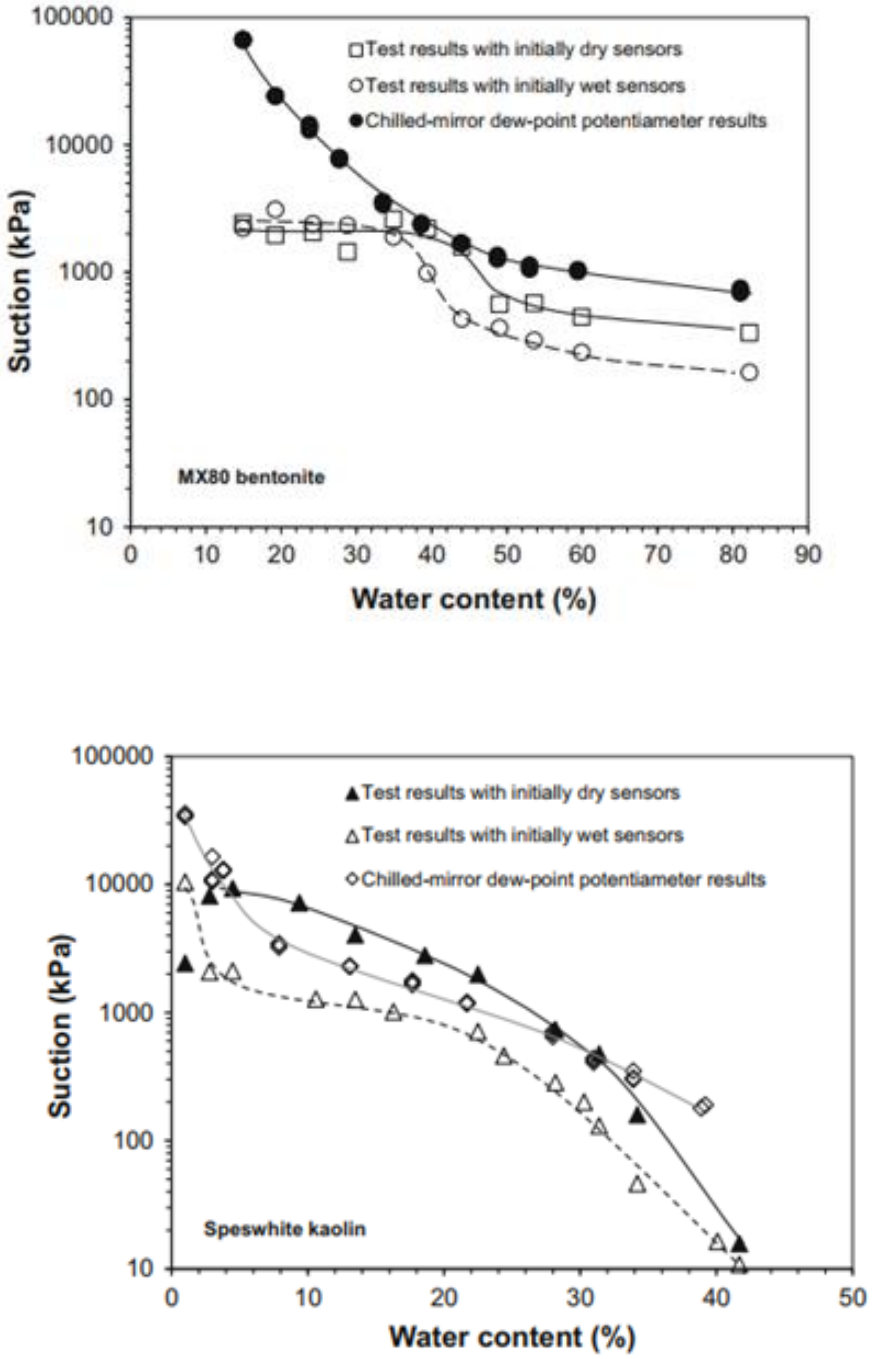

Figure 2.25 SWCC for bentonite (up) and kaolin (down) measured by MPS-6 and chilled mirror device (after Tripathy et al., 2016)

There are other indirect methods for measuring suction beyond 90 kPa in the soils. As stated earlier, these methods are measuring another soil property related to the suction in that soil.

Thermal conductivity sensors are based on reaching thermal equilibrium between the sensor and the soil. FTC-100 sensor manufactured by GCTC, Tempe, Arizona is an example of such sensor. Chilled mirror psychrometer is another device for measuring suction. In that approach, the vapor pressure potential which is related to relative humidity is measured. The suction is determined using the relation between suction and relative humidity presented in Equation 2.13. Both techniques are expensive and limited to lab usage. Those also require calibration.

Figure 2.26 shows ranges of accuracy for available instruments and sensors for measuring suction. It can be noticed that none of the instruments can measure the entire range of suction in the soil with consistent accuracy. Based on Figure 2.26, the MPS-6 sensor was selected to provide good accuracy for the range of suction chosen in this study (35-600 kPa). MPS-6 is affordable, requires much less maintenance, can be used in laboratory and field applications, and provides acceptable accuracy for research-level studies.

2.5.4 Soil Water Characteristic Curve (SWCC)

It was mentioned earlier that soil above the water table is primarily unsaturated. This soil has negative pore water pressure (suction) which is associated with a reduced degree of saturation in the voids of that soil. The increment in suction and reduction in saturation evolve towards approaching the ground surface. The relation between the suction and the degree of saturation in soil is called Soil Water Characteristic Curve (SWCC). Fredlund et al. (2011) stated that SWCC provides conceptual understanding between the mass (or volume) of water in a soil and the energy state of the water phase. SWCC also provides information about the distribution of the water in the voids and the ability of that soil to retain water. SWCC is the most fundamental constitutive relation that describes the behavior of partially saturated soils.

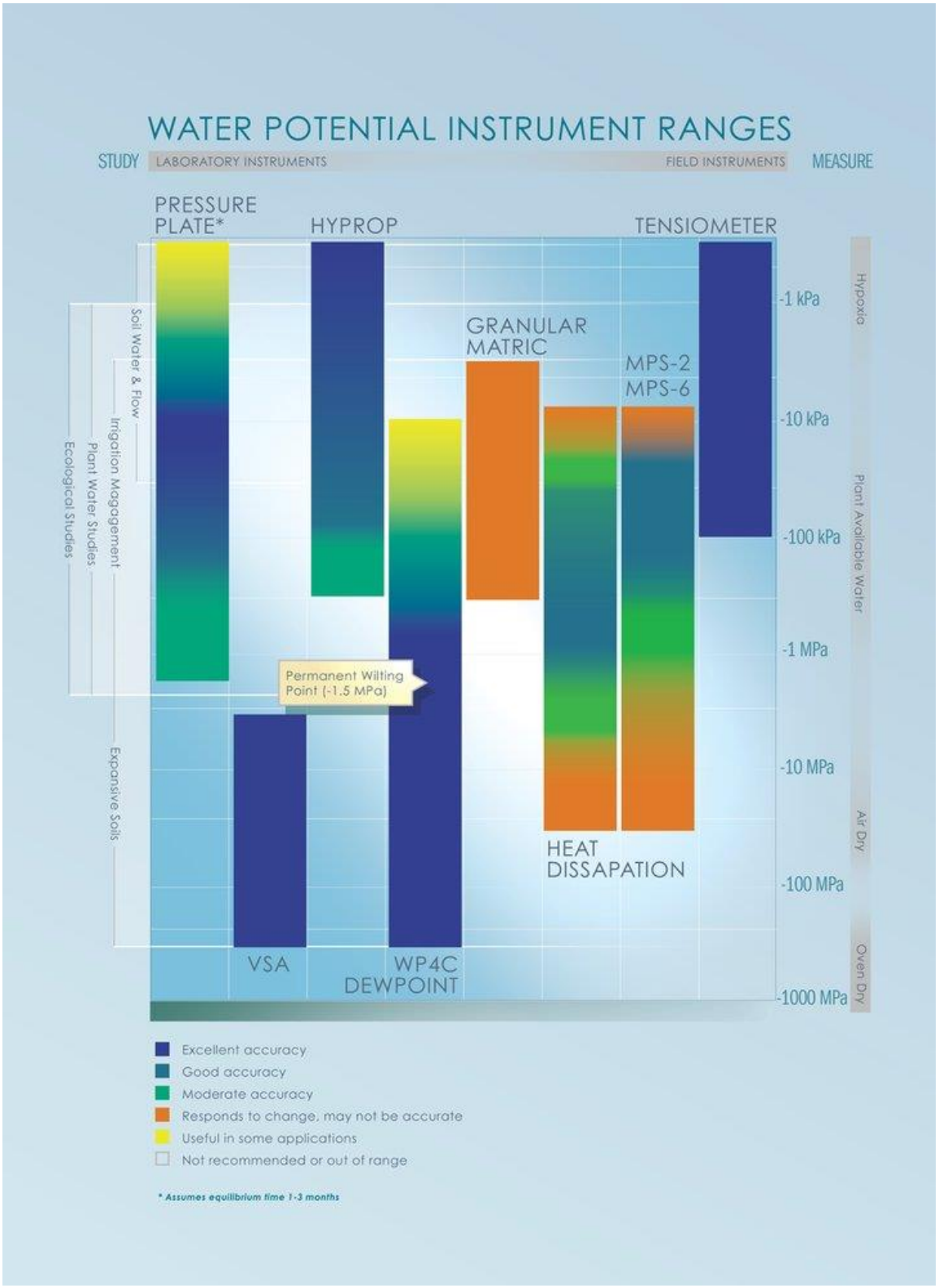

Figure 2.26 Ranges of different instruments for measuring suction (Decagon Inc.)

SWCC can be used with saturated soil properties to formulate partially saturated soil properties functions such as volume change, shear strength, and permeability functions. Depending on the saturation path followed, SWCC can be either constructed following drying (desorption curve) or wetting (adsorption curve) as shown in Figure 2.27. In this figure, there are three distinct stages. The first one is boundary effect stage followed by transition stage, while the third stage is called residual stage.

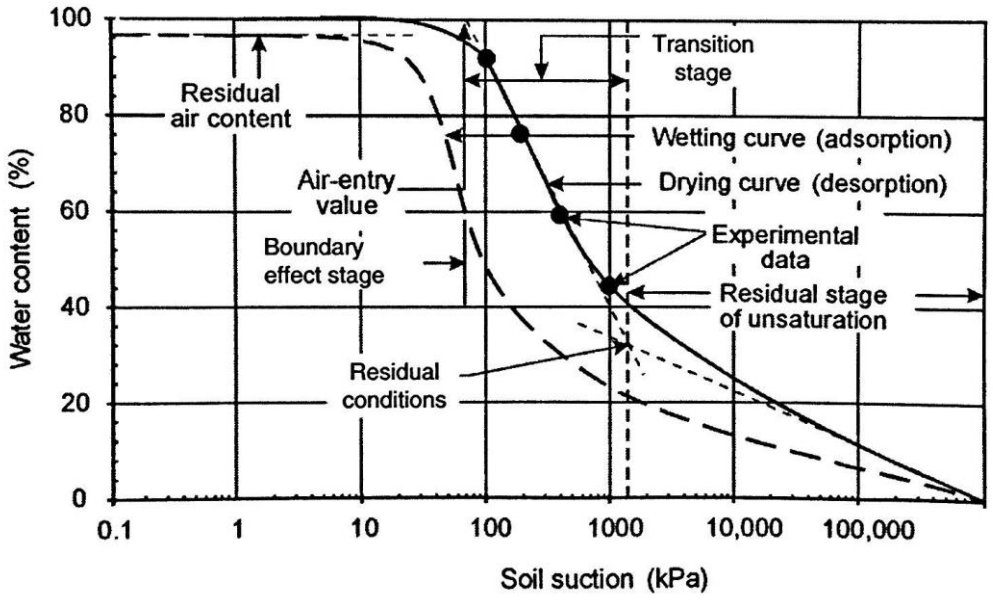

Figure 2.27 Definition of variables associated with typical SWCC (Fredlund et al., 2011)

2.5.4.1 Estimation and Determination of SWCC

The variation of moisture with suction can be represented using gravimetric water content, volumetric water content, or degree of saturation. Gravimetric water content does not require volume measurement, and the amount of water is referenced to a constant quantity which is the weight of dry soil. Gravimetric water content can be used to represent the moisture variable in non-deformable soils such as sand and low plasticity cohesive soils. The volume of these soils does not change significantly as the suction increased and the current volume (V_i) is nearly equal

to the original volume (V_o). In highly compressible soils, only volumetric water content (Θ_v), or degree of saturation (S_r) must be used to express moisture variables. Both variables are referenced to a current volume of the soil specimen.

Fredlund et al. (1997b) stated that the initial state of the soil must be indicated whenever SWCC test is conducted. Figure 2.28 shows stress history and the method of specimen preparation on SWCC. The preconsolidation pressure applied to the cohesive soil must be stated when performing SWCC. Figure 2.29 shows SWCC for Regina clay conducted on a sample preconsolidated to different pressures. The effect of applied net normal stress (total stress-air pressure) must also be considered. Some soils undergo a reduction in void ratio upon wetting (collapse behavior) while other soils may show expansive behavior upon wetting.

It can be observed from Figure 2.27 that there are two distinct points separating between three stages on the SWCC. The first point is the Air Entry Value (AEV) and the second one is the residual pressure.

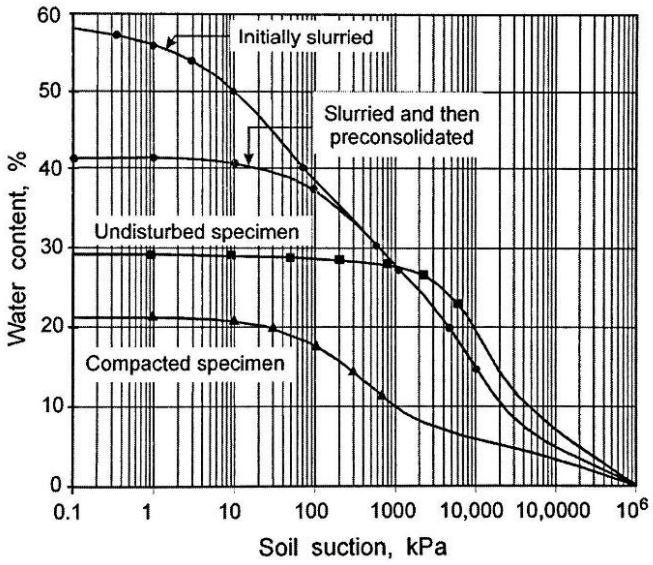

Figure 2.28 Effect of stress history and method of specimen preparation on measured SWCC (Fredlund et al., 2011)

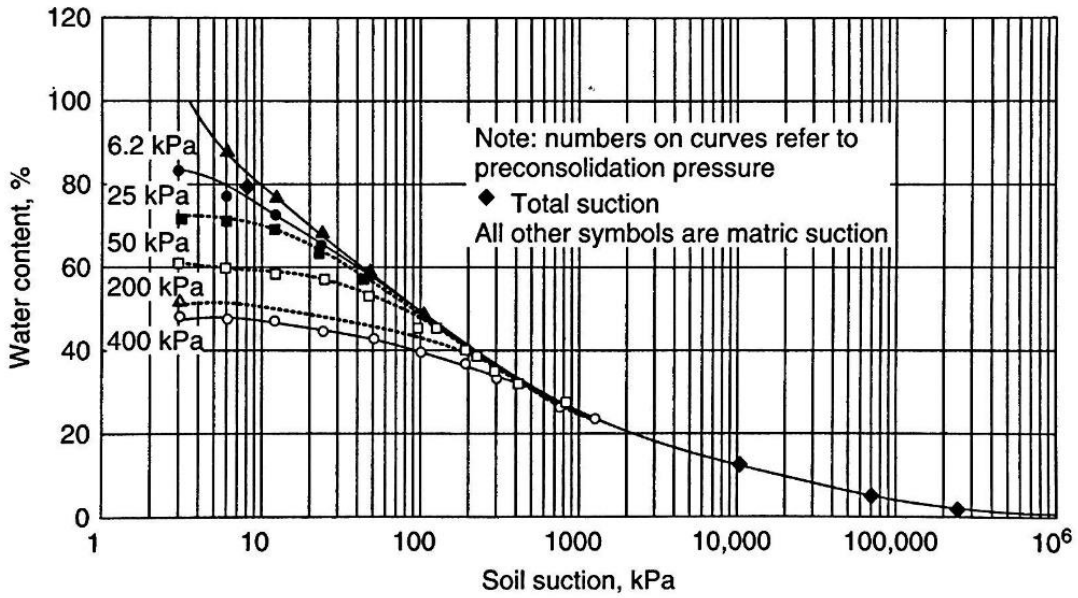

Figure 2.29 Soil suction vs. gravimetric water content for initially slurry Regina clay (Fredlund et al., 2011)

The air entry value differentiates between boundary effects stage and transition stage on the SWCC. Air entry pressure can be defined as the pressure at which the largest pore diameter starts to drain. In boundary effect stage, most of the soil voids are still filled with water, and the mechanics of fully saturated soil are still applied. In the transition stage, a considerable amount of water is drained, but the water phase is still continuous. The residual pressure is the pressure beyond which no significant change in water content occurs as the suction increases. The water vapor flow is dominated at this stage, and it is called residual stage.

SWCC can be constructed or estimated using empirical, analytical and experimental procedures. Analytical equations utilize the pore size distribution that has the form of a normal distribution curve. Analytical equations work better in uncompacted sandy or silty soils, but not discussed further in this study. For preliminary studies and low budget projects, SWCC can be estimated using empirical equations fitted from previous experimental results.

Fredlund et al. (2011) indicated that Brooks and Corey (1964) equation was among the earliest equations proposed for estimating SWCC using the power law as follows :

$$\theta_n = \left[\frac{\psi}{\psi_{aev}}\right]^{-\lambda bc} \qquad 2.14$$

where

Θ_n =normalized volumetric water content = $(\theta - \theta_r) / (\theta_s - \theta_r)$, where θ_s and θ_r are the saturated and residual volumetric water contents, respectively.

Ψ= soil suction,

Ψ_{aev}= air-entry value (or bubbling pressure)

λ= pore-size distribution index, and

b, *c* = soil parameters

Equation 2. 14 can also be made on the degree of saturation or the gravimetric water content if there is negligible volume change when measuring the SWCC.

Van Genuchetn (1980) presented the flowing continues equation to estimate SWCC :

$$\theta_n = \frac{1}{\left[1+(a_{vg}\psi)^{n_{vg}}\right]^{m_{vg}}} \qquad 2.15$$

where

Θ_n = normalized water content (i.e., normalized saturated water content, ϑ_s by residual water content, ϑ_r

Ψ= soil suction, and

a_{vg}, n_{vg}, m_{vg} = soil fitting parameters

Fredlund et al. (2011) indicated that empirical equations, in general, undergo some difficulties in the boundary effect stage where the slope of the SWCC curve gives nearly equal to zero. The zero value causes numerical instability. There is another difficulty in the residual stage where SWCC becomes asymptote to the horizontal line, and it causes numerical issues. Brooks and Corey (1964) and other empirical equations assumed that there is a sharp discontinuity in the SWCC around the air entry value. However, it is generally observed that medium and fine soils have a gradual transition between the boundary effect stage and transition zone.

The most common devices for determining SWCC experimentally are pressure plate and modified triaxial devices. Figure 2.30 shows a single pressure plate device. The device consists of a closed air pressure chamber with a burette for measuring water volume change. A specimen with known initial properties is placed on high air entry ceramic disc (HAECD). The ceramic disk works as a separator between the water and the air phases. The suction is applied using axis translation technique that was discussed earlier. The air displaces the water in the soil specimen until the equilibrium is reached when no more water comes out of the specimen at that pressure. The equilibrium time depends on the permeability and thickness of HAECD and the soil specimen. Maximum applied pressure depends on the air entry pressure of the HAECD and the capacity of the air source available in the laboratory. The pressure plate is a simple and inexpensive device. However, the test is time consuming. The time required to reach equilibrium in each step depends on the type and size of the soil sample and the initial state in the sample. This method is suitable for fine sand or coarse silt with moderate to high coefficient of permeability. However, it cannot measure the instantaneous change in the total volume of the sample, and therefore it does not work for highly compressible soils. This method does not offer tests with the stress controlled path.

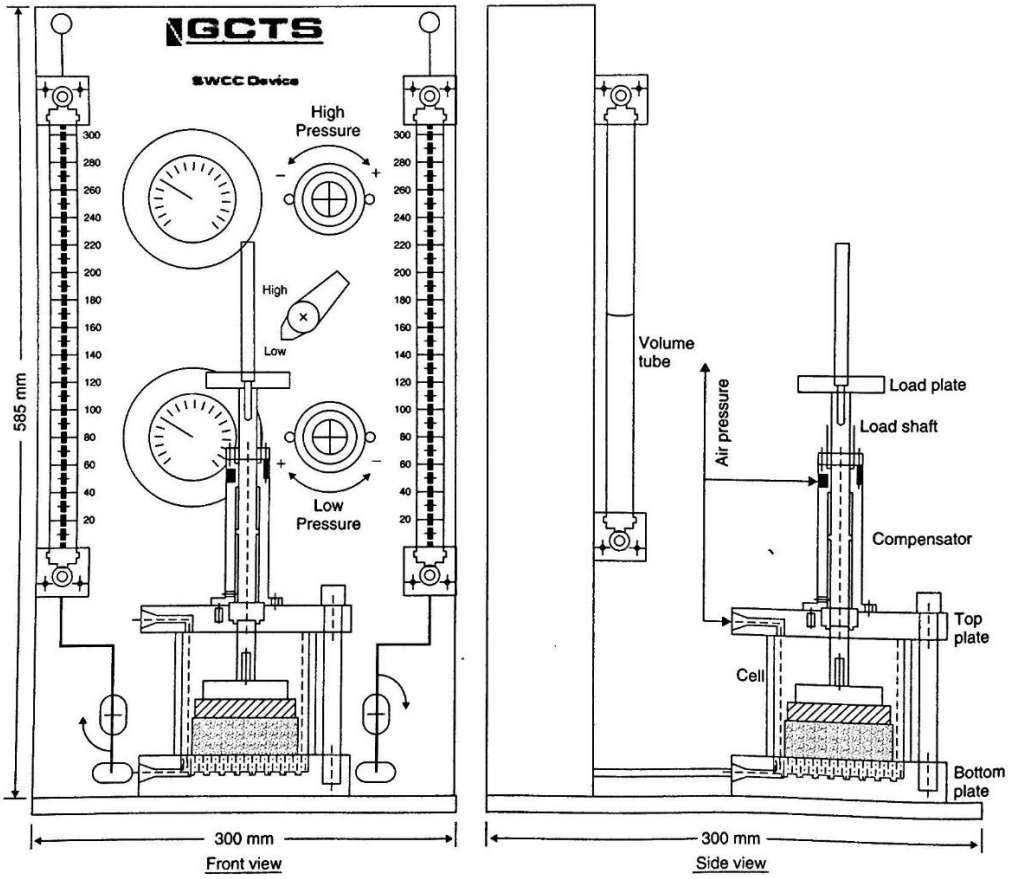

Figure 2.30 Front and side views of the GCTS pressure plate cell and the control panel (GCTS, Tempe, AZ)

Triaxial device can be modified to conduct SWCC tests (Figure 2.31). This method has the following advantages over the pressure plate device.

- Different pressure path can be applied.
- It can provide confinement on the sample.
- The sample can be saturated by applying back pressure on the specimen.
- Measurement of coefficient of permeability for the fully saturated specimens can be made.
- It can consolidate the specimen under the required pressure.

- It can measure instantaneous water and total volume change when suitable instruments are attached.
- The ability to test undisturbed soil specimens.
- It works well for all types of soils.

The biggest disadvantage of using the triaxial cell is the time consuming issues especially for cohesive soils with a low coefficient of permeability. As an example, testing on a cohesive soil specimen may take 7- 10 days for saturation and another 7-10 days for desaturating the specimen and reaching equilibrium for the applied pressure, although the negligible amount of water is coming out of the specimen. In general, 7 points SWCC test would require 6-8 weeks to be completed.

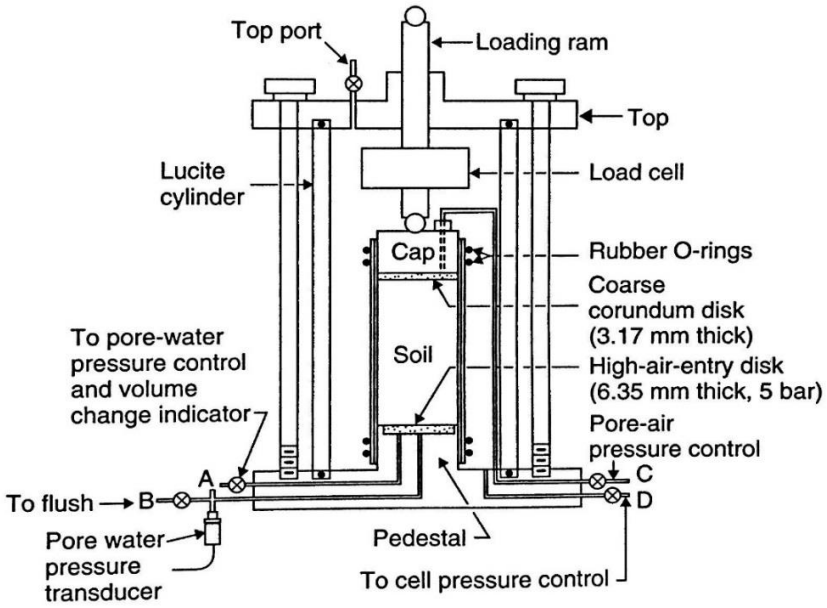

Figure 2.31 Modifications to convert conventional triaxial cell for testing unsaturated soils (Thu et al., 2007)

For low permeability specimens, a continuing flushing process is required to get rid of diffused air underneath the ceramic disk. Diffused air volume must be deducted from the volume change of water. Inaccurate water volume change may occure when ignoring or underestimating the flitting process (Fredlund, 1975). The air pressure is applied to the air entry value (AEV) of the ceramic disk. A ceramic disk of high AEV has a low coefficient of permeability that would retard the desaturation process. In summary, it has stated earlier that the modified triaxial device is suitable for establishing SWCC for all type of soils. However, time consumption issue limits its applications to sandy or silty soils.

Thu et al. (2007) conducted drying and wetting SWCC tests on silty soil specimens of (50 dia.x100 high) mm using a modified triaxial test. Different confining pressures were applied to study the effect of confinement on the AEV of the tested specimens. Thu et al. concluded that the AEV was increased with confinement pressure as shown in Figure 2.32. Confining pressure consolidates the specimen and reduces the pore sizes, which implies that higher pressure is required for the air to get through the soil pores.

There are other devices for constructing SWCC such as chilled mirror or psychometers. These apparatuses are expensive and used for high suction levels that is out of interest in this study.

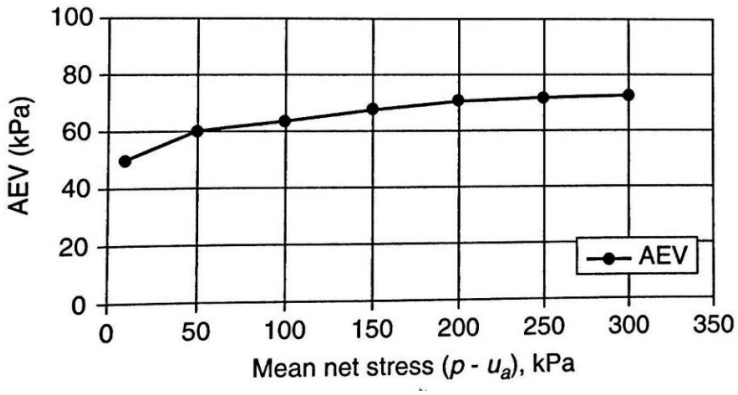

Figure 2.32 Variation of AEV with confining pressure, (Thu et al., 2007)

In Summary, direct measurements of suction were adopted in this study using small tensiometer tip (Figure 2.19) for suction below 85 kPa. MPS-6 sensor was used for suction higher than 85 (Figure 2.24).

2.5.5 Shear Strength of Partially Saturated Soil

Bearing capacity is a key design parameter in any foundation design. The bearing capacity in all types of soils depends on the shear strength of that soil. Same shear strength principles are applied on both fully and partially saturated soils. For instance, the dependency of shear strength on stress state, strain level, dilatancy, and stress history is applicable on both types of soils. Several identical samples are needed to determine the shear strength equation of partially saturated soil. Soil specimens that are considered to be identical must be prepared with the same initial water content and statically compacted with the same effort. Modified triaxial or modified direct shear devices can be used for determining shear strength equation for partially saturated soils.

2.5.5.1 Measurement of Shear Strength of Partially Saturated Soil

Shear strength of partially saturated soil is commonly obtained using modified triaxial test or modified direct shear test device. The modification process mainly includes the following:

- It shall install an appropriate High Air Entry Ceramic Disk (HAECD) to seat the specimen on. The ceramic disk works as a separator between the air and water phases and provides continuity between the water phase in the specimen and the testing system. The maximum applied air pressure depends on the air entry value of the disk. The rate of desaturation depends mainly on permeability and thickness of HAECD (Fredlund et al., 2011).

- A system shall have the ability to flush diffused air bubbles underneath HAECD. The frequency of flushing processes depends on the type of the soil and the level of suction applied. Fredlund (1975) indicated that ignoring flushing processes results in inaccurate readings of water volume change and possibly negative water content at the end of the test in cohesive soils.
- The mechanism for measuring total volume change must be provided when testing compressible soil.

Modified triaxial devices provide more options when conducting path dependent tests as well as more drainage controlled tests. Figure 2.33 shows stress conditions at various stages of constant water content compression (CWU) test.

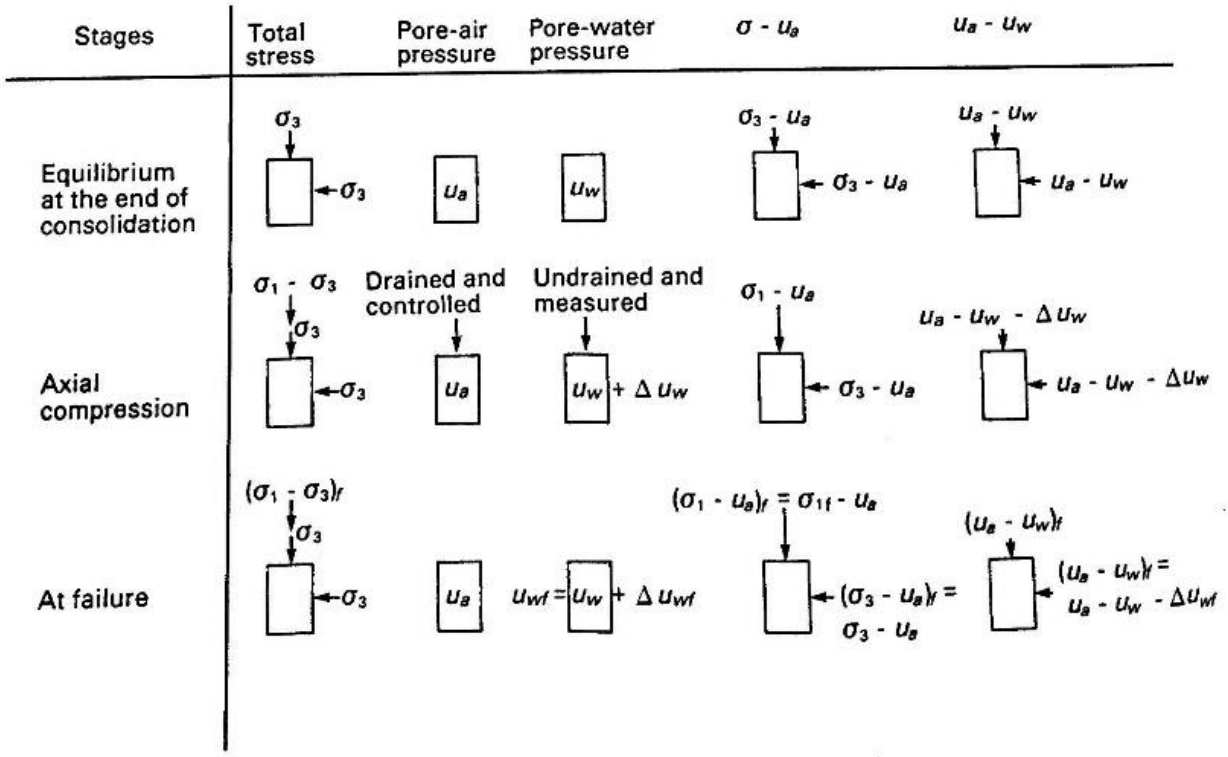

Figure 2.33 Stress conditions at various stages of CWU test (Fredlund et al., 2011)

Thu et al. (2007) conducted a series of CD and CWU triaxial tests to investigate the shear strength of partially saturated soils. The results of their tests confirmed the nonlinearity in (ϕ^b) over an extended range of matric suction, where ϕ^b is the friction angle resulted from the suction component in the shear strength equation of unsaturated soils. Experimental determination of shear strength requires testing series of fully and partially saturated specimens. The main challenge in such tests is the time required for saturating and desaturating the specimens as discussed earlier in 2.5.7.

To overcome the time consumption issue when conducting such experimental tests, Sandra et al. (2008) followed a more efficient method to prepare the specimens. In this method, the specimen was allowed to dry out at the outside of the triaxial cell until reaching the water content corresponding to the target suction. Such preparation method is more time efficient than a conventional preparation method. It utilizes SWCC to obtain the target suction. As shown in Figure 2.27 however, there are two primary paths in SWCC; drying and wetting, which makes two different suction values at the same water content and those differences unable to distinguish in this method. A more convenient approach would be inserting a suction sensor to read the suction value in the specimen directly, rather than using SWCC to get the target suction.

Adopting multi-stage tests in direct shear or triaxial devices is another approach to address the disadvantage of a conventional preparation method concerning time consumption and a large number of required specimens. Bishop (1960), Ho and Fredlund (1982 b), and Krahn et al. (1989) conducted multi-stage CD and CW tests. Sookie et al. (2011) successfully performed multi-stage direct shear tests (Figure 2.34 a) and proposed a relation between shear strength and suction from the multi-stage test results as shown in Figure 2-34 b. The most significant precaution that must be considered in this method is to shear the specimens just below the peak shear stress to the strain

softening region. Another precaution is to make sure that the sample is completely consolidated at every new effective normal stress level. Application of the above precautions require some experience and trials.

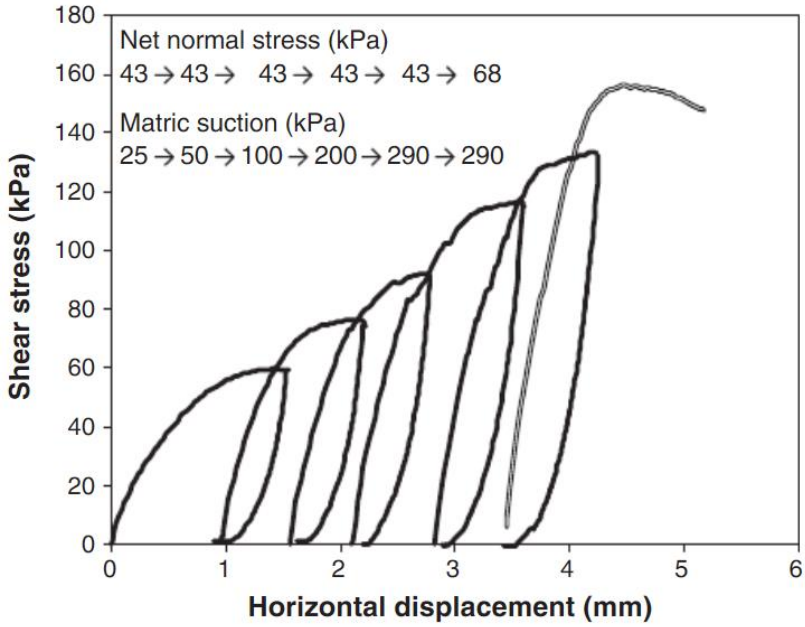

(a)

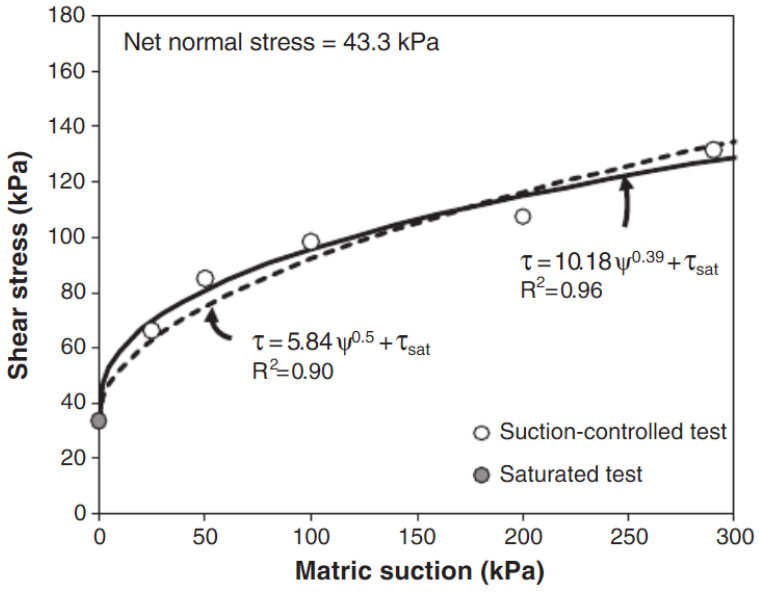

(b)

Figure 2.34 (a)Multi-stage direct shear test of unsaturated soil specimen, (b) the relation between shear strength and suction (Sookie et al., 2011)

2.5.5.2 Shear Strength Equations for Partially Saturated Soil

Essentially, shear strength equations can be categorized into fitted and predicted equations. Fitted equations require conducting a series of shear tests on identical soil specimens of different suction values. Predicted equations use soil properties of fully saturated soil and SWCC. Guan et al. (2010) listed a group of published equations for computing shear strength equations for partially saturated soil in Table 2.1.

Table 2.1 Shear strength equation of partially saturated soil (Guan et al., 2010)

Authors	Nature	Shear strength equations
Fredlund et al. (1978)	Fitting	$\tau = c' + (\sigma - u_a)\tan\phi' + (u_a - u_w)\tan\phi^b$
Shen and Yu (1996, Eq. 1)	Fitting	$\tau = c' + (\sigma - u_a)\tan\phi' + (u_a - u_w)\left(\frac{1}{1+(u_a-u_w)d}\right)\tan\phi'$
Shen and Yu (1996, Eq. 2)	Fitting	$\tau = c' + (\sigma - u_a)\tan\phi' + (u_a - u_w)\left(\frac{1}{\cot\alpha + \frac{(u_a-u_w)}{\beta_1}}\right)\tan\phi'$
Vanapalli et al. (1996b, Eq. 1)	Fitting	$\tau = c' + (\sigma - u_a)\tan\phi' + [(u_a - u_w)\Theta^{\kappa}]\tan\phi'$
Vanapalli et al. (1996b, Eq. 2)	Prediction	$\tau = c' + (\sigma - u_a)\tan\phi' + (u_a - u_w)\left[\tan\phi'\left(\frac{\theta_w - \theta_r}{\theta_s - \theta_r}\right)\right]$
Oberg and Sallfors (1997)	Prediction	$\tau = c' + (\sigma - u_a)\tan\phi' + (u_a - u_w)[(\tan\phi')(S)]$
Bao et al. (1998)	Prediction	$\tau = c' + (\sigma - u_a)\tan\phi' + (u_a - u_w)(\zeta)(\tan\phi') \quad \zeta = \left[\frac{\log(u_a-u_w)_r - \log(u_a-u_w)}{\log(u_a-u_w)_r - \log(u_a-u_w)_b}\right]$
Khalili and Khabbaz (1998)	Prediction	$\tau = c' + (\sigma - u_a)\tan\phi' + (u_a - u_w)[(\lambda')(\tan\phi')] \quad \lambda' = \left\{\frac{(u_a-u_w)}{(u_a-u_w)_b}\right\}^{-0.55}$
Rassam and Cook (2002)	Fitting	$\tau = c' + (\sigma - u_a)\tan\phi' + \psi\tan\phi' - \varphi(\psi - \psi_e)^{\beta} \quad \varphi = \frac{\psi_r\tan\phi' - \tau_{Sr}}{(\psi_r - \psi_e)^{\beta}} \quad \beta = \frac{\tan\phi'(\psi_r - \psi_e)}{\psi_r\tan\phi' - \tau_{Sr}}$
Tekinsoy et al. (2004)	Prediction	$\tau = c' + (\sigma - u_a)\tan\phi' + \tan\phi'(\psi_e + P_{at})\ln\left[\frac{\psi + P_{at}}{P_{at}}\right]$
Lee et al. (2005)	Fitting	$\tau = c' + [(\sigma - u_a) + (u_a - u_w)]\tan\phi'$ if $(u_a - u_w) \le AEV$ $\tau = c' + [(\sigma - u_a) + AEV]\tan\phi' + [(u_a - u_w) - AEV]\Theta^{\kappa}[1 + \lambda(\sigma - u_a)]\tan\phi'$ if $(u_a - u_w) > AEV$
Garven and Vanapalli (2006)	Prediction	$\tau = c' + (\sigma - u_a)\tan\phi' + [(u_a - u_w)\Theta^{\kappa}]\tan\phi'$ $\kappa = -0.0016I_p^2 + 0.0975I_p + 1$
Vilar (2006)	Fitting	$\tau = c' + (\sigma - u_a)\tan\phi' + (u_a - u_w)/[a + b(u_a - u_w)] \quad 1/a = \tan\phi' \quad b = 1/(c_{ult} - c')$

Bishop (1959) extended the effective stress principle in fully saturated soil to partially saturated soils expressed in the following equation:

$$\tau = c' + [(\sigma_n - u_a) + x(u_a - u_w)]\, tan\varphi' \qquad 2.16$$

where

c' : effective cohesion of the soil,

(σ_n - u_a) : net normal pressure,

(u_a - u_w): matric suction in soil,

χ: soil parameter related to degree of saturation, and

φ′ : friction angle associated with the net normal stress state variable, (σ_n-u_a).

The validity of the Bishop equation was questioned by Jennings and Burland (1962),who stated that the Bishop equation could not represent the collapse behavior upon wetting. They performed several consolidation tests on different partially saturated specimens and noticed that upon reducing the suction, the void ratio decreased (collapsed) rather than expanded as is stated by the Terazagi effective stress equation. Burland (1965) further stated that from a microscopic point of view, it is improper to combine (σ_n-u_a) and (u_a-u_w) into one equation.

Another drawback pointed at the Bishop equation is that there is no direct relation between χ and the degree of saturation Sr. Coleman (1962) indicated that the parameter χ is mostly related to the soil structure rather than the degree of saturation. However, researchers such as Kohgo et al. (1993), Modaressi and Abou Bekr (1994), Zon et al. (1996), Loret and Khalili (2000), Khalili and Loret (2001) stated that the Bishop equation was invariably formulated within the context of linearly elastic theoretical framework. Those investigators have shown that the recoverable plastic deformation such as collapse can be readily described within an effective stress frame work by

defining the yield surface as a function of suction and taking into account the hardening effect at suction on the soil response.

In their support of the Bishop equation, Khalili et al. (2004) stated that even in saturated soils,

some unrecoverable deformation such as dilation or collapse in metastable structures can not be explained in terms of effective stress alone unless they were related to a suitable plasticity model. Khalili and Khabbaz (1998) indicated that it is possible to have a unique relationship between the parameter χ and the suction ratio (the ratio of the suction to the air entry value.) as shown in Figure 2.35.

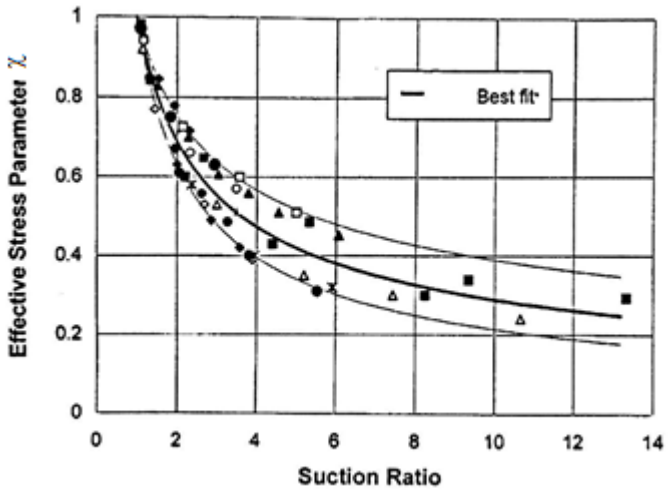

Figure 2.35 Relation between χ vs. suction ratio (Khalili and Khabbaz, 1998)

Khalili et al. (2004) analyzed results of a series of conducted tests and literature data. They provided experimental evidence to verify the effective stress principle in partially saturated soil presented by Bishop.

Another approach for describing the shear strength of partially saturated soils was presented by Fredlund et al. (1978) as shown in Equation 2.17. In this equation, two stress state variables were used, and the effect of suction on shear strength was separated

$$\tau = c' + (\sigma_n - u_a)\tan\varphi' + (u_a - u_w)\tan\varphi^b \qquad 2.17$$

where
c' = effective cohesion

$(\sigma_n - u_a)_f$ = net normal stress at failure,

$(u_a - u_w)_f$ = matric suction in soil at failure, and

φ^b = angle demonstrating the rate of increase in shear strength with respect to a change in matric suction.

In Equation 2.17, the contribution of suction to shear strength was assumed to be linear. A linear shear strength envelope was proposed by using three dimensional extended Mohr-coulomb failure envelope as seen in Figure 2.36. In the two dimensional plot shown in Figure 2.37, a horizontal projection onto the shear strength is plotted on U_a plane. This envelope can be constructed by testing a series of saturated and partially saturated specimens.

It is shown in Figure 2.38 by Vanapalli et al. (1996). Also many other researchers, such as by Escario and Saez (1986), Gan et al. (1988), Escario and Taca (1989), Fredlund et al. (1995) and more recently, by Thu et al. (2006), Sandra et al. (2008), Hamid et al. (2009), and Snookie et al. (2011) have indicated that the increase in shear strength is linear up to the air entry value of that soil and then, as the desaturation process continues, the increase in effective stress becomes less effective and exhibits a nonlinear trend. Approaching towards the residual stage where the water phase is discontinuous, the increment in shear strength becomes insignificant and minor.

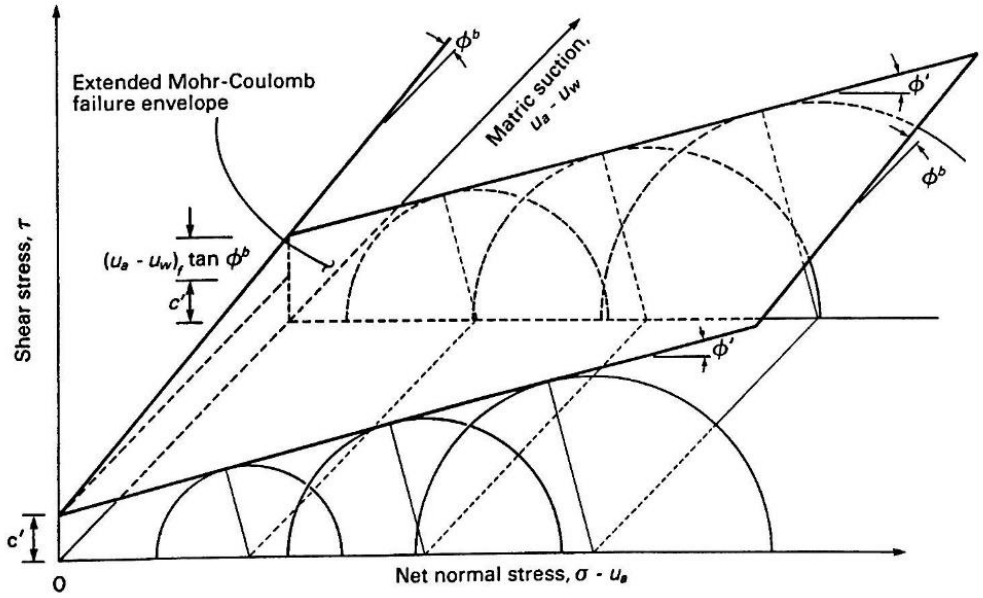

Figure 2.36 Extended Mohr-Coulomb failure envelope for unsaturated soil (Fredlund et al., 2011)

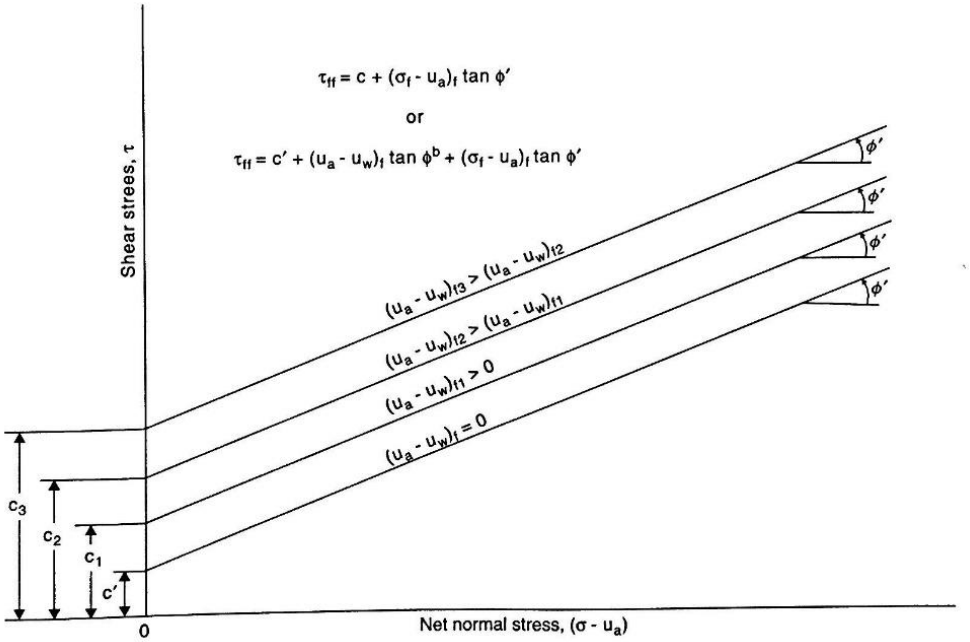

Figure 2.37 Horizontal projection of failure envelope onto τ vs. σ-u_a (Fredlund et al., 2011)

Figure 2.39 compares the linear version of shear strength equations presented by Bishop (1959) and Fredlund (1978). It can be noticed that the contribution of suction in Fredlund equation is expressed by vertical translation from the saturated failure envelope point (A), while in Bishop equation the increment represented in horizontal translation point (A′).

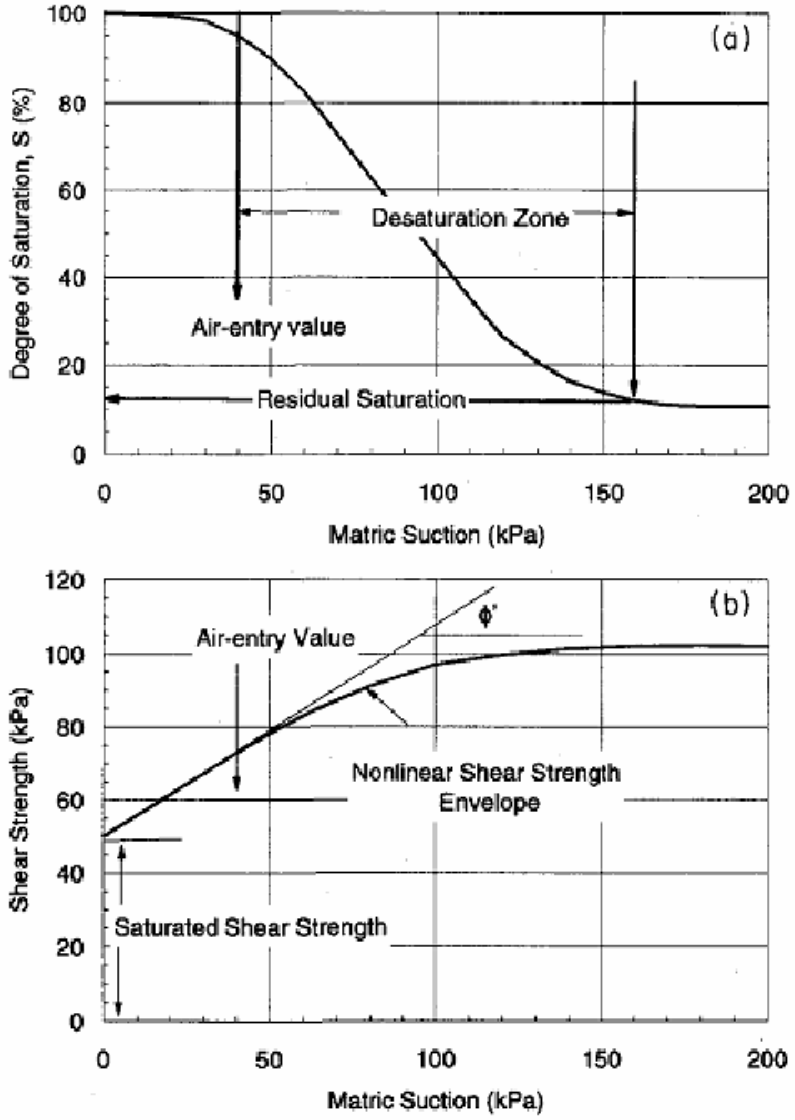

Figure 2.38 Nonlinearity of shear strength envelope with suction (Vanapalli et al., 1996)

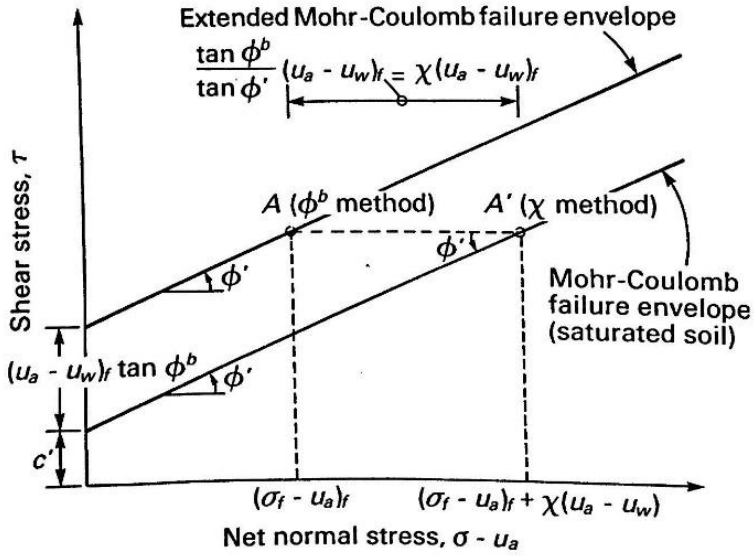

Figure 2.39 Comparision between χ and ϕ^b methods of designating shear strength (Fredlund et al., 2011)

Some of proposed fitted and predicted equations are compared with experimental results conducted by Escarion and Juca (1989) in Figure 2.40. It can be noticed that all equations commenced with linear behavior then exhibit nonlinear behavior beyond certain suction values.

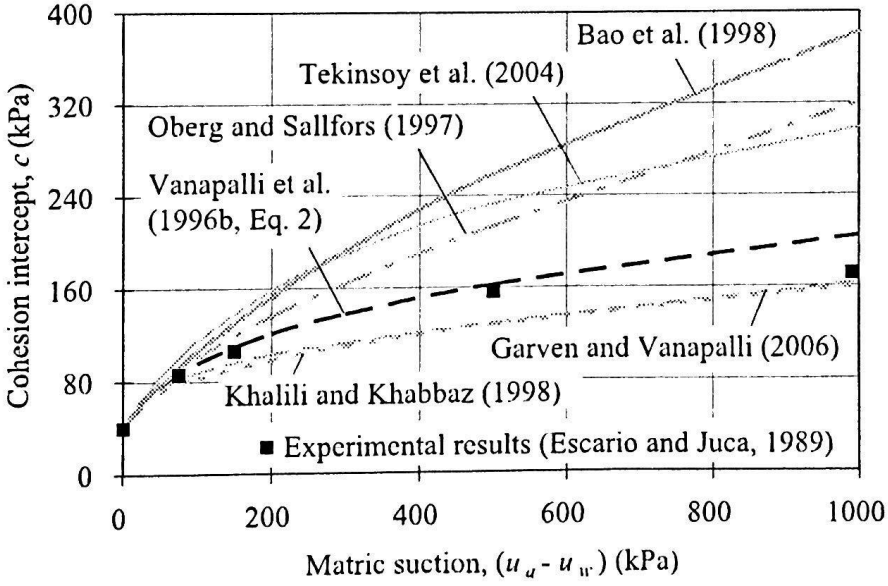

Figure 2.40 Comparison between different methods for determining shear strength with experimental results (Fredlund et al., 2011)

2.6 Numerical Modeling

Accurate modeling of the piled raft foundation is necessary to simulate the behavior of the foundation and surrounding soil. Primarily, the finite element model contains geometric, constitutive and contact modeling. One of the crucial aspects that must be appropriately considered in the modeling process is nonlinearity. Typically, there are three types of nonlinearity; geometric, material, and contact nonlinearities.

2.6.1 Geometric Modelling

Geometric modeling is the first step in constructing a finite element model. The geometry of the model is defined including all solid extrusions, cut, and fillets. Nonlinearity effects in geometric modeling become important when the load on a model results in large displacement. In linear geometry, the dimensions of the element are not updated as the load changes. Meanwhile in nonlinear geometric modeling, Abaqus is capable of updating the size, shape, and position of the element at each loading step. For nonlinear geometric analysis reference (undeformed) and current (deformed) configurations are not the same, and the higher strain orders are considered in the analysis. Abaqus theory manual stated that as a rule of thumb if strains are exceeding 5%, then the measures of stress and strain are different and nonlinear geometric analysis should be adopted. The nonlinear analysis was adopted in this study.

2.6.2 Constitutive Modeling

Constitutive modeling is used to describe the mechanical behavior of materials. It is known that soil are anisotropic, non-homogenous, three-phase material and consist of a number of discrete

particles. Soils are pressure dependent materials that exhibit hardening behavior as a function of plastic strain. Therefore, those cannot be modeled by the pure elastic theory. Hence, constitutive behavior of fully and partially saturated soils is represented by means of elastoplastic models obtained mainly from Abacus theory guide and other literature.

2.6.2.1 Elasticity

Conventional linear isotropic elasticity represented by Young's modulus and Poisson's ratio can be used to define the elastic behavior of soil. Another option that can be used also is porous elasticity. Porous elasticity is a nonlinear elasticity model in which volumetric strain is a function of applied pressure as shown in Equation 2.18 below:

$$\frac{\kappa}{(1+e_0)} \ln\left(\frac{p_0 + p_t^{el}}{p + p_t^{el}}\right) = J^{el} - 1 \qquad 2.18$$

where

J^{el} -1 is nominal volumetric strain, J is the Jacobian determinant and equal to dV/dV^o ,

κ= slope of normal consolidation reloading line,

p_o = the initial value of the hydrostatic pressure,

p^{el}_t = elastic tensile stress limit (allowed to be zero or non-zero),

p = the final value of the hydrostatic pressure, and

e_o = initial void ratio.

The behavior of the deviatoric tensor S_{ij} is defined by selecting a constant Poisson's ratio which makes the deviatoric stiffness dependent on the pressure stress as follows:

$$d\boldsymbol{S}_{ij} = 2G\hat{}d\boldsymbol{e}^{el} \quad 2.19$$

where e^{el} is the instantaneous void ratio in the elastic range, and the instantaneous shear modulus $\hat{G}$ is given by:

$$\hat{G} = \frac{3(1-2\nu)(1+e_0)}{2(1+\nu)\kappa}(p+p_t^{el})\exp(\varepsilon_{vol}^{el}) \quad 2.20$$

where

ε_{vol}^{el} = elastic volumetric strain, and

ν = Poisson's ratio.

2.6.2.2 Plasticity

Plasticity of soil is characterized by unrecoverable strain property when the applied stress goes beyond a certain level. Plasticity can be related to the collapse of soil skeleton and the permanent displacement of soil particles. Plasticity theory was originally developed to simulate the plastic behavior of metal and then extended to include model describing the pressure dependent plastic behavior of soil, concrete, and polymers.

Modified Cam Clay model and Drucker Prager Cap models are among other available plastic models to describe the plastic behavior of soil in Abaques. Helwany (2007) stated that an ideal plasticity model should include: (1) a yield criterion that predicts material behavior whether it is elastic or plastic, (2) a strain hardening rule that controls the shape of the stress-strain response during plastic straining, and (3) a plastic flow rule that determines the direction of the plastic strain increment caused by a stress increment.

The first completed elasto plastic model presented explicitly for partially saturated soil was Barcelona Basic Model (BBC). The model was first proposed by Alonso et al. (1990) and was

formulated in terms of net stresses ($p - u_a$) and suction ($u_a - u_w$). The three-dimensional yield surface in ṕ - q – s space is demonstrated in Figure 2.41.

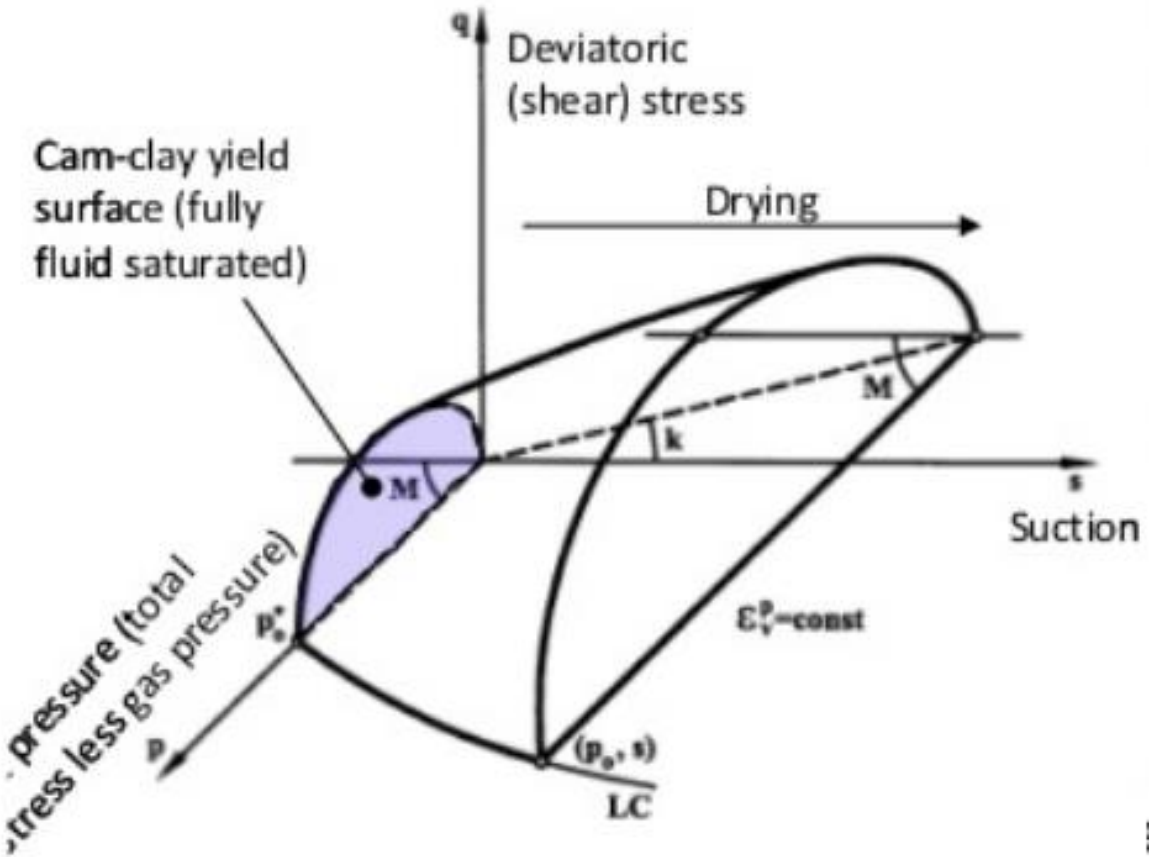

Figure 2.41 Three-dimensional yield surface in BBM (Rutqvist, 2006)

The model retrieves the elliptical yield surface of the Modified Cam Clay (MCC) in fully saturated soils. It can be noticed that the size of the elastic domain grows as the suction increases. The Loading Collapse (LC) curve represents the rate of increase in the elastic domain. Sheng et al. (2008) stated that there is a rough simplification in the model such as the assumption that there is a linear increase of apparent cohesion with suction. Another simplification was the use of the

straight line for the e – ln p relation. The latter simplification implies that there is continuous increase of the collapse upon wetting. However, one of the biggest benefits of this simplification is the need for only limited parameters over MCC parameters to describe the behavior of partially saturated soils. Alonso et al. stated that despite rough simplifications included in the model it can explain the variation of wetting-induced swelling or collapse strains depending on the magnitude of applied stresses. It also describes the reversal of volumetric strains sometimes observed during the wetting-induced collapse, the increase of shear strength with suction, and many other typical features of the mechanical behavior of partially saturated soil.

Following the introduction of BBM, Josa et al. (1992) adopted nonlinear relationships for the variation of e-ln p which make the collapse strains not increase endlessly but rather reach a maximum before tending to zero at high stresses. Sanchez et al. (2005) generalized the BBM for highly expansive soils by considering the effect of microstructure behavior on macrostructure behavior of soils as well as the generalized plasticity theory. Wheeler nad Sivakumer (1995) used more model functions based on experimental results. Sheng et al. (2008) presented an improved constitutive model which was extended from MCC model. Sheng et al. stated that the model provides a continuous and smooth transition between saturated and partially saturated states along the yield surfaces as shown in Figure 2.42. The model also presents in Figure 2.43 shows smooth curvature of the normal compression line at a constant suction as a natural result of the proposed volume-stress-suction relationship. A comprehensive overview for constitutive modeling in the partially saturated soils can be found Sheng et al. (2008).

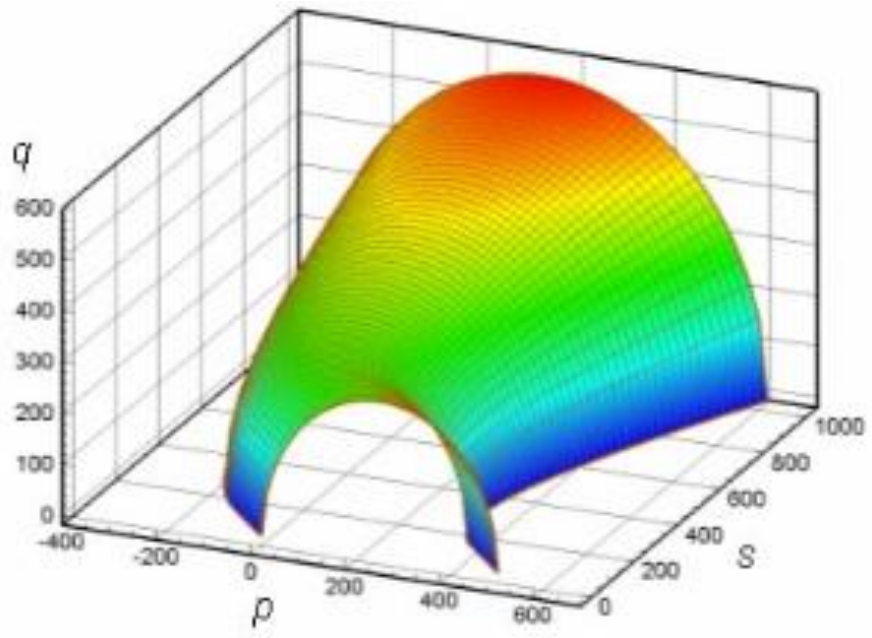

Figure 2.42 MCC yield surfaces extended to suction axis (S_{sa} =100 kPa) (Sheng, et al. 2008)

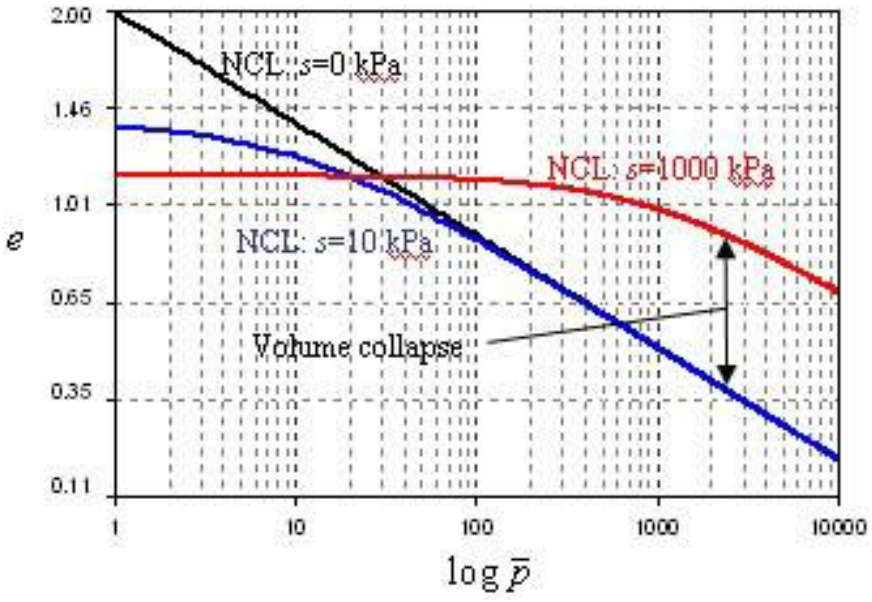

Figure 2.43 Smooth curvature of e-lop p′relationship (Sheng, et al. 2008)

In this study, the Modified Drucker-Prager Cap model was used for fully saturated soils. The same model was utilized for partially saturated soils by incorporating the soil water characteristic curve (SWCC) and hydraulic hysteresis in the model. The original Drucker Prager model (1952) was unbounded (open surface). Capped yield surface was added to the linear Drucker-Prager model which, according to Abaqus theory guide, serves two main purposes, it bounds the model in hydrostatic compression, and it helps control the volume dilatancy when the material yields in shear. Yield surface of the modified Drucker-Prager Cap model is demonstrated in Finger 2.44. Figure 2.45 illustrates the pressure dependent behavior in the model. It can be noticed in Figure 2.45 b that the material behaves perfectly plastic on the failure surface and hardening or softening as a function of plastic strain on the cap yield surface.

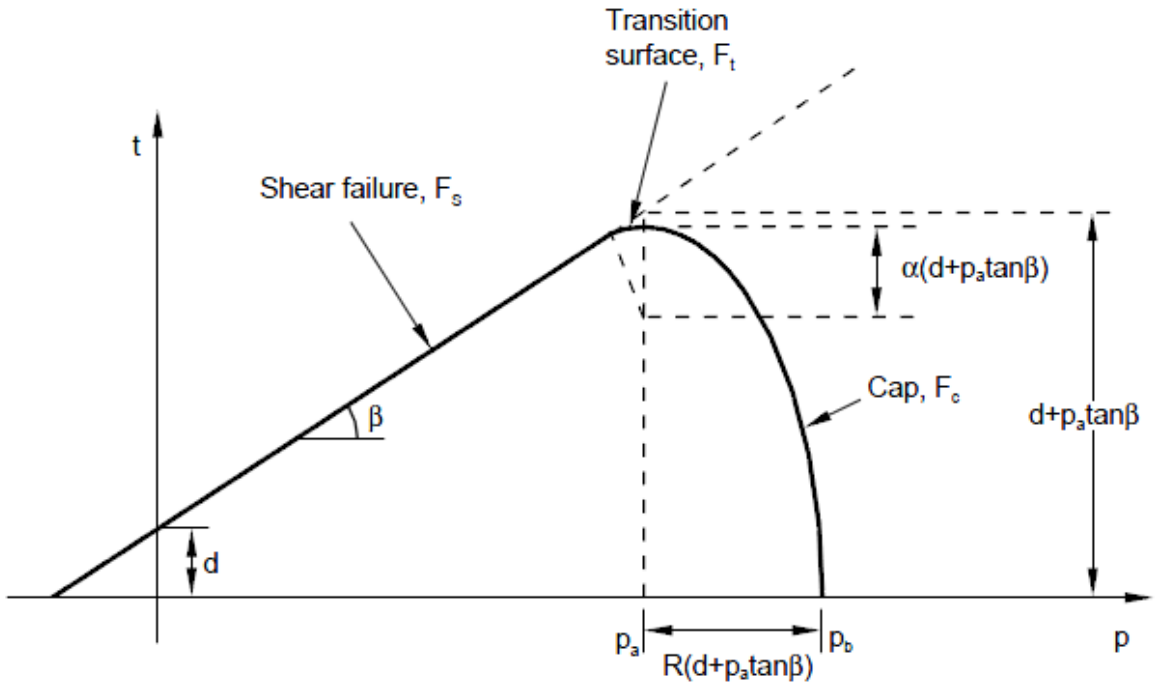

Figure 2.44 Modified Drucker-Prager Cap model yield surfaces in the *p-t* plane (Abaqus manual)

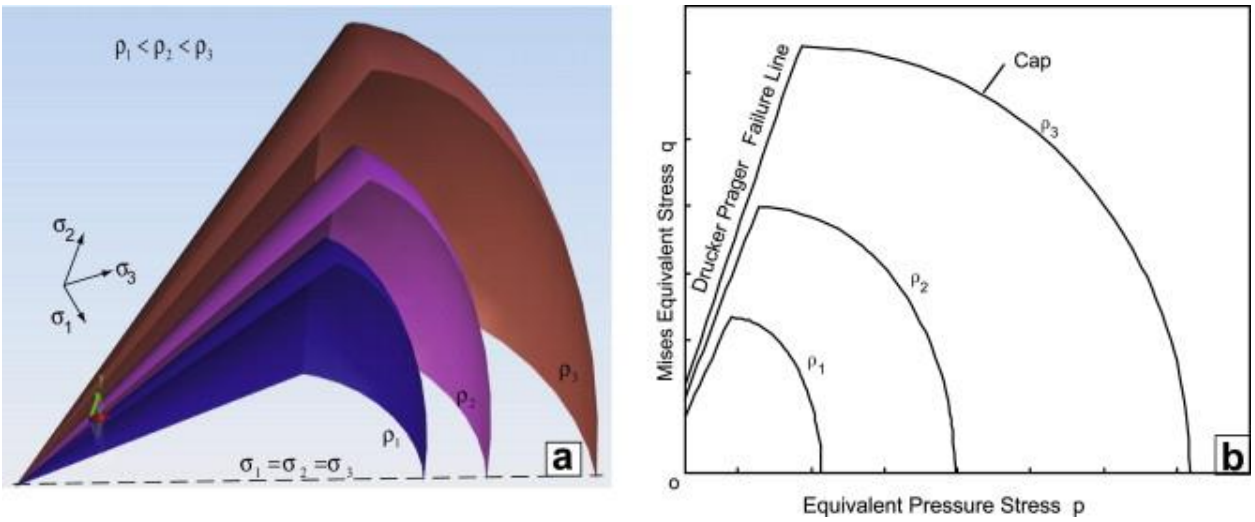

Figure 2.45 Schematics of a pressure-dependent Drucker-Prager Cap model, (a) 3D yield surfaces in principal stress space (1/4 model), (b) 2D representation (E.T Han et al., 2008)

DPC model uses two yield surfaces as seen in Figures 2.45. The first one is a linear pressure-dependent Drucker-Prager shear failure surface and the second yield surface is a compression cap yield surface. The Drucker-Prager failure surface itself is perfectly plastic, but plastic flow on this surface produces inelastic volume increase causing the cap to soften. The shear failure surface in DPC model can be written as :

$$F_s = t - p\tan\beta - d = 0 \qquad 2.21$$

where β is the material friction angle, d = cohesion, $p = -\frac{1}{3}\,trace\,(\boldsymbol{\sigma})$, and p is the hydrastaic pressure:

$$t = \frac{q}{2}\left[1 + \frac{1}{k} - \left(1 - \frac{1}{k}\right)\left(\frac{r}{q}\right)^3\right] \qquad 2.22$$

where q is the equivalent Mises stress, $q = \sqrt{\frac{3}{2}}\,(\boldsymbol{S}:\boldsymbol{S})^{0.5}$ and $r = \left(\frac{9}{2}\boldsymbol{S}.\boldsymbol{S}:\boldsymbol{S}\right)^{1/3}$, $\boldsymbol{S}$ is deviator

stress, $\boldsymbol{S} = \boldsymbol{\sigma} + p\,\boldsymbol{I}$, k = q_e /q_c and is shape parameter to define yield surface which equals the yield stress in triaxial extension q_e to the yield stress in triaxial compression q_c. k ratio ranges between (0.778 to 1) as shown in Figure 2.46, $\boldsymbol{I}$ is identity matrix, and r is the third invariant of deviator stress.

When K = 1, it means that no third stress invariant (r) effects are taken into account. In such a case, the deviator stress "t" is equal to the equivalent von Mises stress "q", and the yield surface has a circular von Mises shape in the deviator stress plane as shown in Figure 2.46.

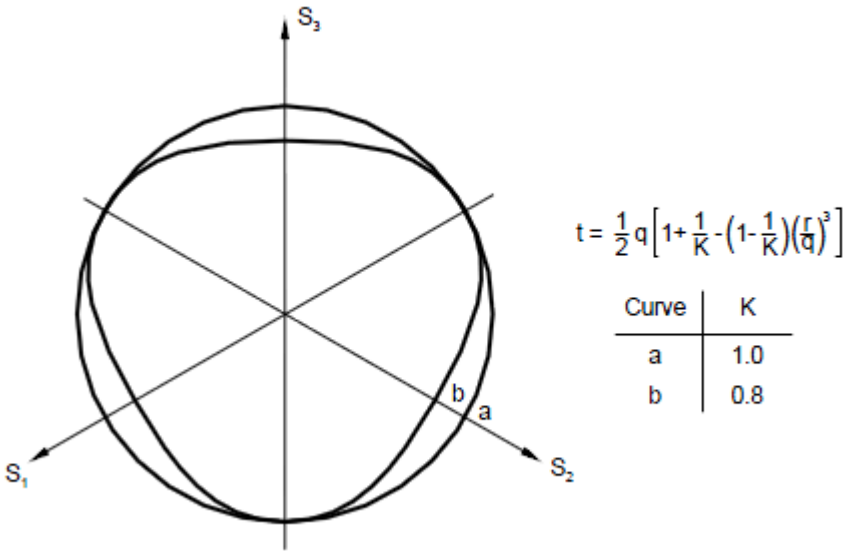

Figure 2.46 Typical yield/flow surface in the deviatoric plane (Abaqus user guide)

The elliptical cap yield surface in the *p-t* plane is given by Equation 2.23:

$$F_c = \sqrt{(p - p_a)^2 + \left(\frac{Rt}{1 + \alpha - \alpha / \cos\beta}\right)^2} - R(d + p_a \tan\beta) = 0 \qquad 2.23$$

where, R is constant eccentricity and material parameter that controls the shape of the cap, and p_a is an evolution parameter that controls the hardening–softening behavior as a function of the volumetric plastic strain and can be computed from Equation 2.24.

$$P_a = \frac{P_b - Rd}{1 + R\ tan\beta} \qquad 2.24$$

The hardening–softening behavior can be described by a piecewise linear function relating the mean yield stress and the volumetric plastic strain ($p_b = p_b\ (\varepsilon_{vol}^{pl})$) as demonstrated in Figure 2.47. This relation can be obtained from the result of one isotropic consolidation test with several unloading and reloading cycles.

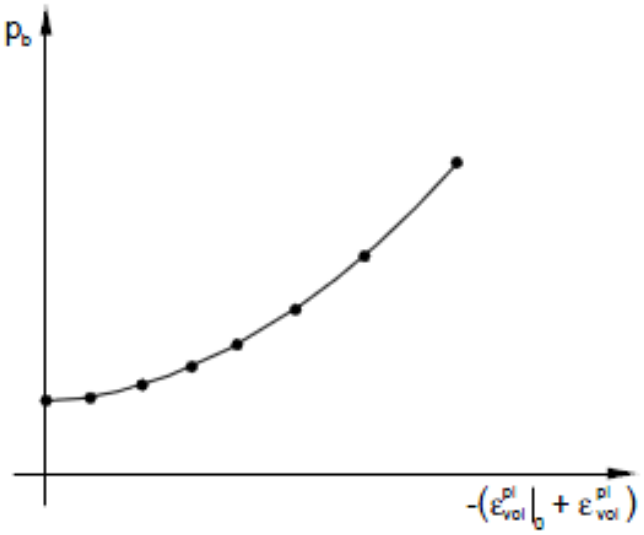

Figure 2.47 Typical Cap hardening behavior

Parameter α in Figue 2.44 is a small number (usually, 0.01 to 0.05) and is used to define a smooth transition surface between the Drucker-Prager shear failure surface and the elliptical cap surface.

Apparently, the value of α equal to 0 indicates that no transition zone is allowed in between the shear failure and cap surface. *t*, β and d in Equation 2. 23 are the yield stress, the material friction angle, and cohesion, respectively.

This elliptical cap intersects the mean effective stress (*p*) axis at a right angle. The expansion or contraction of the cap is governed by the increase or decrease of the plastic volumetric strain. When the material yields on the cap, the plastic volumetric compaction of the material results in hardening, while yielding on the shear failure surface induces softening behavior.

Drucker-Prager yield surface and the elliptical cap is connected to a smooth transitioning curve surface expressed in Equation 2.25

$$F_t = \sqrt{(p - p_a)^2 + \left[t - \left(1 - \frac{\alpha}{\cos\beta}\right)(d + p_a \tan\beta)\right]^2} - \alpha(d + p_a \tan\beta) = 0 \quad 2.25$$

2.6.3 Contact Modeling

The contact zones usually referred to the interfaces where stresses are transferred between structural members of soils. The interaction between fully or partially saturated soils with the structural element influence the interface behavior and consequently affects the behavior of skin friction along the pile's length. Navayogarajah et al. (1992) stated that the interface zone is subjected to highly concentrated stresses and undergoes considerable strain variations due to extreme displacement field. Therefore, the formulation of mathematical models describing the

interface behavior is complicated. Thus, experimental observation and numerical simulation are a reasonable alternative to understand the behavior of the interface.

2.6.3.1 Contact Parameters

Laboratory apparatuses such as direct shear test and triaxial test are used for determining interface parameters between the soils and the structural member. Tariq and Miller (2009) conducted a series of interface tests on partially saturated low plasticity fine grained soil and two coarse and smooth stainless steel counterfaces. Figure 2.48 demonstrates a sketch of the suction controlled direct shear device used in the experimental program. Equations 2.26 and 2.27 were experimentally validated to model the shear strength of partially saturated soils from twenty-seven direct shear tests. The interface tests were conducted with controlled matric suction. The shear strength of the interface was obtained from the SWCC using three magnitudes of net normal stress and matric suction.

$$\tau_f = c'_a + (\sigma_{nf} - u_{af}) tan\delta' + (u_{af} - u_{af}) \tan \delta^b \quad 2.26$$

$$\tau_f = c'_a + (\sigma_{nf} - u_{af}) tan\delta' + (u_{af} - u_{af}) \tan \delta' ((\theta - \theta_r)/(\theta_s - \theta_r)) \quad 2.27$$

where:

τ_f = shear stress on the failure plane at failure,

c'_a = effective adhesion intercept for the interface,

σ_{nf} = total normal stress on the failure plane at failure,

u_{af} = the pore-water pressure on the failure plane at failure,

δ' = interface friction angle with respect to net normal stress,

δ^b = the interface friction angle with respect to matric suction.

θ = current volumetric water content,

θ_r = the residual volumetric water content from a soil-water characteristic curve (SWCC), and

θ_s = the saturated volumetric water content from an SWCC.

The study concluded that the angle of friction with respect to net normal stress was similar for the soil-soil and soil-rough interfaces. Both of these were considerably larger than the corresponding friction angle for the smooth interface. Figure 2.49 shows the peak failure envelope projection in matric suction-shear stress plane from partially saturated interface from direct shear tests with coarse and smooth counterfaces. Estimating interface friction factor using a direct shear device does not take into consideration the variation of lateral stresses along the structural member. In addition, Friction fatigue at shallow depths of piles can not be considered using a direct shear device.

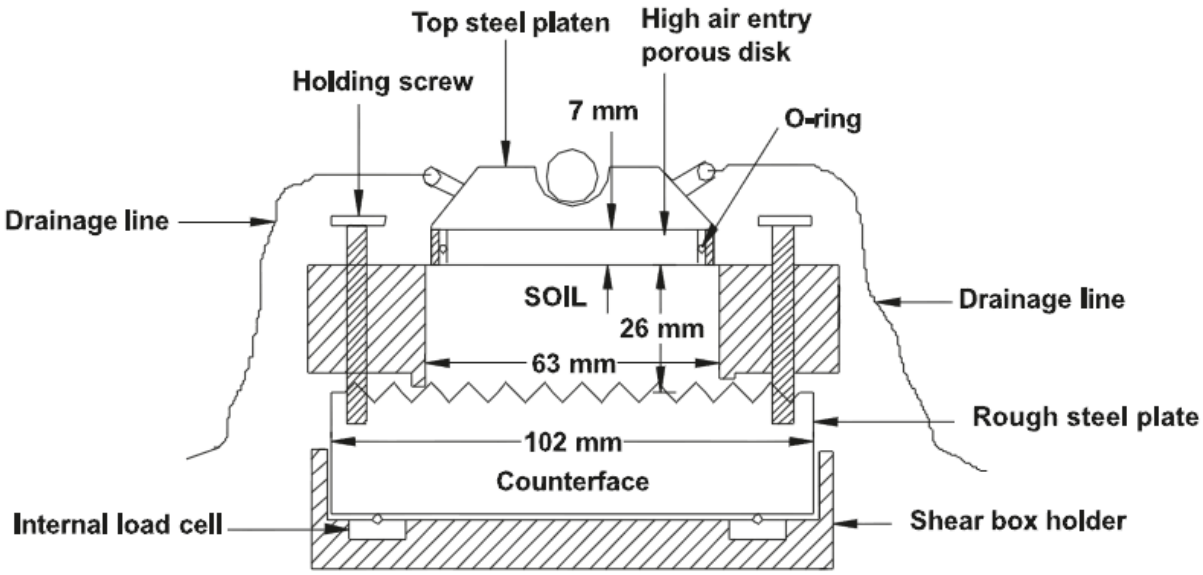

Figure 2.48 Schematic cross-sectional view of the rough interface shear box (Tariq and Miller, 2009)

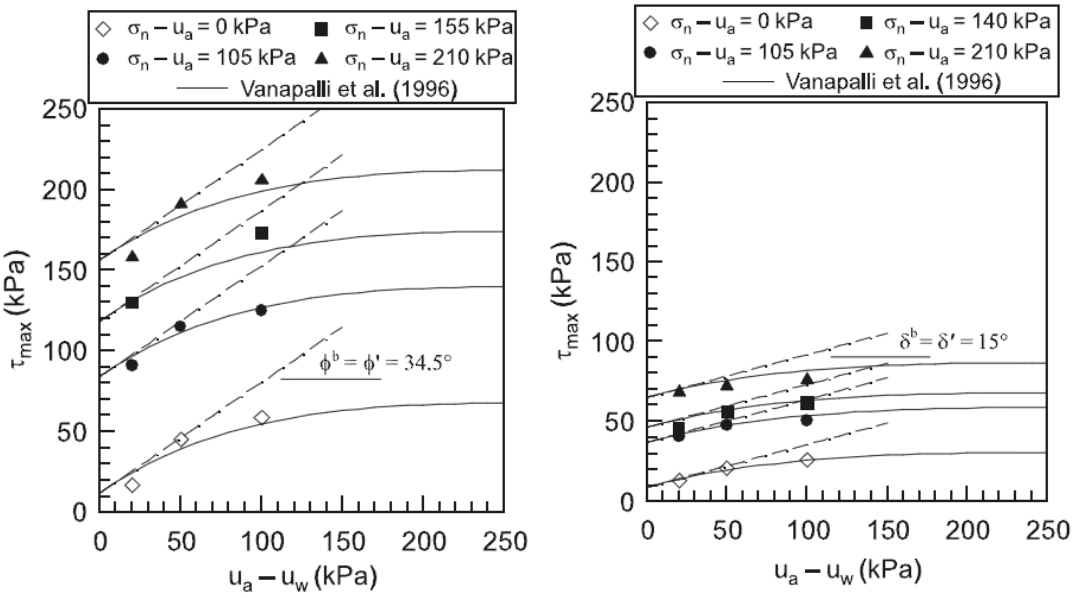

Figure 2.49 Peak failure envelope projections for coarse counterface (left) and smooth counterface (right)

2.6.3.2 Numerical Aspects

Realistic modeling of the contact zone between the soil and the structural member demands critical consideration of interaction factors between the foundation components. Numerically, the interaction is handled by taking into account the aspects of contact formulation. The formulation primarily includes the contact discretization, contact enforcement method, and contact tracking. Interacted surfaces in Abaqus can be defined using either contact pairs or contact general algorithms. When contact pair is used, interacted surfaces, contact discretization, and interaction properties must be specified. Several techniques for defining the contact zones are discussed below.

The concept of using a one-dimensional interface element in geotechnical applications uses the stiffness of springs obtained from *p-y*, *t-z* and *Q-z* curves. This technique was first proposed by McClelland et al. (1958) and Reese et al. (1956). These springs are conventionally called Winkler spring model.

A zero thickness interface element which was proposed by Goodman et al. (1968) demands the use of high stiffness values to prevent penetration of the contact bodies. Desai et al. (1984) stated that such high stiffness values lack physical meaning.

Adopting a thin layer interface element was first presented by Zienkiewicz et al. (1970) and later extended by Desai (1981), and Desai et al. (1984). The element was capable of simulating stick, slip, debonding and rebonding behavior reasonably well. Desai et al. (1988) developed a constitutive model for this type of interface element to capture the cyclic behavior in dynamic soil-structure interaction problems. Guessing typical thickness is not a straightforward process and required trial and error.

The use of the master-slave concept was proposed by Wriggers (1995). This concept involves the formulation of the contact geometries and the interface constitutive laws for both the tangential and normal stresses components in the contact area. The concept is frequently followed at present due to its closest response to the measured behavior, and due to the capability of simulating large deformations.

When the master-slave technique is adopted, interacted surfaces can be described using either surface to surface or node to surface techniques. Abaqus manual states that in the node to surface technique, the nodes on one surface (the slave surface) contact the segments on the other surface (the master surface) discrete points (slave nodes). In surface to surface technique, each contact constraint is formulated based on an integral over the region surrounding a slave node.

Figures 2.50 and 2.51 schematically demonstrate both techniques. Figure 2.52 illustrates that surface to surface contact showed better accuracy in distribution of contact stresses than the node to surface technique in classical Hertz contact problem.

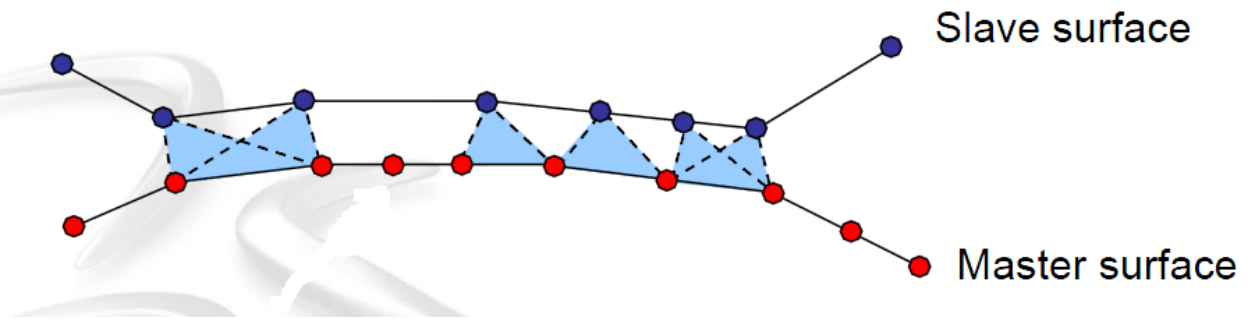

Figure 2.50 Schematic representation of node to surface technique (Abaqus manual, 2013)

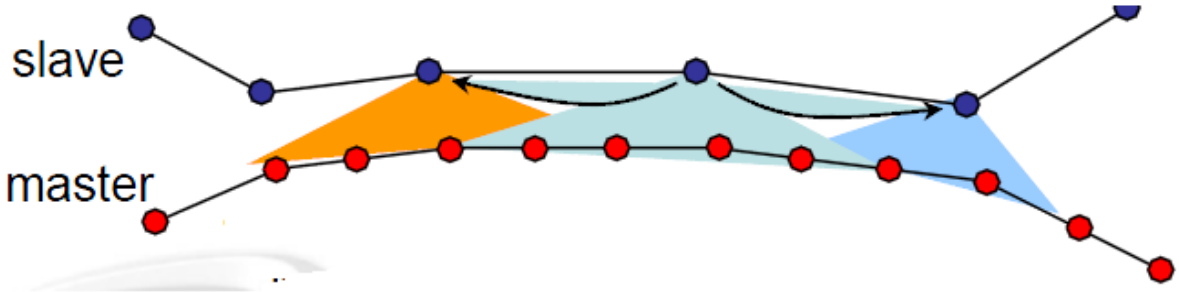

Figure 2.51 Schematic representation of surface to surface technique (Abaqus manual, 2013)

Contact between interacted surfaces can be enforced directly using the Lagrange multiplier method or with a penalty by using penalty method. The method of Lagrange multiplier is used for strict enforcement of contact which may make it challenging for Newton iterations to converge. Another drawback is adding cost to the computational time of the analysis. Penalty method is a

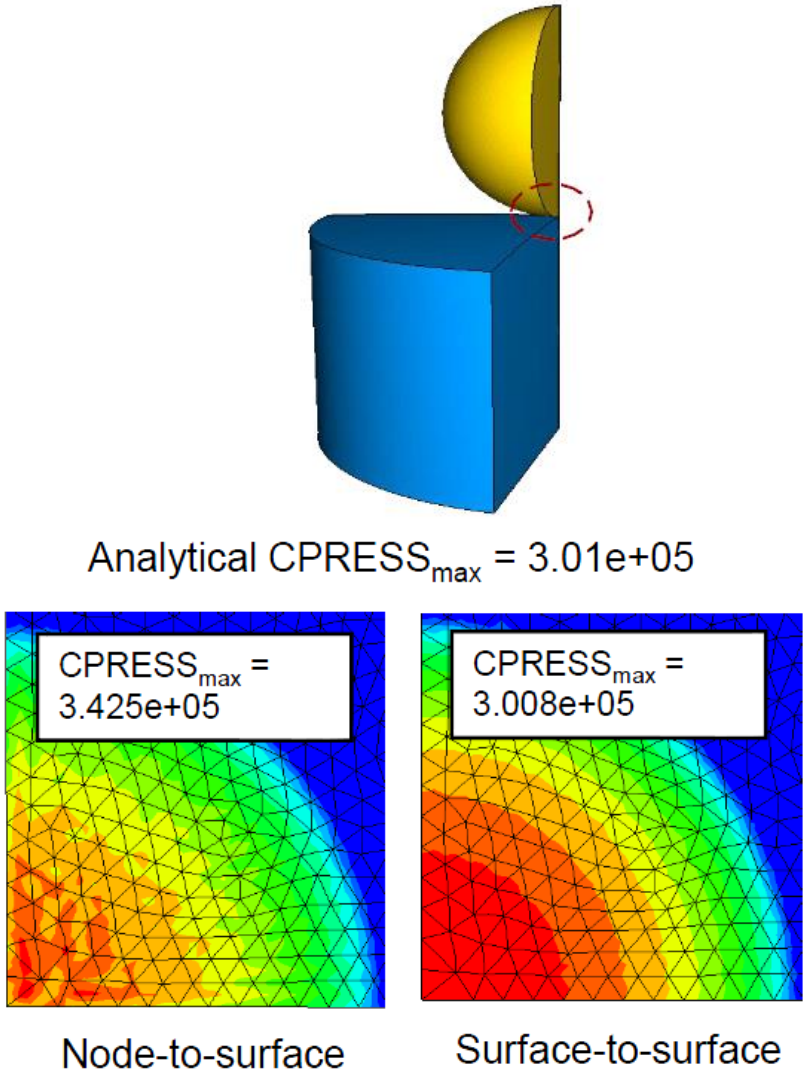

Figure 2.52 Numerical and analytical solution of classical Hertz problem using surface to surface and node to surface techniques (Abaqus manual, 2013)

stiff approximation of hard contact as shown in Figure 2.53 from Abaqus manual. Beside the insignificant amount of allowed penetration, penalty method has many advantages over the strict method. It improves convergence rates and results in better equation solver performance. It also has better treatment of overlapping constraints. Abaqus chooses default penalty stiffness based on the representative stiffness of underlying elements as a good medium between low and high values

of penalty stiffness. Low penalty stiffness results in excessive penetration values while high value causes degradation in convergence rate.

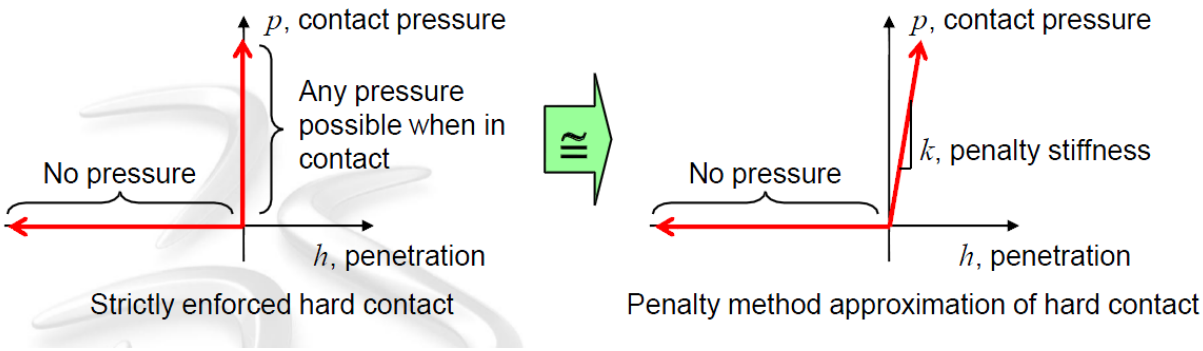

Figure 2.53 Strict vs. penalty enforcement of contact (Abaqus manual, 2013)

There are two formulations available in Abaqus to describe the evolution of the constraints upon sliding. The first one is rigorous nonlinear evolution (finite) sliding and the second one is approximate (small) sliding. Figure 2.54 demonstrates the main differences between finite and small sliding. In finite sliding, the point of interaction on the master surface is updated using a true representation of the master surface. With small sliding, planar representation of master surface per slave node is obtained based on initial configuration. Small sliding is intended to reduce the cost of the contact simulation by utilizing less nonlinearity and consequently fewer iterations for a converged solution. Utilizing this technique may result in bad simulation if the contact motions do not remain small.

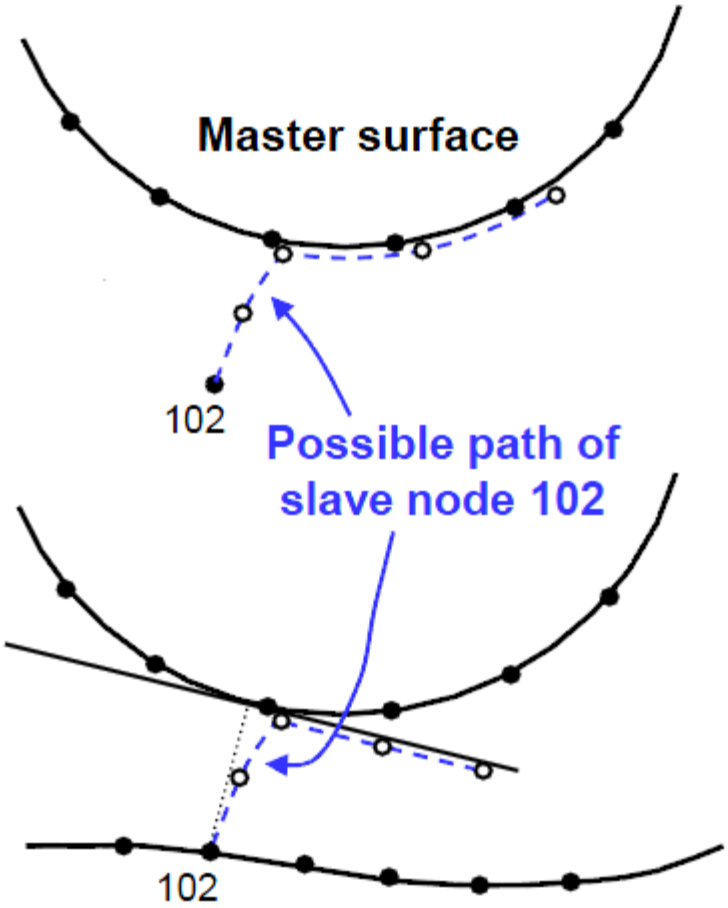

Figure 2.54 Possible path for a node in contact zone using finite sliding (top) and small sliding (bottom)

2.7 Capacity of Single Pile in Partially Saturated Soil

In many situations, foundations are interacting with partially saturated soils particularly in zones where the water table is at a considerable depth. Few studies in the literature investigated the influence of capillary zone on the pile capacity. Georgiadis et al. (2003) explored the effect of partially saturated soil on the behavior of a single pile embedded in soil with the variable water table. Figure 2.55 illustrates a profile for the pore pressure distribution and the finite element mesh

for the pile used in the analysis. A total stress constitutive model was developed and implemented in a finite element program at the Imperial College (ICFEP). No interface element was used in the analysis and the angle of the interface was considered to be equal to the angle of shearing resistance of concrete.

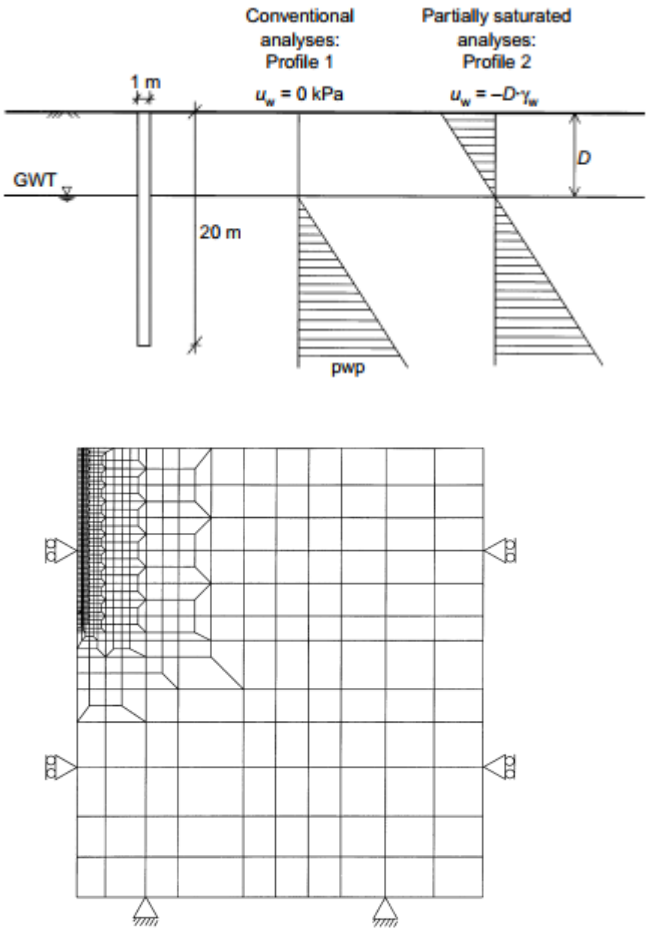

Figure 2.55 Pore pressure profile and finite element mesh used in single pile analysis (Georgiagis et al.,2003)

The outputs of the study indicated an increase of the ultimate capacity of the single pile with the increase of the suction in the soil. Figure 2.56 demonstrates that conventional finite element analysis considerably underestimated the capacity of the single pile for large depths of the groundwater table.

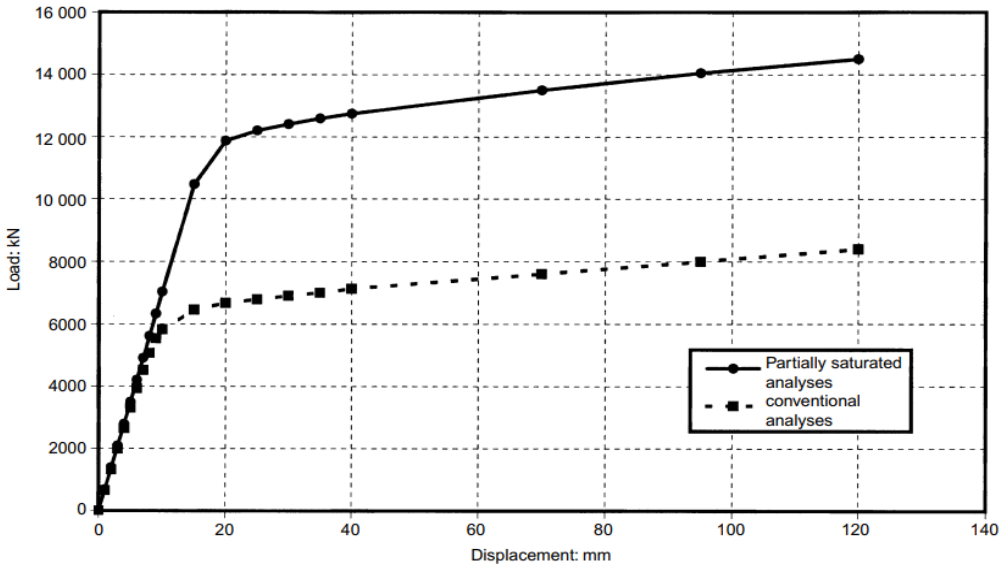

Figure 2.56 Load-displacement curve for single pile with 25 m water table depth (Georgiadis et al., 2003)

Vanapalli and Taylan (2012) conducted a series of single pile tests in a laboratory environment to investigate the effect of matric suction on skin friction capacity in a statically compacted fine-grained soil. Figure 2.57 shows tests setup adopted and Table 2.2 summarizes their soil parameters in their experimental program.

Test setup for model pile loading test: ① Adjustable height loading frame ② Test tank ③ LVDT ④ Load cell ⑤ Model pile, ⑥ Compaction base plate.

Figure 2.57 Test setup (Vanapalli and Taylan, 2012)

Table 2.2 Properties of soil used in the study (Vanapalli and Taylan, 2012)

Soil Properties	Value
Optimum water content (%)	18.6
Maximum dry unit weight (kN/m^3)	16.7
Saturated unit weight (kN/m^3)	18.5
Specific Gravity G_s	2.7
Sand, Silt, and Clay (%)	28, 42, 30
Liquid limit and Plastic limit (LL and PL) %	36.2 and 15
Plasticity index (PI)	21.2
Air Entry Value (AEV) at 16 % WC (kPa)	14
Effective cohesion, c′ 9kPA) (Sat)	15
Effective friction angle, φ′ (deg.) (Sat)	23
Undrained shear strength, c_u (kPa)	11.5

Vanapalli and Taylan modified the conventional α method to predict skin friction capacity $Q_{f\,(us)}$ of single pile tested under unsaturated soil condition using Equation 2.28. Variation of undrained shear strength c_u with matric suction is incorporated in the equation and is a function of *SWCC* and undrained shear strength for saturated condition.

$$Q_{f(us)} = \alpha c_{u(sat)} \left[1 + \frac{(u_a - u_w)}{(P_a / 101.3)} S^{\upsilon} / \mu \right] \pi dL \qquad 2.28$$

where α is adhesion factor, S is degree of saturation, $c_{u\,(sat)}$ is undrained shear strength for saturated soil, P_a is atmospheric pressure (i.e. 101.3 kPa), and μ and ν are fitting parameters

depending on the plasticity index of the soil. *d* and *L* are the diameter and the length of the pile, respectively.

Table 2.3 shows a comparison between predicted and measured ultimate skin friction capacity. It can be observed from Table 2.3 that despite that the soil used in the study was cohesive, undrained shear strength did not increase consistently with matric suction. For example, the measured undrained shear strength for 205 kPa suction was 15 % less from the specimen of 110 kPa suction. It is unexpected to have less shear strength as the matric suction increased in cohesive soils. This behavior may be related to the quality of the specimen used in the study. It is worth noted that c_u was measured experimentally using an unconfined compression test which ignores the contrition of lateral stresses in specimen's shear strength.

Table 2.3 Comparison between predicted and measured ultimate skin fiction capacity (Vanapallia and Taylan, 2012)

$w_{initial}$	$(u_a - u_w)$	Meas. c_u	Est. c_u	α	Back Cal. α value	**Est.[4] $Q_{f(us)}$**	**Meas. $Q_{f(us)}$**
(%)	kPa	kPa	kPa	-	-	**kN**	**kN**
13	0	11.5	-	0.90	0.70	**0.13**	**0.10**
13	205	68	57	0.75	0.79	**0.64**	**0.68**
16	110	80	65	0.67	0.55	**0.67**	**0.55**
18	55	58	62	0.82	0.68	**0.59**	**0.50**

Fattah et al. (2013) conducted a finite element analysis on a single pile with a diameter of 0.6 m and 12 m long embedded in fully and partially saturated clayey. SWCC was used to obtain

the unsaturated modulus which relates the volumetric strain of the soil to the change in suction obtained from SWCC. The analysis found that that ultimate capacity of single pile embedded in partially saturated soils with deep water content increase (3-5) times for piles in fully saturated soil.

Chung and Yang (2014) developed a finite element model to simulate the nonlinear behavior of a small scale single pile in partially saturated soil under a static axial loading. Interface elements were used to simulate the pile-soil interface, and the analysis parameters were obtained from experimental tests. The outputs of the numerical study were compared with physical pile load tests performed in the lab. The relation in Figure 2.58 shows that the effect of the dilatant behavior of unsaturated soil during shear on the load-bearing capacity of a small scale single pile. The analysis, however, did not show the development of the shear strength with suction in partially saturated soils.

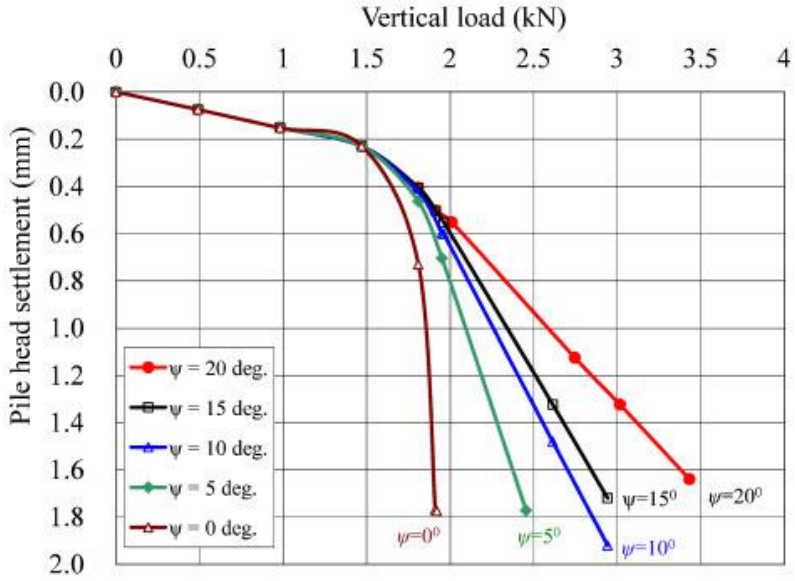

Figure 2.58 Effect of dilatancy angle on ultimate bearing capacity (Chung and Yang, 2014)

2.8 Summary of the literature review

An extensive literature review was conducted. In most cases, the influence of partial saturation on deep foundation soils was considered for single pile only. Numerical simulations were also for the single pile and limited to two dimensional studies only. Therefore, it can be stated that up to date, there were no references regarding the behavior of group piles in the partially saturated soils.

CHAPTER 3

EXPERIMENTAL STUDIES

3.1 Introduction

Load transfer mechanism between deep foundation and surrounding soil is complicated and depends on many variables. A full scale load settlement test is required to capture the real behavior of such foundation. However, besides the fact that a full scale test is expensive and time consuming, it is hard to control the test environment because of homogeneousness, density, and type of soil and measurement of pore pressure. The small scale model test is an alternative that can simulate the behavior of deep foundations and yet provides better control on the test environments and boundary conditions.

This chapter is dedicated to describe the experimental works in this study including testing procedures, soils used, and instruments. The results of the tests are discussed and analzed in Chapter 5.

3.2 Preparation of the Soil Used

White coarse kaolin clay, produced by IMERYS Inc. in Georgia, US (commercially known as Hydrite Flat DS kaolin), was mixed with fine sand in 55% kaolin to 45% sand. There was about 80 % clay and 20 % silt in the kaolin. The sand was uniform with 80% fine sand passing sieve # 40 with D_{50} equal to 0.5 mm. The mixture produced a cohesive soil with low compressibility. The soil was initially mixed with 19% water and left in sealed buckets for 24 hours to reach moisture equilibrium. Figure 3.1 shows the test setup used for consolidating the soil. The soil was placed in three layers in 520 X 520 X 520 mm rigid box with perforated base. Three layers of 170 mm

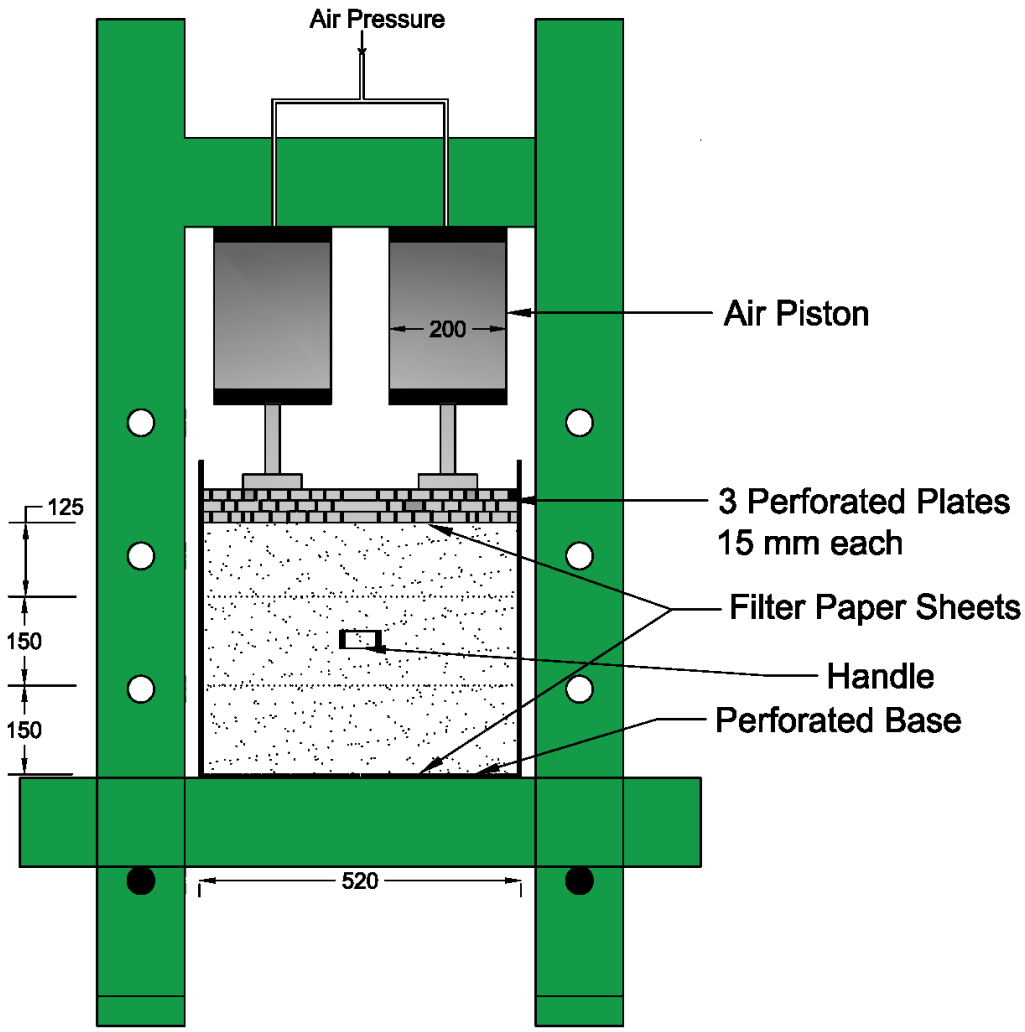

Figure 3.1 Set up for consolidating soil mix, all dimensions are in mm

thickness each were subjected to 100 kPa consolidation pressure for 48 hours. Two air cylinders of 200 mm diameters were used to apply the pressure on top of three perforated 19 mm thick aluminum plates. The soil was considered fully saturated at the end of the consolidation process. Physical properties of the mixed soil after consolidation are listed in Table 3.1.

Table 3.1 Physical properties of the soil used in the study

Property	Value	Standard
Constituent of the soil	45% sand (80% fine , 20% coarse) 55% kaolin (20 % silt, 80 % clay)	ASTM D7928
Atterberge Limits (LL, PL)	23 % and 15.8 %	ASTM D 4318
$\gamma_{d\ max}$, OMC	17.78 kN/m^3 13.2 %	ASTM D 689
Permeability coefficient (k)	3.67×10^{-10} m/s	ASTM 2434

3.3 Testing Program

3.3.1 Preliminary Tests

The results and parameters obtained from these tests (ASTM 2434) are used for analyzing the results of experimental models and as inputs when performing numerical analysis in Chapter 4 of this study.

3.3.1.1 Sample Preparation for Shear Strength Tests

Conventional consolidated undrained (CU) tests were conducted on two fully saturated specimens. In addition, consolidated undrained water phase tests (CUW) were performed on two specimens having 35, 55, 85, 120, 200 and 600 kPa suctions. Fifteen identical fully saturated specimens, which were prepared following the procedure discussed in Section 3.2, were extracted, extruded and placed in a plastic container. Each specimen dimensions were 73 mm in diameter

and 153 mm high as shown in Figure 3. 2, (b). Conventionally, axis translation technique is used for applying the target suction on the specimen. Time consuming issues associated with using axis translating technique in cohesive soil specimens were discussed in Section 2.5.5.1. A more efficient approach was followed to reach the target suction at a much shorter time. The adopted approach is similar to that followed by Sandra et al. (2008). In this approach, MPS-6 and small tip tensiometers were inserted in a randomly selected soil specimen inside the plastic container as shown in Figure 3.2, (a). The container was kept open during the day to let the water inside the specimens evaporate and closed during the night to reach moisture equilibrium in the specimens. Suction inside the

Figure 3.2 (a) Extracted specimens with two tensiometers placed inside (b) mounting the specimens on triaxial cells

specimen was and considered to be the same in all other specimens since they are subjected to the same environments. Several months of a desaturating process were saved by adopting this procedure. CUW tests were conducted using modified triaxial device shown in Figure 2.31.

3.3.1.2 Isotropic Consolidation Test

Isotropic consolidation tests were conducted on soil specimens of 0, 55 and 200 kPa suctions. Dimensions of specimens were 150 mm in diameter and 73 mm high. Before conducting the tests, target suctions were monitored by small ceramic tip and MPS-6 tensiometers. Partially saturated specimens were placed on High Air Entry Ceramic Disk (HAECD) in a modified triaxial cell. Incremental confinement pressures of 50, 100, 200, 400, 700 kPa were applied and corresponding water volume changes were recorded.

3.3.1.3 Soil Water Characteristic Curve (SWCC) Test

The significance of SWCC and methods of conducting the SWCC test were discussed in Section 2.6.3. One of the specimens preparation procedure discussed in Section 3.3.1.1 was selected for conducting SWCC test in this study. The specimen was placed on a sensitive scale. MPS-6 and small tip tensiometers were planted inside the soil specimen. The specimen on the scale was placed inside an air controlled chamber to control the moisture. Initial gravimetric water content and other properties of that specimen were known. The reduction in weight represents the loss in the weight of water phase. The weight and corresponding suction were recorded at certain intervals. A sample was taken at the end of the test to measure the final water content and compared with recorded one. Stress dependent SWCC cannot be conducted with this simplified procedure. However, the test lasted about seven days and saved about 75% of the time that would have been required if axis translating technique was adopted. Total volume changes of the specimen were minor when the suction increased because the specimen was non-deformable.

3.3.2 Configuration of Foundation Models and Test Setup

Figure 3.3 shows the configurations of Single Pile Foundation (SPF), Piled Raft Foundation (PRF), Pile Group Foundation (PGF), and Unpiled Raft Foundation (URF) models. The pile was modeled by a closed-end aluminum pipe of 19 mm diameter and 285 mm long with length over diameter (L/D) ratio of 15 in all SPF, PGF and PRF models. The modulus of elasticity of the aluminum piles was 69,000 MPa. The raft was modeled by 19 mm thickness aluminum plate. Figure 3.4 shows the tests setup followed in this study. The vertical load was applied through two air cylinders and measured by a 50 kN load cell attached to those cylinders as shown in the figure. The capacity of individual piles was measured utilizing two small load cells attached to the top and the bottom of each pile. The bottom load cell measures the end bearing capacity, and the top one measures the total of the end bearing and skin friction of single pile. Foundation settlement was monitored using two dial gauges or LVDTs placed at opposite corners on the raft plate. Two pore water pressure sensors and two MPS-6 suction sensors were used for tests conducted in fully and partially saturated soils, respectively. One sensor was inserted in the soil at the middle of the pile length in all models. The second one was positioned underneath the pile in SPF model and below the center of piles group in PRF and PGF. Both sensors were inserted at 25 mm away from the piles. In URF model, PWP or suction sensor was planted at B/2 underneath the center of the raft, where B is the raft width. Settlement and excess pore pressure responses were recorded using multipurpose data acquisition system 7,000 as seen in Figure 3.5 (a), which was manufactured by micro measurement Inc. Suction readings were recorded using data logger Em 50, produced by Decagon Inc., as also seen in Figure 3.5 (b).

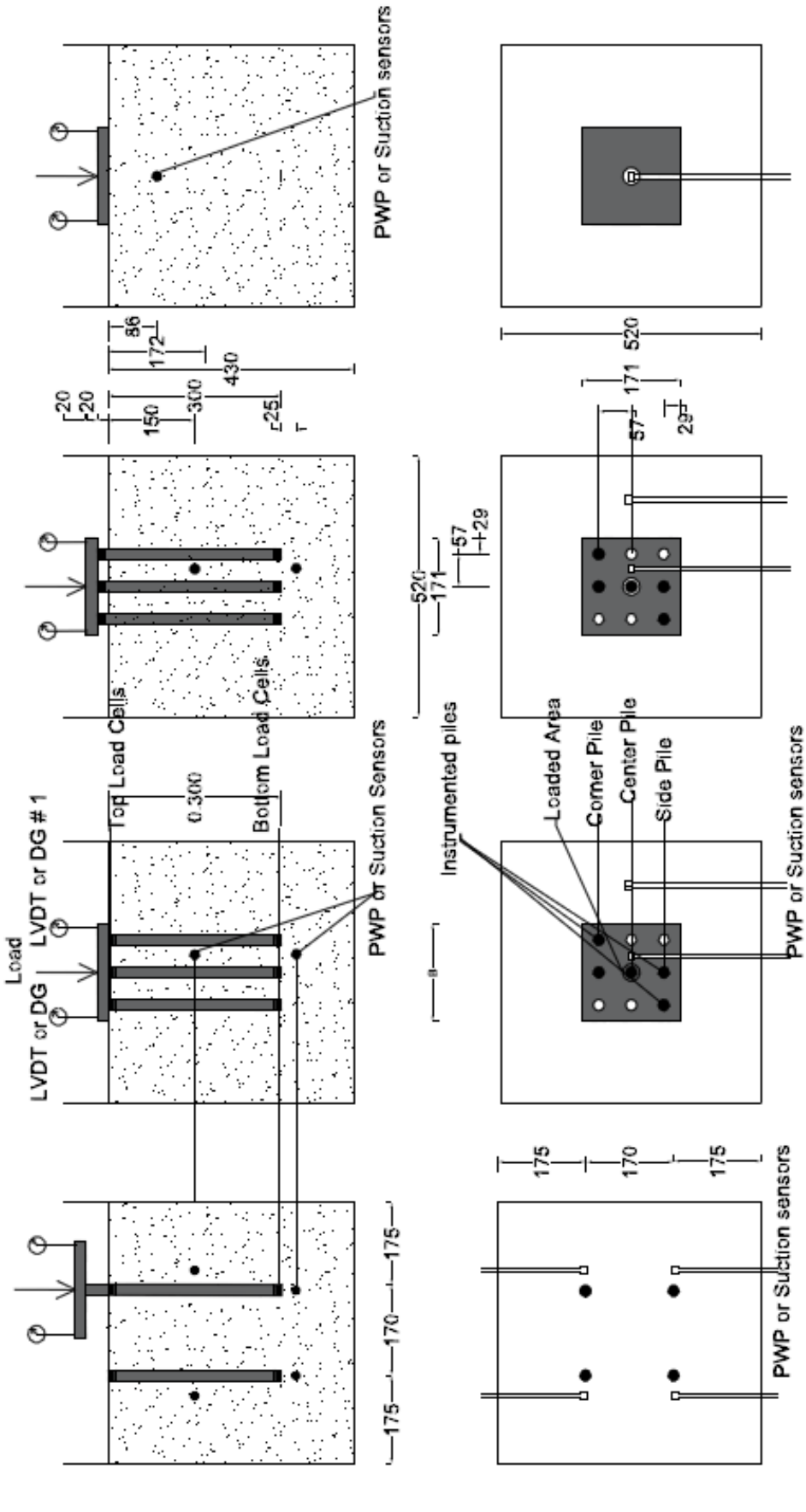

Single Pile Foundation SPF Piled Raft Foundation PRF Pile Group Foundation PGF Unpiled Raft Foundation URF

Figure 3.3 Configuration of experimental models

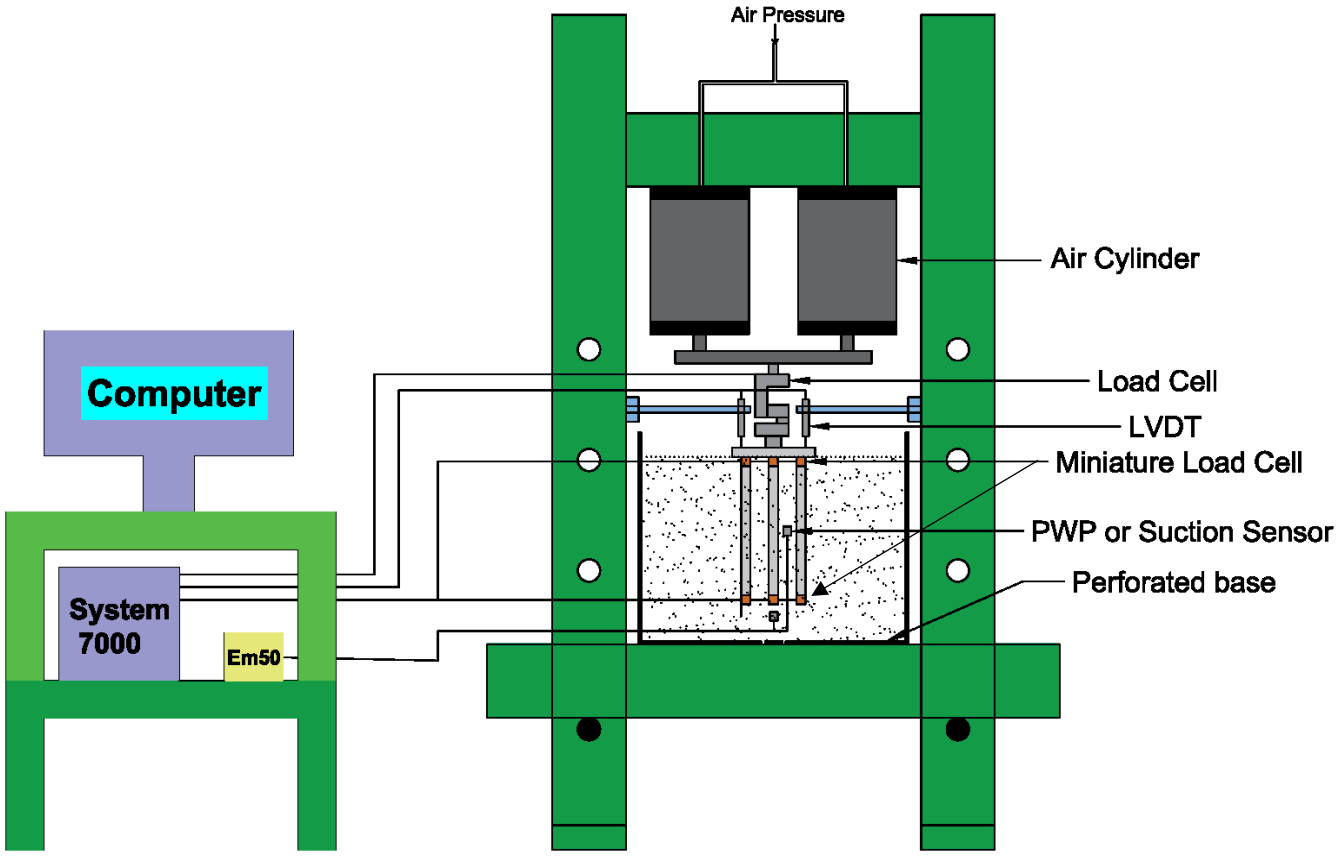

Figure 3.4 Typical test setup for PRF model

Figure 3.5 (a) data logger for suction sensors (b) Multi-purpose data acquisition system 700

3.3.3 Testing Procedure of Foundations Models

Four SPF tests with 0, 35, 55, 85 kPa suction were tested in one box with a distance of 9d (d: pile diameter = 19 mm) between the piles. The interaction between the piles was considered negligible beyond a distance of 8d, (Poulus et al., 1980). Tests of 120, 200, 600 kPa suction were conducted in another box when the soil reached the target suction in each test. In all models, tests in fully saturated soils were conducted first, then tests in soils with suctions of 35, 55, 85, 120, 200 and 600 KPa were performed, respectively. Figure 3.6 shows an organizing chart of experimental procedures.

Pre-boring was done by jacking a hollow pipe of 15 mm diameter down to 225 mm depth. A guided model pile was then jacked down slowly into the hole until the full depth was reached. The box was covered and sealed for 24 hours to reach equilibrium condition and for setup purposes. The load was applied in increments which is equal 5 to 10 % of the estimated ultimate load. The next load increment was added after 10 minutes or until no additional settlement was observed from the current increment. Average settlement and pore water pressure or suction readings were recorded at each increment. The pile test was ended if the pile plunged suddenly or reached settlement equal to 10% of pile diameter (2mm).

Testing procedures in URF, PGF, and PRF were similar to that followed in SPF. A 30 mm thick plastic plate with holes configured similarly to that in multi piles foundation was used as a guide in pre-boring. Center pile as well as two side piles and two corner piles were instrumented with miniature load cells as indicated in Figure 3.7. The load cell measurements at side piles and corner piles were averaged, respectively. In some tests, one side or corner load cell reading was ignored if there was a big jump in that load cell reading compared with other load cells in the group

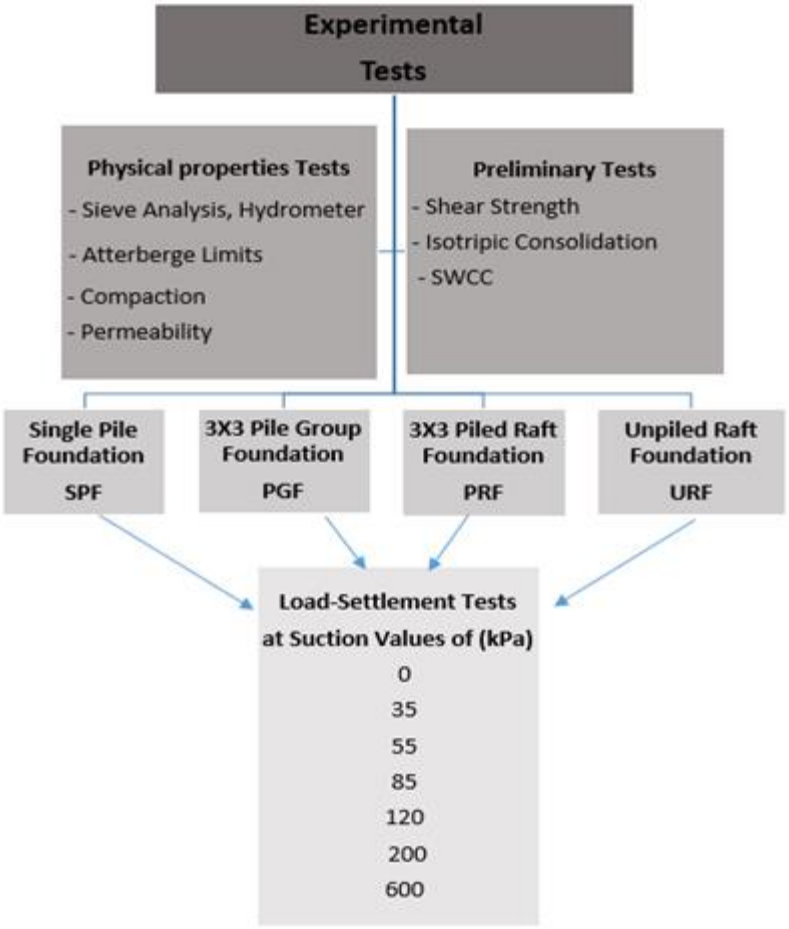

Figure 3.6 Organizing chart for experimental tests

Figure 3.7 Instrumented piles in PGF model (left) and PRF model (right)

or previous tests. The pile cap was placed in contact with soil in PRF tests and 10 mm above the soil surface in PGF tests. The cap was glued to the piles using commercial epoxy called Kwik Weld. Dead weight of 5 kg was applied on the cap overnight to get better bondage between the piles and the cap. The box was sealed and left for 24 hours or until reaching the target suction. The loading test was then conducted similarly to that followed in SPF test.

After the completion of the previous test, the piles were pulled out using the air cylinders. The top soil was then gently scraped. The scrapped soil placed back in the pile holes in three layers. Each layer was statically compacted under 100 kPa for 24 hours. Suctions were monitored during the compaction process. After each test with given suction, the entire soil box was sealed, and the suction value was monitored for the next test with new suction value. Sufficient time was given to reach moisture equilibrium and required suction value. The pre-boring and insertion of the piles for the next test were conducted in on new soil spots (different holes) following the same procedure adopted in the previous test.

The raft was tested in a similar procedure followed in other models. The procedure followed in preparing the soil for the multiple test may not be perfect. However, it saved a substantial amount of time and effort. The simplified process was necessary when testing three different foundation models in cohesive soils with seven suction values for each foundation model.

3.4 Results of experimental tests

3.4.1 Results of Preliminary Tests

3.4.1.1 Results of Soil Water Characteristic Curve (SWCC)

The first test that must be conducted when dealing with partially saturated soil is SWCC. The procedure followed in this test is discussed in Section 3.3.3. Figure 3.8 shows the results of SWCC test of the soil adopted in this study. Originally gravimetric water content was measured experimentally and then converted to degree of saturation (S_r) using mass volume relations. From this SWCC, the air entry value was estimated to be equal **105** kPa.

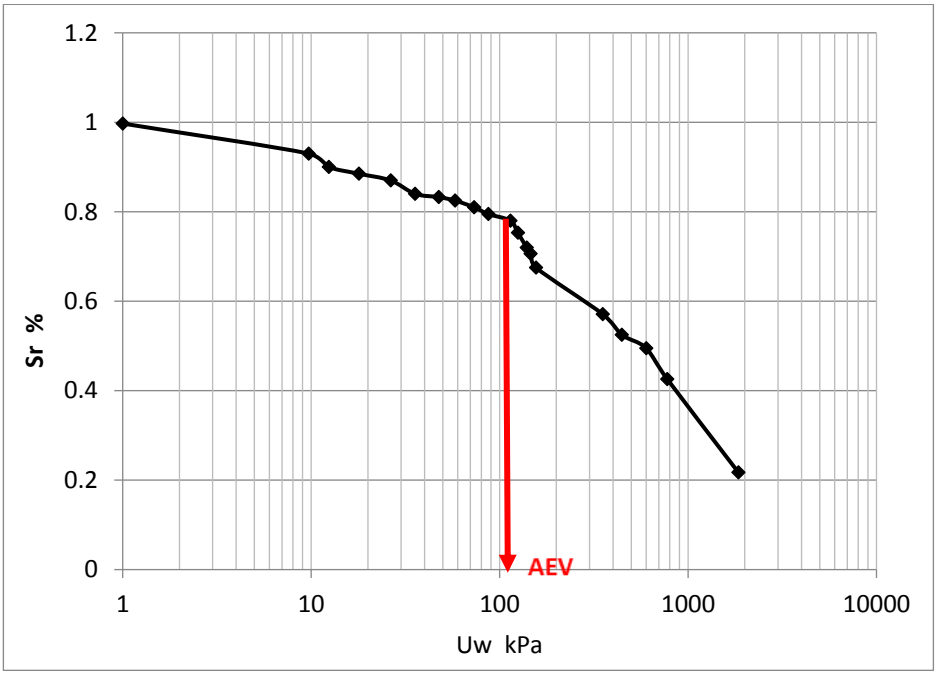

Figure 3.8 SWCC of the soil adopted in this study

3.4.1.2 Shear Strength Tests

Conventional Consolidated Undrained (CU) tests were conducted on two fully saturated specimens at consolidation pressures of 100 and 200 kPa. The relations between deviatoric stress

(σ_1-σ_3) versus corresponding axial strain (ε) as well as pore water pressure (PWP) versus axial strain (ε) are shown in Figures 3.9 through 3.14. The samples were unloaded-reloaded at the beginning. The slope of the unloading (or reloading) line in σ_3 = 200 kPa test was chosen to be the elasticity modulus of that soil.

It can be noticed in Figure 3.10 that the excess pore water was less than 10 % of the deviatoric stress in both fully saturated specimens. The relations between the excess pore water pressure and strain were not reported for partially saturated specimens since PWP values in the tests were negligible. Consolidated Undrained Water (CUW) shear tests were conducted for specimens under 35, 85, 120, 200 and 600 kPa suctions as shown in Figures 3.11 through 3.14. In the shearing stage of these tests, the air is allowed to drain by keeping the upper drainage valve open. The lower drainage water valve is closed, and no water is allowed to drain. CUW shear test simulates the situation where the air pressure in the soil dissipates while the pore water pressure cannot.

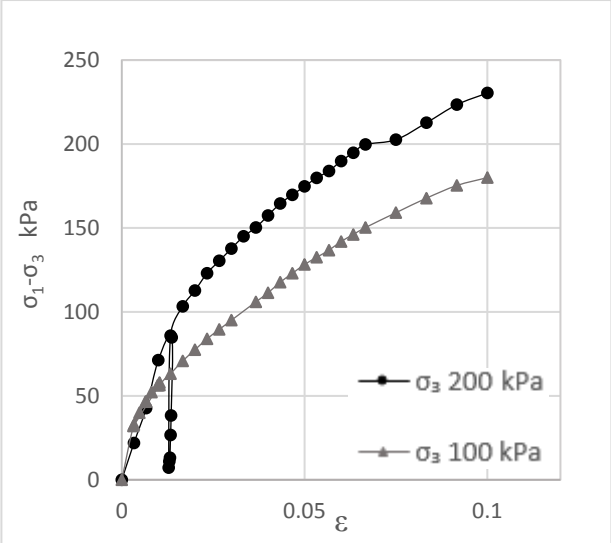

Figure 3.9 (σ_1-σ_3) vs. ε at zero suction specimen

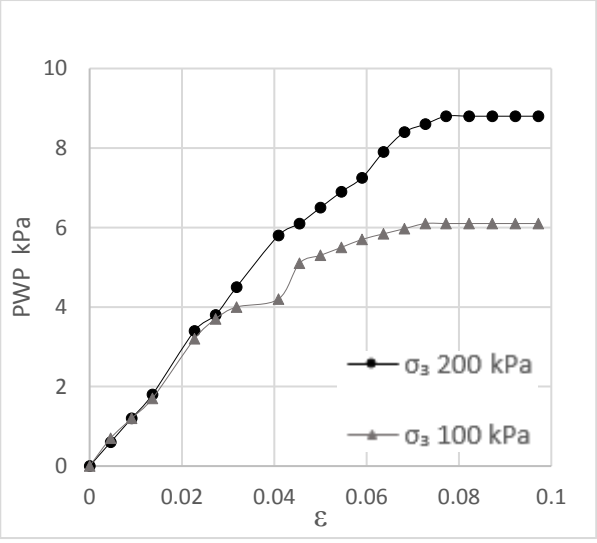

Figure 3.10 PWP vs. strain for zero suction

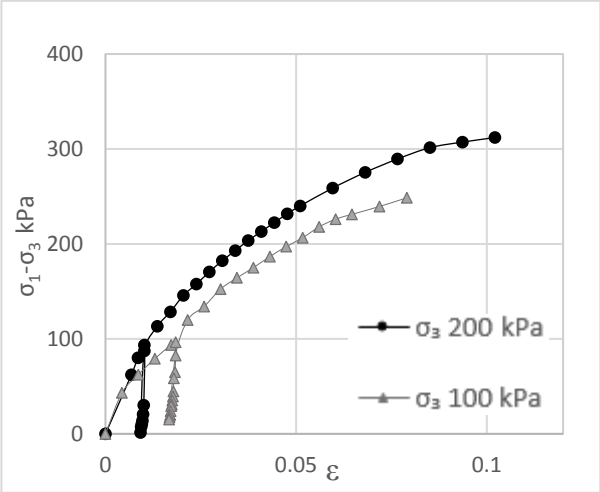

Figure 3.11 (σ_1-σ_3) vs. ε at 35 kPa suction

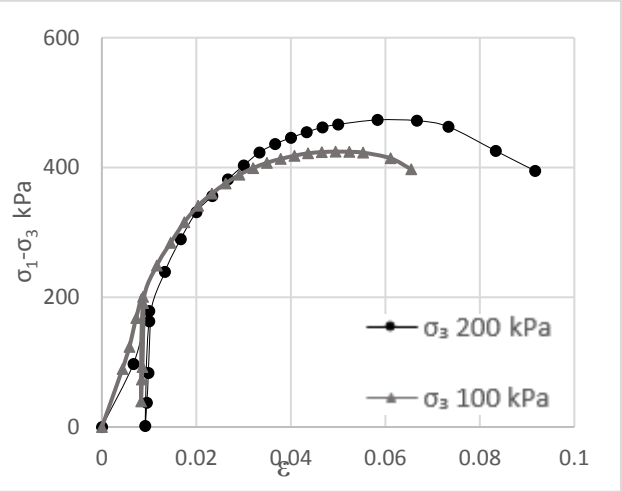

Figure 3.12 (σ_1-σ_3) vs. ε at 85 kPa suction

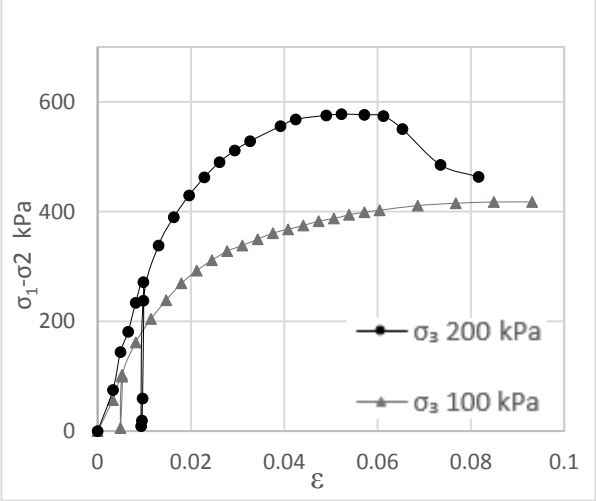

Figure 3.13 (σ_1-σ_3) vs. ε at 120 kPa suction

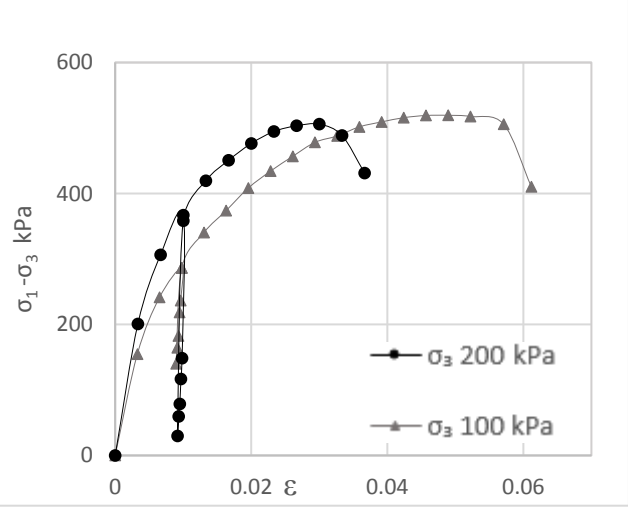

Figure 3.14 (σ_1-σ_3) vs. ε at 200 kPa suction

It can be noticed from the results of CUW tests that as the suction increased, the specimen failed in peaked pattern (more brittle). At at higher suction values, the effect of confining pressure becomes less effective that is, it does not help in increasing the total strength of the soil specimen,

in comparison with the zero suction test results. The increase in the maximum deviatoric stress values ceased at higher suction values (600 kPa).

3.4.1.3 Isotropic Consolidation Tests

Figure 3.15 shows the results of isotropic consolidation tests conducted on three soil specimens with different suction values. It can be noticed that as the suction increases the pre-consolidation pressure increases and the specimens became less compressible. The yield surface of the partially saturated specimen expands as the suction goes higher due to the hardening effect caused by the suction in the soil.

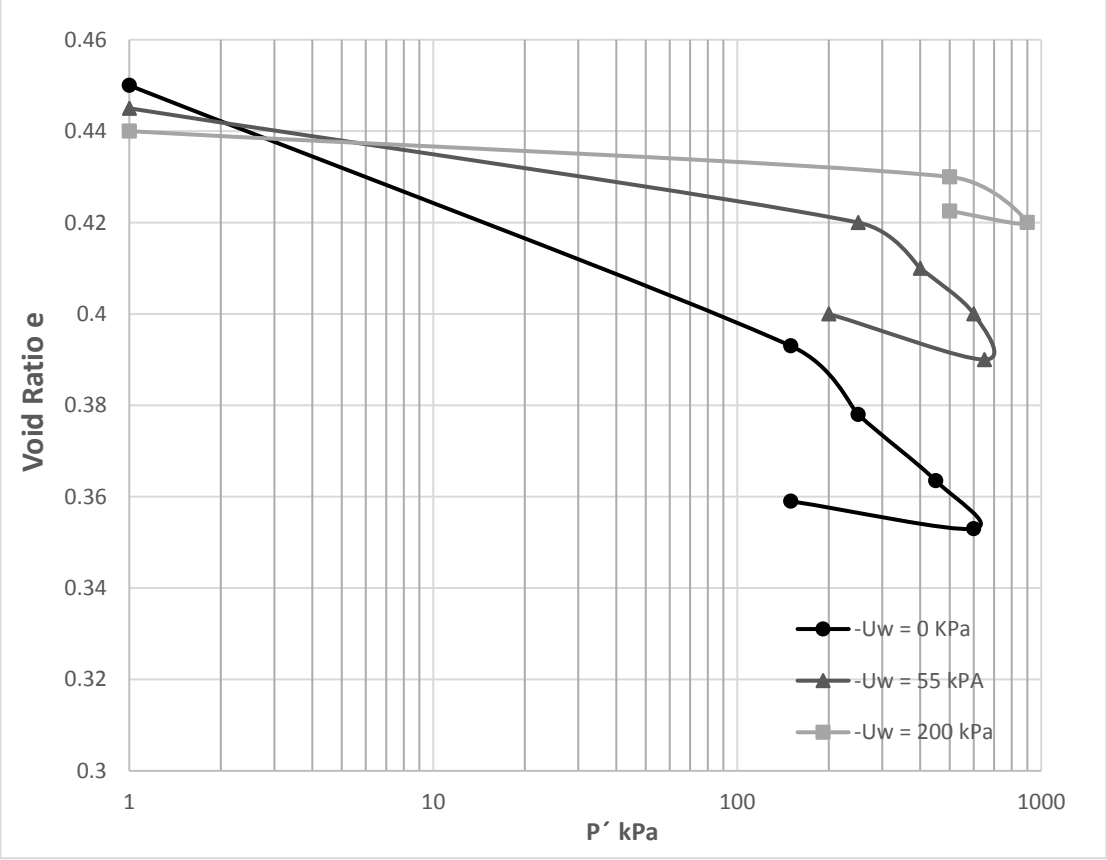

Figure 3.15 Void ratio vs effective stress at 0, 55, 200 kPa suction

3.4.2 Results of Model Tests

3.4.2.1 Total Load vs. Settlement for SPF, PRF, PGF and URF Model Tests

Figure 3.16 through Figure 3.19 show the load-deformation curves of SPF, PRF, PGF and URF models tested in soils at different suction values. It can be observed in Figure 3.16 (SPF tests), that at lower suction values up to 85 kPa suction, the pile plunged and failed suddenly. As the suction goes higher, the failure point becomes less distinctive. In all tests, it can be observed that the suction in the soil did not contribute to the increase in the pile capacity at higher suctions. This behavior can be attributed to the reduction in shear strength at high suction values, since components of pile resistance are related to the shear strength of the soil in which the pile is embedded.

In Figures 3.17 to 3.19, it can be noticed that PRF showed higher resistance than PGF and URF at same suction values. The resistance of PRF and PGF slightly decreased when tested under 600 kPa suction compared to their resistance in 200 kPa soil suction. The reduction can be related to the degradation of skin friction resistance with increasing of suction beyond the Air Entry Value (AEV). The degradation in Skin Friction Resistance (SFR) at high suctions will be shown clearly in other Figures later. Influence of suction on resistances of PRF (Figure 3.17) and PGF (Figure 3.18) was similar to that shown in SPF (Figure 3.16). That is, a considerable increase in the resistance was noticed up to the AEV, and then, the increase becomes insignificant or declined beyond that value. The resistance of URF (Figure 3.19) increased continuously with suction, and this behavior may lead to the conclusion that suction contribution is higher in total bearing resistance in comparison to that in skin friction.

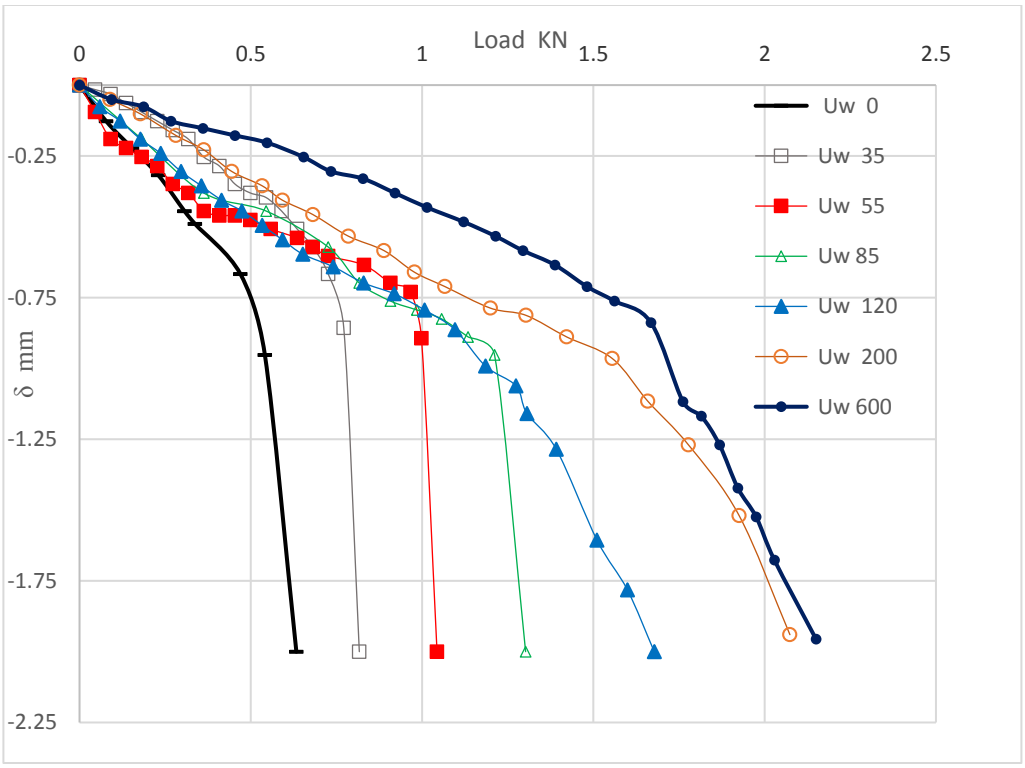

Figure 3.16 Load-settlement curve of SPF models in various suctions (U_w in kPa)

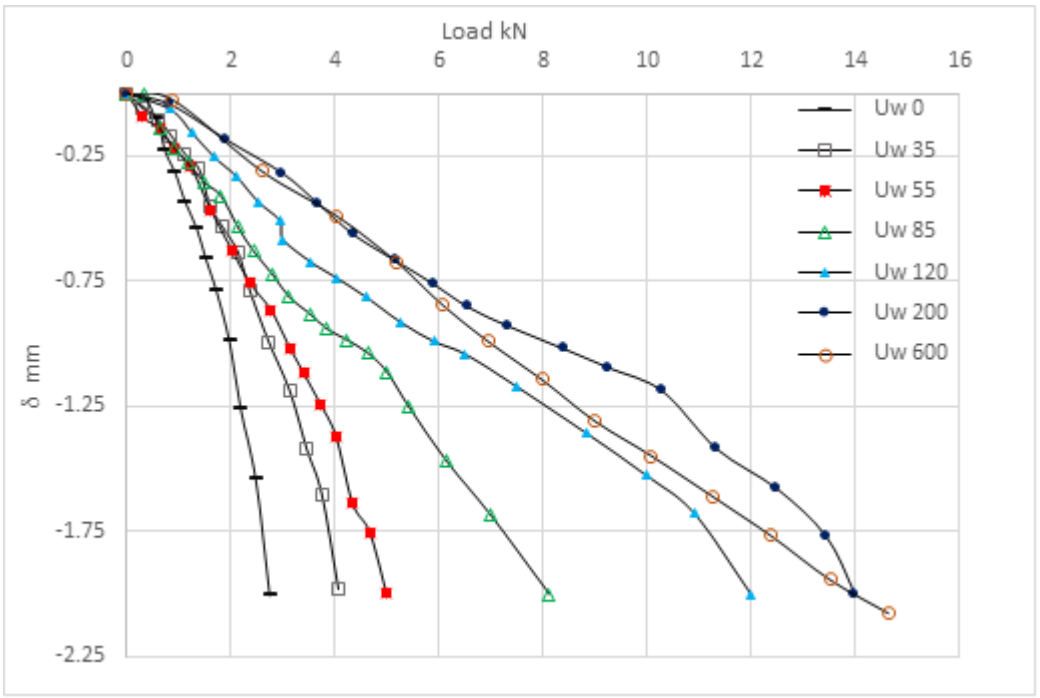

Figure 3.17 Load-settlement curve of PRF models tested in various suctions (U_w in kPa)

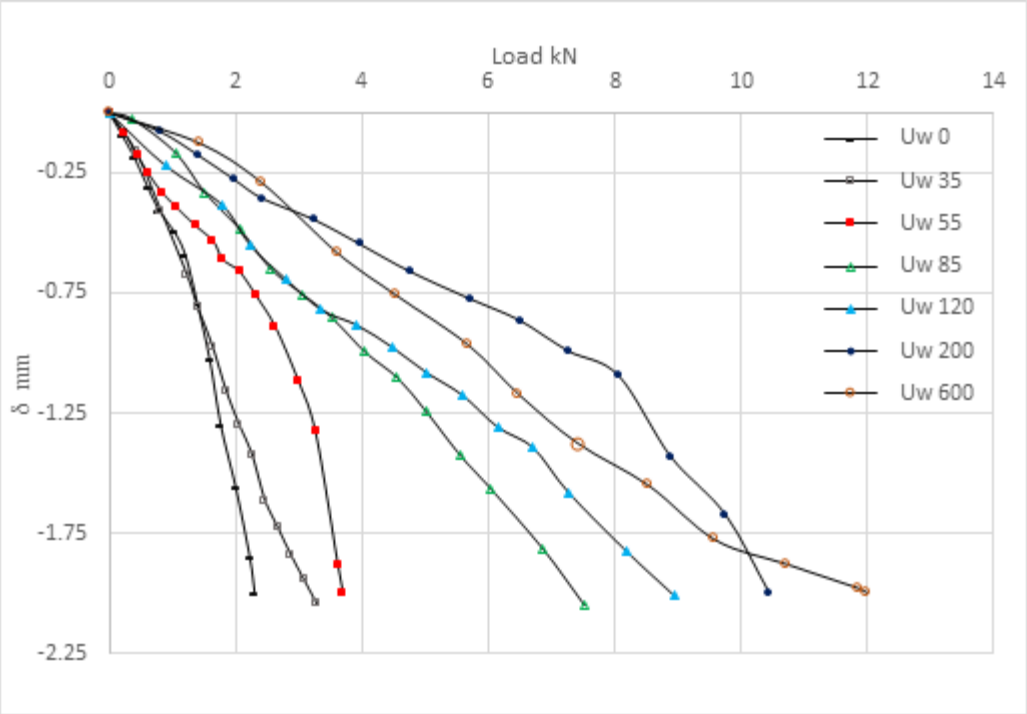

Figure 3.18 Load-settlement curve of PGF models tested in various suctions (U_w in kPa)

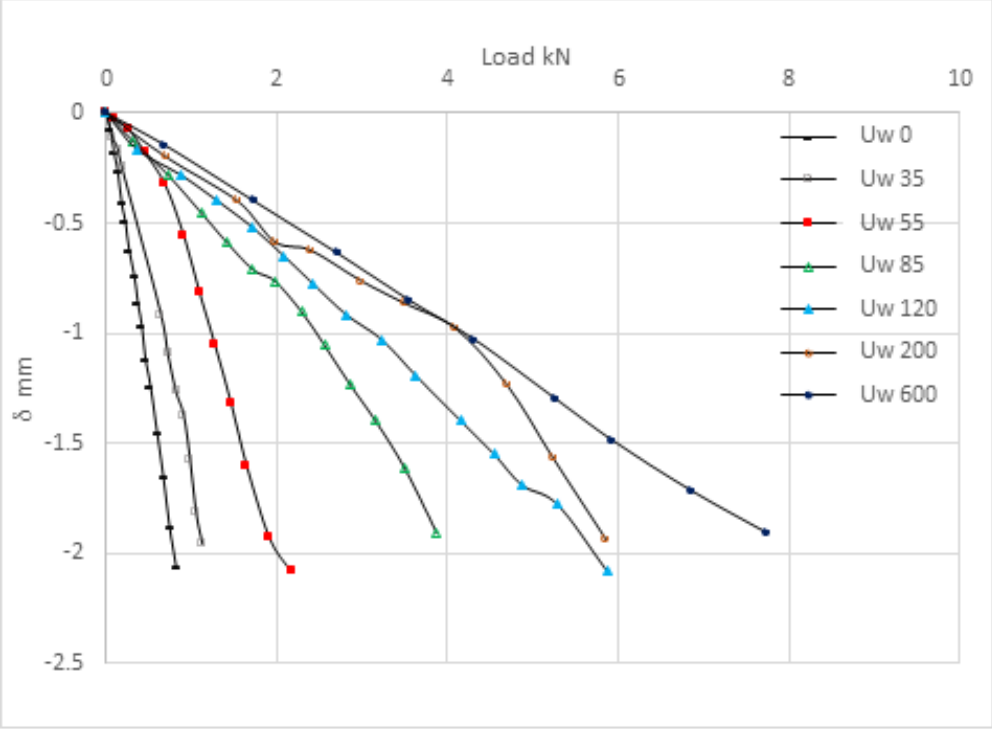

Figure 3.19 Load-settlement curve of URF models tested in various suctions (U_w in kPa)

3.4.2.2 Effect of Foundation Type on Load Deformation Curves for Various Suctions

Load deformation curves from PRF, PGF, URF model tests and combined test data (PGF and URF) with different suction values are shown in Figures 3.20 through 3.26. In general, PRF showed higher resistance than PGF and URF due to the contribution of the raft in PRF capacity. The capacity of PRF was less than the combined capacities of PGF and URF. The difference can be attributed to the interaction between the components of PRF. The PRF alone capacities at the ultimate stages were 81%, 91%, 83%, 75%, 78%, 87% and 70% of combined PGF and URF capacities for 0, 35, 55, 85, 120, 200, 600 kPa suctions, respectively.

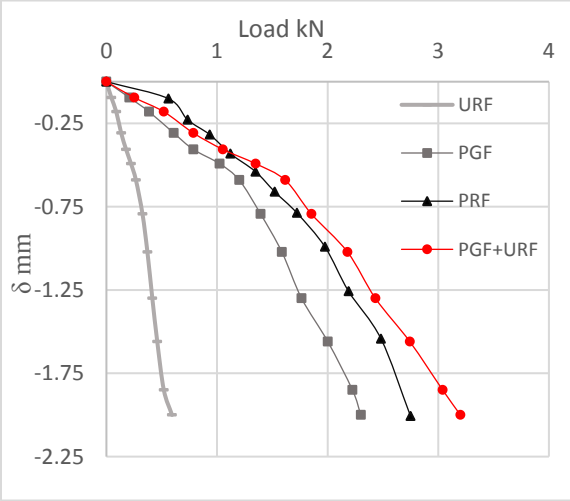

Figure 3.20 Load-settlement curves, at 0 kPa suction

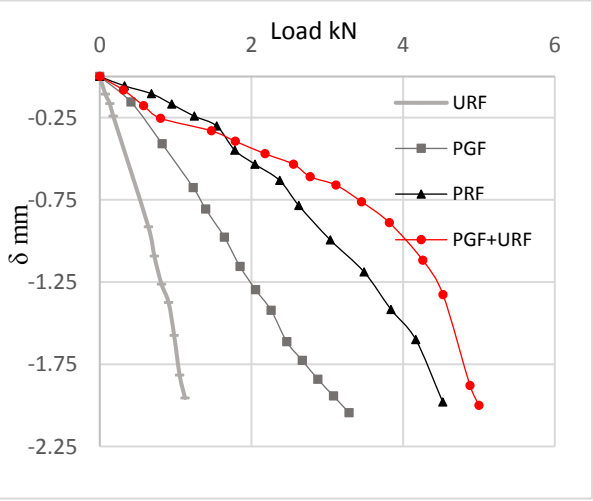

Figure 3.21 Load -settlement curves, 35 at kPa suction

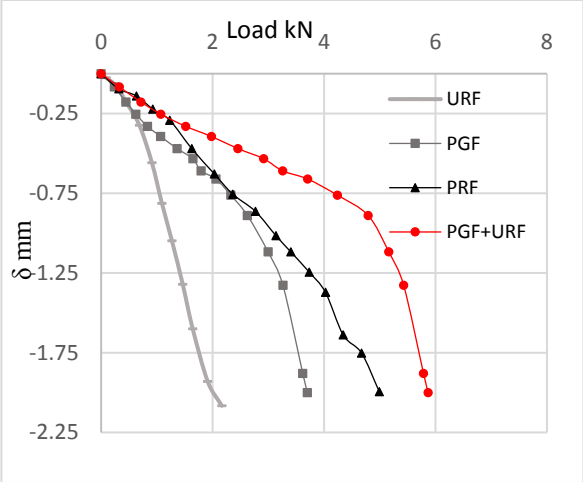

Figure 3.22 Load-settlement curves at 55 kPa suction

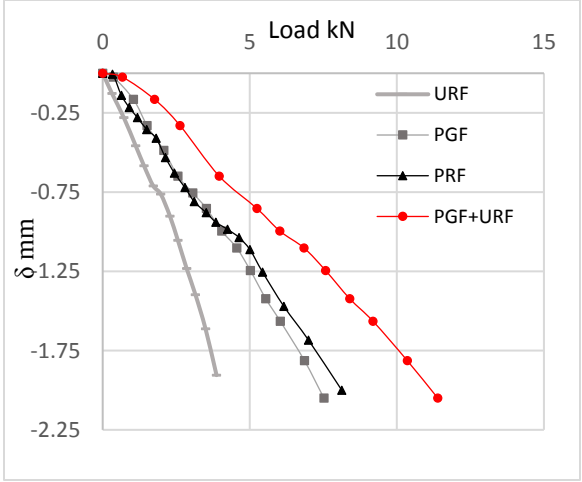

Figure 3.23 Load-settlement curves at 85 kPa suction

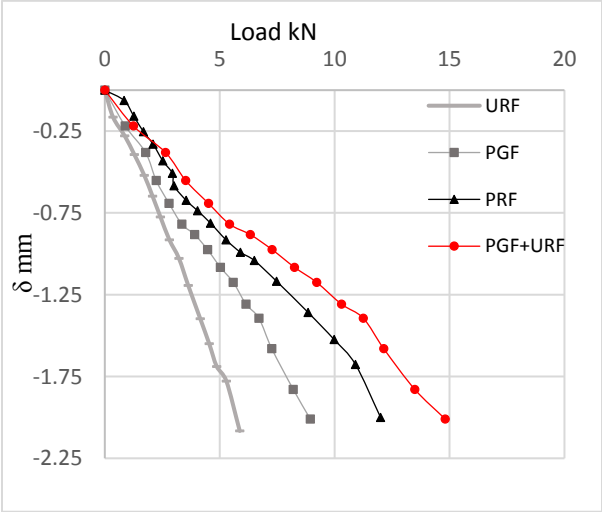

Figure 3.24 Load-settlement curves at 120 kPa suction

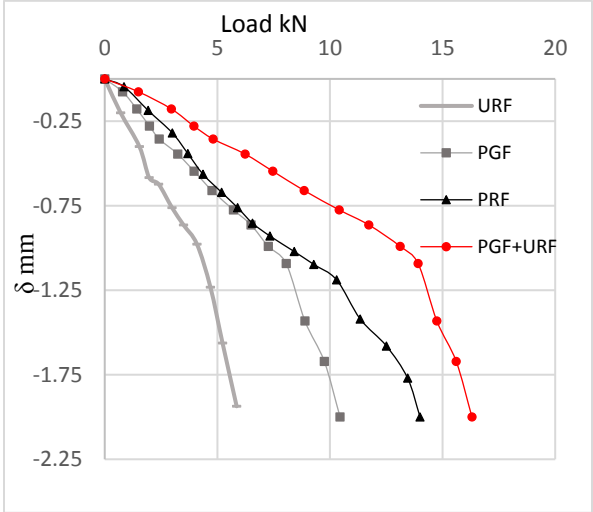

Figure 3.25 Load-settlement curves at 200 kPa suction

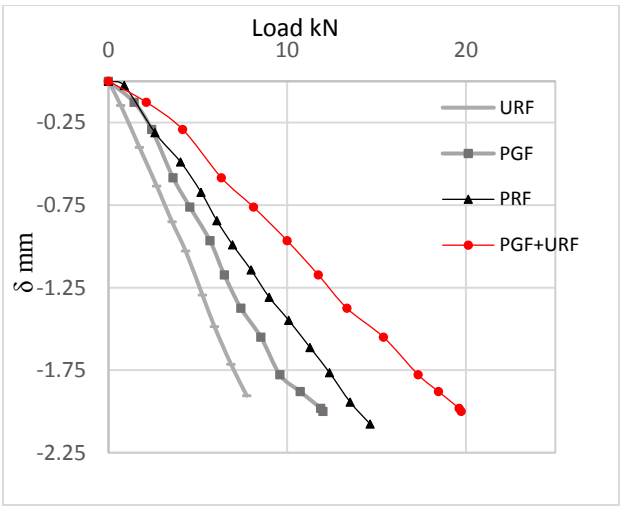

Figure 3.26 Load -settlement curves at 600 kPa suction

3.4.2.3 Load-Settlement Curves of Single Piles of PRF and PGF Model Tests based on Their Locations

PRF and PGF models adopted in this study consist of 3 x 3 piles. Piles in PRF and PGF can be classified based on their location in the model test to Center pile (CR), Side piles (S) and Corner piles (C). Figures 3.27 through 3.33 show load-settlement curves of each pile in PRF and PGF. It can be noticed that the central piles in PGF and PRF showed higher resistance than the side and the corner piles. The higher capacity of central piles can be attributed to the nature of the applied load (concentrated on the raft directly above the central pile) and to the rigidity of the raft.

Piles in PRF showed slightly less resistance than corresponding piles in PGF due to raft – piles interaction. The interaction may be resulted from the load taken by the raft which may minimize the mobilization of full skin friction resistance in PRF model.

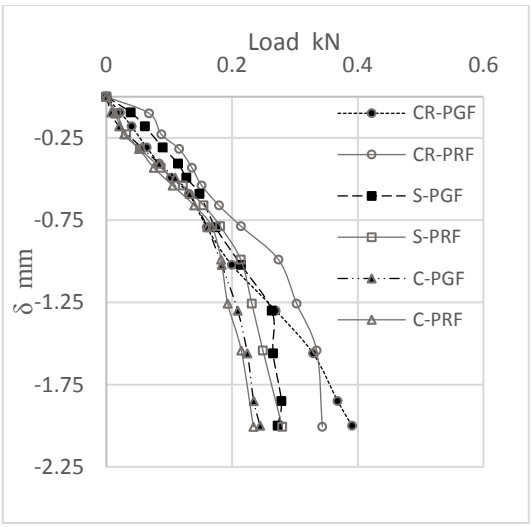

Figure 3.27 Load-settlement curve at 0 kPa suction

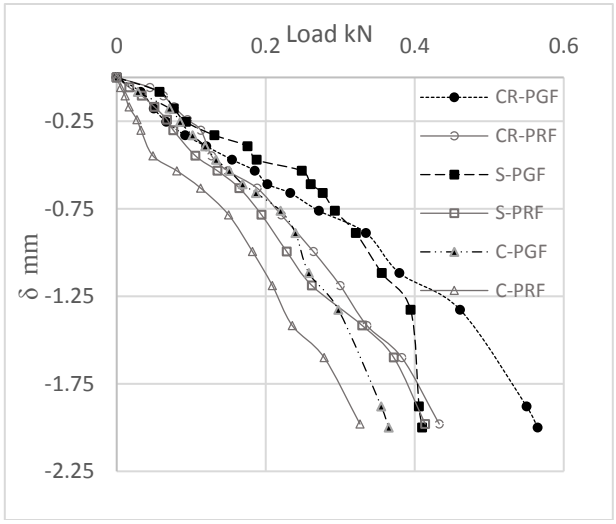

Figure 3.28 Load-settlement curve at 35 kPa suction

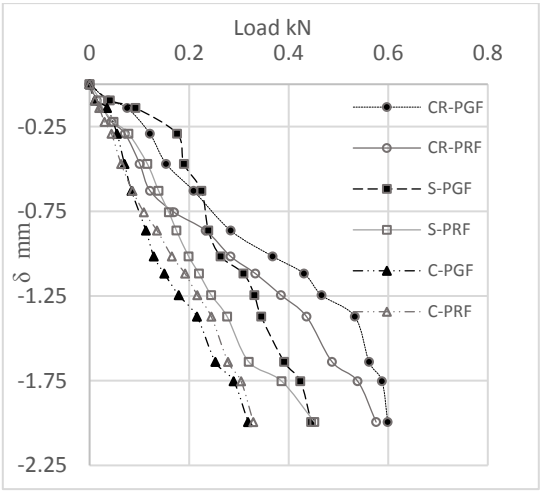

Figure 3.29 Load-settlement curve at 55 kPa suction

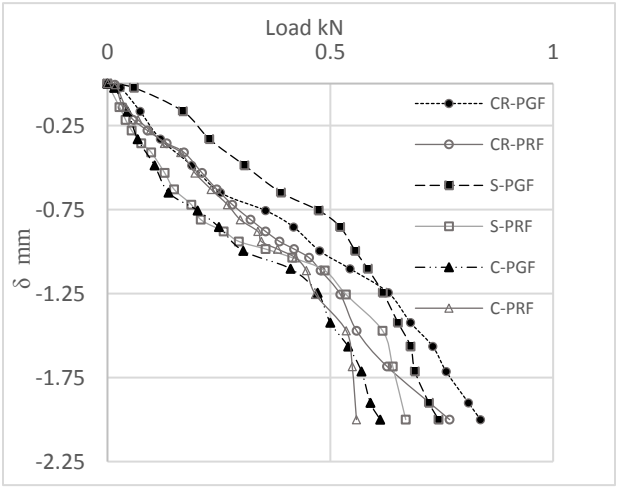

Figure 3.30 Load-settlement curve at 85 kPa suction

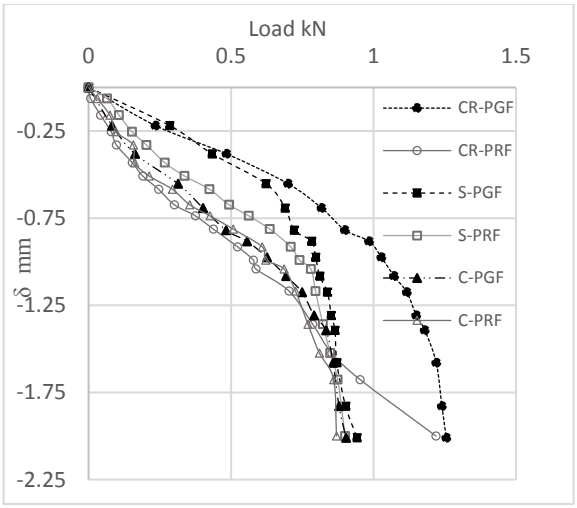

Figure 3.31 Load-settlement curve at 120 kPa suction

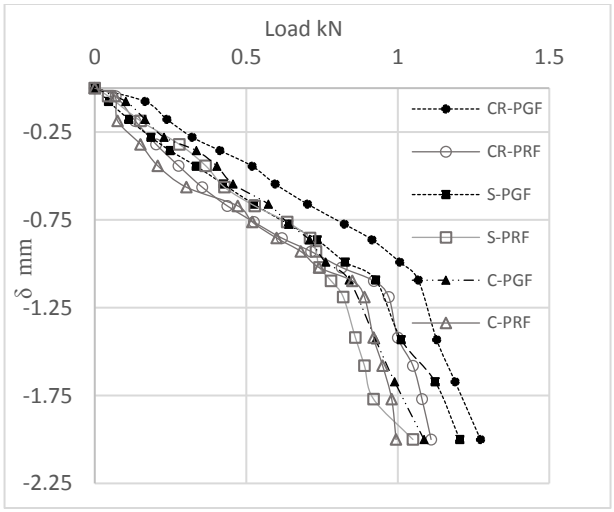

Figure 3.32 Load-settlement curve at 200 kPa suction

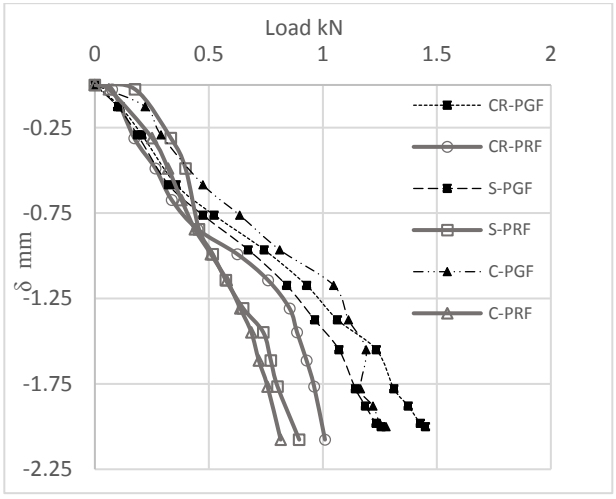

Figure 3.33 Load-settlement curve at 600 kPa suction

3.4.2.4 Skin Friction Resistance (SFR) of Pile(s) in SPF, PRF, and PGF Model Tests

Figure 3.34 shows Skin Friction Resistance (SFR) settlement curve of SPF model tested under different suctions. It can be noticed that SFR values for single piles were fully mobilized at about 0.75 - 1 mm settlement (4 to 5 % of the pile diameter). Ultimate SFR for pile tested under 600 kPa was less than the pile tested under 200 kPa. The decrease in ultimate SFR at higher suctions may be due to the deterioration in SFR beyond the air entry value. It shall be noticed, however, that SFR for pile tested in 600 kPa suction was three times larger than that for piles tested in the fully saturated soil ($U_w = 0$).

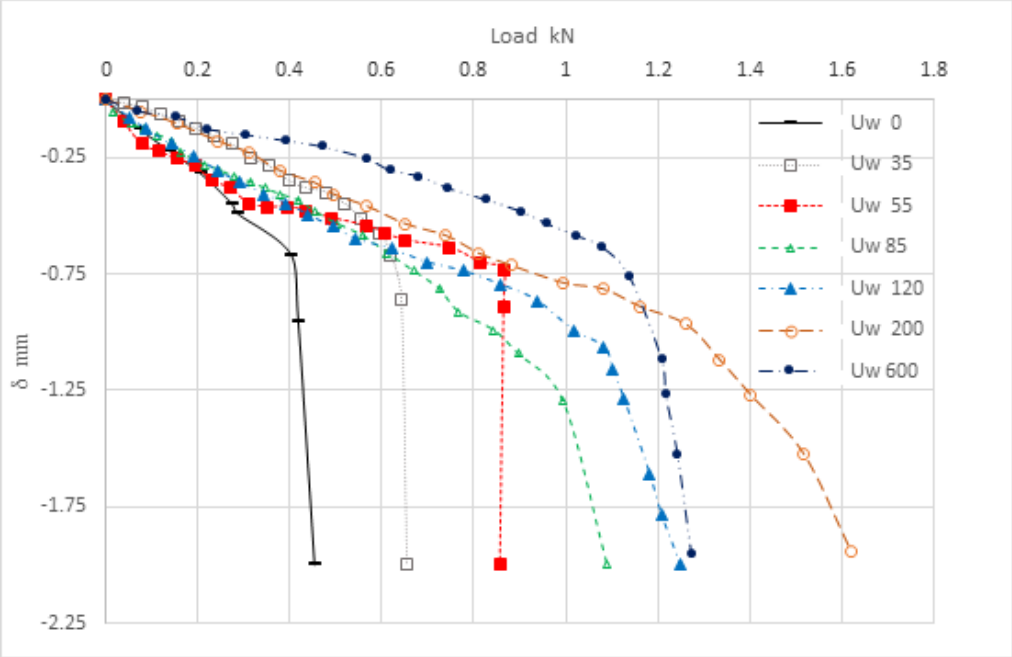

Figure 3.34 SFR vs. settlement of SPF at different suctions (U_w in kPa)

Figures 3.35 through 3.40 show SFR versus settlement curves at different pile locations in the foundation. It was observed that in most cases SFR in PGF and PRF with 200 and 600 kPa suctions were less than the pile tested in 120 kPa. The degradations in SFR at higher suction in PGF and PRF were even higher than that observed for single piles (SPF) as seen in Figure 3.34.

This observation might be related to the interaction of piles in the group. It will be seen later that the increase in EBR (End Bearing Resistance) for PGF and PRF offsets some of this reduction in Total Foundation Resistance vs. settlement curves at high suction values. By comparing Figures 3.35 through 3.37 for PGF with Figures 3.38 through 3.40 for PRF, it is observed that SFR values for PGF were slightly higher than PRF at all pile locations due to raft interaction with piles in PRF.

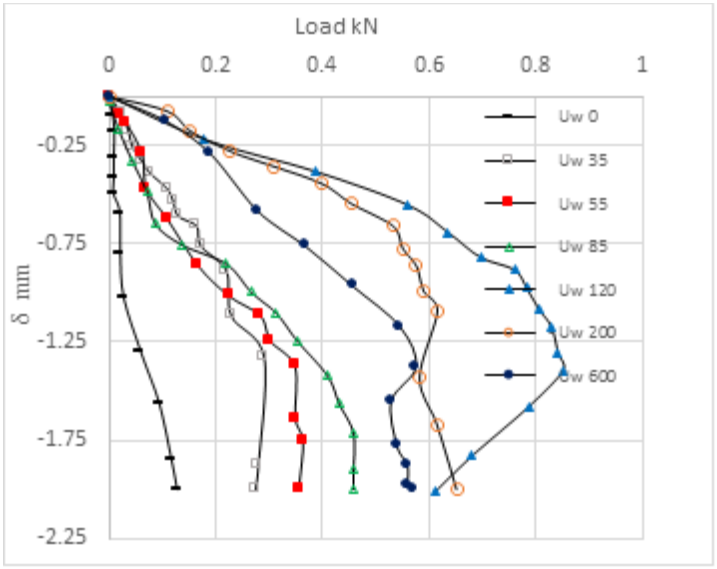

Figure 3.35 SFR vs. settlement for center piles in PGF model at different suctions (U_w in kPa)

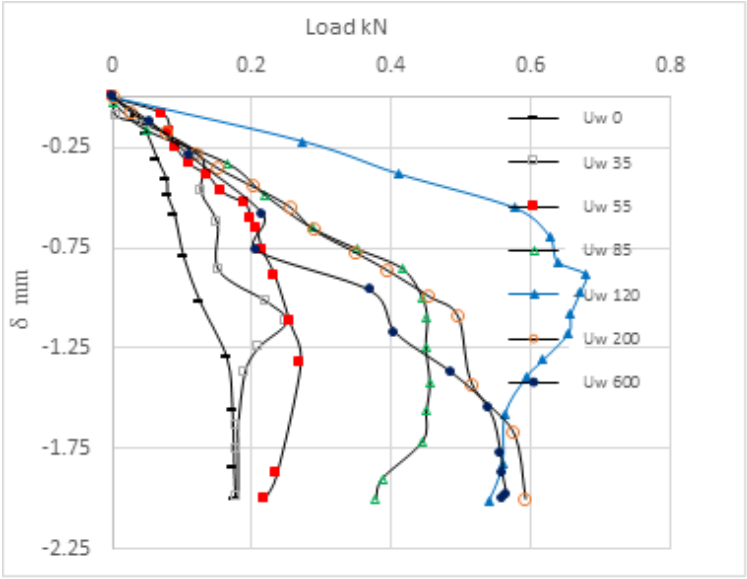

Figure 3.36 SFR vs. settlement for side piles in PGF model a different suctions (U_w in kPa)

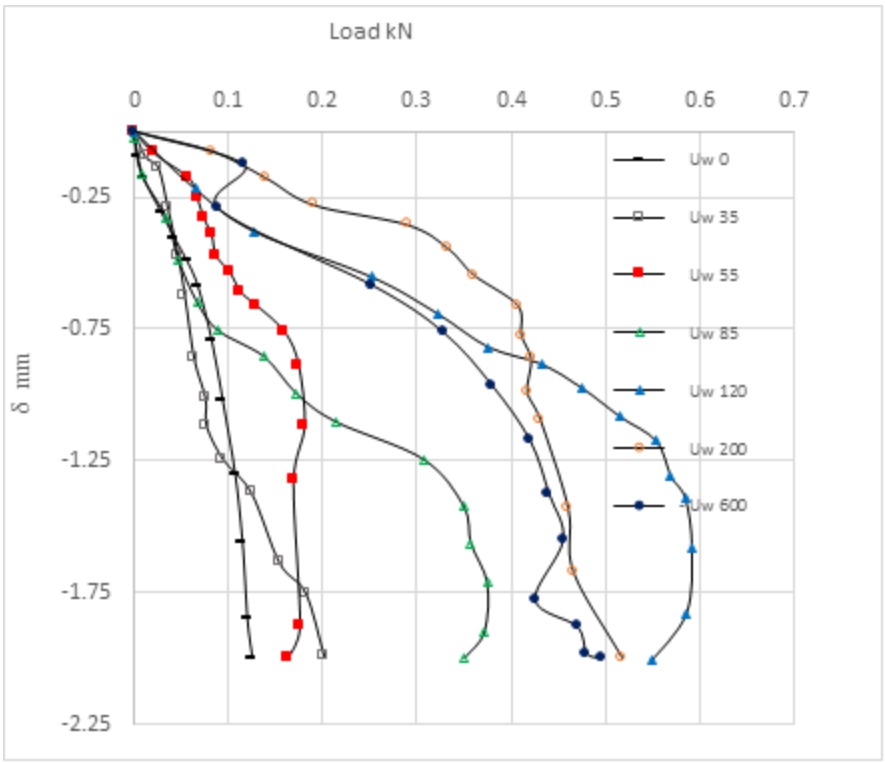

Figure 3.37 SFR vs. settlement for corner piles in PGFmodel at different suctions (U_w in kPa)

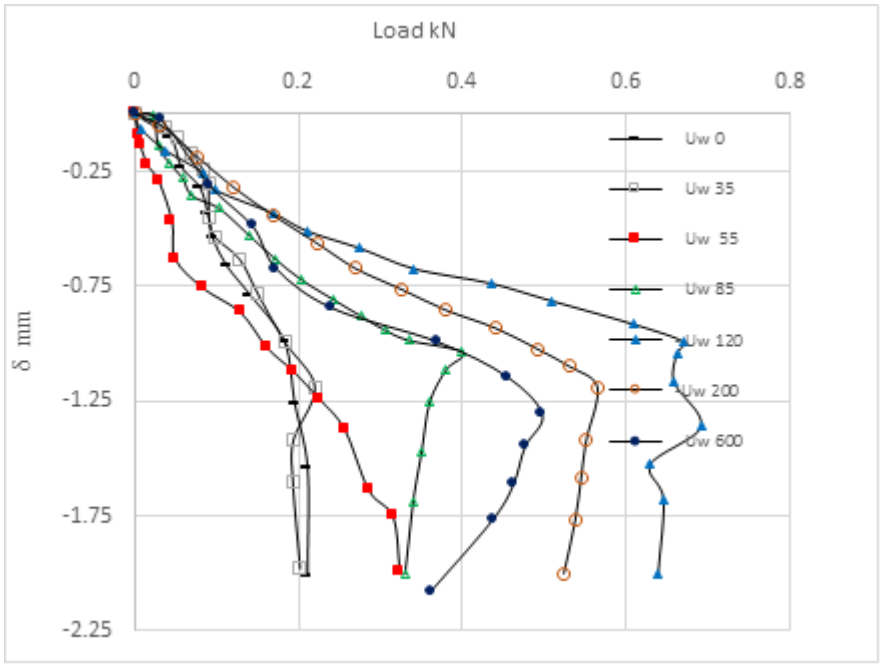

Figure 3.38 SFR vs. settlement for center piles in PRF model at different suctions (U_w in kPa)

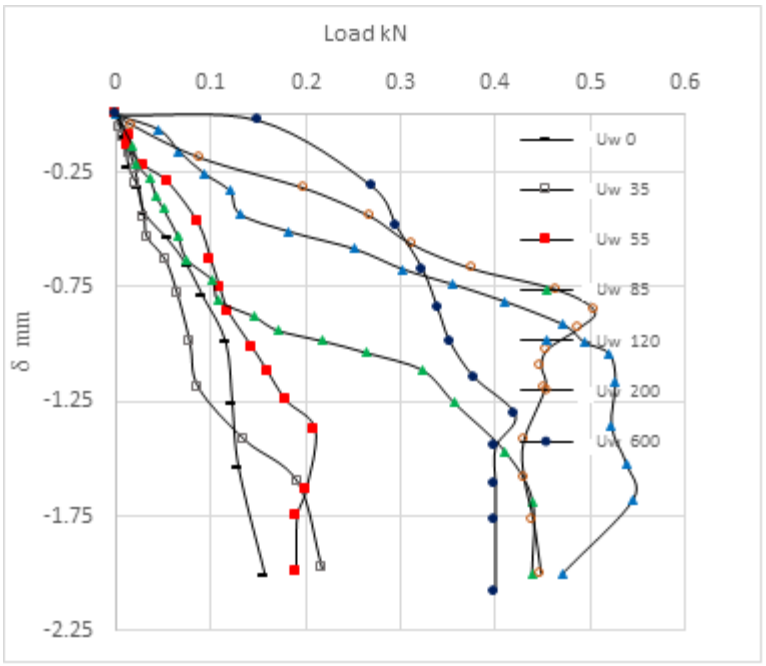

Figure 3.39 SFR vs. settlement for side piles in PRF mode at different suctions (Uw in kPa)

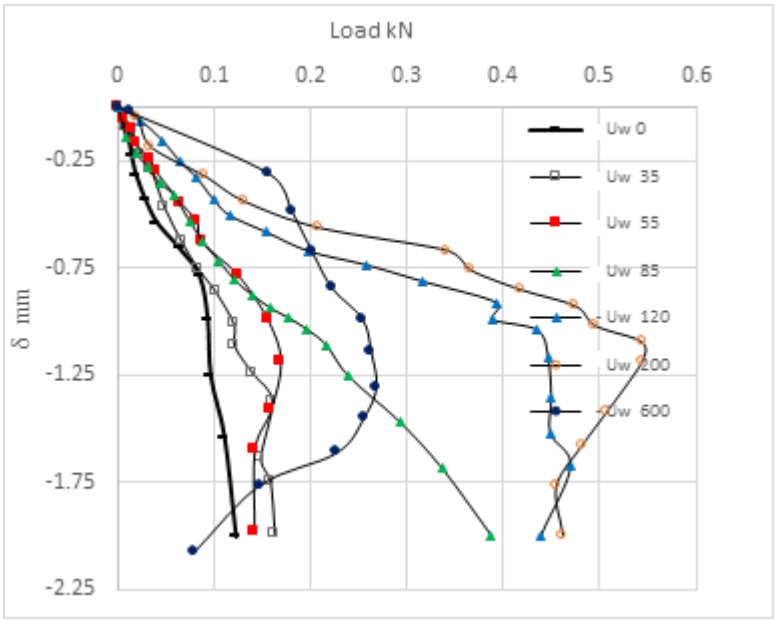

Figure 3.40 SFR vs. settlement for corner piles in PRF model at different suctions (Uw in kPa)

3.4.2.5 End Bearing Resistance (EBR) of Pile(s) in SPF, PRF, and PGF Model Tests

Figure 3.41 plots EBR versus settlement curves for SPF with different suctions. It shows that EBR for single piles have increased with suction and the maximum values were attained at the end of the tests at 2 mm settlement. The largest EBR was in a foundation tested at the highest suction (600 kPa). Ultimate EBR for pile tested under 600 kPa suction was 3.6 times that for the pile tested in the fully saturated soil ($U_w = 0$).

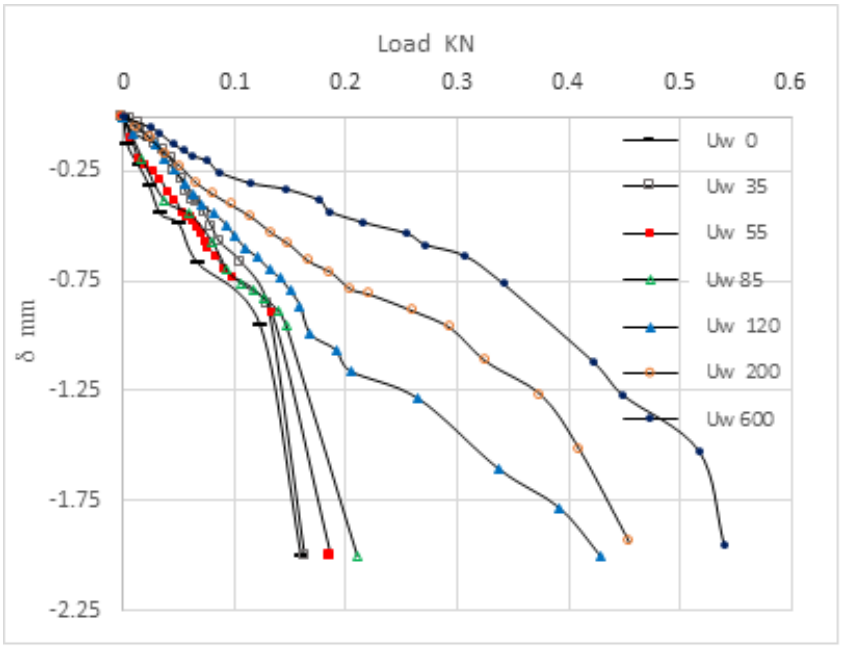

Figure 3.41 EBR vs. settlement of SPF at different suctions (U_w in kPa)

Figures 3.42 through 3.47 plot EBR versus settlement curves for PGF and PRF at different pile locations. When comparing those results with SPF data shown in Figure 3.41, it can be seen that EBRs of piles in all locations (central, side and corner) tested with suctions less than AEV (105 kPa) were close or even slightly higher than EBR of single piles tested at same suctions. EBR values for PGF and PRF tested under higher suctions were noticeably higher than EBR of single piles tested at the same suction.

It can be concluded that there was no group effect in EBR values at suction less than the AEV and there was positive group effect (increasing in EBR) for foundations tested at higher suctions. The above discussion and conclusion can be visualized in a relationship showing the positive group effect of suction on EBR in both PGF and PRF in Chapter Five.

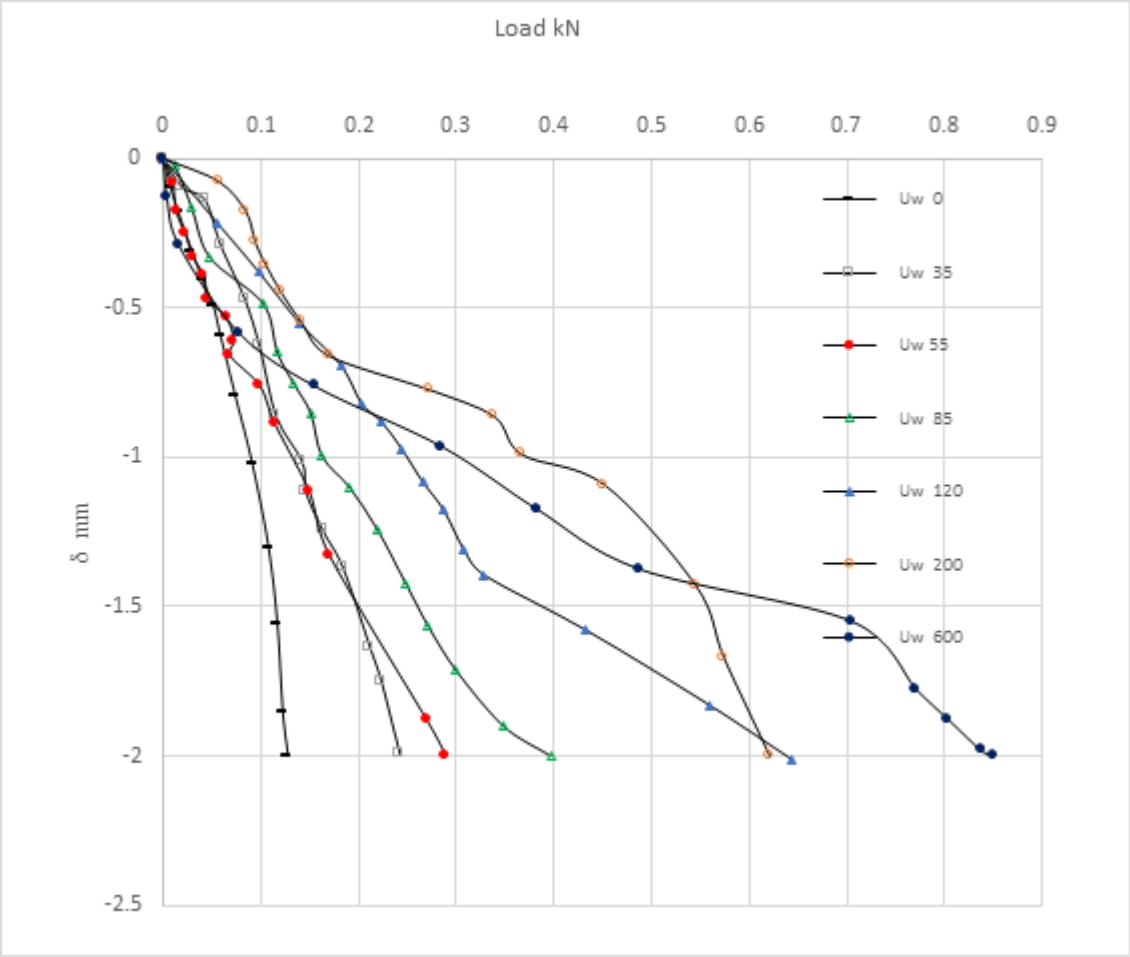

Figure 3.42 EBR vs. settlement of PGF, center piles at different suctions (U_w in kPa)

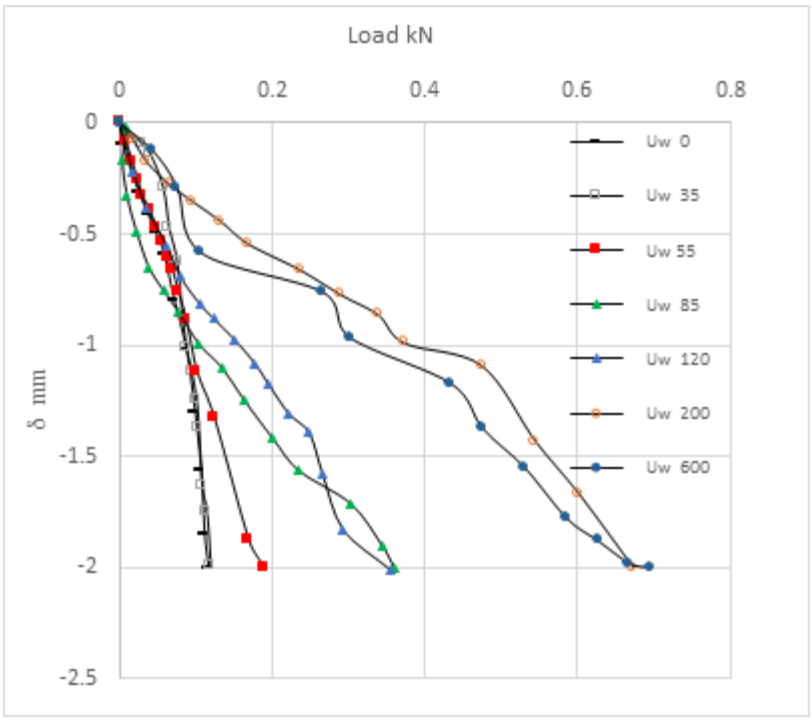

Figure 3.43 EBR vs. settlement of PGF, side piles at different suctions (U_w in kPa)

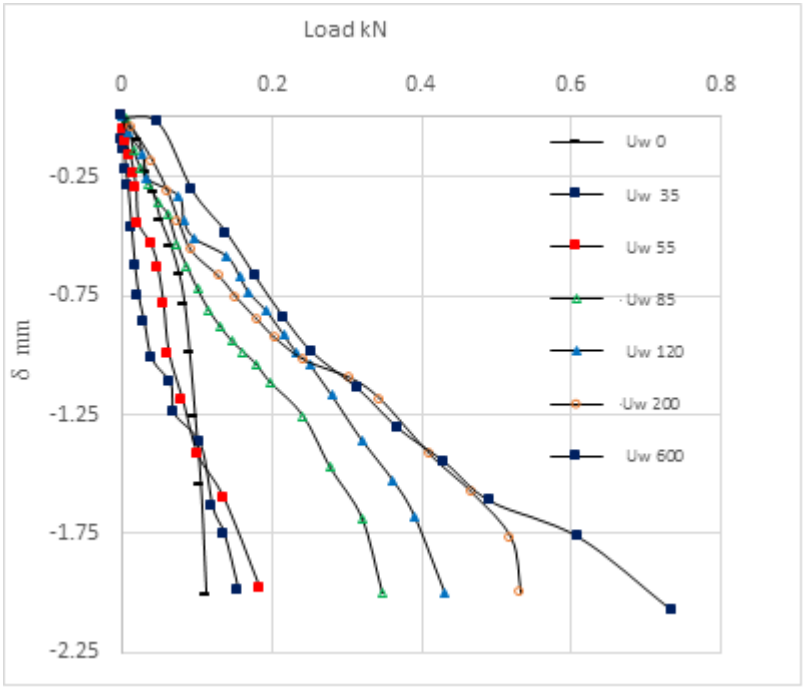

Figure 3.44 EBR vs. settlement of PGF, corner piles at different suctions (U_w in kPa)

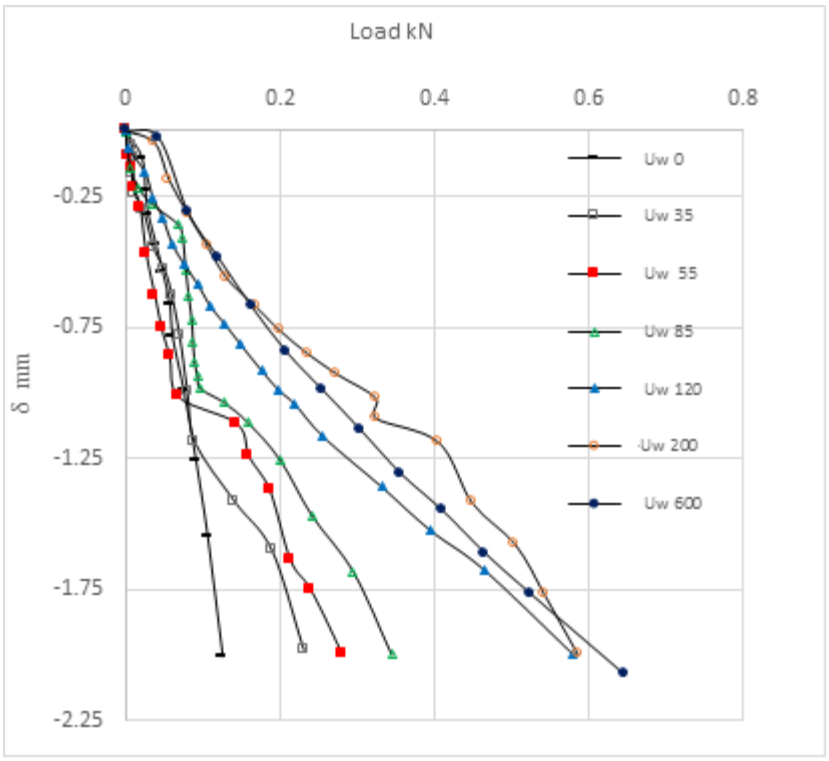

Figure 3.45 EBR vs settlement of PRF, center piles at different suctions (U_w in kPa)

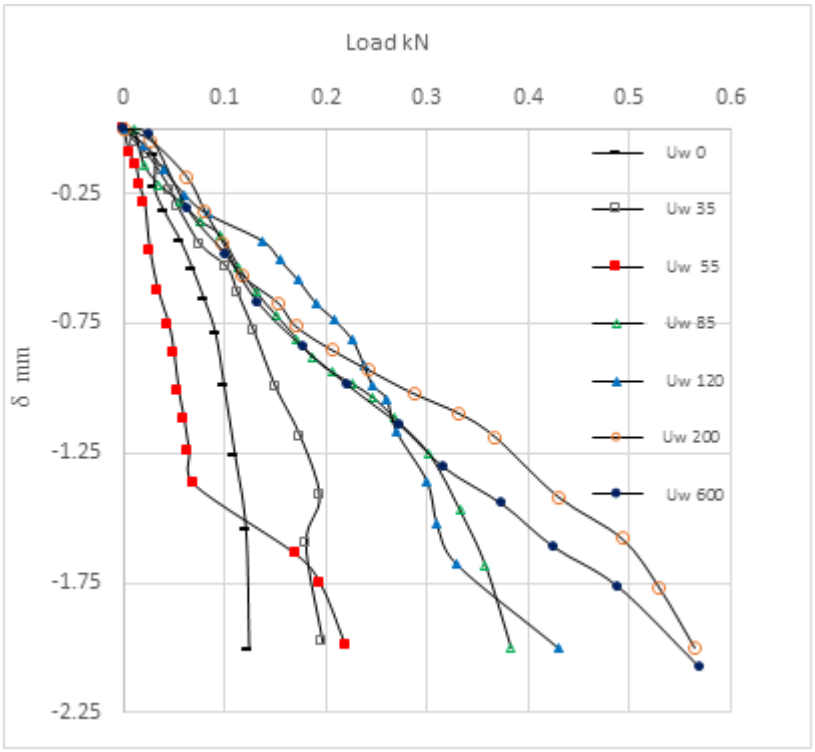

Figure 3.46 EBR vs settlement of PRF, side piles at different suctions (U_w in kPa)

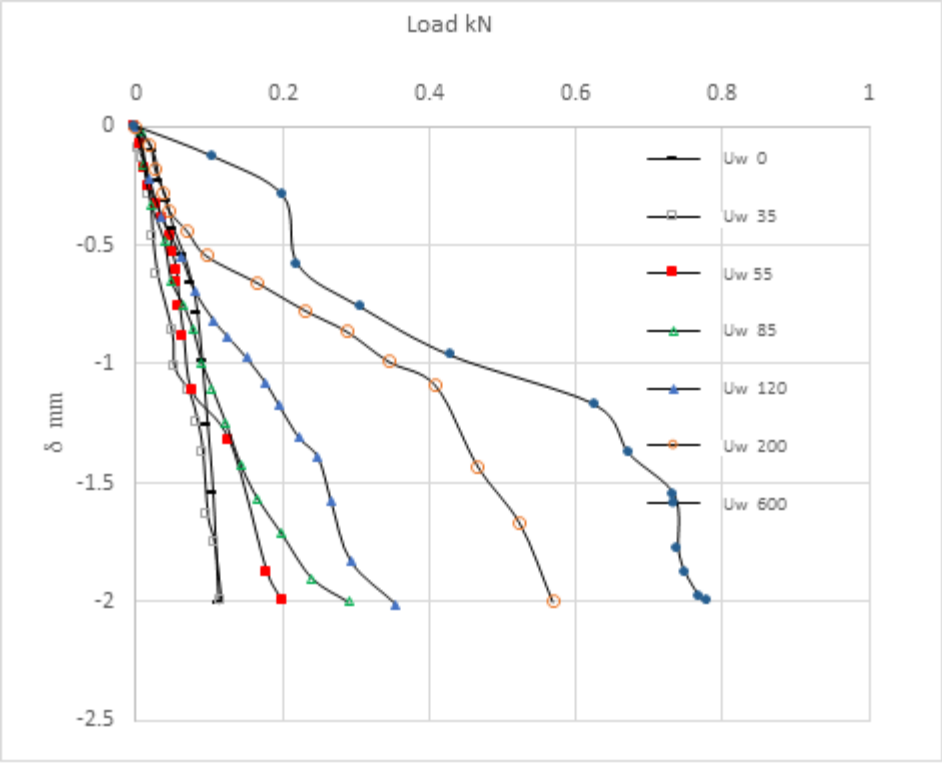

Figure 3.47 EBR vs settlement of PRF, corner piles at different suctions (U_w in kPa)

3.4.2.6 Effect of Pile Locations on SFR and EBR of PGF and PRF

Figures 3.48 through 3.61 plot load versus settlement curves (SFR in Figures 3.48 through 3.54 and EBR in Figures 3.55 through 3.61) at different pile locations at different suction values. Those indicate that SFR and EBR were slightly higher in center piles than side and corner piles in both PRF and PGF due to the nature of applied load and the rigidity of the raft. In general, SFR and EBR values at center, side and corner piles in PGF exhibit slightly greater values than corresponding piles in PRF. The difference can be attributed to raft-pile interaction. SFR of PGF and PRF at all locations showed considerably less values comparing to SFR of single pile when tested at higher suctions. On the other hand, EBR at all locations for both PRF and PGF showed significantly higher values compared to EBR of single pile when tested at higher suctions. The

increase in EBR offsets the decrease in SFR at higher suctions in both PGF and PRF. EBR of all piles showed less scattering than SFR in both foundation types.

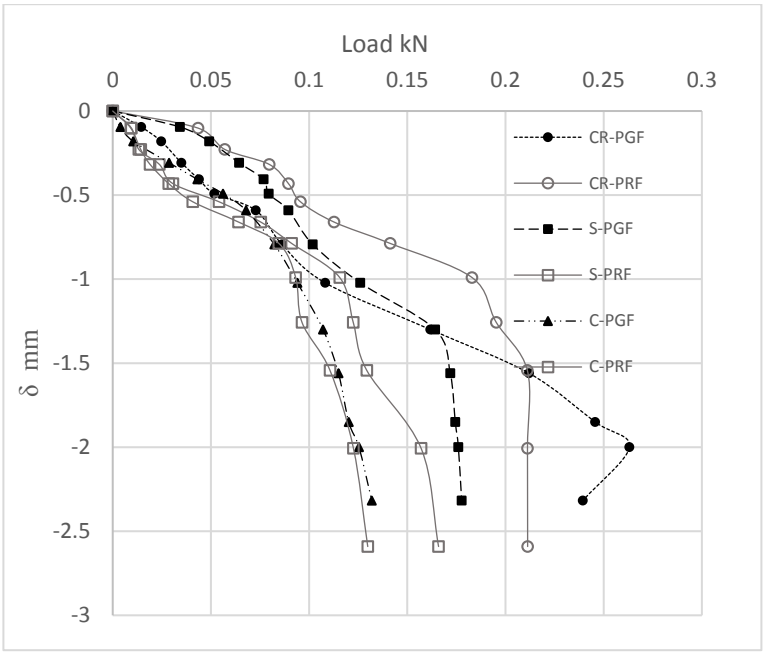

Figure 3.48 SFR vs. settlement curves at center, side and corner piles at zero suction

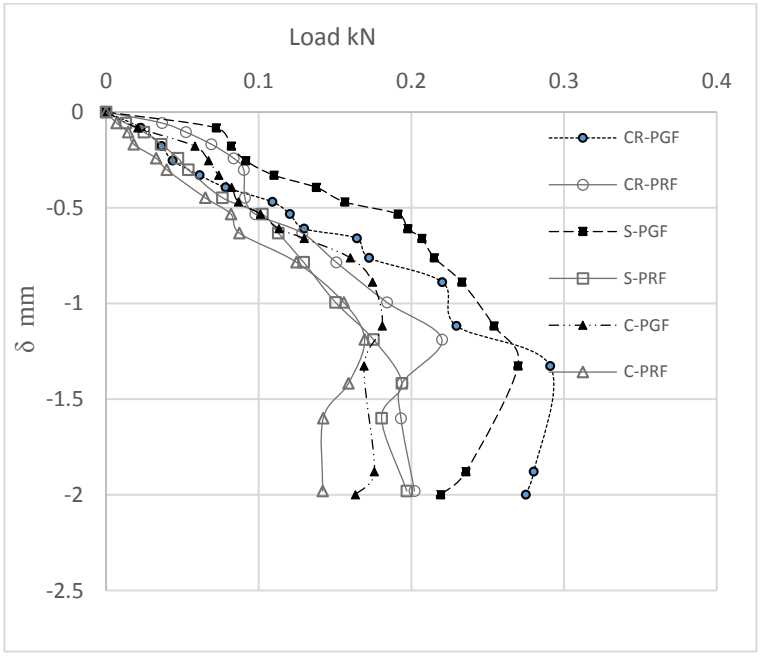

Figure 3.49 SFR vs. settlement curves at center, side, and corner piles at 35 kPa suction

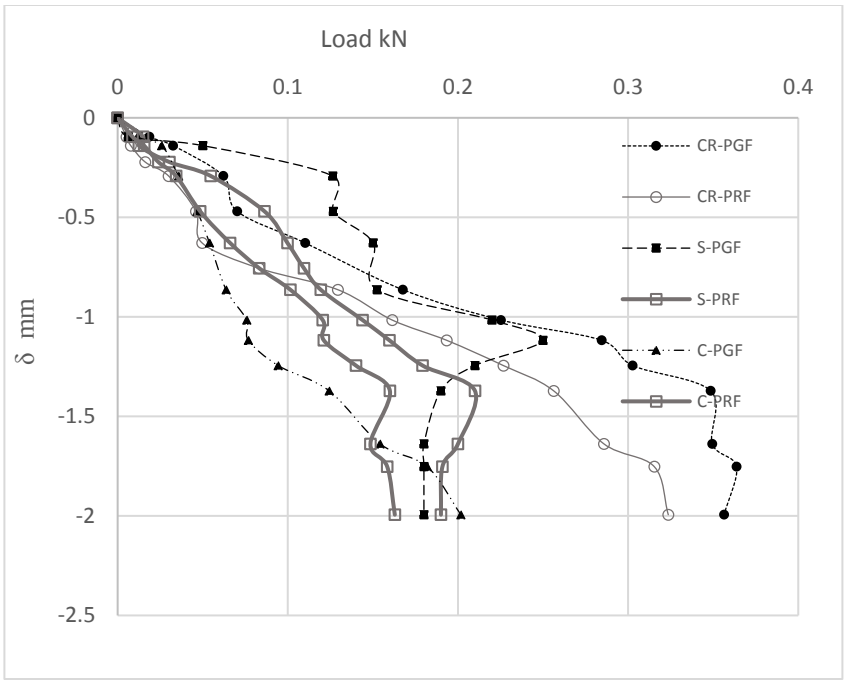

Figure 3.50 SFR vs. settlement curves at center, side, and corner piles at 55 kPa suction

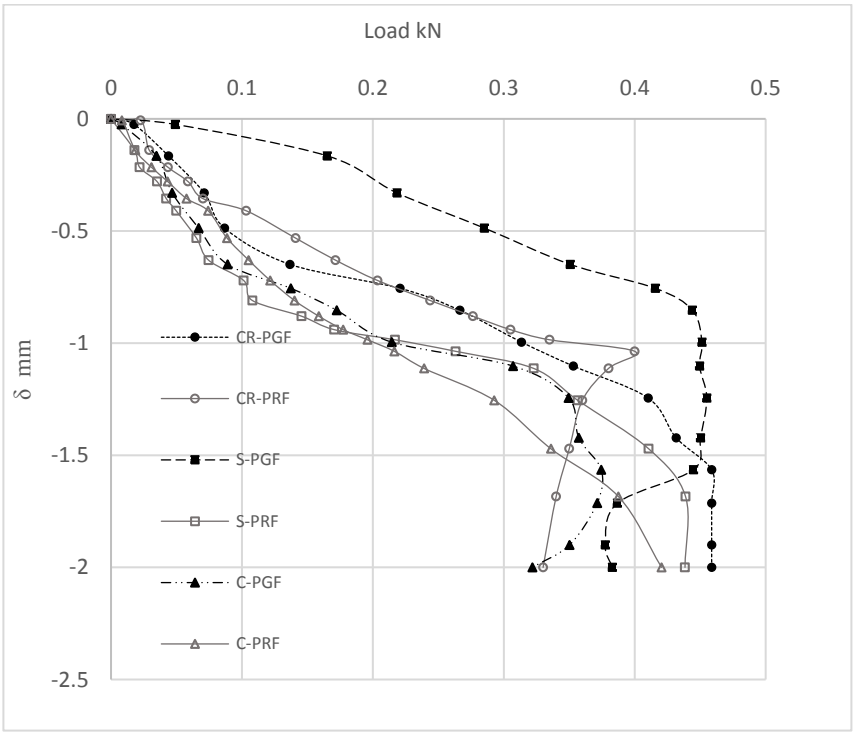

Figure 3.51 SFR vs. settlement curves at center, side, and corner piles at 85 kPa suction

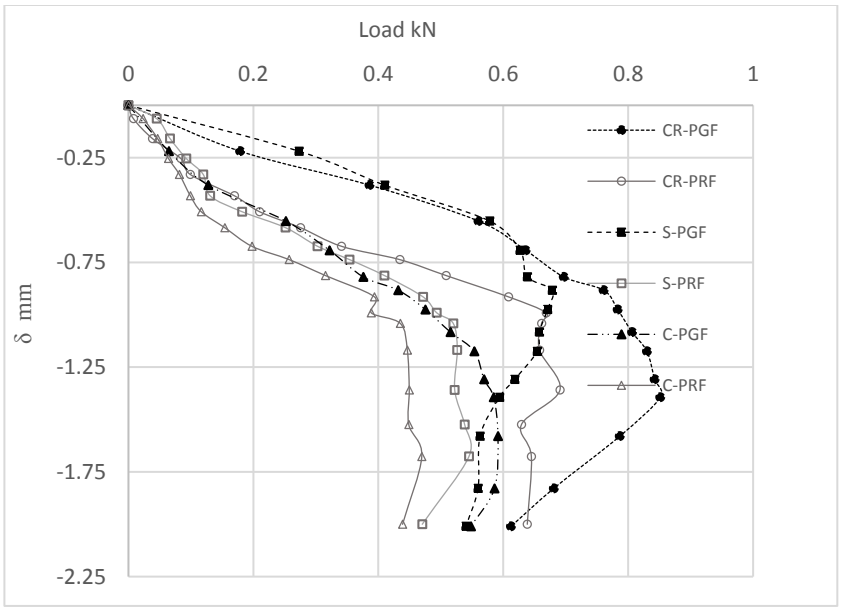

Figure 3.52 SFR vs. settlement curves at center, side, and corner piles at 120 kPa suction

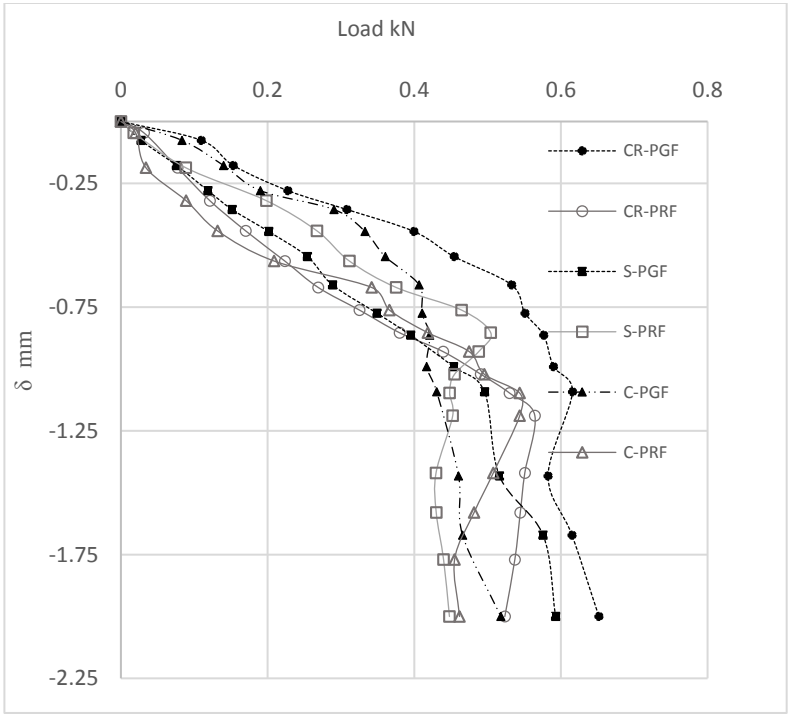

Figure 3.53 SFR vs. settlement curves at center, side, and corner piles at 200 kPa suction

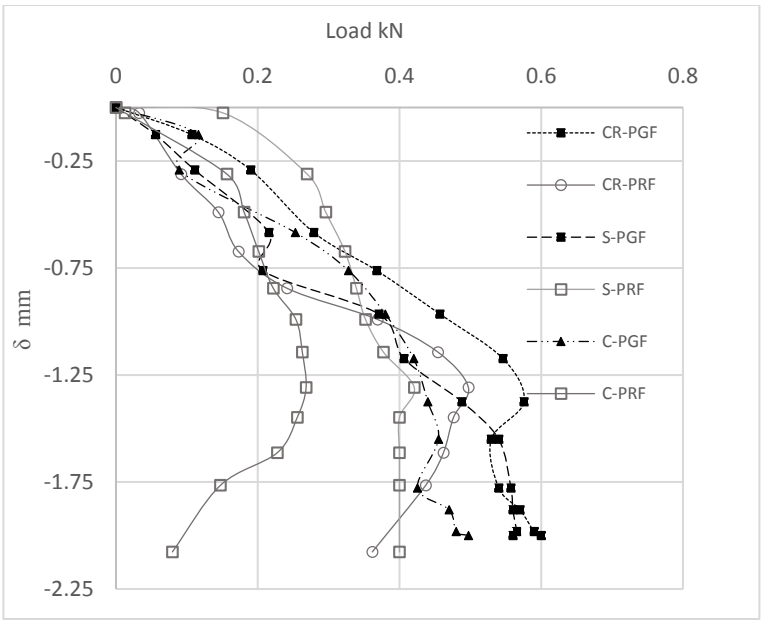

Figure 3.54 SFR vs settlement curves at center, side and corner piles at 600 kPa suction

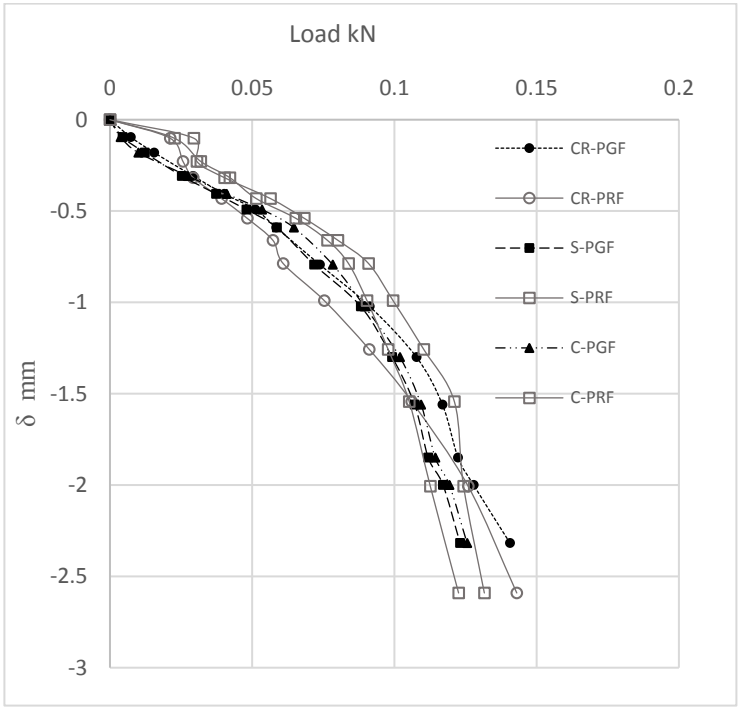

Figure 3.55 EBR vs settlement curves atcenter, side and corner piles at zero suction

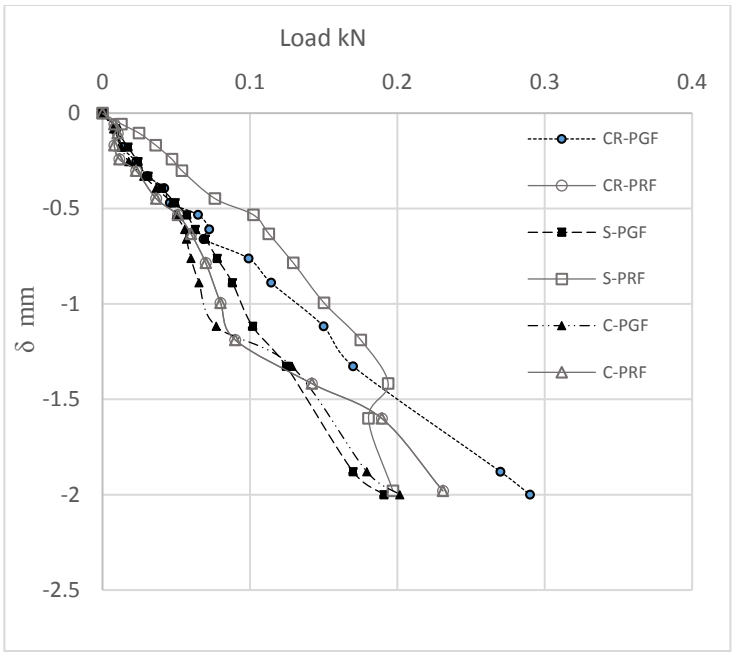

Figure 3.56 EBR vs settlement curves for center, side and corner piles tested at 35 kPa suction

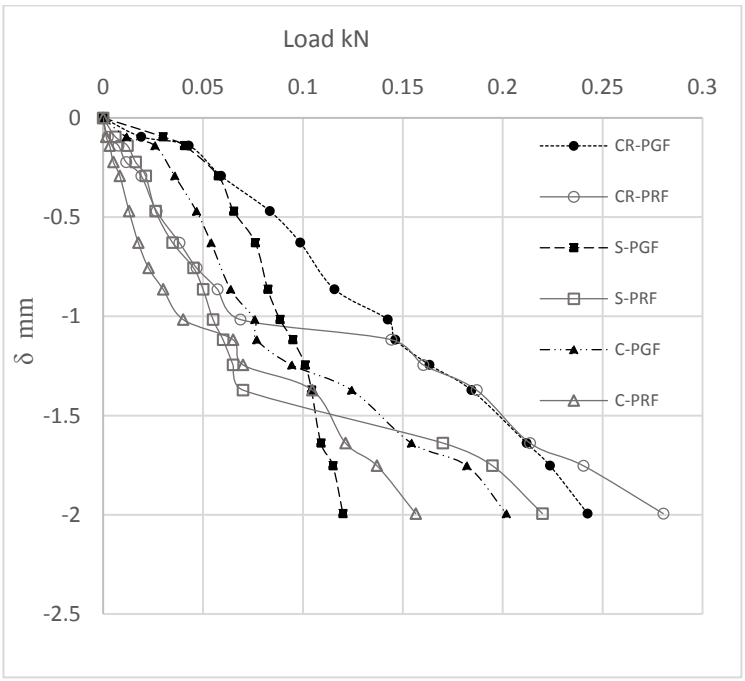

Figure 3.57 EBR vs settlement curves at center, side and corner piles at 55 kPa suction

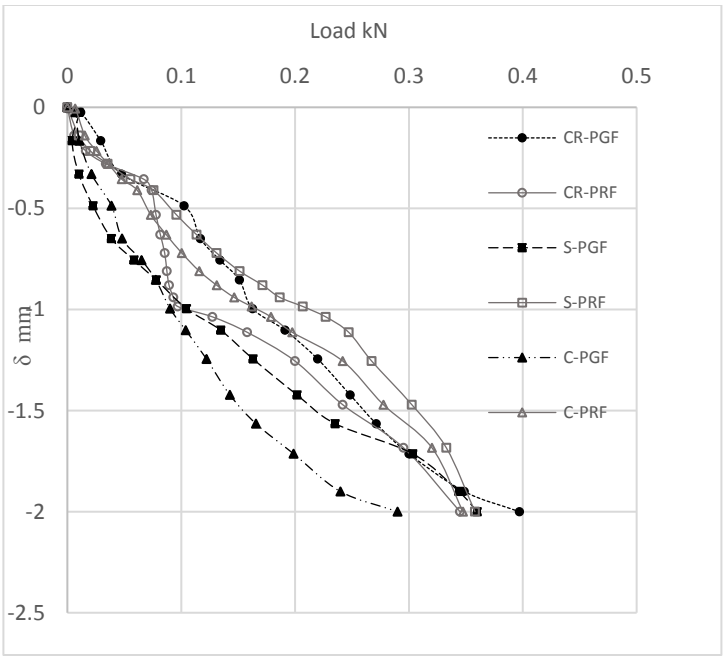

Figure 3.58 EBR vs settlement curves at center, side and corner piles at 85 kPa suction

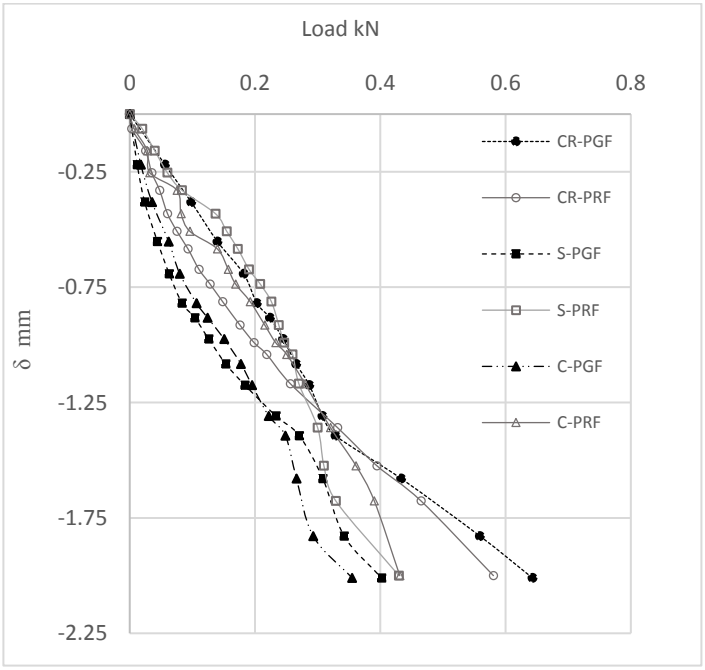

Figure 3.59 EBR vs settlement curves at center, side and corner piles at 120 kPa suction

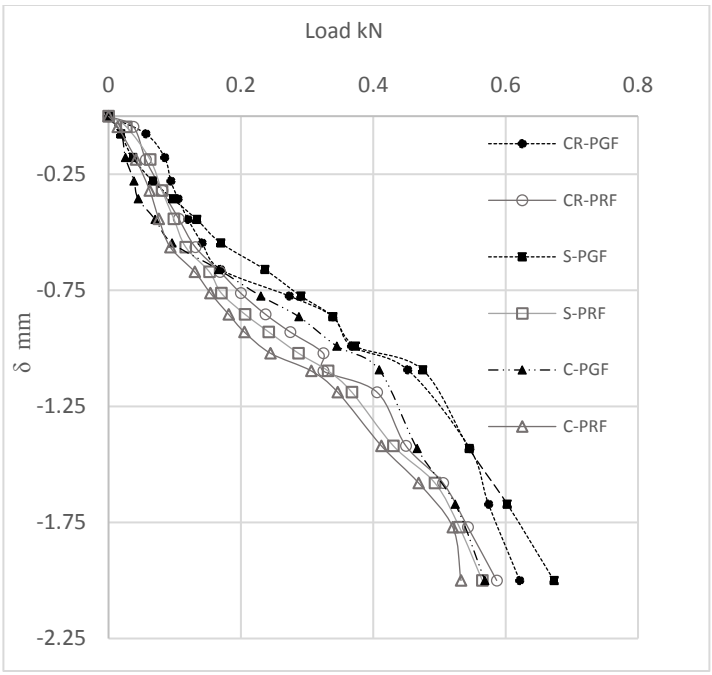

Figure 3.60 EBR vs settlement curvesat center, side and corner piles at 200 kPa suction

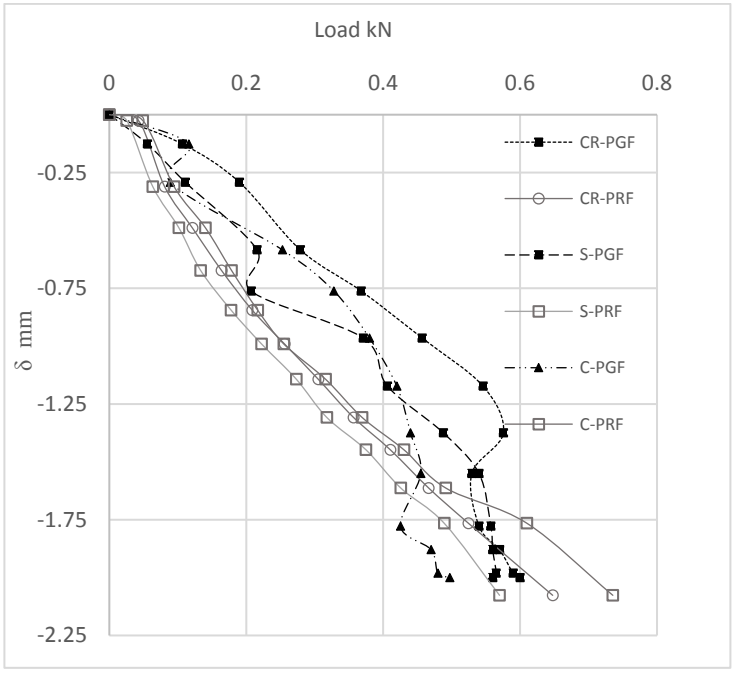

Figure 3.61 EBR vs settlement curves for center, side and corner piles at 600 kPa suction

3.4.2.7 PWP and Suction versus Settlement

Figures 6.62 through 6.67 plot pore water pressure (PWP) and suctions versus pile settlement measured at various locations. It can be noticed that PWP has increased and suction has reduced upon the application of the load. In most cases, the decrease in soil suctions at the center of foundations (25 mm below the pile tip) was higher in PGF than PRF. The reason could be related to the trend of higher EBR in PGF than corresponding one in PRF. Meanwhile, the reduction in suction was greater underneath the raft in PRF due to the contribution of the raft in PRF which imposing contact pressure on the soil. The reductions in suction were about 10% in the soil below the pile tip and the reduction at 150 mm below the soil surface for both foundations were relatively small.

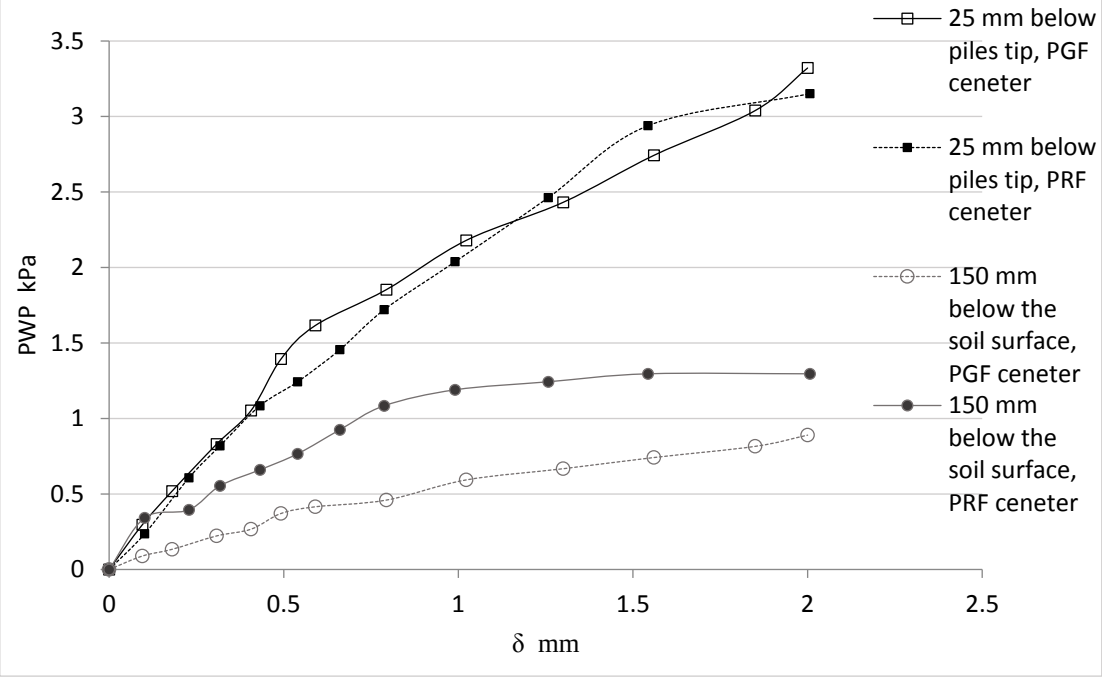

Figure 3.62 Variation of PWP with settlement for PGF and PRF at zero suction

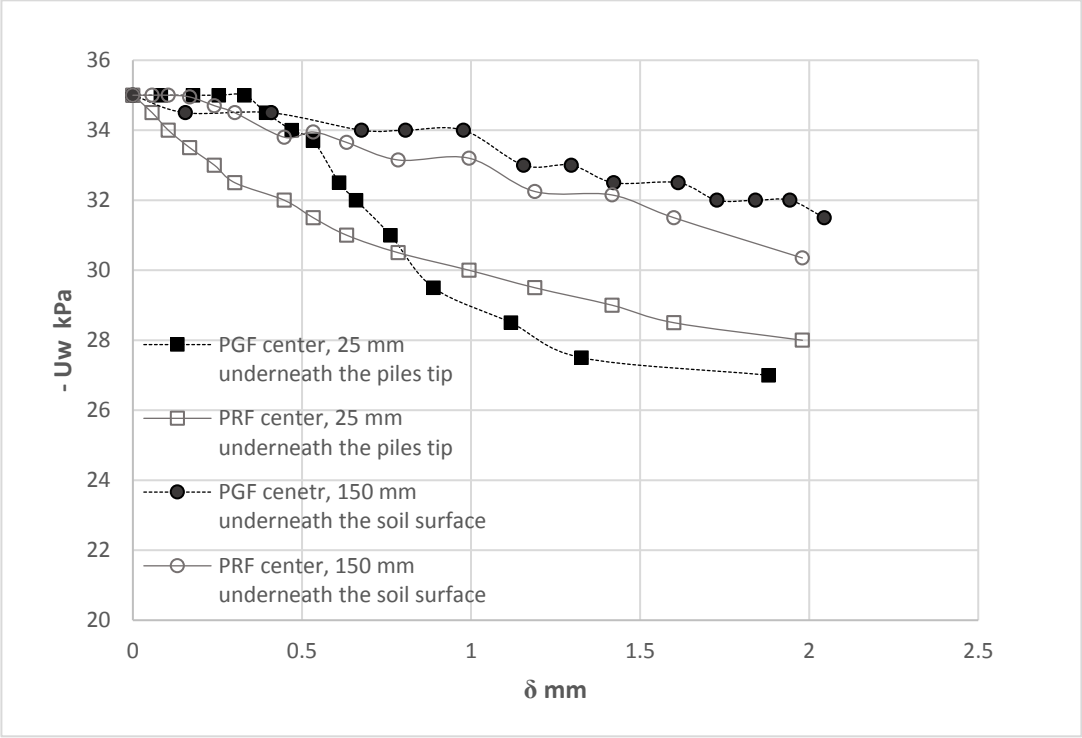

Figure 3.63 Variation of suction with settlement for PGF and PRF at 35 kPa suction

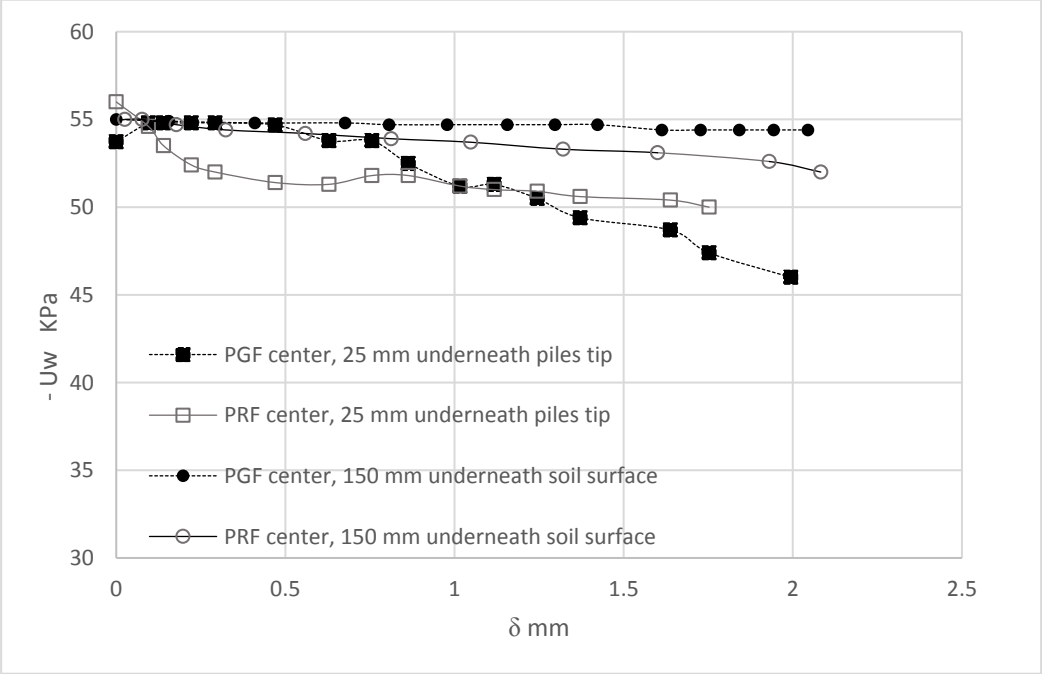

Figure 3.64 Variation of suction with settlement for PGF and PRF at 55 kPa suction

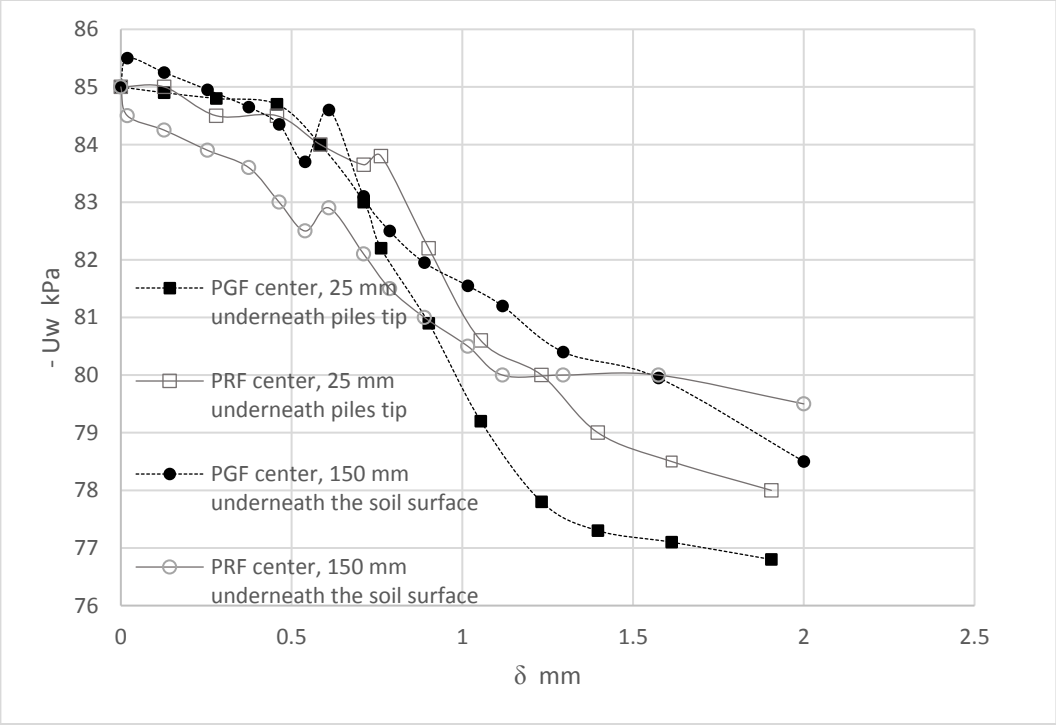

Figure 3.65 Variation of suction with settlement for PGF and PRF at 85 kPa suction

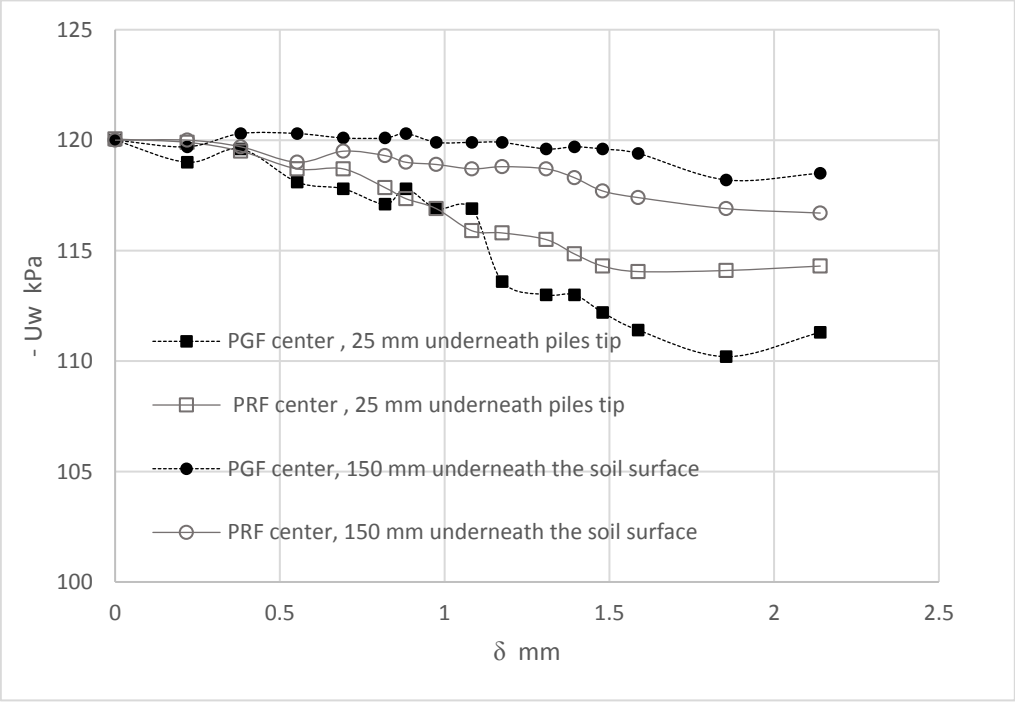

Figure 3.66 Variation of suction with settlement for PGF and PRF at 120 kPa suction

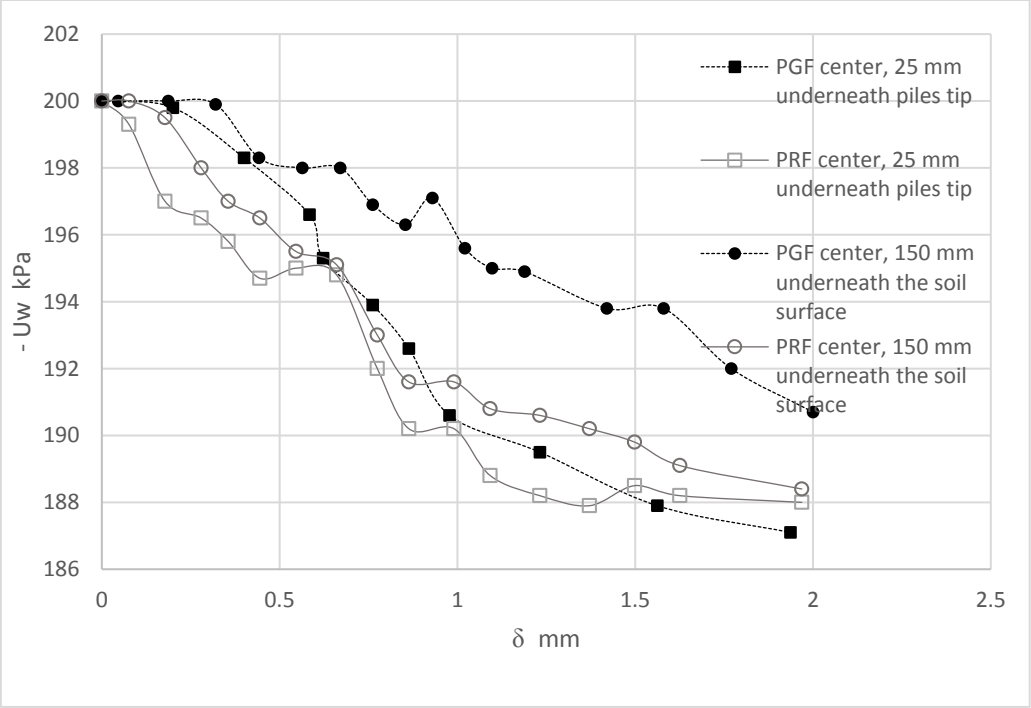

Figure 3.67 Variation of suction with settlement for PGF and PRF at 600 kPa suction

CHAPTER 4

NUMERICAL MODELING

4.1 Introduction

When designing a preliminary proposed foundation, simplified analytical methods may be sufficient to roughly assess the design values. It is known that in piled raft foundation, the components of piled raft foundation interact with each other and with the surrounding soil as well. The effect of this interaction is complex in nature and could be investigated in three-dimensional models. Therefore, once the feasibility of the proposed foundation is justified, three-dimensional finite element analysis is essential in the advanced design stage.

4.2 Three-Dimensional Numerical Model

Developed finite element model must simulate the main features of the real model foundations. Numerical models have the advantage of simulating complex situations that are experimentally difficult or time consuming. Figure 4.1 shows the organization chart of the primary sub models included in this numerical modeling.

Finite element models for SPF, PGF, URF, and PRF were developed using commercial finite element software Abaqus. Old Dominion University has the privilege of using teaching license of Abaqus 2016. The license is limited to 250,000 nodes in one model. This number of nodes was sufficient for the models developed in this study. Finite element models having the same scale of experimental models were developed. The outputs of these models were verified against the results of corresponding experimental models tested in soil of zero, 55 and 200 kPa suctions. The air entry

value (AEV) for the soil used in this study was 105 kPa as indicated in Chapter three. This number lays within the range of selected suction values.

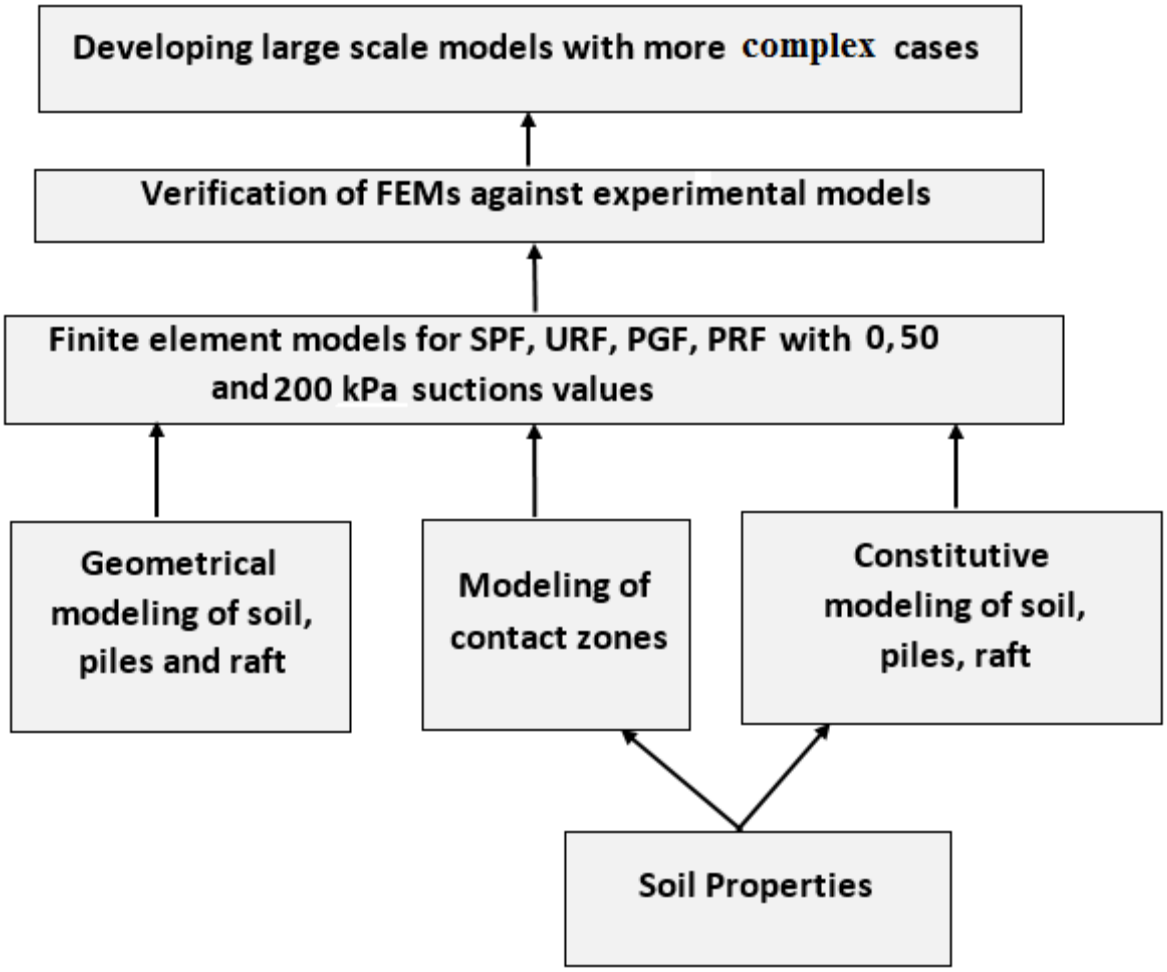

Figure 4.1 Organization chart for numerical modeling

4.2.1 Constitutive Modeling

The choice of constitutive model is critical in any finite element analysis. Parameters of the constitutive model are usually extracted from conventional experimental tests. In this study, the piles and raft were modeled as fully elastic materials. It is stated in Abaqus user guide (2013) that any of the constitutive models in Abaqus can be used to model the material skeleton of porous materials. SWCC should be incorporated in the selected model as the constitutive equation for the partially saturated soil. The soil was modeled as a multi-phase elastoplastic material. Linear Drucker- Prager Cap model was used, which is one of the simplest models for simulating frictional materials. It is stated in Abaqus documents that the model simulates material response under monotonic loading such as the limit load analysis of soil foundations under static loads.

Two triaxial tests and one isotropic consolidation test were conducted to obtain friction angle (φ), cohesion (c) component and elastic response of the soil for each suction value. The modulus of elasticity was obtained from the unloading-reloading curve in the triaxial tests. It is known that parameters of Mohr-Coulomb model (friction angle, φ, and cohesion, c) are different from the friction angle β and cohesion *d* used in the (*p*,*q*) plane in the linear Drucker-Prager model. The parameters (β & *d*) were matched to the corresponding parameters in Mohr-Coulomb model (φ, c) following Equations 4.1 and 4.2 given by Helwany (2007).

$$\beta = \frac{3\sqrt{3}\tan\varphi}{\sqrt{9+12\tan^2\varphi}} \quad 4.1$$

$$d = \frac{3\sqrt{3}\,c}{\sqrt{9+12\tan^2\varphi}} \quad 4.2$$

The hardening softening behavior was described by a piecewise linear function relating the mean effective yield stress (P_b) and the volumetric plastic strain. Figure 4.2 shows this function

for fully saturated specimen. Volumetric plastic strain represents the irrecoverable change in the specific volume. This function was obtained from the results of an isotropic consolidation test with loading and reloading cycles.

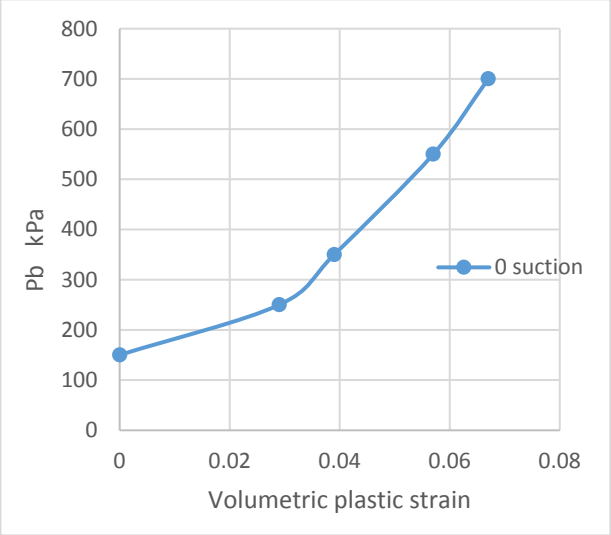

Figure 4.2 Evolution of volumetric plastic strain for linear Drucker Prager Cap model under zero suction

4.2.2 Modeling of Contact Zones

It has been mentioned earlier in this chapter that analysis of a three dimensional model considers soil structure interaction in addition to the interaction between the structural components of the foundations. A realistic model should be chosen to handle the interaction effects in the contact or the interface zones in the foundations.

There are three contact zones that must be modeled in a PRF model; pile-soil, pile-raft and raft-soil interfaces. Modified Mohr-Coulomb friction model was followed in modeling the pile-soil interface. The model was discussed in Section 2.6.3. Friction factors was back calculated from measured SFR value of the designated pile using α method as following :

$$\alpha = SFR / \tau A_s \quad (4.3)$$

where

α = friction factor,

τ = shear strength of the soil and,

A_s = surface area of the pile.

Master-slave technique was followed in modeling the contact zones. This technique was discussed in Section 2.6.4. Piles were considered as the master surface, while the soil was selected to be the slave surface. Surface to surface contact option is preferred over node to surface option when discretizing contact surfaces. More realistic results can be obtained with a finite sliding option for describing the rigorous nonlinear evolution of contact discretization, which was used in this study. Penalty method was used to enforce the contact constraint. Abaqus automatically selects the penalty factor that optimizes the relation between the penetration and convergence rates of the contact problem. Piles-raft and raft-soil contact surfaces were tied together with no separation allowed when the analysis runs.

Realistic modeling of contact zones is critical in any finite element analysis. The analysis that includes contact zones becomes highly nonlinear and requires special considerations. The following considerations were found to be useful in achieving a converged solution and followed in this analysis. Some of these recommendations were mentioned in Abaqus documents, and others from the author' s builtup experience.

- Application of displacement load was utilized instead of force load to establish an initial contact with less possibility of singularity and rigid body movement in the model.
- Frictionless tangential contact was adopted first to verify that there were no other modeling problems.

- Low friction factor value (0.3 and less) was assigned initially to the analysis. If the analysis completed successfully, the actual higher friction factors was then assigned to the analysis. Assigning high friction factor in the beginning may cause converging issues in the model.
- For all analyses, fully elastic soil properties are assigned. Plasticity was added to the soil later when the fully elastic analysis with full contact assignment had completed successfully.
- Small time step increment at the beginning of the analysis was used to get a better converged solution with minimum cut backs in the solution.
- Tied surfaced interfaces were replaced with a frictional one when normal stresses become so high that penetration errors become higher than that tolerated ones in the software.
- Surface to surface option was used to discretize the contact surface instead of node to surface option.
- Master surface was selected to be the one with higher rigidity to simulate the pile penetration in the soil.
- Slave surfaces were meshed with higher density than master surfaces to simulate penetration of master surface accurately and to prevent excessive distortion of the elements representing the slave surface.
- Utilization of first order brick element in the contact zones gave better results than second order elements as stated in Abaqus user manual.

4.2.3 Geometric Modeling

By making use of the symmetry in the model, only quarter model was submitted for analysis to minimize the computation cost of the simulation. Similar dimensions to those used in experimental models were followed in the numerical models. Assigning proper boundary

conditions is essential for realistic simulation. Figure 4.3 shows dimensions and boundary conditions assigned to SPF model. No x-translation is allowed in yz plane (symmetry around x plane) and no y translation is allowed on xz plane (symmetry around y plane). Similarly, the rotational degree of freedom Rx and Rz are not allowed in xz plane and the same for Ry and Rz in yz plane. No x, y, z translation were allowed in the bottom nodes. The soil around the foundation was extended horizontally to a distance equal to the raft width (B) and to 6d below the pile tips vertically, where d is the diameter of the piles as seen in Figure 4.4. In the figure, models in (b) and (c) have similar dimensions to those shown in (a) for applicable members, and the dimensions in Figures 4.3 and 4.4 are in mm.

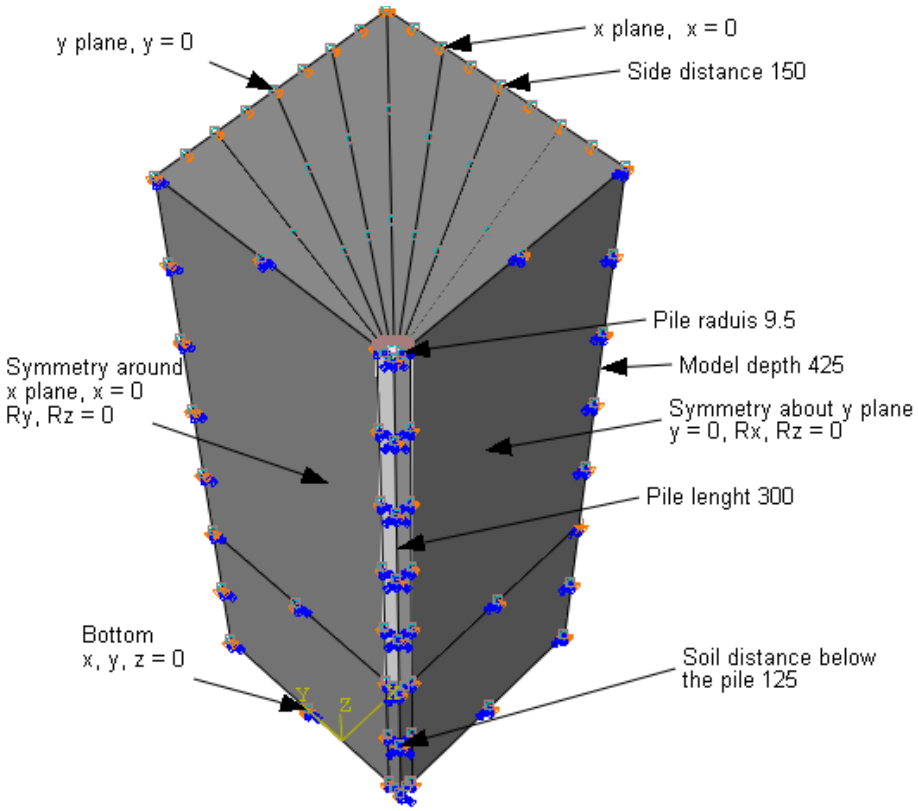

Figure 4.3 Dimensions and boundary conditions of a 3-D quarter SPF model

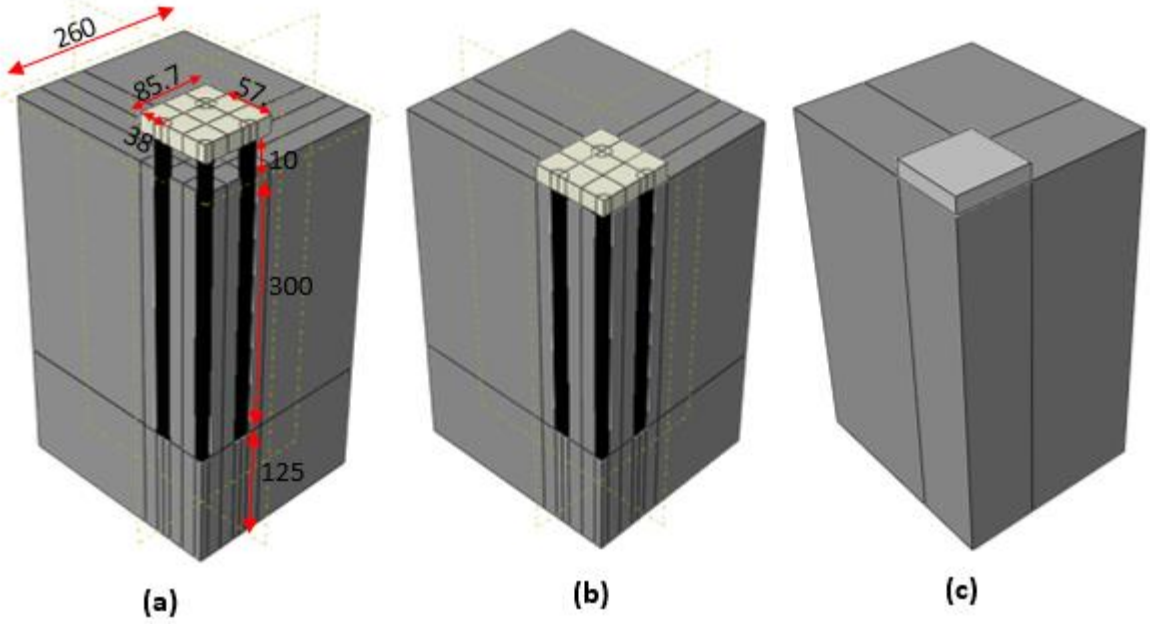

Figure 4.4 Geometry of a 3-D quarter (a) PGF, (b) PRF and (c) URF models

4.2.4 Types of Analysis for Single-Phase Flow in Porous Media in Abaqus

Among other analyses, Abaqus is capable of conducting coupled deformation-pressure analysis in fully and partially saturated soils for three dimensional models. The analyses can be performed in terms of total pore fluid pressure or excess pore fluid pressure. Total pore pressure solution is provided when the total stress is used to define the gravity load on the model. Excess pressure solution is followed when the gravity loading is defined with effective stress. The latter analysis was followed in this study.

Four requirements must be satisfied when analyzing poromechanics problems in any numerical model. These requirements include conservations equations, constitutive equations, continuity of displacement and pressure fields, and initial and boundary conditions.

4.2.5 Stress Equilibrium and Flow Continuity

Stress equilibrium equation for the solid phase can be derived from conservation of linear momentum equation by writing the principle of virtual work for the volumetric element in the current configuration at time (t) as follows;

$$\int_V (\sigma' - \chi\, u_w\, \boldsymbol{I}) : \delta\varepsilon\, dV = \int_S \boldsymbol{t} \,.\, \delta\boldsymbol{v}\, dS + \int_V \boldsymbol{f} \,.\, \delta\boldsymbol{v}\, dV + \int_V sn\, \rho_w\, \boldsymbol{g} . \delta\boldsymbol{v}\, dV \qquad 4.4$$

where, $\delta\varepsilon$ can be defined as the virtual rate of deformation and is equal to sym($\partial\mathbf{v}/\partial\mathbf{x}$). $(\sigma' - \chi\, u_w \boldsymbol{I})$ is Bishop's effective stress for partially saturated soil, $\delta\boldsymbol{v}$ is a virtual velocity field, **t** are surface tractions, **f** are body forces (excluding fluid weight) per unit volume which is the density of the fluid, **g** is the gravitational acceleration (assumed constant and in a fixed direction) and ***I*** is the identity matrix.

Using conservation of mass equation, a continuity equation for the fluid phase was derived by equating the rate of increase in fluid volume stored at a point to the rate of volume of fluid flowing into the point within the time increment as follows.

$$\frac{d}{dt}\left(\int \frac{\rho_w}{\rho_w^o}\, sn\, dV\right) = -\frac{\rho_w}{\rho_w^o}\, sn\, \boldsymbol{n} \,.\, \mathbf{v}_w\, dS \qquad 4.5$$

where $\mathbf{v}_w$ is the seepage velocity, ***n*** is the outward normal to S. In Equation 4.5 fluid density (ρ_w) was normalized by ρ_w^o (the reference density of the fluid).

For low fluid flow velocities as the case in this study, Darcy' s law can be used as constitutive law for the fluid phase as shown in Equation 4.6 below

$$\mathbf{v}_w = -\frac{1}{sng\rho w}\ \widehat{\boldsymbol{k}}\ .\left(\frac{\partial u_w}{\partial \boldsymbol{x}} - \rho_w \boldsymbol{g}\right) \qquad 4.6$$

where, $\widehat{\boldsymbol{k}}$ is the permeability of the medium, and **g** is the magnitude of the gravitational acceleration.

It is known that the coefficient of permeability depends on the void ratio and saturation ratio of the soil. Based on experimental observations, Abaqus consider $K_s = S_r^3$ by default, where S_r is the degree of saturation. Negative pore water pressure indicates suction in the soil. SWCC represents the constitutive equation that governs the relation between degree of saturation S_r, and the suction in the soil U_w.

4.2.6 Discretization of Stress Equilibrium and Continuity Equation

Abaqus documents state that Equation 4.4 is discretized using a Lagrangian formulation for the solid phase with displacements as the nodal variables. It is also mentioned that Equation 4.5 is integrated in time using the backward Euler approximation and discretized with finite elements using pore pressure as the variable. In the coupled deformation pore pressure analysis, the stress equilibrium and fluid continuity equations must be solved simultaneously. Newton scheme is used in Abaqus to solve general nonlinear equations. Discretized coupled poroelastic problem of nonlinear material, small strain, linear permeability, and incompressible grains and fluid in fully saturated soil can be expressed in Equation 4.7.

$$\begin{bmatrix} \boldsymbol{K}_s(\acute{\sigma}) & \boldsymbol{B} \\ \boldsymbol{B}^{\mathrm{T}} & \Delta t\, k \end{bmatrix} \begin{bmatrix} \boldsymbol{d}_c \\ u_c \end{bmatrix} = \begin{bmatrix} \boldsymbol{F}_r \\ \Delta V_r \end{bmatrix} \qquad 4.7$$

where, $\mathbf{d}_c$ represents the vector of displacement corrections (c_a, c_b in Figure 4.5), and F_r is the force residuals conjugate to the displacements (R_a, R_b in Figure 4.5). u_c is the pore pressure correction and ΔV_r is the residual change in fluid volume over the time increment conjugate to the pore

pressure. $\boldsymbol{K}_s(\acute{\sigma})$ is the stress stiffness term with material nonlinearities. **B** and $\mathbf{B^T}$ are the stress-pore pressure coupling term, and Δt k is the permeability term. Those are defined below.

$$\boldsymbol{K_s} = \int_V \beta : \boldsymbol{D'} : \beta \, dV \tag{4.8}$$

$$\boldsymbol{B}^T = \int_V \boldsymbol{I} : \beta \, dV \tag{4.9}$$

$$k = -\int_V \frac{\partial \delta u}{\partial \boldsymbol{x}} . \boldsymbol{k}^* . \frac{\partial \delta u}{\partial \boldsymbol{x}} \, dV \tag{4.10}$$

where β is the strain displacement matrix and D′ is the constitutive matrix.

In partially saturated soils, discretized coupled elastoplastic problem of nonlinear material, small strain, linear permeability, incompressible grains and fluid can be written as shown in Equation 4.11.

$$\begin{bmatrix} \boldsymbol{K}_s(\acute{\sigma}) & \boldsymbol{B} + \boldsymbol{B_s}(\boldsymbol{u}) \\ \boldsymbol{B}^{\mathrm{T}} & \Delta t \; k + \Delta t \; k_{es}(e) + K_s^* \end{bmatrix} \begin{bmatrix} \boldsymbol{d}_c \\ u_c \end{bmatrix} = \begin{bmatrix} \boldsymbol{F}_r \\ \Delta V_r \end{bmatrix} \tag{4.11}$$

where $\boldsymbol{B}_s$ is a partially saturated coupling term, Δt k is the permeability term. $\Delta t \; k_{es}(e) + K_s^*$ are partially saturated permeability terms. It can be noticed that Equation 4.11 is unsymmetrical. The other terms in Equation 4.11 are:

$$\boldsymbol{B}^T = \int_V s \, \boldsymbol{I} : \beta \, dV \tag{4.12}$$

$$\boldsymbol{B}_s = -\int_V u \, \frac{ds}{du} \, \beta : \boldsymbol{I} \, dV \tag{4.13}$$

$$\boldsymbol{K}_s^* = -\int_V \frac{ds}{du} \left(1 - \frac{1 - n^o}{J}\right) dV \tag{4.14}$$

$$\boldsymbol{K}_s = \int_V \beta : D' : \beta \, dV \tag{4.15}$$

$$\boldsymbol{K}_{es} = -\int_V \frac{S}{K_s} \frac{ds}{du} \frac{\partial \delta u}{\partial \boldsymbol{x}} . \boldsymbol{K}^* . \left(\frac{\partial u}{\partial \boldsymbol{x}} - \rho_w g\right) dV \tag{4.16}$$

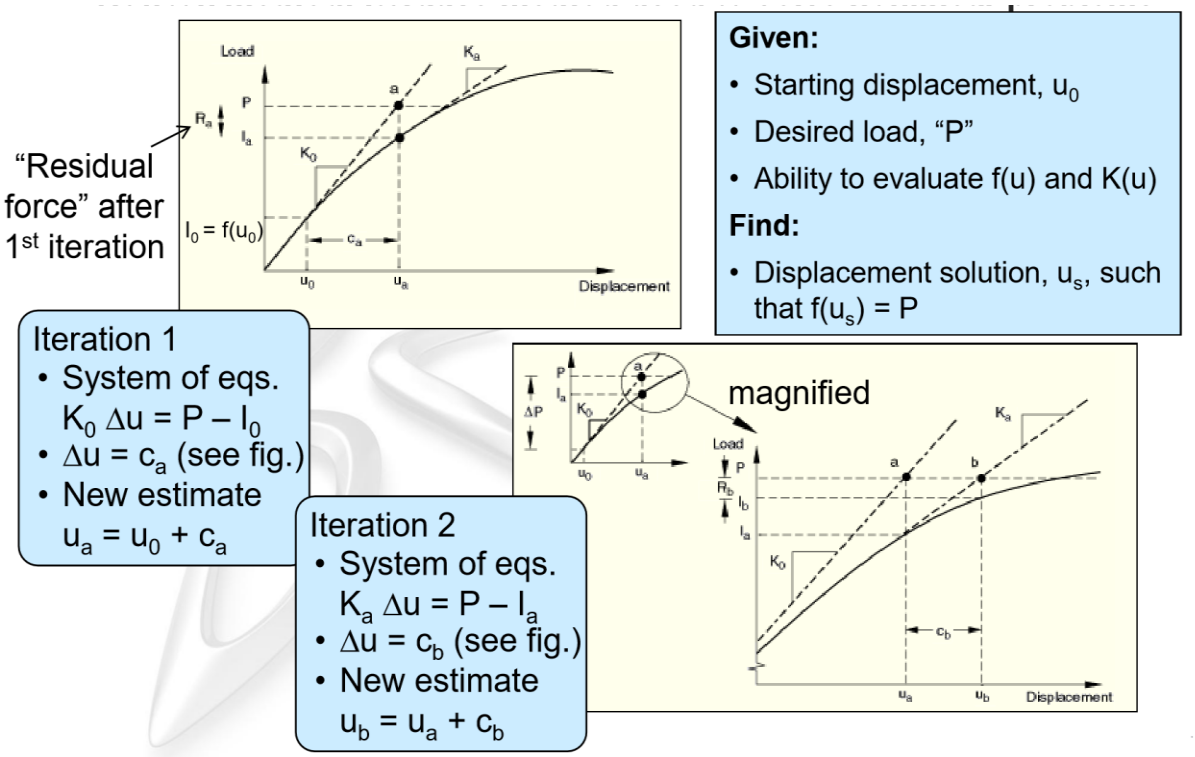

Figure 4.5 Iterative Newton method for solving nonlinear problems (Abaqus User Guide, 2013)

4.3 Analysis Steps

Analyses conducted using Abaqus were solved in two steps. These steps were geostatic and coupled transient steps. Gravity loads were first applied to the model in the geostatic step. Gravity loads determine the initial stresses in all soil elements, so it is critical to assign them accurately. Abaqus computes the total stress which is in equilibrium with the gravity loads. Equilibrium is achieved within the soil layer when the predicted initial stresses calculated by Abaqus are within the convergence criterion. The difference in initial geostatic stresses between external gravity stresses and that computed by Abaqus are displayed in terms of displacement. Robert and Britto (2007) stated that deviation of the initial stress values from the actual would result in incorrect higher soil displacements of the model which in turn leads to instabilities and analysis termination.

Initial stress condition in any element within the soil layer must be within the initial yield surface of Drucker Prager Cap model followed in this study.

In the second step, coupled transient displacement and pore pressure analysis was implemented. The pile load was applied utilizing vertical displacement boundary condition to drive the top surface of the pile to move downward with a final distance equal to 10% of the pile diameter. The transient analysis was performed using automatic time incrementation. Pore pressure tolerance (UTOL in Abaqus code) which controls the automatic incrementation was selected to be relatively large value since the nonlinearity of the material is restricting the time increment size as stated in Abaqus User Guide (2016).

4.4 Sensitivity Analysis

Mesh refinement study was conducted on several mesh configurations to minimize the effect of element type, number and size of elements, and bias ratio in vertical direction (z-direction) on the bearing capacity of piles. These analyses were performed using the configurations shown in Table 4.1. In each analysis, material properties and all other parameters were kept constant. For the sake of simplicity, SPF model shown in Figure 4.3 was used for this analysis.

The bias ratio is the difference between the length between nodes at either end of the edge. LEl is linear brick stress-pore water pressure element. El, Bi and C3D8R stand for element, bias ratio and coupled three dimensional eight nodes with reduced integration, respectively.

Figure 4.6 (left) shows typical SPF model in which the soil was meshed with 8 elements around the quarter diameter of the pile and 10 elements in the z directions with bias ratio of 10. Figure 4.6 (right) shows typical failure shape of SPF model. Total Pile Resistance (TPR) was calculated for each configuration.

Table 4.1 Configurations of meshes used in the model

Configuration symbol	Type, geometry of element	Number of elements around 1/4 pile diameter	Number of pile elements in the z direction	Bias ratio in the z direction*
8_LEl_P, 10 EL_Z, 10 Bi_Z	C3D8R, linear	8	10	10
4_LEl_P, 10 EL_Z, 10 Bi_Z	C3D8R, linear	4	10	10
8_LEl_P, 15 EL_Z, 10 Bi_Z	C3D8R, linear	8	15	10
8_LEl_P, 20 EL_Z, 10 Bi_Z	C3D8R, linear	8	20	10
8_LEl_P, 10 EL_Z, 15 Bi_Z	C3D8R, linear	8	10	15
8_LEl_P, 10 EL_Z, 20 Bi_Z	C3D8R, linear	8	10	20
8_QEl_P, 10 EL_Z, 10 Bi_Z	C3D20R, Quad	8	10	10

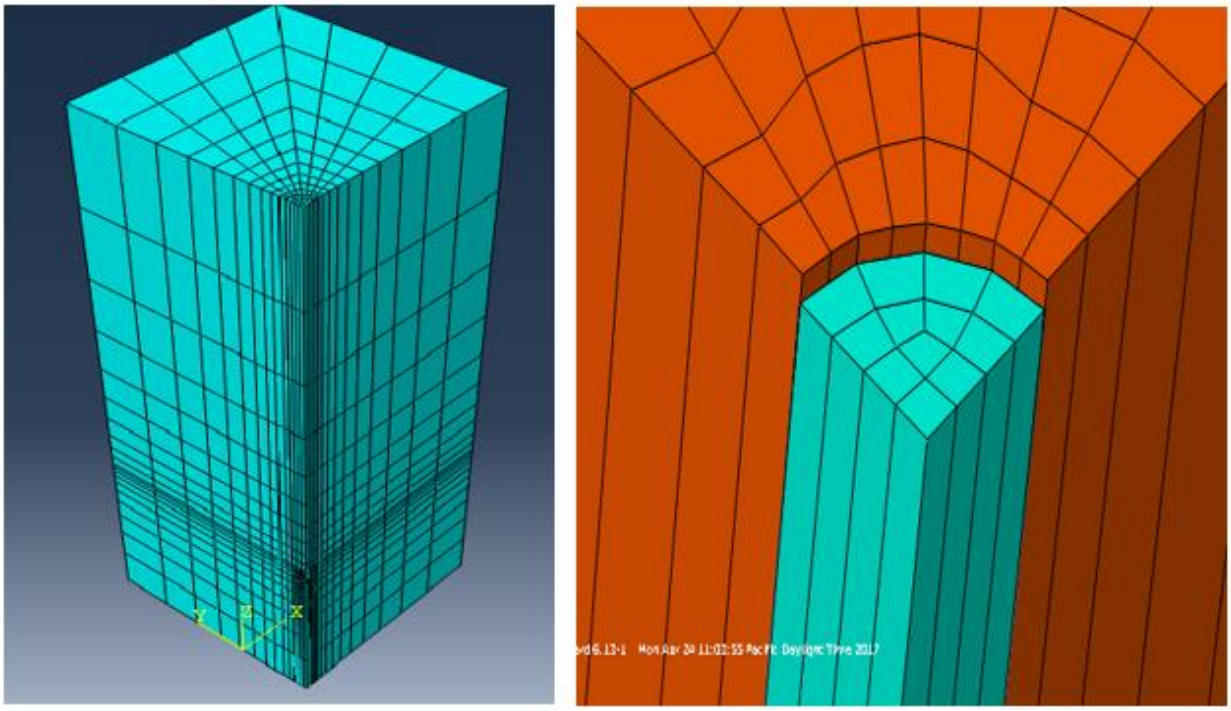

Figure 4.6 Meshing of typical SPF model (left) initial and (right) at failure

Total Pile Resistance (TPR) is calculated by multiplying average values of stresses in the Z direction (S_{33}) over with the cross-sectional area at the top of the pile. End Bearing Resistance (EBR) is determined by multiplying S_{33} with cross-sectional area of the soil elements underneath the pile tip. Skin Friction Resistance (SFR) is then computed as the difference between TPR and EBR.

Figure 4.7 shows plots of load-settlement curves with different configurations. It can be noticed from the figure that quadratic element (QEl20 nodes) is not a proper choice for simulating the behavior of single pile. First order elements (LEl) exhibited insignificant differences within 7% between the upper and lower band.

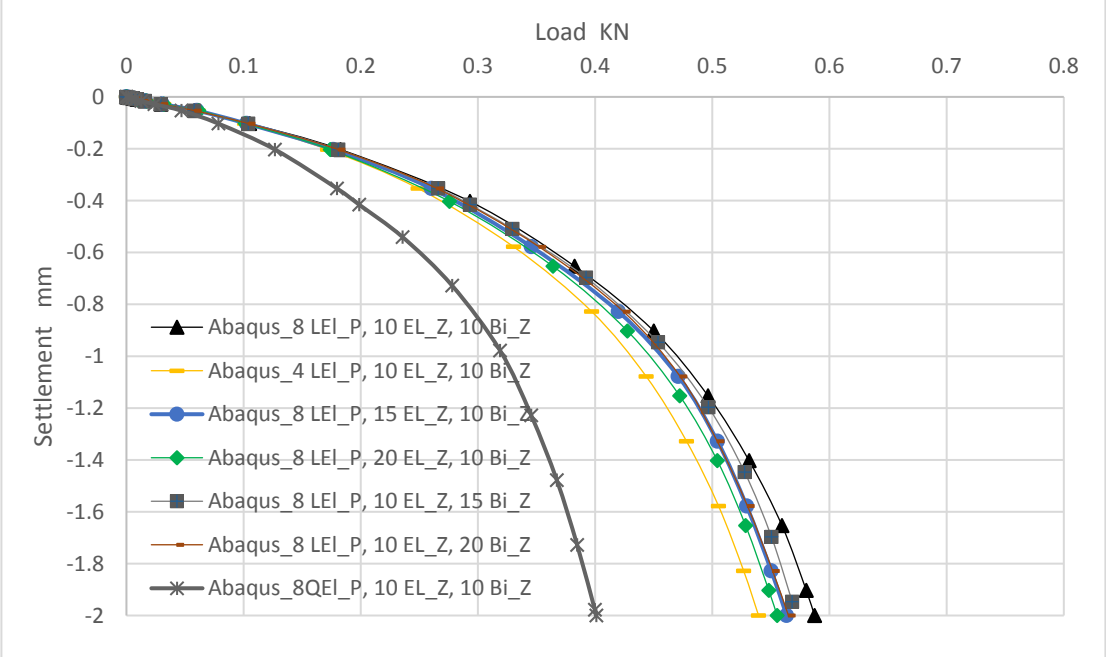

Figure 4.7 TPR vs settlement of SPF model with different configurations

4.5 Verification of Numerical models

4.5.1 Verification of SPF model

SPF embedded in soils with zero, 55 and 200 kPa suctions were selected to be simulated in Abaqus. The selected suction values represent the range of most interest in this study. Zero suction is corresponding to fully saturated soil. The second suction, 55 kPa, is below the air entry value of the soil used in this study (105 kPa) and has relatively low suction value in cohesive soils. Beyond the third suction value, 200 kPa, there is an insignificant increase in the shear strength of partially saturated soil used in this study. TPR, EBR, and SFR values of the experimental and Abaqus models are compared in Figures 4.8, 4.9, and 4.10.

When observing those figures, it can be noticed that Abaqus simulation of TPR generally gave less resistance to that in experimental results. The reason may be attributed to the idealization of soil properties in the numerical models (constant E, e, k). The comparisons of EBR values showed excellent agreement with each other. SFR values had wider differences, in particular, at 55 kPa suction. It can also observe that TPR and EBR curves showed better agreements with corresponding experimental curves than SFR curves in all suction values. Larger differences in SFR values may be related to assigning constant value of a friction factor along the pile length. The differences between the results of simulated and experimental models were less than 20% in all models. Figure 4.11 shows plots of measured and computed suctions at the end of the test at 25 mm below the pile tip of SPF model tested with 55 and 200 kPa suction. Those showed excellent agreement.

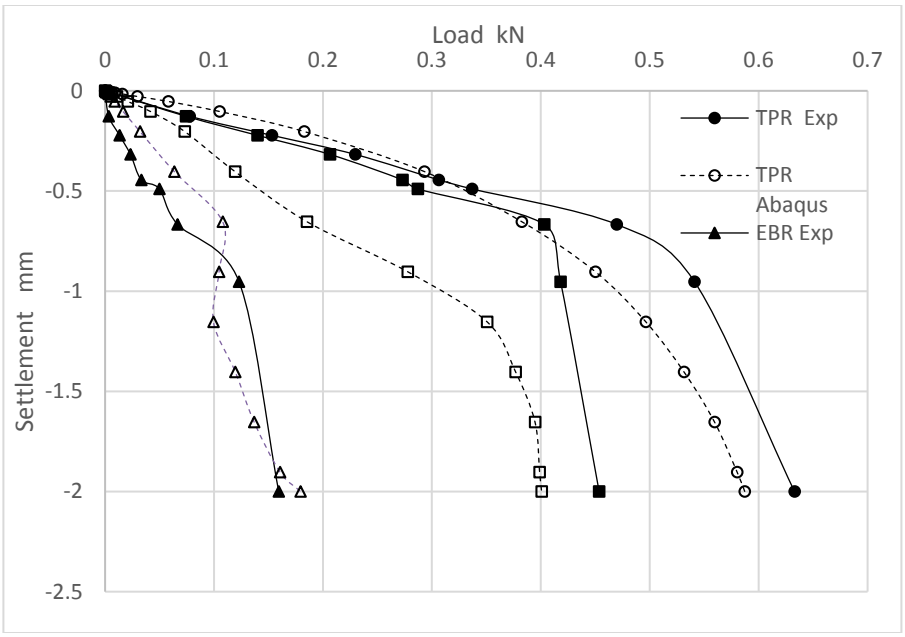

Figure 4.8 Load-settlement relation for EBR and SFR model for experimental and Abaqus models at zero suction

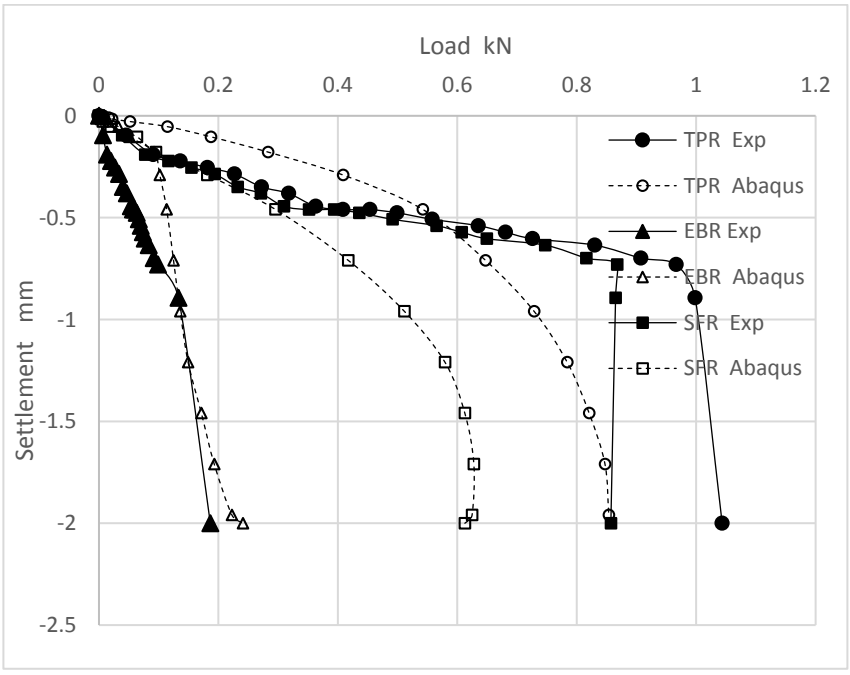

Figure 4.9 Load-settlement relation, EBR and SFR for experimental and Abaqus models at 55 kPa suction

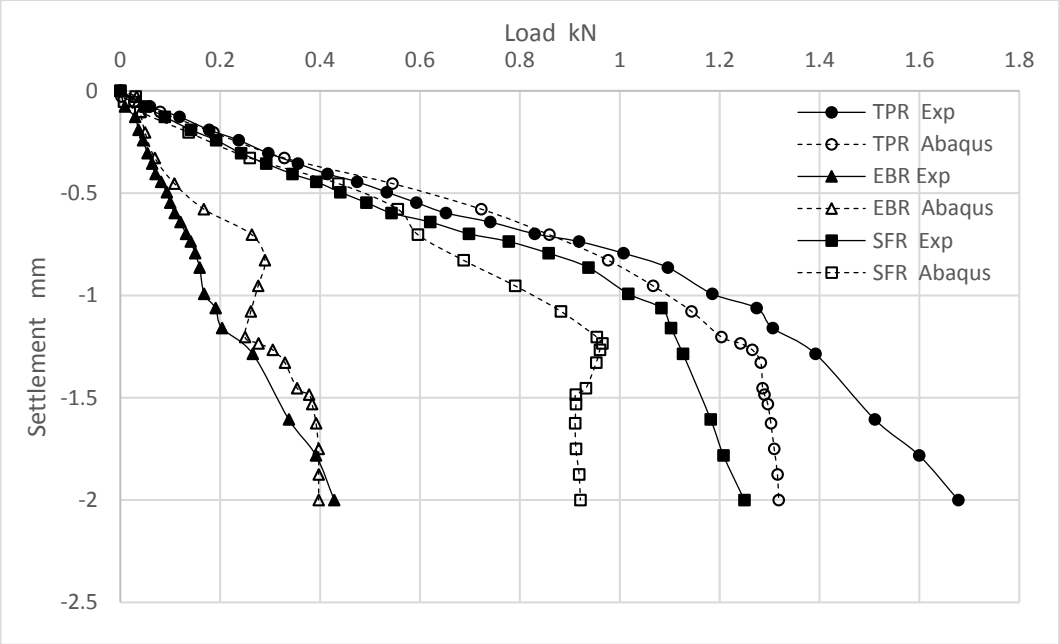

Figure 4.10 Load-settlement relation EBR and SFR for experimental and Abaqus models at 200 kPa suction

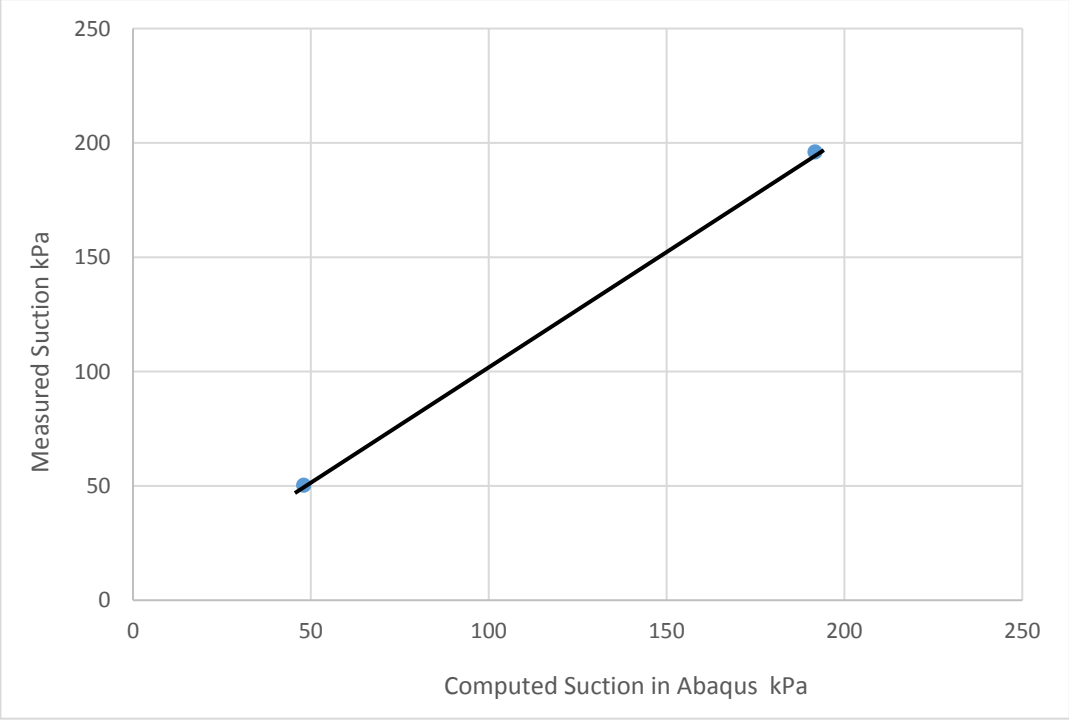

Figure 4.11 Experimental suction vs suction extracted from Abaqus of SPF at 50 and 200 kPa, suction

4.5.2 Verification of PRF, PGF, URF Models

The behavior of PGF, PRF and URF models in fully and partially saturated soils was simulated in Abaqus. The models were built using similar scale to that followed in the experimental models. Geometry and dimensions of these models were shown in Figure 4.4. Same suction values used in SPF model are followed in these models.

Meshing techniques followed in FE models are shown in Figure 4.12. Generally, the models were meshed with denser elements at zones where concentrated stress levels are expected to occur. Single bias ratio was followed in PGF model where elements around the pile tips are 10 times smaller than the element at piles top, while in URF the bias direction was from top to bottom since the stress concentrated area is in the soil zone near the raft. PRF model was meshed with double bias ratio, by which top and tip of pile elements are 10 times smaller than the elements in the middle of the piles since both pile tip and top sections are equally significant.

The external load was applied by imposing a final displacement equal to 10 % of the pile diameter (2 mm) as a boundary condition directly over the raft area above the cross-sectional area of the central pile. Total foundation resistances of PRF and PGF were calculated by multiplying average stresses in the z-direction (S33) of the nodes over the area of application on the raft. For determining URF resistance, S33 stresses in the soil elements underneath the raft were averaged and multiplied by the raft area. The same pile and soil properties used in SPF model were utilized in these models.

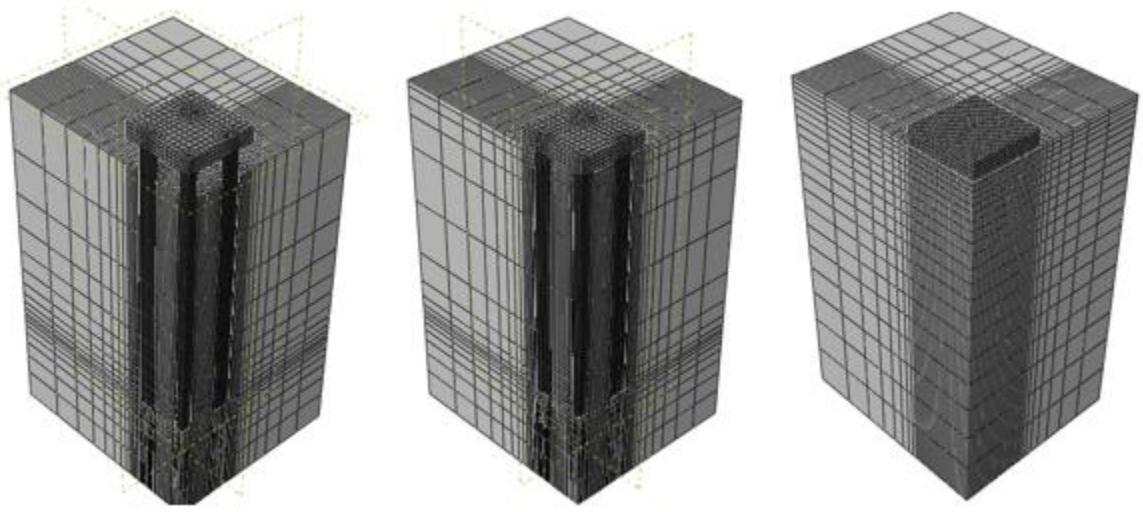

(a) (b) (c)

Figure 4.12 Meshing of (a) PGF, (b) PRF, and (c) URF models

Figures 4.13 to 4.15 show the distribution of displacement and stresses in the vertical direction in PRF, PGF and URF models for 200 kPa suction, respectively. It can be observed that the soil under the raft in PRF model has taken stresses less than the stresses carried by the soil in URF model.

It can be also noticed that piles in PRF model carried slightly less load than the piles in PGF model because of the effect of raft piles interaction. Figures 4.16 and 4.17 show the reduction in pore pressure values underneath the pile tip. The reduction in suction in PRF was slightly less than the one under the piles tip in PGF model. In URF model the maximum reduction in suction was underneath the raft as seen in Figure 4.18.

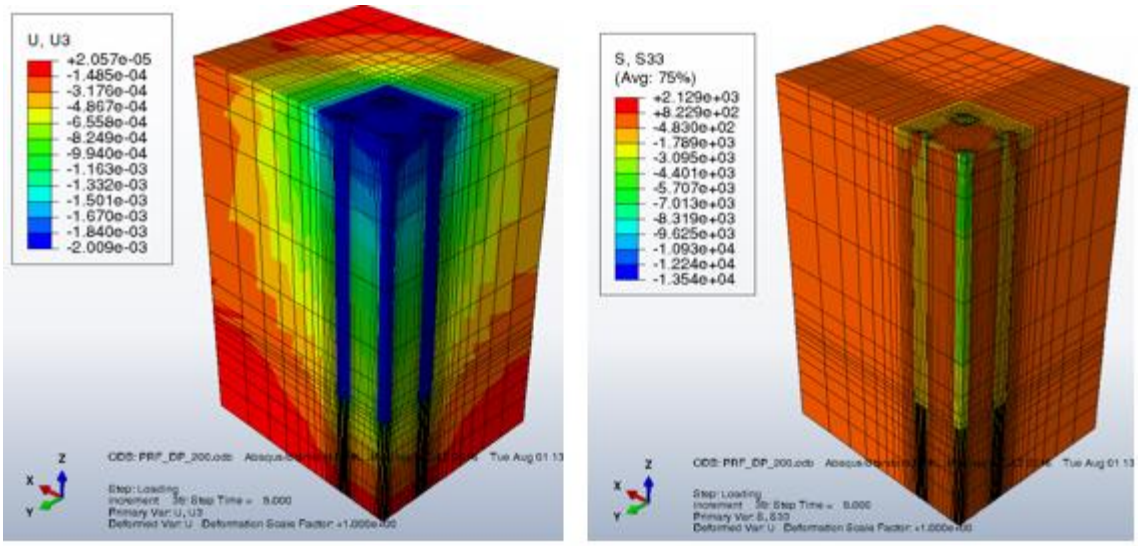

Figure 4.13 Stress and displacement distributions in z-direction of PRF model at 200 kPa suction

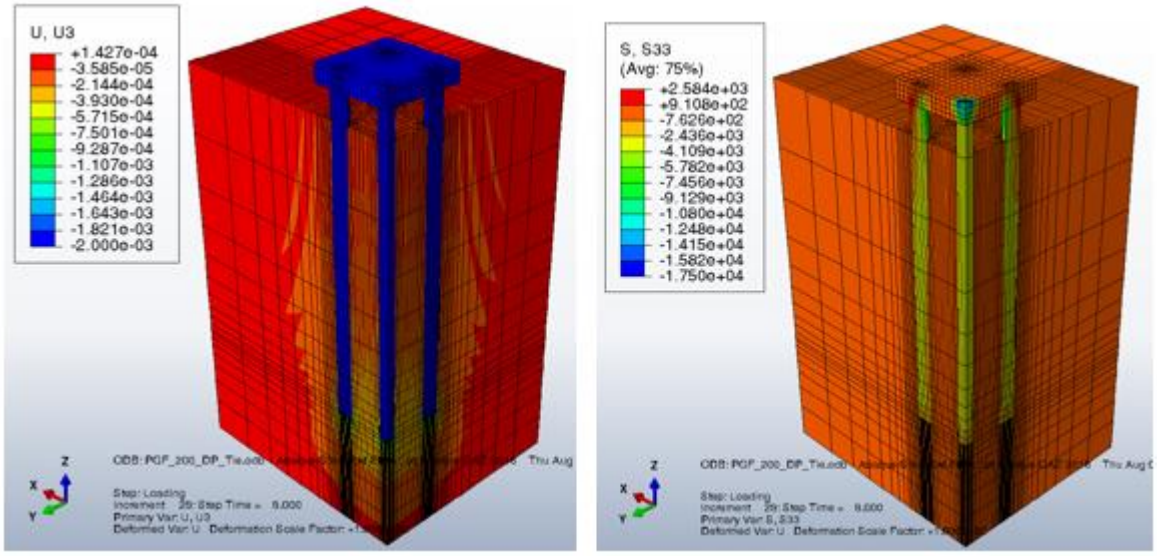

Figure 4.14 Stress and displacement distributions in z-direction of PGF model at 200 kPa suction

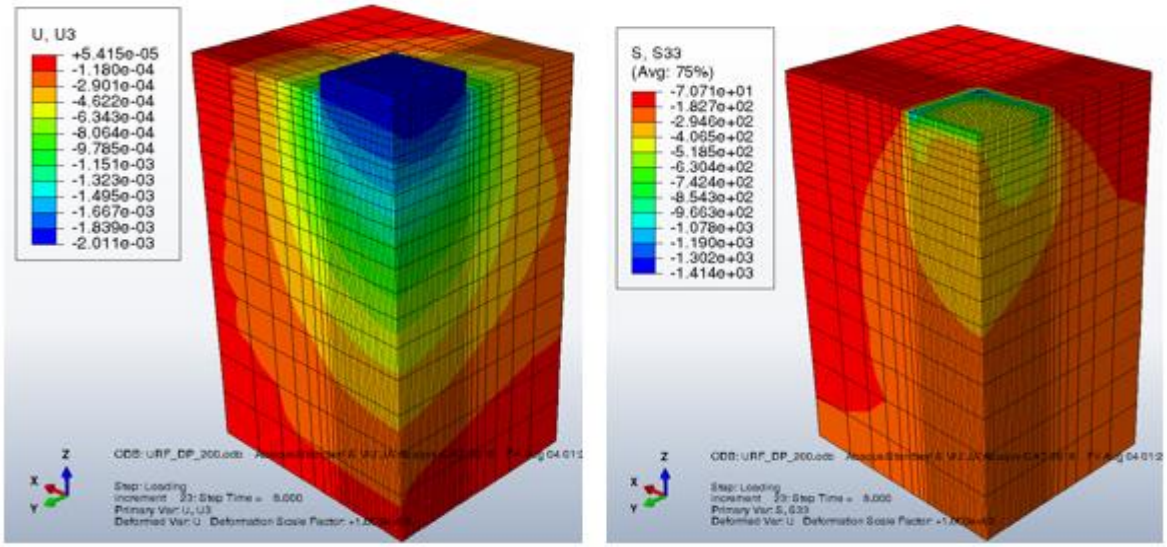

Figure 4.15 Stress and displacement distributions in z-direction of URF model 200 kPa suction

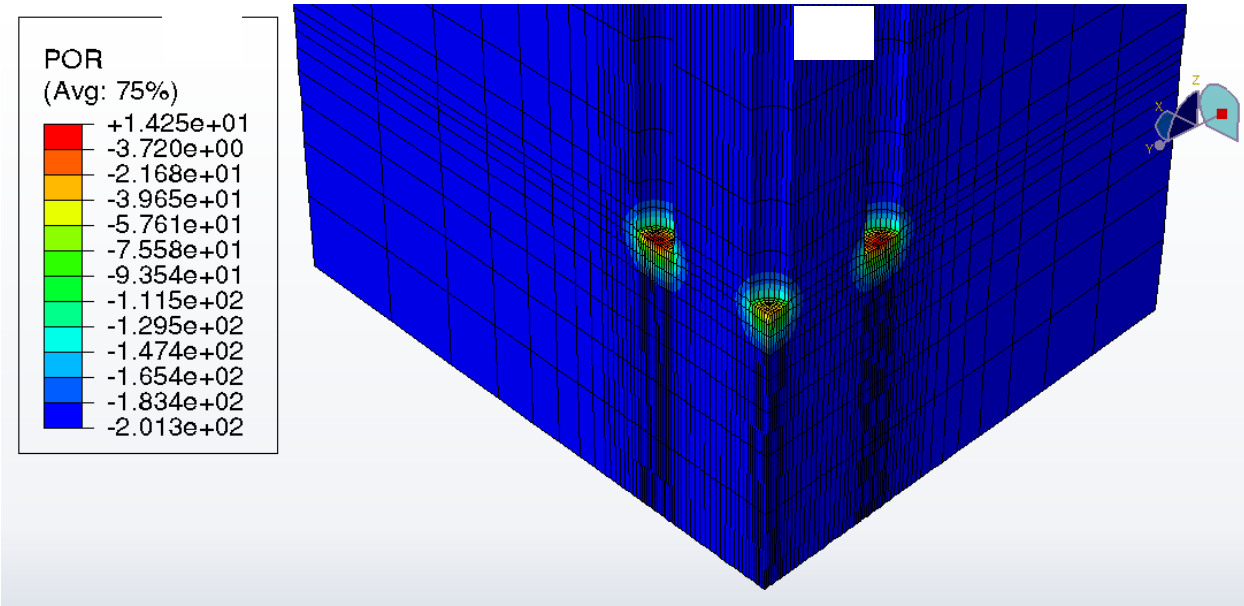

Figure 4.16 Negative pore water distribution in PRF model below the pile tip at 200 kPa suction

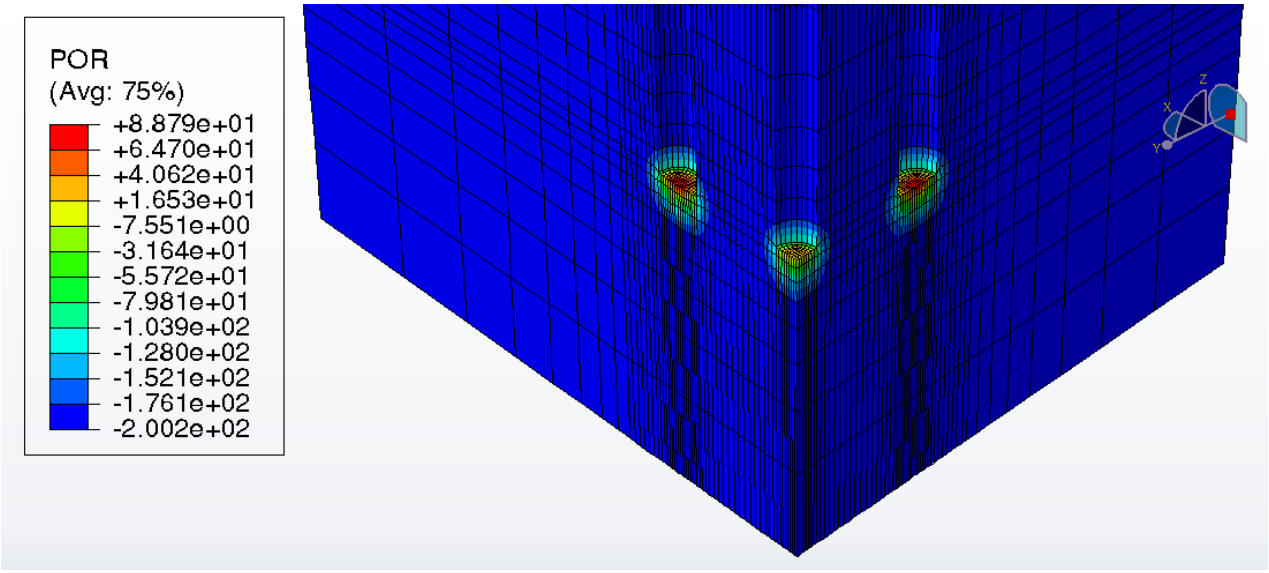

Figure 4.17 Negative pore water distribution in PGF model below the pile tip at 200 kPa suction

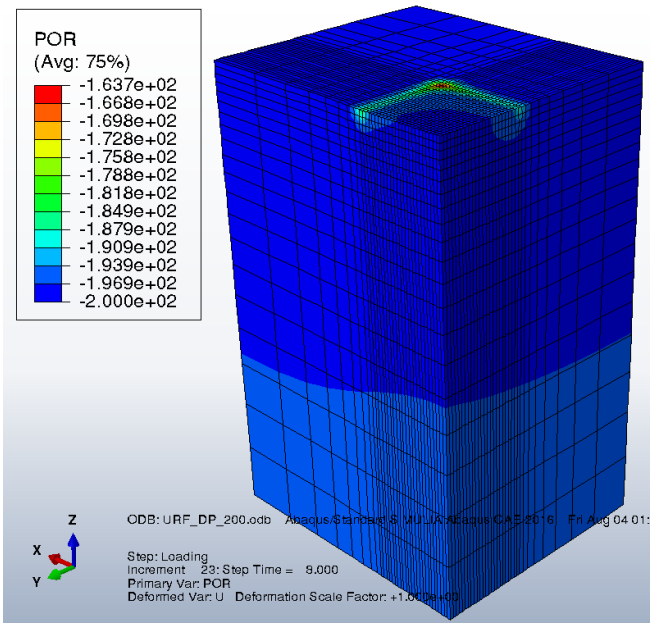

Figure 4.18 Negative pore water distribution in URF model below the piles tip at 200 kPa suction

Load-settlement curves are extracted from the results of each analysis for each model as well as at center (CR), side (S) and corner (C) piles in PRF and PGF models. Figures 4.19 through 4.27 show those curves with corresponding experimental data.

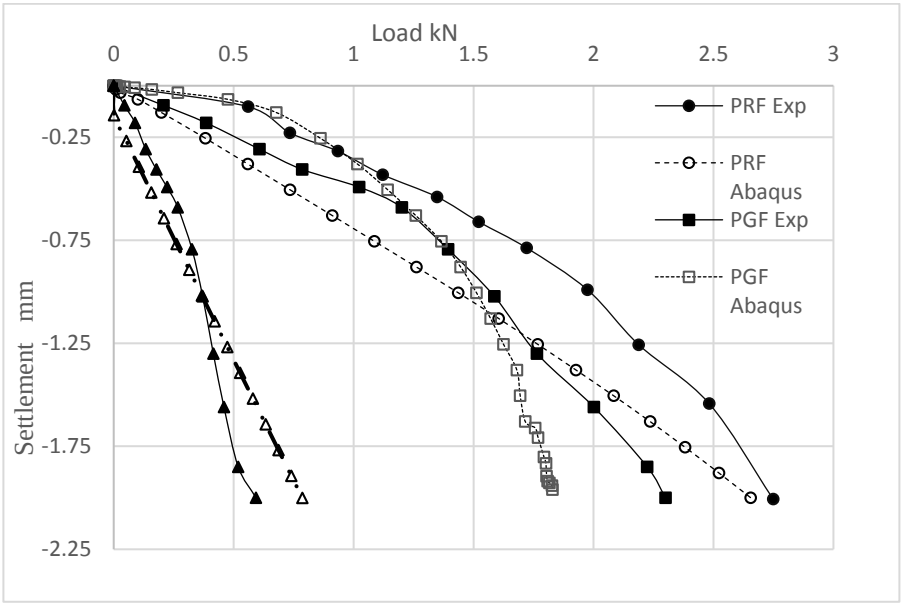

Figure 4.19 Experimental and numerical load-settlement curves for PRF, PGF and URF at zero suction

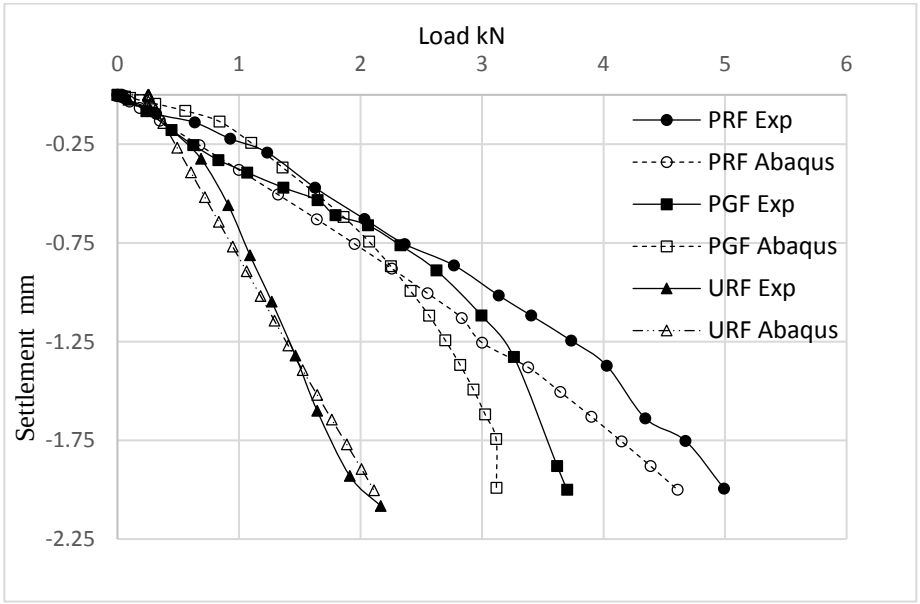

Figure 4.20 Experimental and numerical load-settlement curves for PRF, PGF and URF at 55 kPa suction

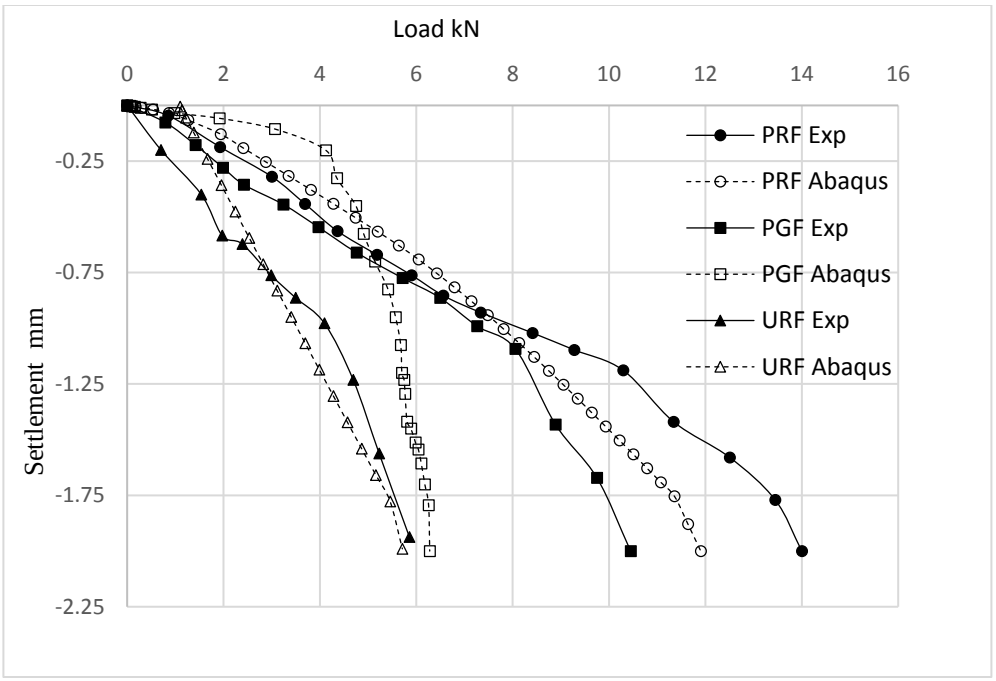

Figure 4.21 Load-settlement curves for PRF, PGF and URF with 200 kPa suction from experimental and numerical analysis

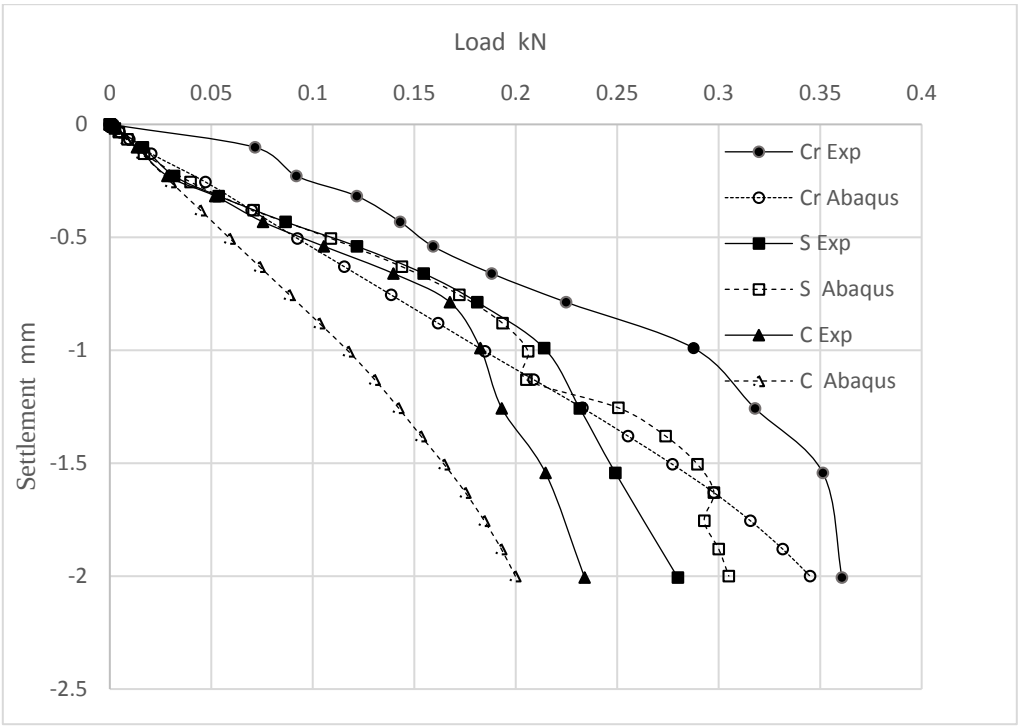

Figure 4.22 Load -settlement curves of center, side and corner piles in PRF with zero suction from experimental and numerical analysis

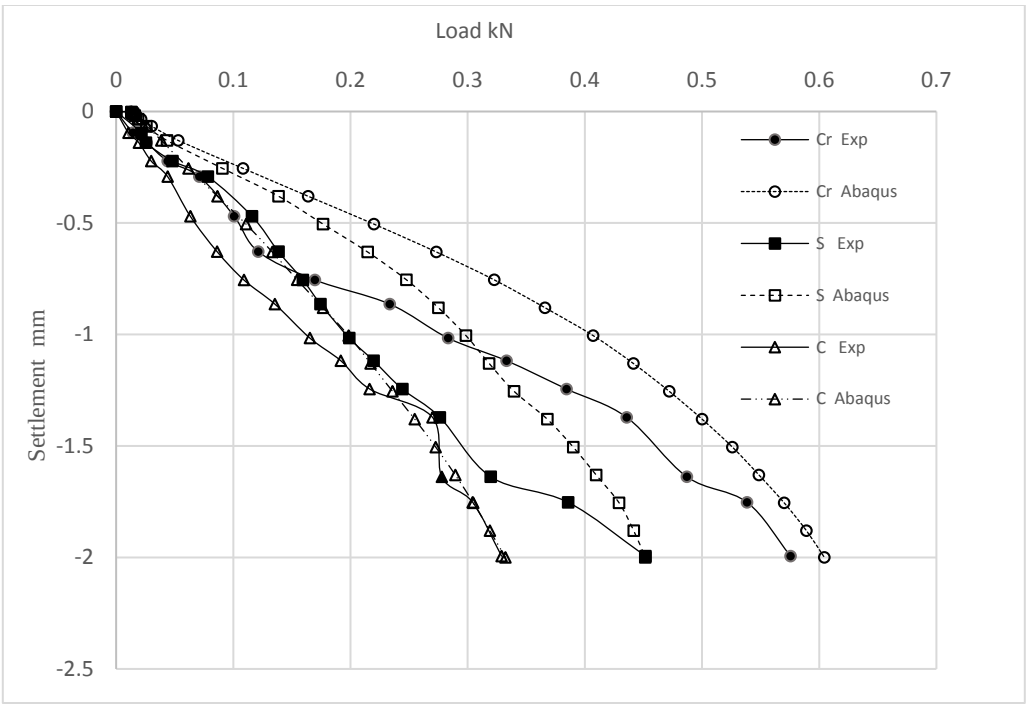

Figure 4.23 Experimental and numerical load -settlement curves of center, side and corner piles in PRF at 55 kPa suctio

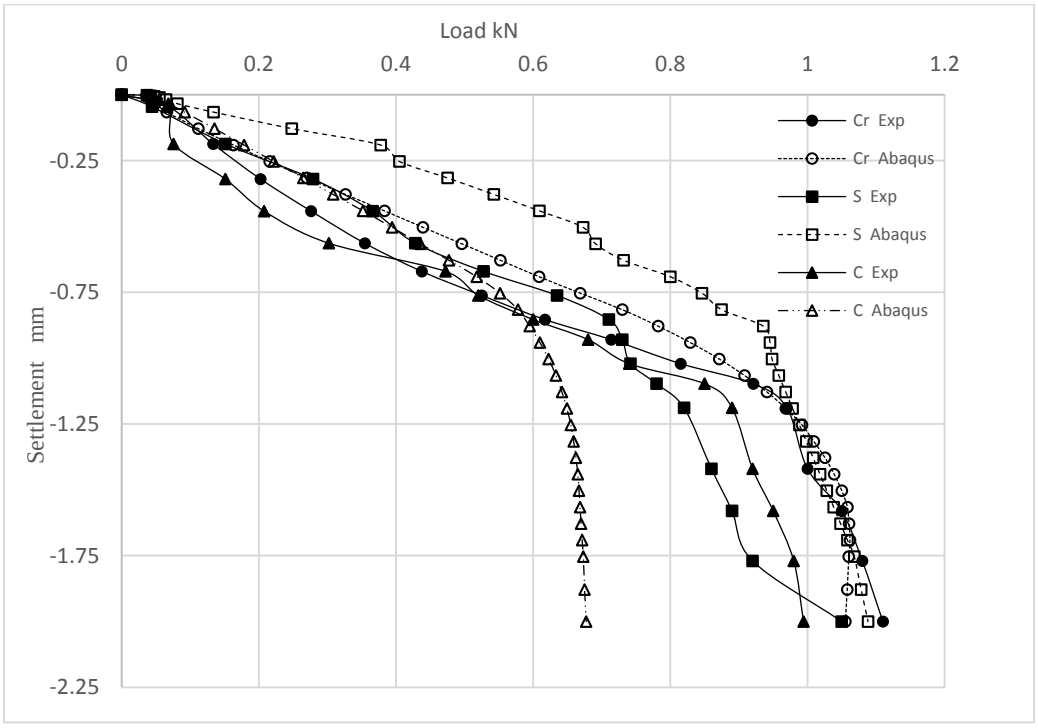

Figure 4.24 Experimental and numerical load-settlement curves of center, side and corner piles in PRF at 200 kPa suction

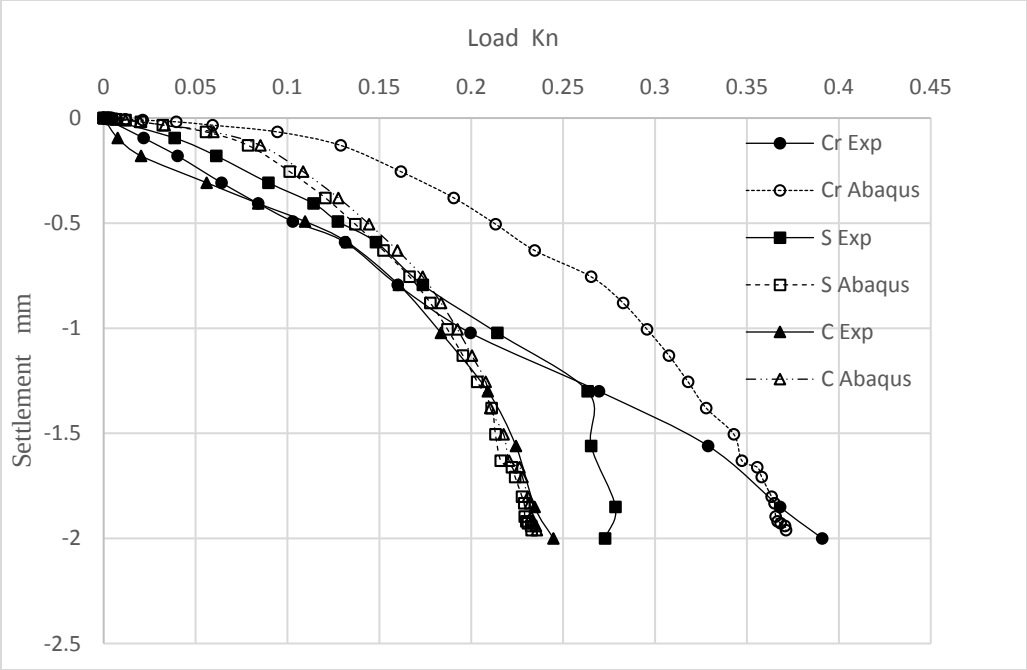

Figure 4.25 Experimental and numerical load-settlement curves of center, side and corner piles in PGF at zero suction

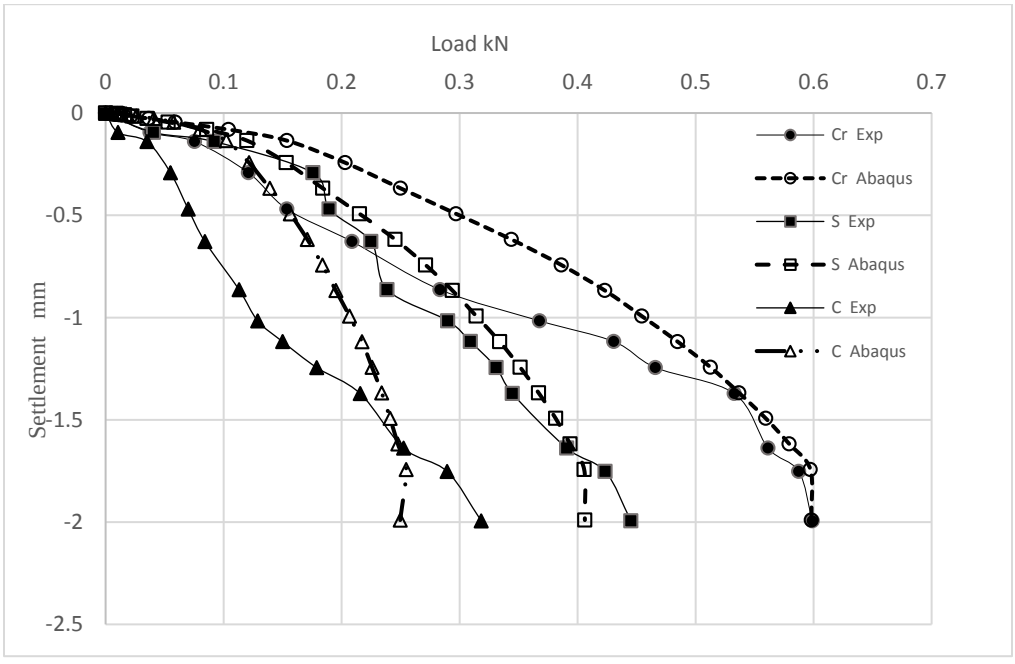

Figure 4.26 Experimental and numerical load -settlement curves of center, side and corner piles in PGF at 55 kPa suction

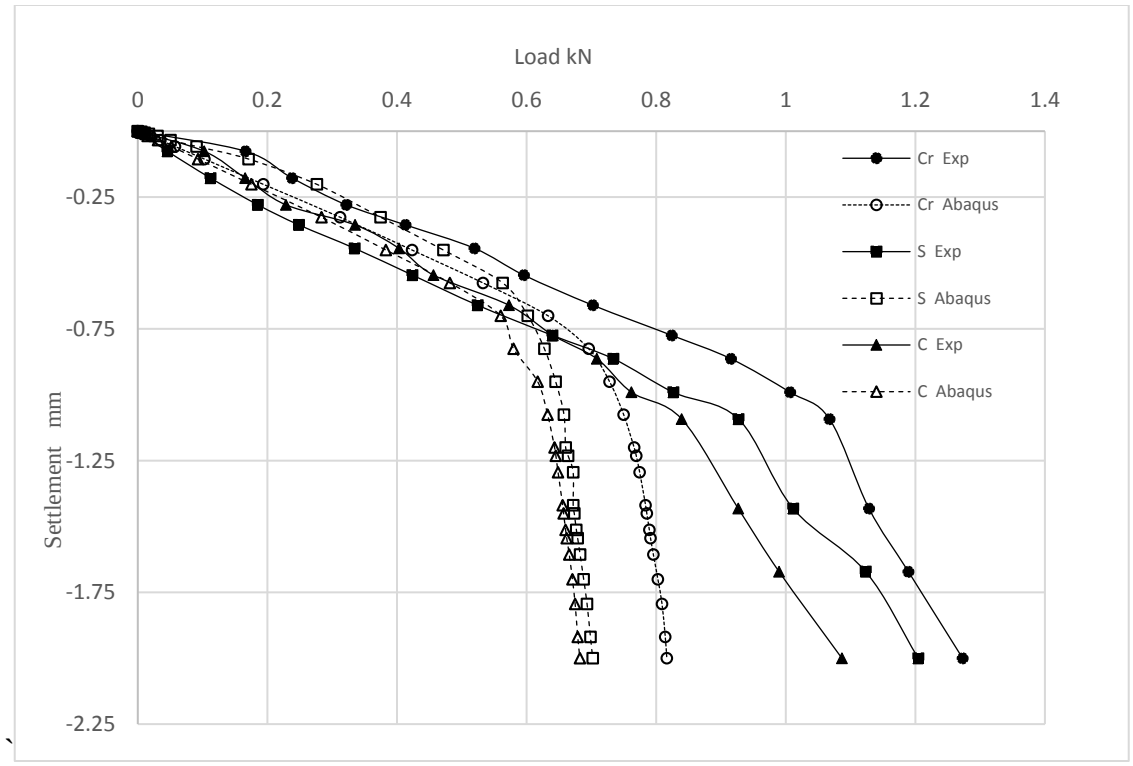

Figure 4.27 Experimental and numerical load -settlement curves of center, side and corner piles in PGF at 200 kPa suction

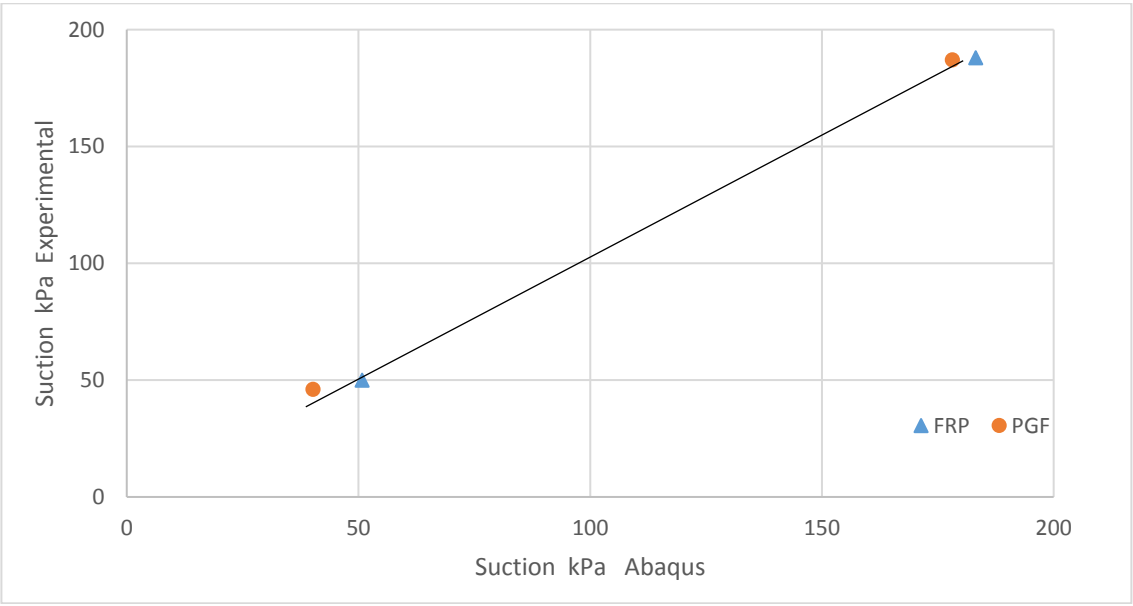

Figure 4.28 Experimental suction vs. computed suctions of PRF and PGF in 50 and 200 kPa suction

When examining Figures 4.19 through 4.27, it can be noticed that Abaqus load-settlement curves showed good agreement with experimental ones for URF with all suctions (Figures 4.19, 4.20, and 4.21). For PRF and PGF, the variations between the numerical and experimental curves were within 20% with similar trends. The only exception was in PGF 200 kPa suction (Figures 4.21 and 4.27) in which, the ultimate resistance of load settlement curves computed by Abaqus was around 60% of the experimental one. In Figures 4.22 and 4.26, central piles exhibited higher resistance than side and corner piles in both Abaqus and experimental load-settlement curves in all cases as expected.

Figure 4.28 shows suction values measured experimentally with those computed by Abaqus. Experimentally, a suction sensor was placed at 25 mm below the center of the pile tip. In Abaqus simulation, suctions were computed from a node located at 20 mm below the center of the piles tip. Both suctions showed excellent agreement.

Overall, the computed results of PRG, PGF, and URF models showed good agreements with corresponding experimental models. Accordingly, large scale model can be developed by Abaqus to study the effect of several key parameters on the behavior of PRF.

4.6 Effect of Parameters on the Behavior of PRF

Large-scale PRF models were developed to study the effect of several key parameters on the behavior of PRF. Thickness of the raft (t), pile spacing (S), and pile length to diameter ratio (L/d) were selected for this purpose. The effect of these parameters on total foundation resistance (TFR) and the percentage of load carried by raft at different suctions were investigated. The influence of the above parameters on TPR, EBR, and SFR at the center pile (CR), side pile (S) and corner pile (C) was also studied. It is noted that distributed total displacement load up to 10% of the pile diameter (that is, 4 cm) was applied on the raft area in all analyses.

4.6.1 Effect of Raft Thickness (t)

PRF models with raft thickness of 0.8, 1.2, and 1.6 m were analyzed with soil suctions of 0, 55, and 200 kPa. Pile spacing (S) in all PRF models were 3d and L/d ratio was 15. Figure 4.29 shows the relation between total foundation resistance TFR and raft thickness for 0, 55, and 200 kPa suctions. It can be noticed that selected raft thicknesses have an insignificant effect on TFR.

Raft thickness had limited influence on the percentage of load carried by the raft to TFR in PRF at all suction values as shown in Figure 4.30. At zero suction value (saturated soil), raft contributed to about 15 % of total load capacity and increased to 22% in 55 kPa suction. The raft contribution was increased to about 36% to 41% of the total resisted load for the selected thicknesses with 200 kPa suction.

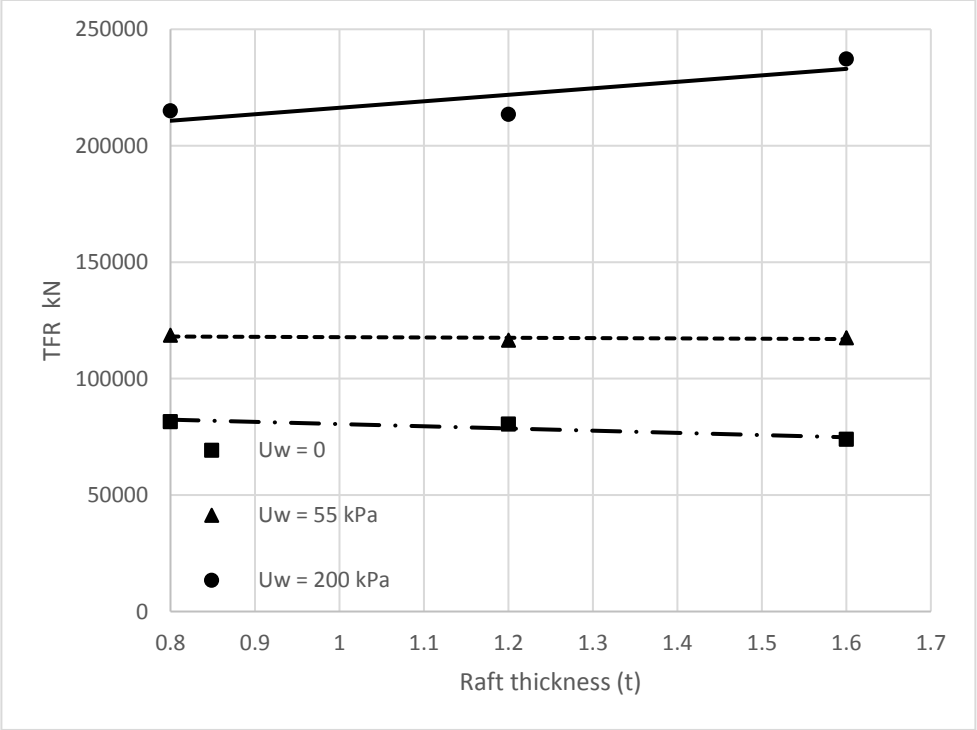

Figure 4.29 Variation of TFR with raft thicknesses

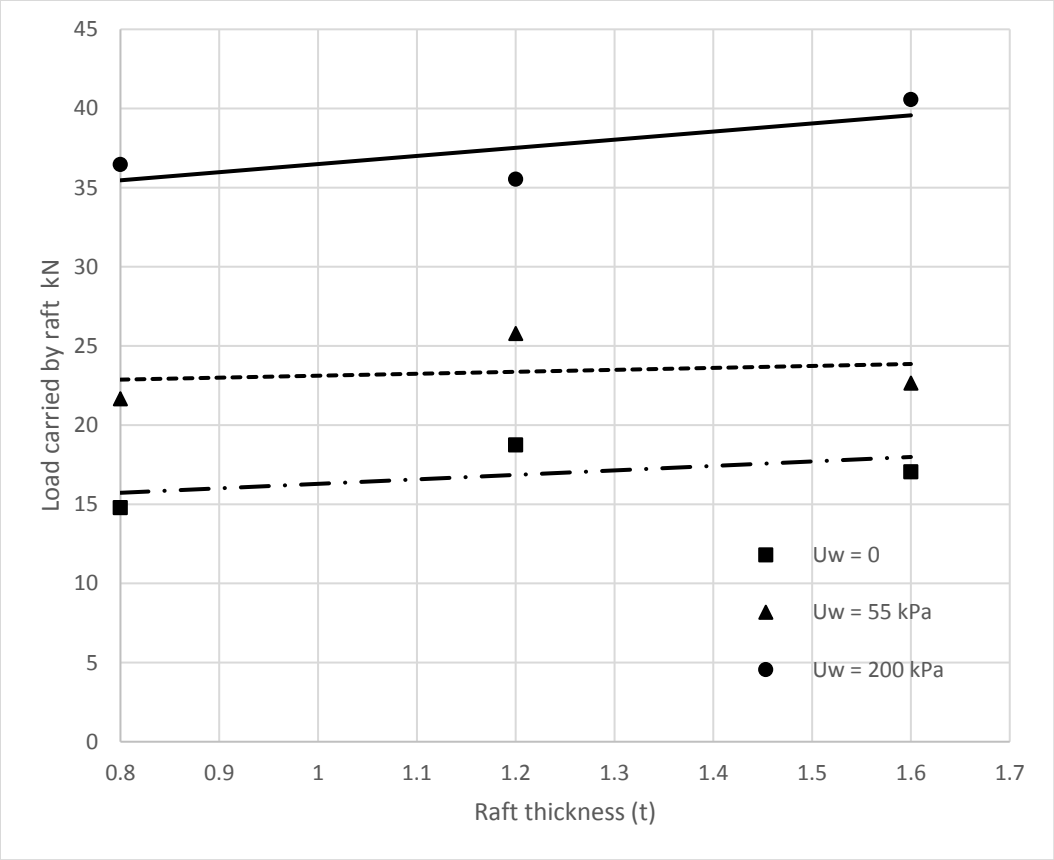

Figure 4.30 Percentage of load carried by raft to TFR of different thicknesses in PRF

4.6.2 Effect of Pile Spacing (S)

Designing deep foundation pile spacing is one of the most critical aspects. It determines the total number of piles in the group and eventually the cost of constructing. Five PRF models for different pile spacing were simulated for this purpose. One URF model was also developed. Same soil properties, boundary conditions, and modeling technique as in the previous models were used. Raft and piles properties are also the same to those used in previous models. The same final distributed load of 10% of the pile diameter was applied on the raft top in each model. Pile diameter of 0.4 m and pile- diameter ratio L/d was equal to 15 and was used. Geometric properties of rafts and piles of various configurations are summarized in Table 4.2. Note that since the raft

dimensions and the pile diameter are fixed, the number of piles decreases with increasing pile spacing.

Table 4.2 Geometric properties of PRF models

Pile Spacing (S)	Raft Dimensions (m)	No. of Piles	Other Properties
3d	24x24x0.8	400	d = 0.4 m,
4d		225	L/d = 15
5d		144	Final distributed load 10% of
6d		100	pile diameter (d)
7d		64	

Figure 4.31 shows TFR-settlement curves of PRF model with different suctions. It is clear that TFR increased with suction. Figure 4.32 shows TFR for PRF of different pile spacing with suction values of 0, 55 and 200 kPa. It also includes TFR of URF at zero pile spacing axis. It can be observed that the pile spacing has a noticeable influence on TFR. However, TFR values for PRF at the highest spacing 7d (2.8 m) was approximately two times of TFR for URF model as shown in Figure 4.32. It is also seen that TFR of PRF models will converge with the capacity of URF models at larger pile spacing.

Figure 4.33 shows the percentage of the load taken by the raft to TFR. The percentage considerably increased with pile spacing in all suction values. The raft carried 15% to 45% in zero suction, 22% to 52% in 55 kPa suction, and 36% to 60% in 200 kPa suction.

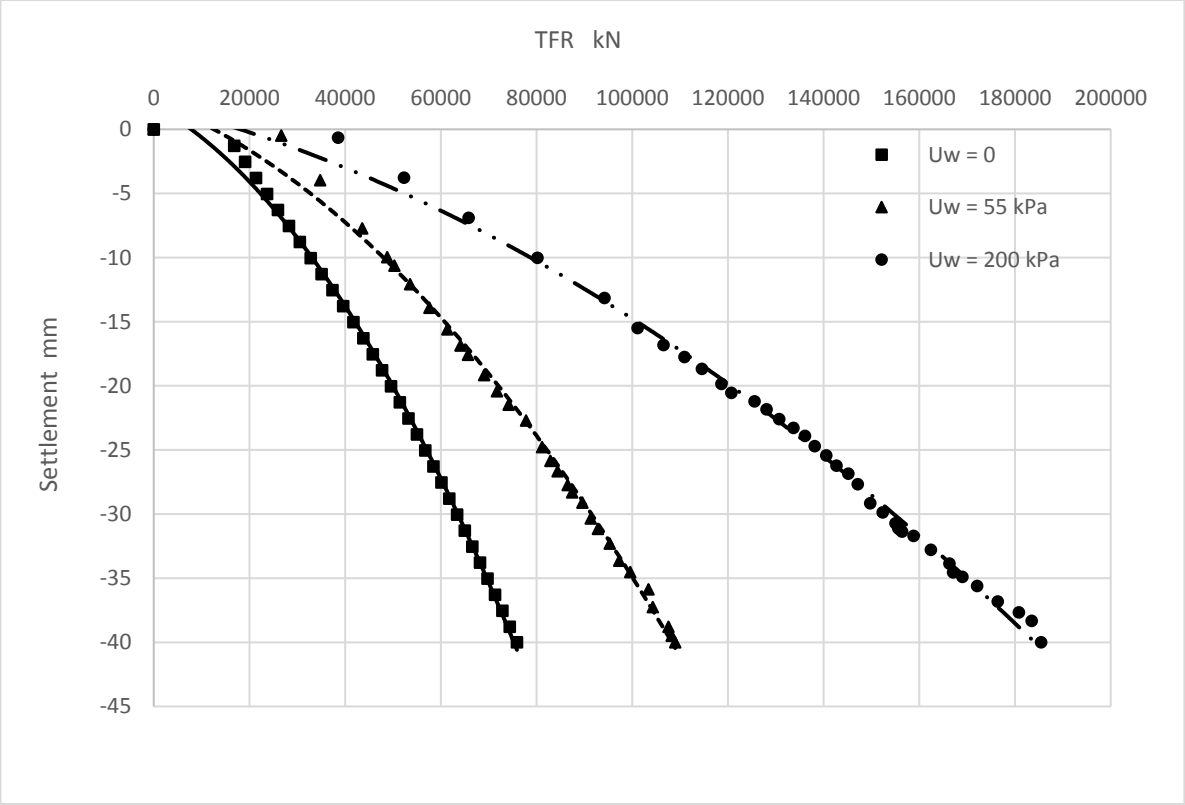

Figure 4.31 Load- settlement curves of PRF of 4d pile spacing under different suctions

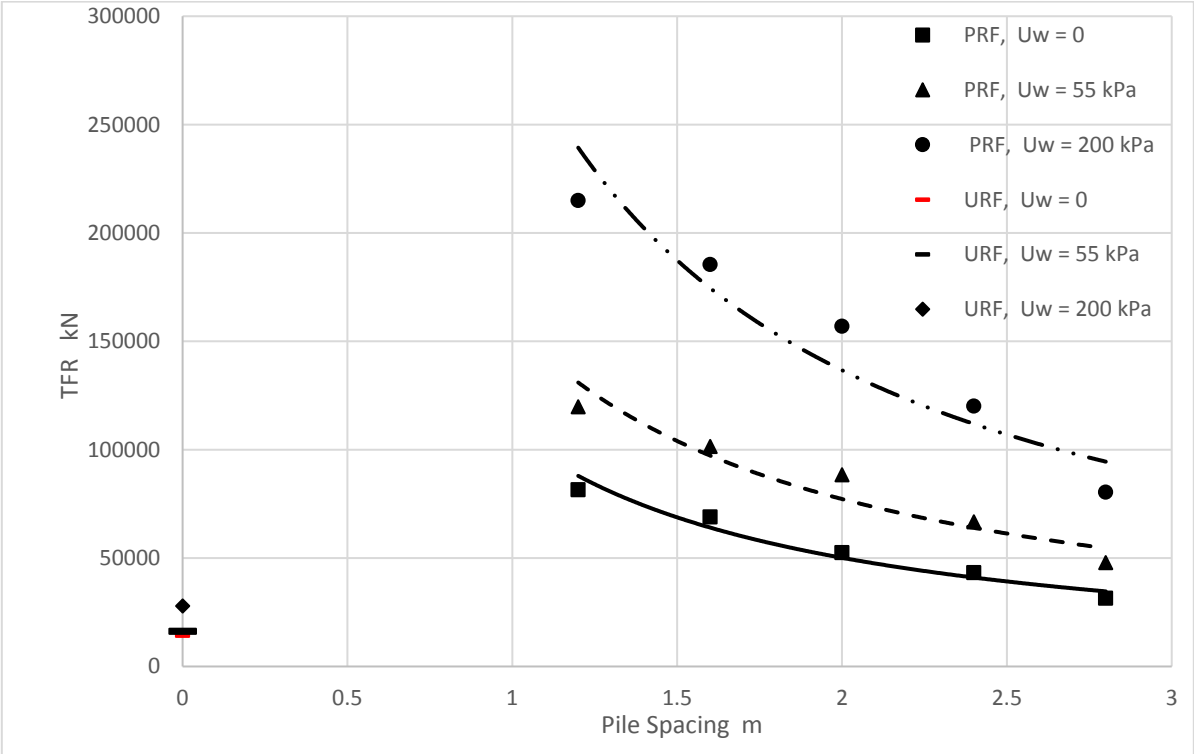

Figure 4.32 TFR for PRF models with different pile spacing with various suction values

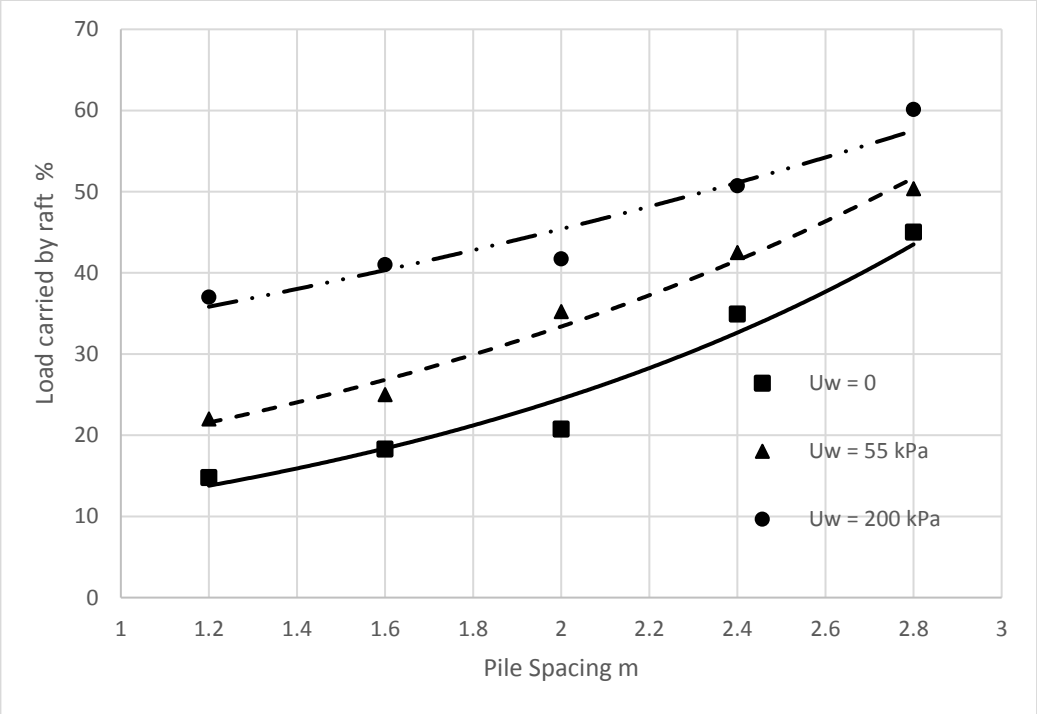

Figure 4.33 Percentage of load carried by raft to TFR in PRF model with different pile spacing

4.6.3 Effect of Pile Length to Diameter Ratio (L/d)

It is known that applied load on a pile is resisted by skin friction and end bearing components. A 24 x 24 m raft with 0.8 m thickness and pile diameter of 0.4 m was assigned to PRF models in this analyses. Piles length to diameter (L/d) equals to 15, 25, 35, 45 with pile spacing of 4d were selected to study the effect of L/d on the total foundation resistance and the percentage of load carried by raft.

Figure 4.34 shows TFR of PRF models with different L/d ratios. As expected, the capacity increased linearly with L/d ratio at all suctions. The increment of rates is similar at all suction values. Figure 4.35 shows that the percentage of load carried by the raft to TFR that is reduced as L/d is increased in all suction values as expected because the longer the pile, the more skin friction resistance is expected.

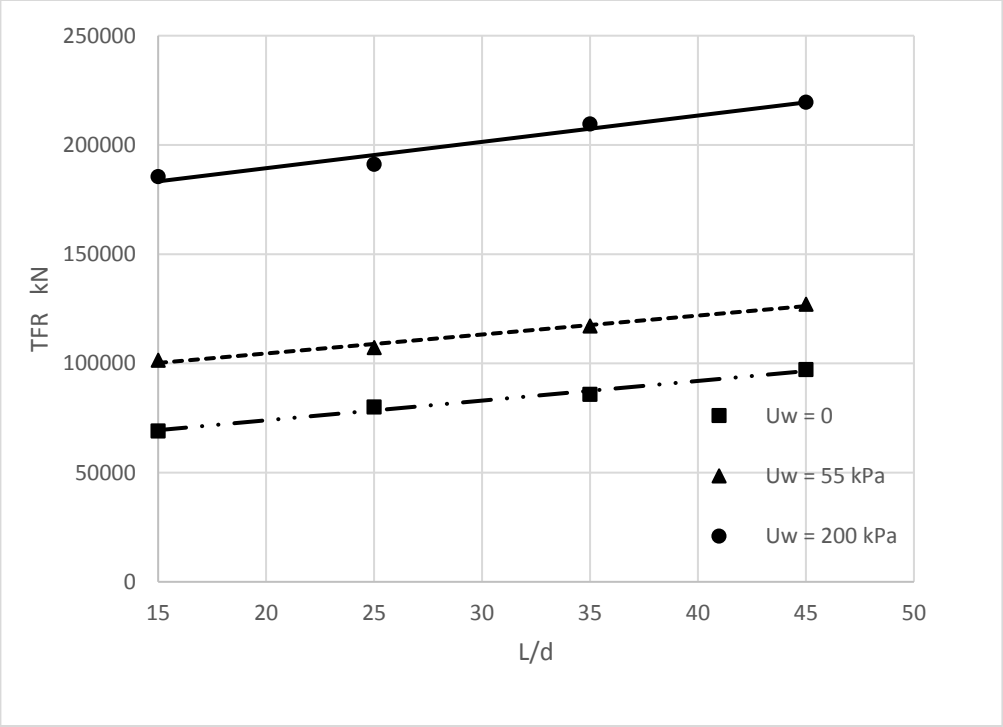

Figure 4.34 Variation of TFR with L/d in different suctions for PRF model with 4d pile spacing

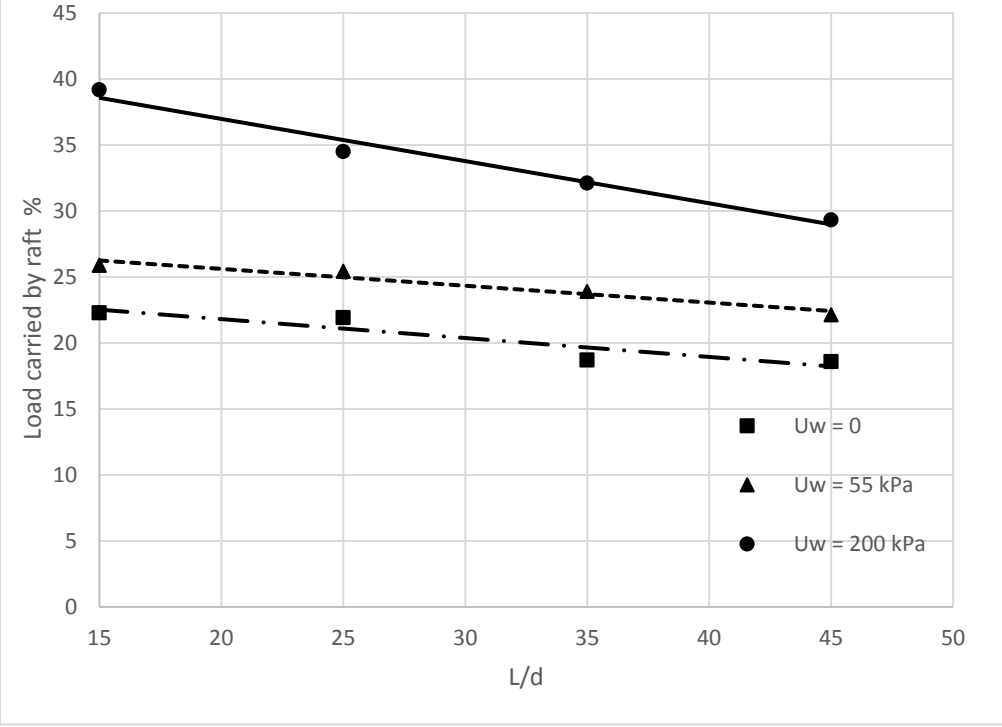

Figure 4.35 Percentage of load carried by the raft to TFR with L/d for PRF model with 4d pile spacing

CHAPTER 5

ANALYSIS OF RESULTS

5.1 Introduction

Results obtained from experimental and numerical works are analyzed in this chapter. The relationships between suction and other parameters or factors that affect the behavior of PRF, PGF, and URF are presented. Models for estimating the bearing capacity of SPF and PRF models with different suctions are proposed in this chapter. The model estimates the Total Pile Resistance (TPR) of SPF based on Skin Friction Resistance (SFR) and End Bearing Resistance (EBR). The relations between interaction factors of PRF, PGF, and URF with suctionss are highlighted. Variation of skin friction and tip bearing factors at different locations of piles with various suctions are also investigated in this chapter also.

5.2 Shear Strength of Partially Saturated Soil

Figure 5.1 shows the relationship between cohesion and suction, which was obtained from undrained shear strength experiments. It can be noticed that cohesion increased linearly up to the Air Entry Value (AEV) as expressed in Equation 5.1. The increase became less significant as the suction increased further. At high suction values (600 kPa and higher) no increase in cohesion was noticed. The relation between cohesion and suction beyond AEV was fitted using Equation 5.2.

$$c = 46 + U_W \quad 5.1$$

where

c = cohesion (kPa) and equal to 46 kPa for fully saturated soil

U_w = suction in soil (kPa)

$$c = 0.65 * S_r * \left[\frac{\ln(U_w)}{\ln AEV}\right] + 23 * \ln(U_w) \quad 5.2$$

where

S_r = degree of saturateion (%)

U_w = suction in the soil (kPa)

AEV = air entry value (kPa)

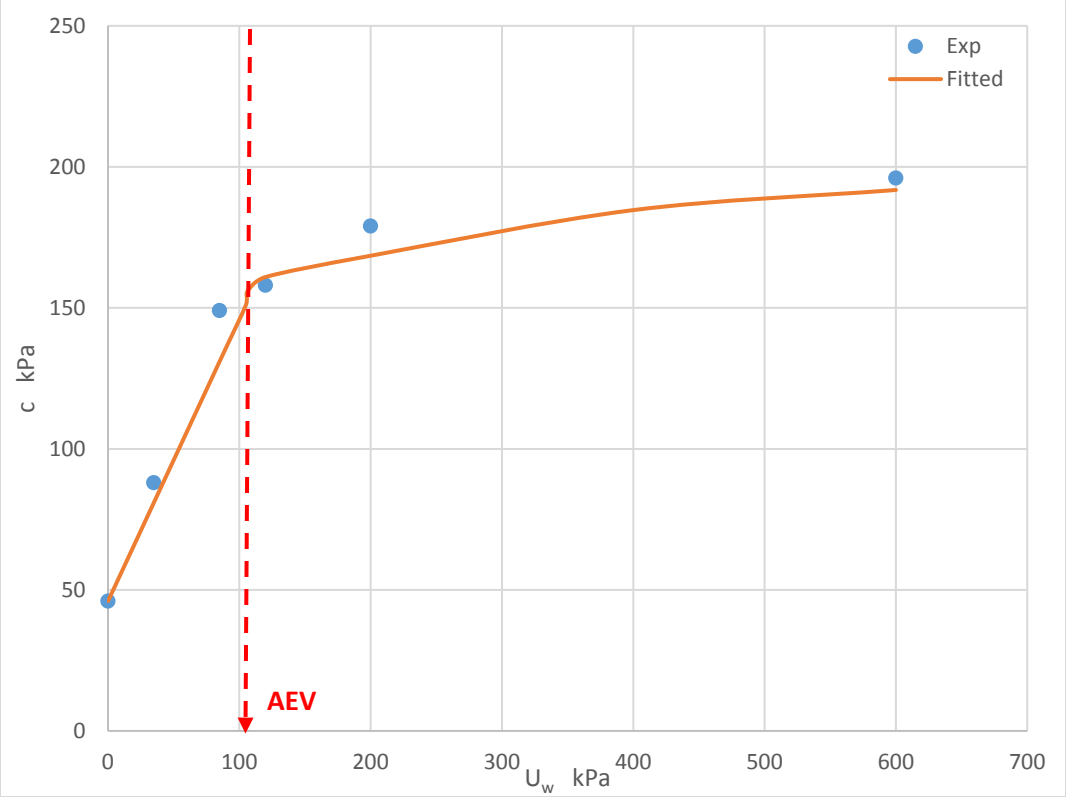

Figure 5.1 Relation between cohesion and suction

Figure 5.2 shows the relation between suction and angle of internal friction (φ), which was obtained from shear strength tests. It can be observed that the variation of suction did not affect φ value significantly or consistently. The average variation in φ values was ± 3 degrees over a suction range of 0- 600 kPa. This observation was supported by Fredlund et al. (2011).

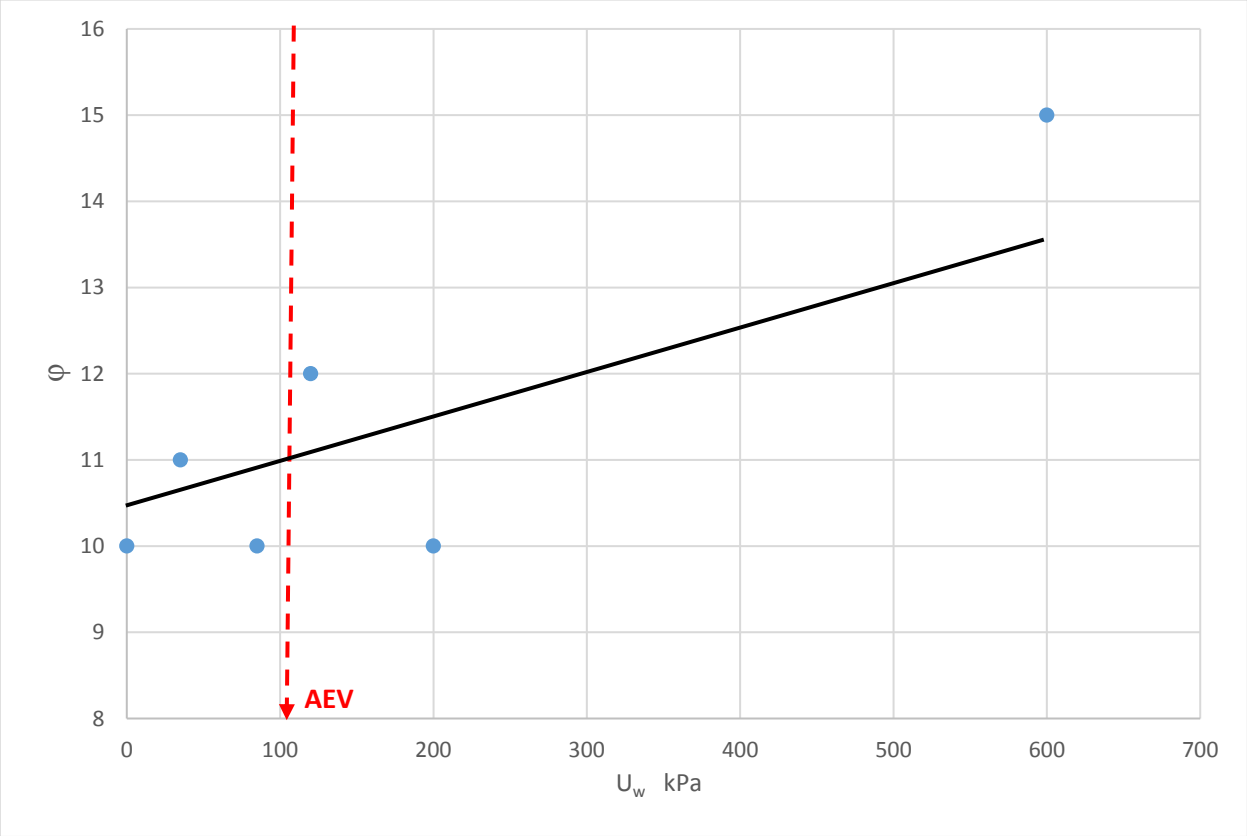

Figure 5.2 Variation of φ values with suction

5.3 Resistance of Single Pile Foundation (SPF)

It is known that pile resists applied load by two components. These components are Surface Skin Friction (SFR) and End Bearing Resistance (EBR). The experimentally obtained resistance of SPF is shown in Figure 5.3. It can be observed that the load is mainly resisted by SFR component up to AEV. Beyond AEV, there was no significant increase in SFR. On the other hand, EBR slightly increases till AEV and starts to increase noticeably after AEV to 2AEV. Then, EBR does not show any significant increase beyond a suction equal to 2AEV. It can be concluded that the TPR of SPF consists primarly from SFR from zero to AEV suction and EBR contribution increases

from AEV to 2AEV. Suction does not provide any further increase in TPR beyond 2AEV. AEV and 2AEV suction values correspond to gravimetric water content of 13.4 % and 10.6 %, respectively, as shown in Figure 5.4.

The relation between SFR and EBR versus suction was fitted in Equations 5.3, 5.4, and 5.5. These relations are expressed in terms of suctions with boundary values at AEV and 2AEV.

For $Uw < AEV$ (105 kPa)

$$SFR\ (kN) = 0.42 + 0.007\ U_w\ (kPa) \quad 5.3$$

$$EBR\ (kN) = 0.18 + 0.0002 * U_w(kPa) \quad 5.4$$

For $AEV < Uw < 2\ AEV$,

$$SFR = 1.155$$

$$EBR\ (kN) = 0.0071 * U_w(kN) - 0.55 \quad 5.5$$

For $Uw > 2AEV$

$$SFR = 1.155$$

$$EBR = 0.94$$

It is worth mentioning here that the optimum moisture content (OMC) was 13.2 % which nearly the same as the water content AEV (13.4%) as shown in Figure 5.4. The maximum dry density ($\gamma_{d\ max}$) was 17.8 KN/m^3 for the soil used in this study.

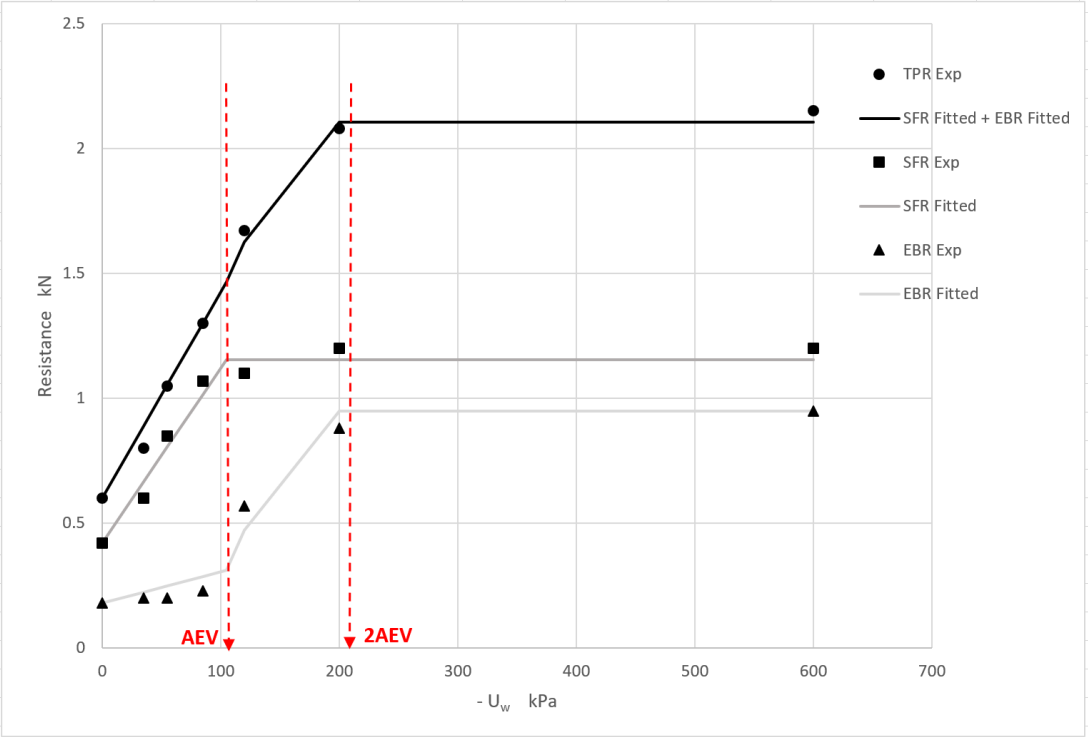

Figure 5.3 TPR, SFR, and EBR of SPF with different suctions

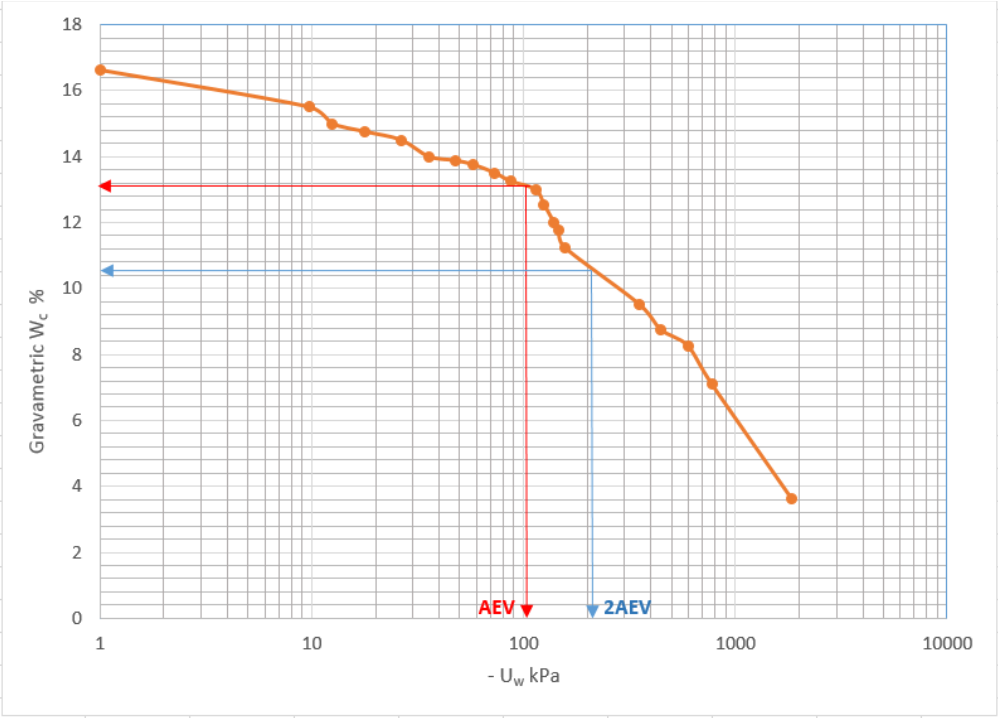

Figure 5.4 Soil Water Characterstic Curve followed in this study

Total Pile Resistance (TPR) of SPF can be estimated from Equation (5.8) as shown below

$$SFR = \alpha \times c \times A_s \quad (5.6)$$

$$EBR = c \times N_c \times A_b \quad (5.7)$$

$$TPR_{SPF} = SFR + EBR \quad (5.8)$$

where

α = adhesion (friction) factor

c = cohesion

N_c = bearing capacity factor

A_s = surface area of SPF and equal to π d L (*d* = pile diameter, and *L* = pile depth)

A_b = end bearing area of the pile and equal to (π/4) d^2

The experimental relation between friction factor (α) and suction are shown in Figure 5.5. It can be observed that friction factor in SPF decreased with suction up to AEV, and beyond AEV, suction had a minor effect on the friction factor. The measured relations between bearing capacity factor (N_c) and the suction are shown in Figure 5.6. The figure indicates that bearing capacity factor went down with suction up to AEV. N_c increased between AEV and 2AEV and remained nearly constant beyond 2AEV. The relations between friction factor (α) and bearing factor (*Nc*) with corresponding suctions were fitted in Equations 5.9 and 5.10.

$$\alpha = 0.167 * e^{-0.023*U_w} + 0.35 \quad (5.9)$$

For U_w < *2AEV*

$$N_c = 13.38 - 0.1436 * U_w + 0.00082 * U_w^2 \quad (5.10)$$

For U_w < *2AEV*

N_c = constant = 18

where U_w (positive value) is the suction value in kPa.

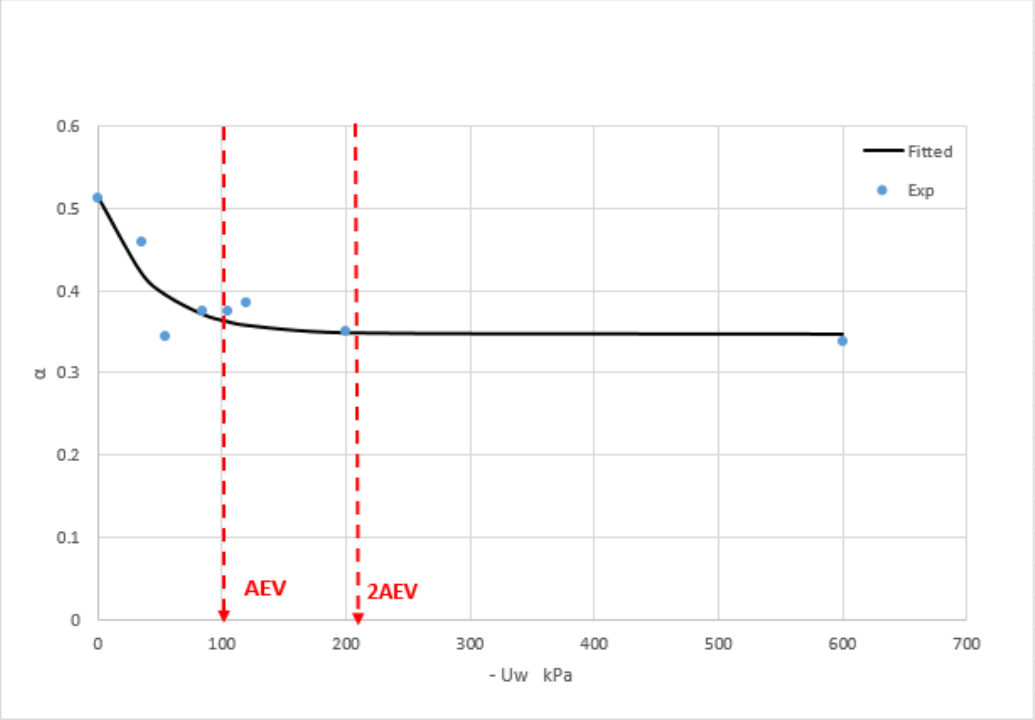

Figure 5.5 Variation of friction factor α with suction for SPF

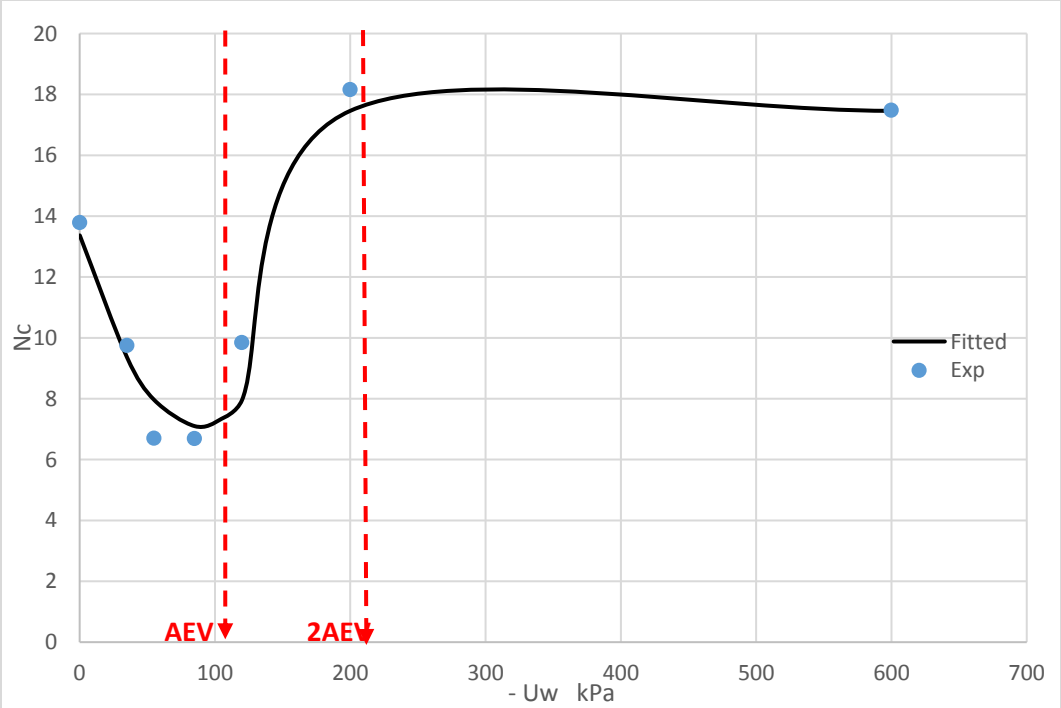

Figure 5.6 Variation of the bearing capacity factor N_c with suction for SPF

5.4 Verification of Single Pile Model

Equation 5.3 for estimating SFR of single pile was compared with experimental results of Vanapalli and Taylan (2012). Properties of the soil used by Vanapalli and Taylan are listed in Table 5.2. The pile used in their study was 0.02 m in diameter and 0.2 m long, while the pile used in this study was 0.019 m in diameter and 0.3 m long.

In order to compare SFR of above two piles, SFR in Equation 5.3 was divided by the surface area of the pile ($\pi * d * L$) to get the unit friction resistance (f_s). The unit friction resistance is then multiplied by the surface area of the pile used in Vanapalli and Taylan study. Table 5.3 compares SFR measured by Vanapalli and Taylan and those computed using Equation 5.3 for four different suctions.

Table 5.1 Properties of the soil used in Vanapalli and Taylan (2012) study

Soil Properties	Value
Optimum water content (%)	18.6
Maximum dry unit weight (kN/m^3)	16.7
Saturated unit weight (kN/m^3)	18.5
Specific Gravity G_s	2.7
Sand, Silt, and Clay (%)	28, 42, 30
Liquid limit and Plastic limit (LL and PL) %	36.2 and 15
Plasticity index (PI)	21.2
Air Entry Value (AEV) at 16 % WC (kPa)	14

Table 5.2 Comparison of SFR measured by Vanapalli and Taylan (2012) and SFR computed by Equation 5.3

Uw	C_u measured by Vanapalli and Taylan	c	SFR measured by Vanapalli and Taylan	*SFR*	Difference in SFR
kPa	kPa	kPa	kN	kN	%
0	11.5	46	0.1	0.25	150
53	58	101	0.5	0.53	6
110	80	153	0.55	0.829	50
203	68	170	0.68	0.829	20

The difference between the two SFR values may be related to the properties of the soil used in both studies. C_u measured by Vanapalli and Taylan was from the unconfined compression test while C_u in this study was measured from CU and CUW tests for saturated and partially saturated soils, respectively. It is evident that cohesion soil increases with suction in the soil. However, C_u in Vanapalli and Taylan study went down by 30% when the suction was increased from 110 kPa to 203 kPa. It has been shown earlier that the behavior of partially saturated soil is related to the AEV of the SWCC in the soil under consideration. Therefore, the difference in shear strength and skin friction resistance values can be attributed to the difference in AEV in both studies. AEV in Vanapalli and Taylan study was about 14 kPa for initial water content of 16 % while AEV in this study was 105 kpa for Initial water content of 16.5 %.

Higher SFR values in this study may be resulted from the type of test followed for determining the cohesion in both soils. It is worth mentioning here that the equation also assumes

no increment in SFR beyond AEV suction and any further increase in total pile resistance comes from the bearing component.

5.5 Resistance of PRF, PGF and URF Models

Figure 5.7 plots measured Total Foundation Resistance (TFR) of PRF, PGF and URF models. TFR of all models increased from zero suction to AEV. It is interested to observe that TFR of PRF and PGF kept increasing with the same rate up to 2AEV and then remained nearly constant with further increasing suction, while TFR of UPR kept increasing with a smaller rate from AEV to 600 kPa suction (the highest suction value in this study).

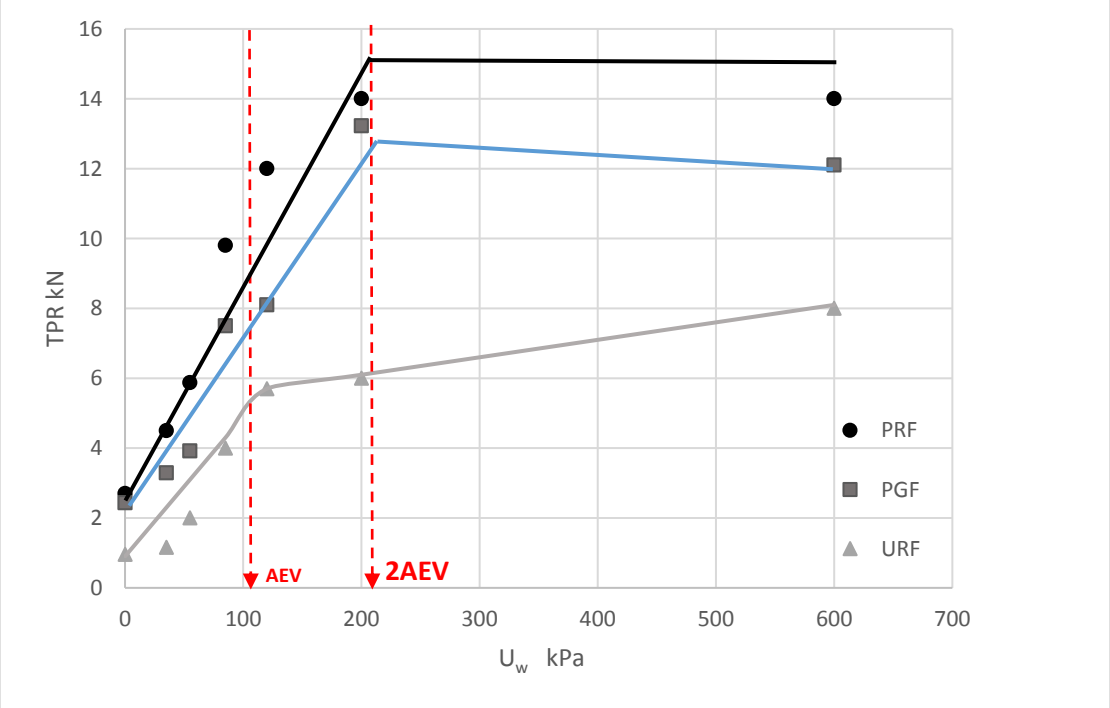

Figure 5.7 TFR of PRF, PGF, and URF with variable suctions

It can be noticed that as the suction increases, the contribution of the raft in PRF increases slightly. The raft contribution in PRF was considered to be the difference between PRF and PGF curves in Figure 5.7. It seems that the raft contribution in PRF maintained nearly constant

resistance in PRF at suctions beyond 2AEV. In PGF, the resistance decreased at suctions beyond 2AEV suctions.

5.5.1 Interaction Factors

Group efficiency factor (η) in PGF is defined in Equation 5.11. Kezdi, (1957) stated that this factor is depending on both pile, and soil type. η value of 3x3 PGF model with 3d pile spacing was back calculated from the results of PGF and SPF tests.

$$\eta = \frac{TFR_{PGF}}{n \times TPR_{SPF}} \qquad 5.11$$

where, n = number of piles in the group, TPR_{SPF} = Total Pile Resistance of single pile foundation, Equation 5.8. TFR_{PGF} = Total Foundation Resistance of pile group foundation, Figure 5.7

It is known that the group efficiency factor for cohesive soils is less than one. Variation of (η) with suction is shown in Figure 5.8. If the data point of 55 kPa suction was ignored, it can be noticed that (η) was about 0.45 for fully saturated soil and increased with suction up to AEV to be 0.575 and then became constant after AEV suction.

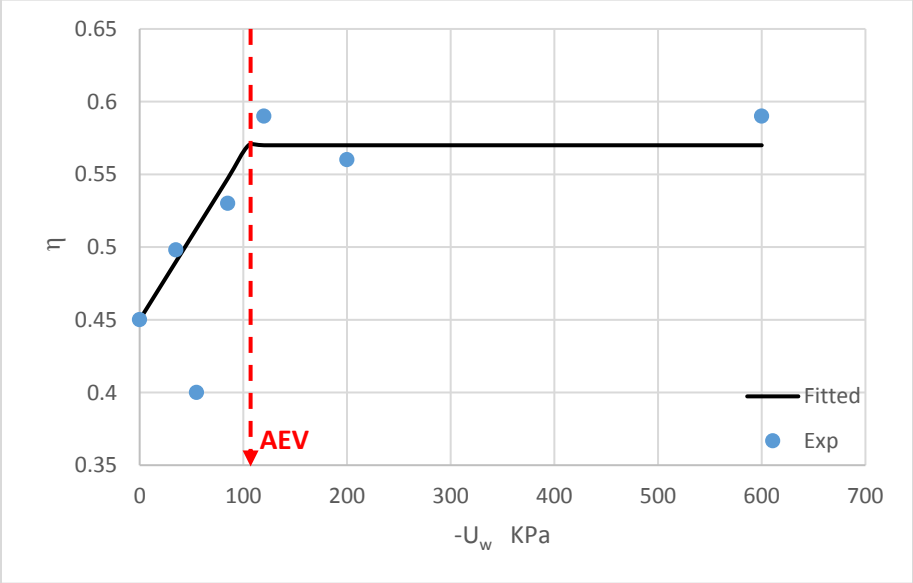

Figure 5.8 Relation between group efficiency factor (η) with suction.

β_{PRF} is factor that representing the gain in PRF capacity over PGF capacity. β_{PRF} is defined in Equation 5.12 and shown in Figure 5.9. It is evident that β_{PRF} is higher than 1, indicating the contribution of the raft in PRF. It can be noticed from the figure that β_{PRF} increased with suction and reached the maximum at AEV suction where the resistance of PRF was about 40% higher than PGF resistance. The experimental data of β_{PRF} with suction was fitted in Equation 5.13. Cooke (1986) and Borel (2001) mentioned that the ultimate bearing capacity resistance of PRF is mobilized with the settlement at 10% of the raft width in PRF. However, the maximum attained settlement in this study was 10% of the pile diameter or 1.167 % of the raft width and therefore β_{PRF} in this study is probably underestimated.

$$\beta_{PRF} = \frac{TFR_{PRF}}{TFR_{PGF}} \quad 5.12$$

For $U_w < AEV$

$$\beta_{PRF} = -2 * 10^{-5} * U_w^2 + 0.0045 * U_w + 1.12 \quad 5.13$$

For $Uw > AEV$

$$\beta_{PRF} = \beta_{PRF}(at\ AEV)$$

where U_w is in kPa

Another factor that indicates the effect of interaction between the components of PRF on the total foundation resistance is referred to ξ_{PRF} defined in Equation 5.14.

$$\xi_{PRF} = \frac{TFR_{PRF}}{TFR_{PGF+URF}} \quad 5.14$$

Figure 5. 10 shows that the value of ξ_{PRF} for fully saturated soil was 0.82. This value agrees with (0.8 -1) range reported by DeSanctis (2006). The relation between ξ_{PRF} and U_w is formulated in Equation 5.15.

$$\xi_{PRF} = 0.823 - 0.0002 * U_w\ (kPa) \quad 5.15$$

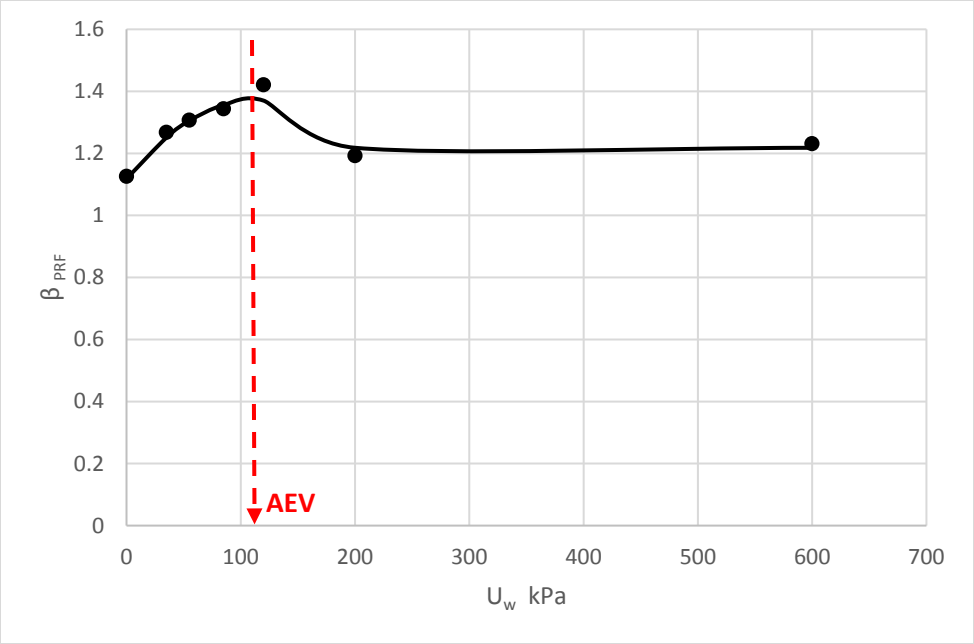

Figure 5.9 Variation of β_{PRF} with suction

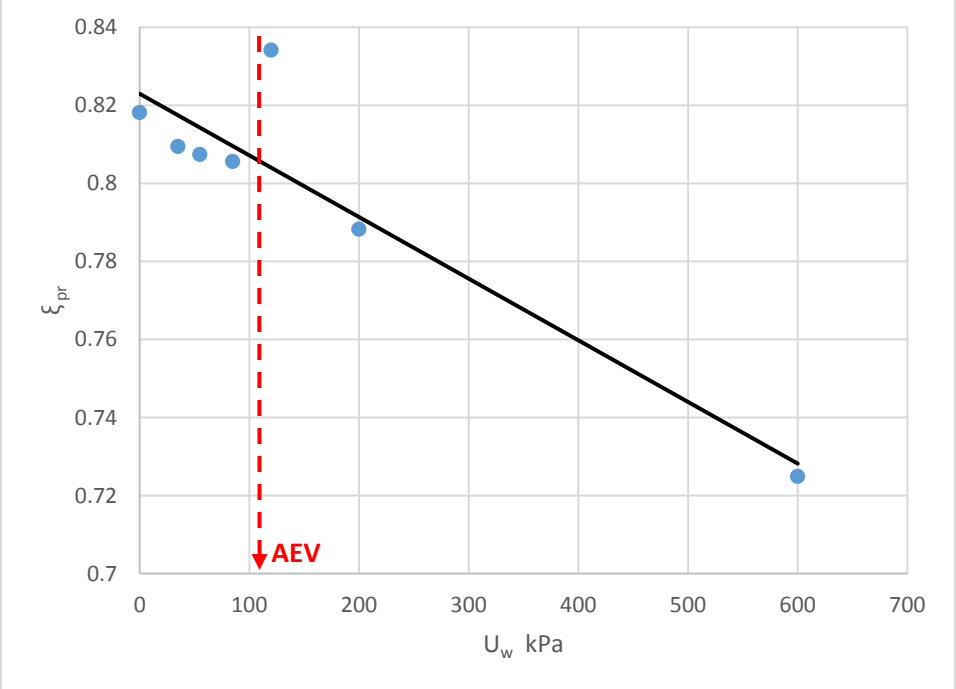

Figure 5.10 Variation of ξ_{PRF} with suction

In order to evaluate the effect of raft on piles capacity in PRF, raft- piles interaction factor ($\alpha_{R\text{-}P}$) of PRF at different suctions was computed utilizing Equation 5.16. Data were plotted and fitted in Equation 5.17.

$$\alpha_{R-P} = \frac{\Sigma TPR_{PRF}}{TFR_{PGF}} \quad 5.16$$

where

ΣTPR_{PRF} = summation of piles resistance in PRF (TFR_{PRF} – raft section resistance in PRF)

$$\alpha_{R-P} = 8 * 10^{-7}\ 8 * U_w^2 - 0.001 * U_w + 0.98 \quad (U_w \text{ in kPa}) \quad 5.17$$

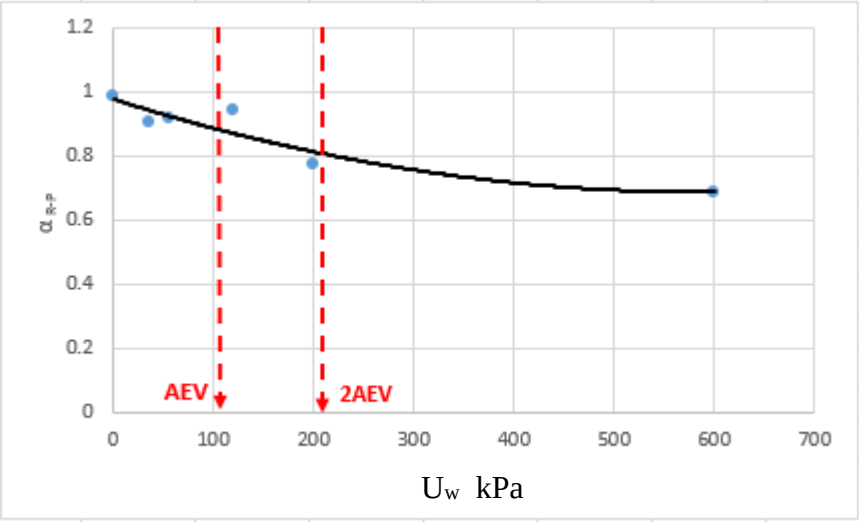

Figure 5.11 Variation of $\alpha_{R\text{-}P}$ with suction

It can be noticed from figure 5.11 that at zero suction soil, the raft section in PRF almost has no effect on the resistance of piles in PRF with α_{R-P} close to 1 (0.98). This effect is more noticeable at the suctions ranged from AEV to 2AEV and then levels off at suctions beyond 400 kPa.

Figure 5.12 shows the relation between Pile-Raft interaction factor $\alpha_{P\text{-}R}$ with suction. $\alpha_{P\text{-}R}$ can be defined as the percentage of the raft capacity in PRF to the capacity of URF and defined in Equation 5.18.

$$\alpha_{P-R} = \frac{TFR_{PRF} - TFR_{PGF}}{TFR_{URF}} \quad 5.18$$

Where *TFR* is total foundation resistance (kN) of particular foundation

For $U_w < 2AEV$

$$\alpha_{P-R} = -2 * 10^{-5} * U_w^2 + 0.0043 * U_w + 0.3313 \text{ (Uw in kPa)} \quad 5.19$$

For $Uw > 2AEV$

$$\alpha_{P-R} = \alpha_{P-R}\,(at\ AEV) = 0.375$$

It can be observed that piles have a considerable effect on the raft capacity in PRF at low and high suctions. $\alpha_{P\text{-}R}$ seems to be influenced by the soil disturbance caused by the installation process of the piles. At low suction, the disturbance may be attributed to the settlement of the soft soil around the perimeter of the piles. This settlement reduces the contact area and leads to less raft capacity in PRF. At high suction, the installation of the piles causes the appearance of big cracks and irregularity in the soil area under the raft which may cause less capacity of the raft in PRF as compared to URF at the same suction.

Experimental data were fitted in Equation 5.19 for suction up to 2AEV. Beyond this suction, $\alpha_{P\text{-}R}$ exhibited minor variation and can be considered to be equal to $\alpha_{P\text{-}R}$ value at 2AEV suction.

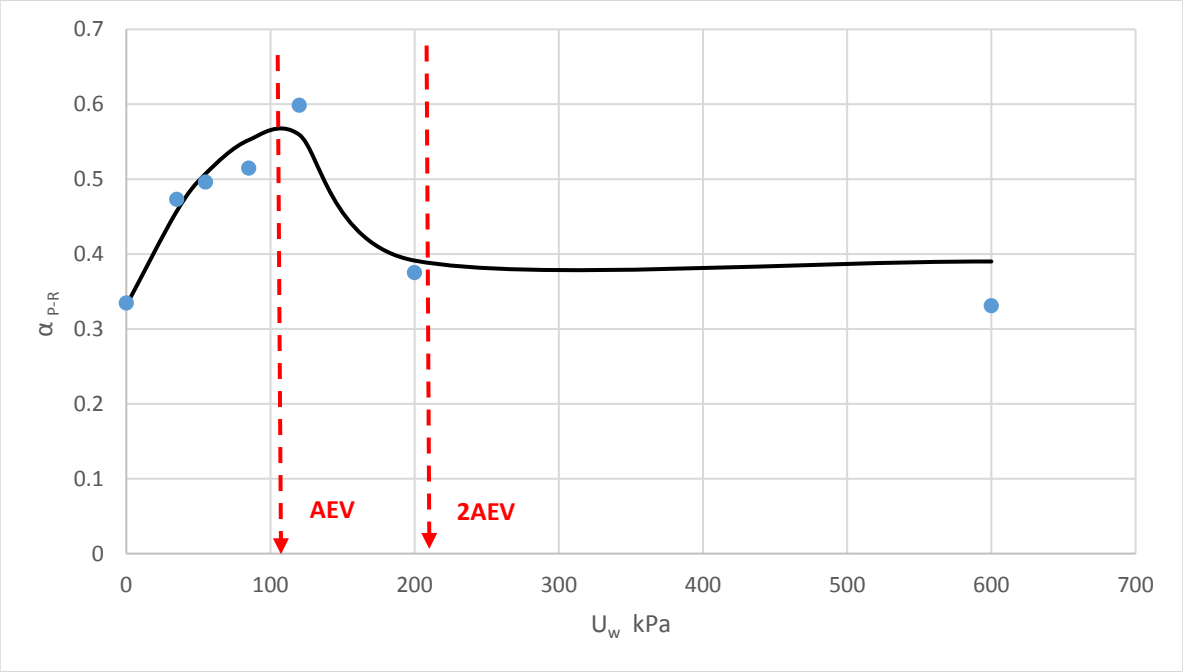

Figure 5.12 Variation of $\alpha_{P\text{-}R}$ with suction

The percentages of load resisted by raft section to PRF (R_{PRF}) at different suctions is shown in Figure 5.13. It can be observed that the raft took only 12 % of the load in PRF at zero suction. The raft carried more load as the suction reached AEV. The load taken by the raft continued to increase with suction at a slower rate from AEV to the highest suction value used in this study. The experimental data shown in the figure were fitted in Equations 5.20 and 5.21 based on AEV suction in the soil as follows:

For $Uw < AEV$

$$Percentage\ of\ load\ carried\ by\ raft\ in\ PRF\ = 12 + 0.18 * U_w \text{ (Uw in kPa)} \quad 5.20$$

where the 12 % in Equation 5.20 represents the percentage of load carried by the raft when the soil has zero suction.

For $Uw > AEV$

$$Percentage\ of\ load\ carried\ by\ raft\ in\ PRF\ = 30.9 + \ 0.022 * U_w \quad 5.21$$

In Equation 5.21, the percentage of load carried by the raft at the suction equal to AEV is 33.2% and its value at 2AEV is 35.5%.

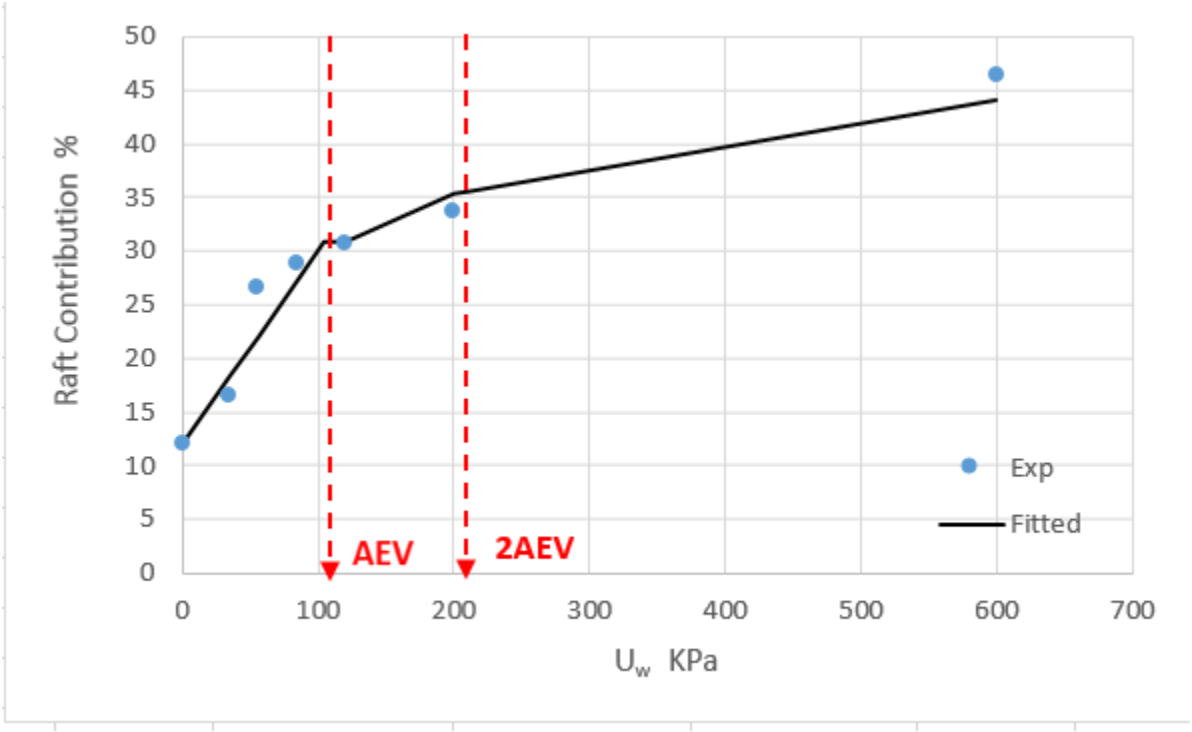

Figure 5.13 Contribution of raft in PRF at different suctions

TFR of URF can be computed using conventional bearing capacity equation shown in Equation 5.22.

$$TFR_{URF} = C_u \times N_c \times A_{raft} \quad 5.22$$

where N_c is the bearing capacity factor and can be back-calculated from Equation 5.22, using experimentally determined TFR_{URF} and C_u values. The relations between N_c and suction are shown in Figure 5.14.

Experimental data were fitted to Equations 5.23 and 5.24 based on AEV.

For $Uw < AEV$

$$N_c = 0.67 + 0.0058 \times AEV \quad 5.23$$

For *Uw* >*AEV*

$$N_c = N_c(AEV) + 0.0028\,(U_w - AEV) \qquad 5.24$$

where U_w and AVE in kPa in Equations 5.23 and 5.24

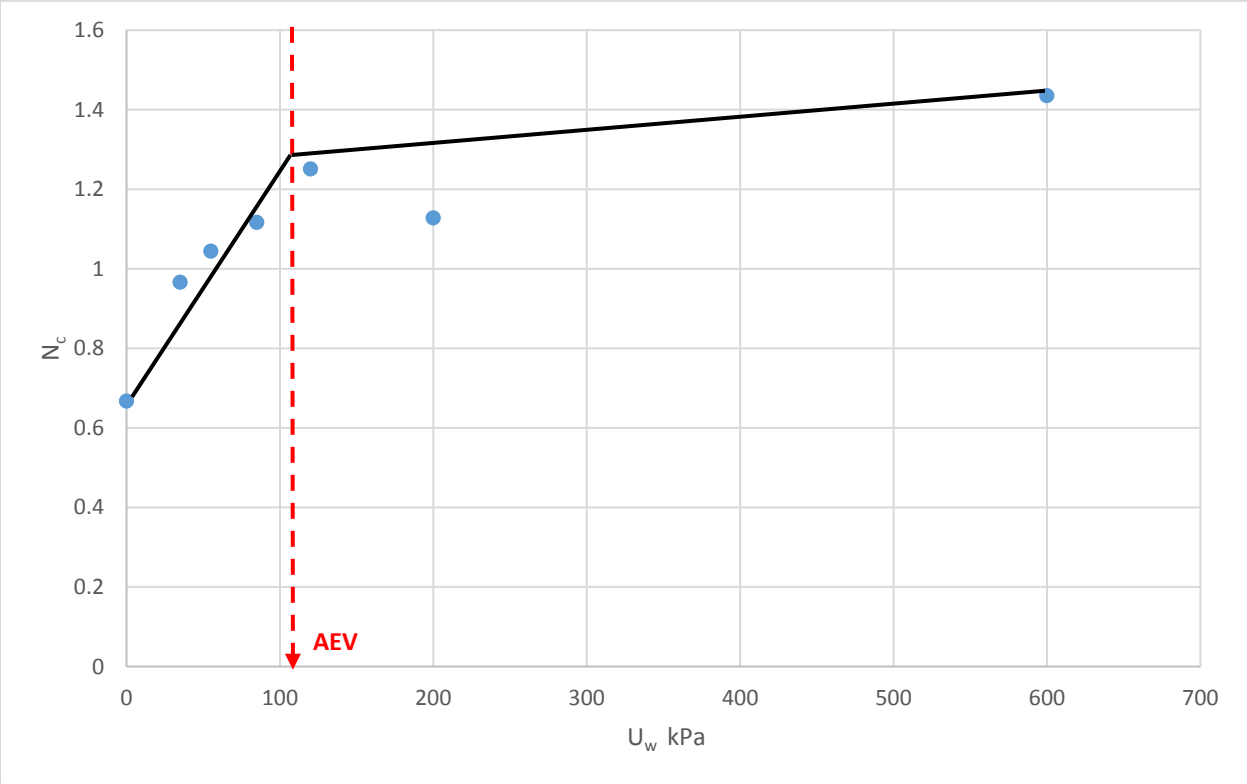

Figure 5.14 Variation of N_c with suction

It is worth mentioning here that there were no bearing capacity failure in the tests conducted in this study. The settlement that mobilizes the ultimate bearing resistance is believed to be around 10% of the raft width in PRF (B_{PRF}) as reported by Conte et al. (2003). However, all foundations in this study were loaded to 10 % of the pile diameter (2 mm) or about 1.2 % of the raft width B_{PRF} which is much smaller than 10% of the raft width. The smaller N_c values obtained in this study can be attributed to the small value of applied load.

5.5.2 Total Foundations Resistance (TFR)

For 3x3 Pile Group Foundation (PGF) with 3d pile spacing, Total Foundation Resistance (TFR) at various suction values can be estimated based on the capacity of single pile and interaction factors as shown in Equation 5.25

$$TFR_{PGF} = n * \eta * TPR_{SPF} \quad 5.25$$

where, n is the number of piles in the group and equal to 9 in this study, TPR_{SPF} can be calculated using Equations 5.8 and η is determined using Figure 5.8.

TFR_{URF} is defind as the total foundation resistance of unpiled raft foundations and computed for Equation 5.26 below

$$TFR_{URF} = C_u * N_c * A_{raft} \quad 5.26$$

where C_u is the undrained shear strength obtained from *CU* and CUW tests, N_c is bearing factor and A_{raft} is the area of the raft.

Finally, TPR_{PRF} for 3x3 foundation with pile spacing of 3d in various suctions can be determined by using the capacity of single piles and the interaction and can be computed using Equation 5.27

$$TFR_{PRF} = \alpha_{R-P} * TFR_{PGF} + \alpha_{P-R} * TFR_{URF} \quad 5.27$$

where, α_{R-P} and α_{P-R} are raft- pile and piles-raft interaction factors, respectively. All terms in Equation 5.27 were defined earlier, that is, α_{R-P} in Equation 5.16, TFR_{PGF} in Equation 5.25, α_{P-R} in Equation 5.18, and TFR_{URF} in Equation 5.26.

Similar equations were suggested by Liu et al. (1994) and Borel (2001) for estimating the total capacity of piled raft foundation. DeSanctis (2006) defined the factors in Equation 5.27 as coefficients affecting the failure load of the grouped piles and the raft when they combined in PRF.

5.6 Load Sharing Between the Piles in PRF and PGF Models

The resistance of piles in PGF and PRF depends on their location in the group and the nature of the applied load. Sharing of loads between the piles was expressed in terms of friction and bearing factors. Friction factors (α_{CR}, α_S, α_C) of Center (C_R), Side (S), and Corner (C) piles were normalized with the friction factor (α) of SPF. The relations between normalized friction factors and suctions for PGF and PRF are shown in Figures 5.15 and 5.16. In both foundations, the shapes of normalized friction factor of center, side, and corner piles with suction are different from the shapes shown in Figure 5.5 for SPF. Variations in normalized friction factor, however, were quite similar in both PGF and PRF models for piles in all locations. Normalized friction factor exhibited no significant variation at low suctions. Friction factor considerably increased around AEV suction for all piles in both PGF and PRF and then decreased with increasing the suction beyond and ended in values close to that for fully saturated soil (zero suction) at 600 kPa suction. It is worth mentioning here that (α_{CR}, α_S, α_C) were all less than one due to interaction effect in the foundations.

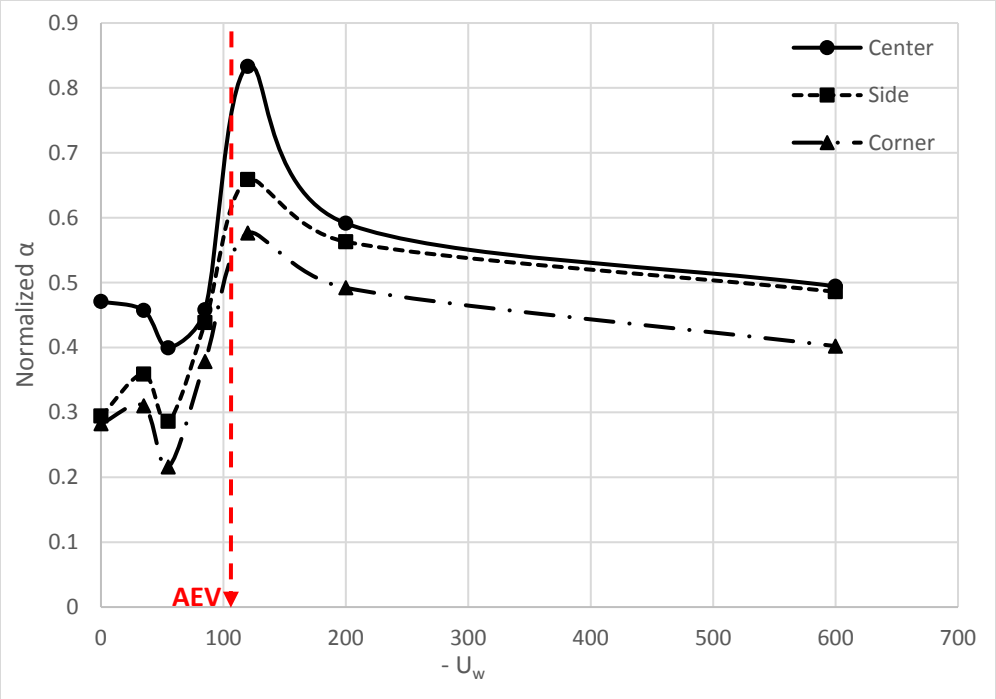

Figure 5.15 Variation of the normalized friction factor in PGF with suction at center, side and corner piles

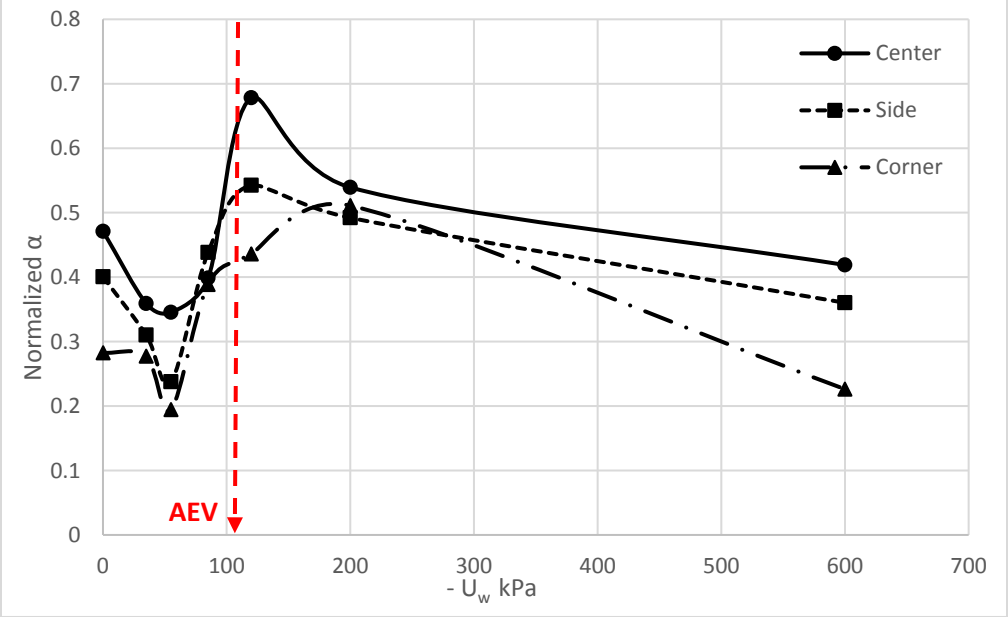

Figure 5.16 Variation of the normalized friction factor in PRF with suction at center, side and corner piles

Variation of bearing capacity factors (N_c) with suction for the center, side, and corner pile tips in PGF and PRF models are shown in Figure 5.17 and 5.18, respectively. The bearing capacity factors were normalized over the bearing factor of SPF. It can be mentioned that the changes of N_c in all piles and both foundations were consistent over the range of the suction. It is worth mentioning here that when comparing the values of normalized α with normalized Nc, it can be told that interaction effects on EBR were less than those on SFR for fully saturated soil in both PGF and PRF. Normalized bearing interaction factors were higher than 1 in suction around AEV suction in both types of foundations. The increment in EBR compensated the reduction in SFR for all piles and helped in producing more consistent gross interaction factors for both PGF and PRF models as shown in Figures 5.17 and 5.18.

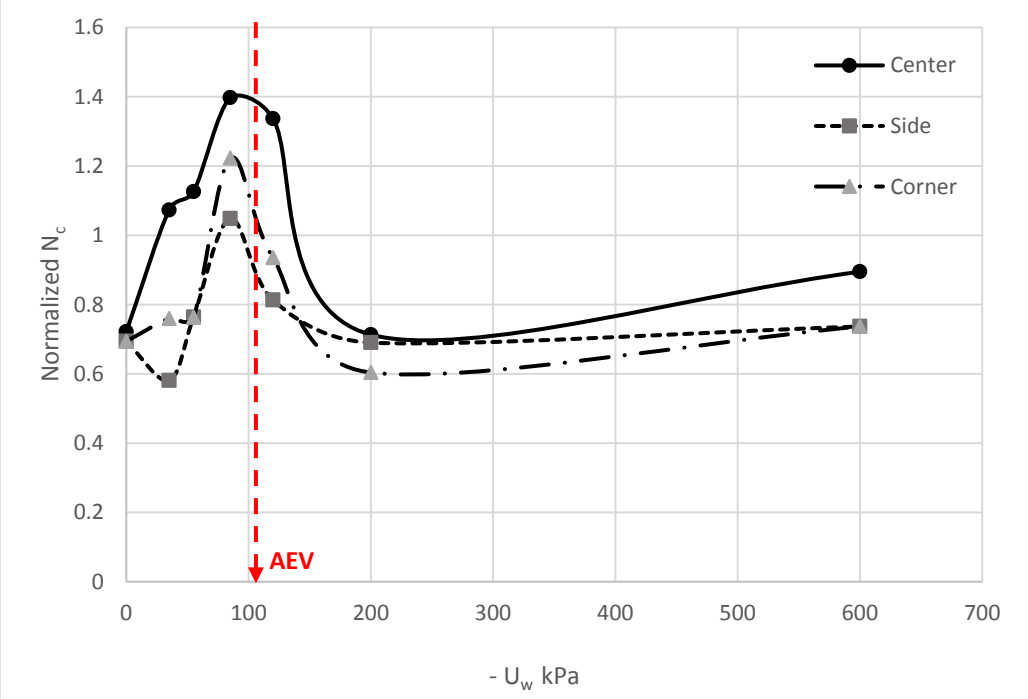

Figure 5.17 Variation of normalized bearing capacity factor with suction in PGF model

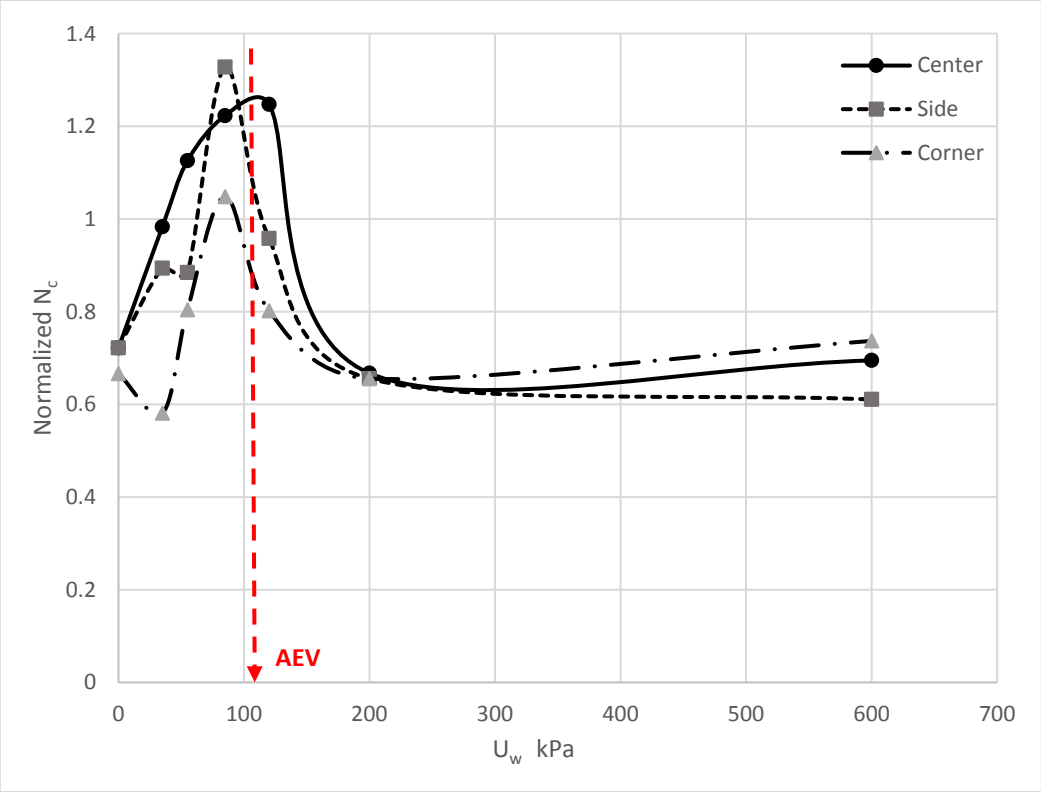

Figure 5.18 Variation of normalized bearing capacity factor with suction in PRF model

5.7 Numerical Expression for Total Foundation Resistance (TFR) of PRF

5.7.1 Development of TFR Models

A numerical model is developed to capture the contribution of foundation's key parameters to the total foundation resistance on the basis of the parametric studies performed in Sections 4.6.1 to 4.6.3. The effect of each of these parameters is shown in terms of numerical formulations. Raft thickness effect on TFR was excluded in this analysis since Figure 4.29 showed that selected raft thicknesses (0.8, 1.2, 1.6) had insignificant influence on the total foundation resistance.

A single numerical model containing the contribution of individual parameters is proposed utilizing multi-regression analysis technique. The construction of the model consisted of three steps. In the first step, the relation between TFR and a designated parameter is fitted into a

numerical expression. These expressions are then used in the second step to generate additional data for the analysis. Finally, multiple regression analyses are conducted to capture the influence of each parameter to the total foundation capacity of PRF at each suction value.

5.7.2 Fitting TFR-Settlement Relationship

The effect of settlement level on the total foundation resistance is depicted based on three-dimensional analysis of Abaqus for a 24 m (wide) x24 m (long) m x0.8 m (thick) PRF. The dimensions of each square pile in the group are 0.4x0.4 m. The pile length is selected to be 6 m with pile spacing of 4d. The properties of soil, pile, and raft utilized in this simulation are the same as those used in Chapter 4. Mathematical expressions that describe the behavior of TFR with settlement (δ) were fitted from load-settlement curves shown in Figure 4.31 and depicted in Figure 5.19 and expressed in Equations 5.28, 5.30, and 5.25 below.

$For\ U_w = 0$

$$\delta = 9 \times 10^{-9}\ (TPR)^{1.99} \qquad 5.28$$

$For\ U_w = 55$ kPa

$$\delta = 5 \times 10^{-11}\ (TPR)^{2.39} \qquad 5.29$$

$For\ U_w = 200$ kPa

$$\delta = 2 \times 10^{-10}\ (TPR)^{1.8} \qquad 5.30$$

where δ is in mm and *TPR* in kPa.

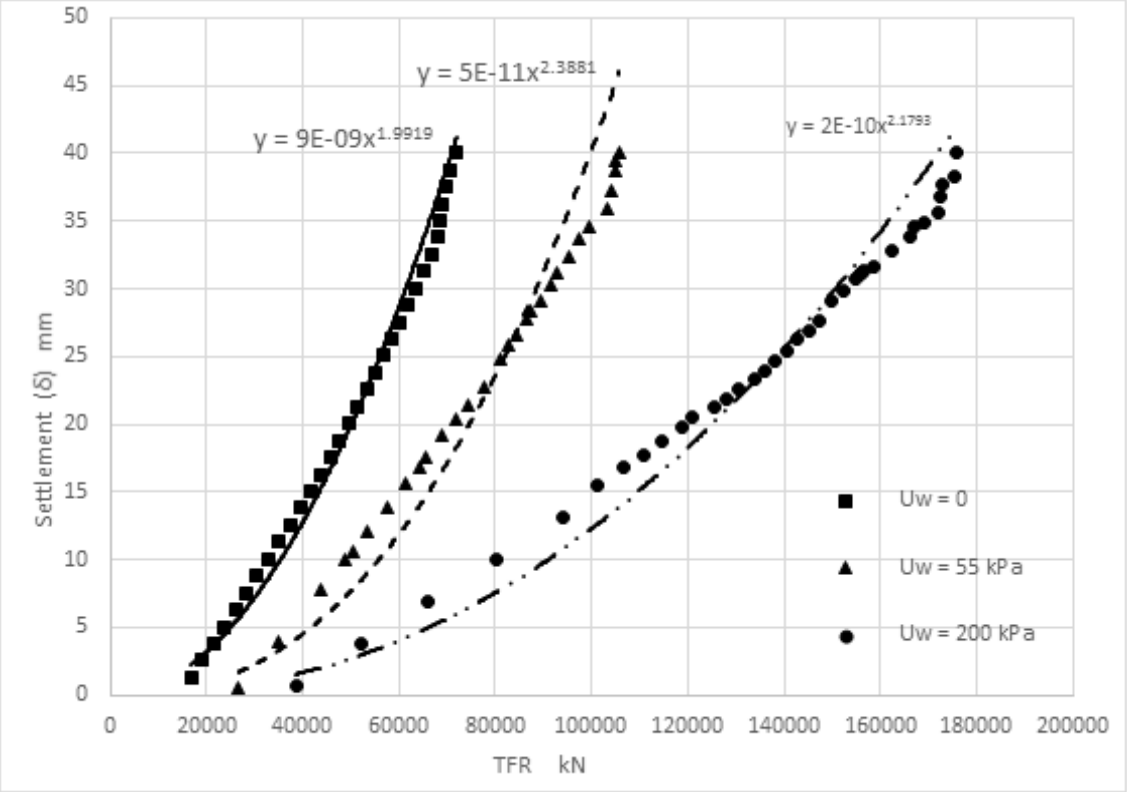

Figure 5.19 Simulated TFR-settlement curves for PRF model of 4d pile spacing at different suctions

5.7.3 Fitting TFR -Pile Spacing (S) Relationship

The effect of pile spacing on total foundation resistance was depicted in Figure 4.32 and rearranged in Figure 5.20. Pile spacing (S) had an inverse relation with TFR in which, the capacity of PRF was noticeably reduced with increasing of pile spacing. The relations between pile spacing S in m and TFR in kPa for different suction values are generated in Equations 5.31 to 5.33.

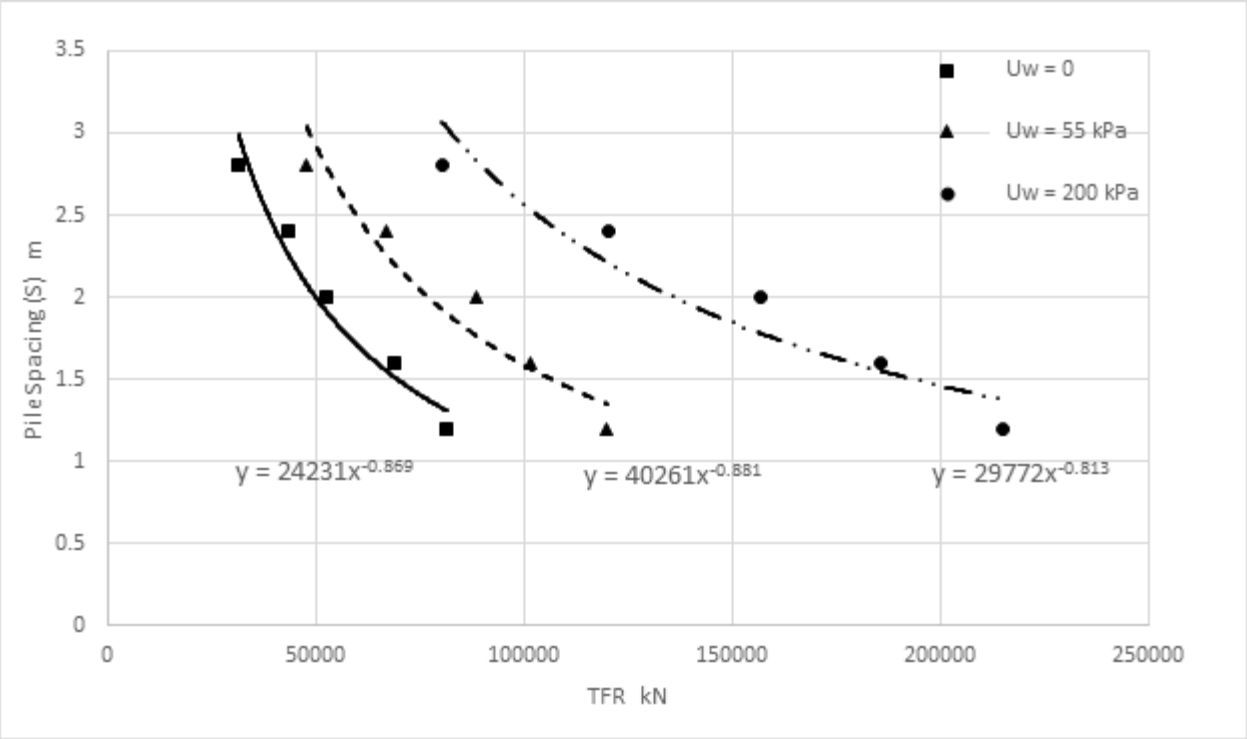

Figure 5.20 Variation of the pile spacing (S) with TFR for PRF model of 4d pile spacing at different suctions

$For \;\; U_w = 0$

$$S = \; 24231 \; (TFR)^{-0.869} \qquad 5.31$$

$For \;\; U_w = 55 \; kPa$

$$S = \; 40261 \; (TFR)^{-0.881} \qquad 5.32$$

$For \;\; U_w = 200 \; kPa$

$$S = \; 29772 \; (TFR)^{-0.813} \qquad 5.33$$

5.7.4 Fitting TFR- Length/Diameter Relationship

The influence of pile/diameter ratio (L/d) on total foundation resistance was shown in Figure 4.34 and replotted in Figure 5.21. The figure and fitted mathematical expressions are expressed in Equations 5.34 to 5.36.

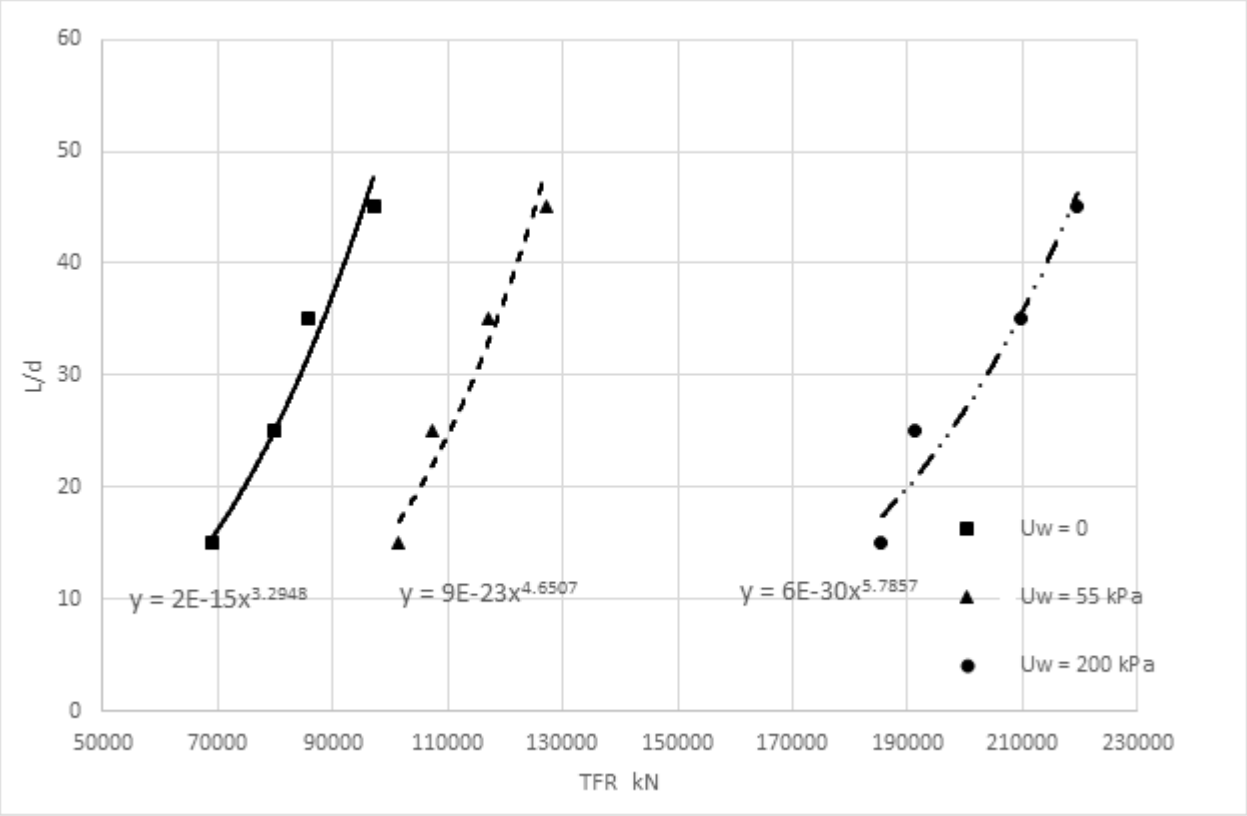

Figure 5.21Variation of pile length to diameter ratio (L/d) with TFR for PRF model of 4d pile spacing

$For \;\; U_w = 0$

$$\left(\frac{L}{d}\right) = 2 * 10^{-15} \, (TFR)^{3.2948} \qquad 5.34$$

F$or \;\; U_w = 55 \;\; kPa$

$$\left(\frac{L}{d}\right) = 9810^{-23}\,(TFR)^{4.6507} \quad 5.35$$

$For \;\; U_w = 200 \;\; kPa$

$$\left(\frac{L}{d}\right) = 6 * 10^{-30}\,(TFR)^{5.7857} \quad 5.36$$

where TFR is in KN

5.7.5 Multi Regression Analysis

Multiple Regression Analysis (MRA) technique was utilized to produce a single model that captures the effect of the above mentioned parameters on TFR. Modeling technique followed in this study is based on statistical theory. The dependent variable was the total foundation resistance (TFR), and three independent variables (settlement δ, pile spacing S, and pile length to diameter ratio L/d) were selected for this purpose.

Linear relationships were constituted between the dependent or predictor variable TFR and the independent or response variables utilizing the method of least square as shown below.

$$TFR = \beta_o + \beta_1\,(\delta) + \beta_2\,(S) + \beta_3\,\left(\frac{L}{d}\right) + \varepsilon \quad 5.37$$

where, β_o, β_1, β_2 & β_3 are the regression coefficients that describe the change in TFR for a unit change in each parameter. ε is the error term that represents the difference between experimental and predicted values of the dependent variables. The least square method built in data analysis tool in Microsoft Excel was used to determine the regression coefficients as shown in Equations 5.38 and 5.39.

$$\beta_o = y' - \beta_i \, x_i' \quad 5.38$$

$$B_i = \frac{\sum(x_i - x')(y_i - y')}{\sum(x_i - x')^2} \quad 5.39$$

where

x' = mean of the independent variable

x_i = value of independent variable

y' = mean of the dependent variable

y_i = value of dependent variable

5.7.6 Numerical Expression for Estimating TFR for PRF for Fully Saturated Soil

The range of the graphed TFR varies from one parameter to another. Therefore, Equations 5.25 through 5.36 were used to generate data set for the independent variables (δ, S, L/d) from the dependent variable TFR. A sample of data sets (total data sets used in the analysis were 99 observations as shown in Table 5.3).For independent variables representing soils with zero suction are shown in Tables 5.3.

For zero suction, summary outputs of the multi-regression analysis is shown in Tables 5.3. The summary tables include regression statics and the analysis of variables (ANOVA). It is statistically known that the higher Adjusted R square (Table 5.3), the better the model. Adjusted R square represents the percentage at which the independent parameters can explain the variation in the predicted dependent variable and was 100 % in this analysis. However, the model shows high Standard Error. The high Standard Error can be related to the big number of observations in the analysis (99) which makes least square method sensitive to outliers and presenting limited extrapolation quality in big data set. Zero P values in the last column of Table 5.4 strongly assures

the effectiveness of the independent parameters to express the change in the dependent variable (TFR).

Table 5.3 Sample of the data set generated for conducting multi-regression analysis with zero suction

Suction = 0			
TFR	$\delta = 9 * 10^{-9}(TFR)^{1.99}$	$s = 24231(TFR)^{-0.87}$	$\frac{L}{d} = 2 * 10^{-15}(TFR)^{3.294}$
kN	**mm**	**m**	
48000	19.00	2.07	5.31
52000	22.29	1.93	6.91
56000	25.83	1.81	8.82
60000	29.64	1.71	11.07
62000	31.64	1.66	12.33
64000	33.70	1.61	13.69
66000	35.83	1.57	15.15
68000	38.03	1.53	16.72
70000	40.29	1.49	18.39
72000	42.62	1.46	20.18
74000	45.01	1.42	22.09
76000	47.46	1.39	24.12
78000	49.98	1.36	26.27

Table 5.4 Regression statics of zero suction soil

Regression Statistics	
Multiple R	1
R Square	1
Adjusted R Square	1
Standard Error	1905
Observations	99

Table 5.5 Analysis of variables (ANOVA) of multi-regression analysis with zero suction soil

ANOVA					
	df	*SS*	*MS*	*F*	*Significance F*
Regression	3.00	349014908118.07	116338302706.02	32026.66	0.00
Residual	95.00	345091881.93	3632546.13		
Total	98.00	349360000000.00			
	Coefficients	*Standard Error*	*t Stat*	*P-value*	
Intercept	58680.43	1197.88	48.99	0.00	
δ	715.44	11.37	62.90	0.00	
S	-9680.36	419.61	-23.07	0.00	
L/d	-144.82	4.72	-30.70	0.00	

Equation 5.40 shows the numerical expression resulted from the multi-regression analysis for estimating TFR for the soil of zero suction.

$$TFR = 58680.43 + 715.44\ (\delta) - 9680.36\ (S) - 144.84\ \left(\frac{L}{d}\right) \quad 5.40$$

Figure 5.22 shows the relations between TFR values obtained from Abaqus simulations and those computed from the suggested regression model. It can be noticed that for the 99 selected observations, there was good agreement between the two values.

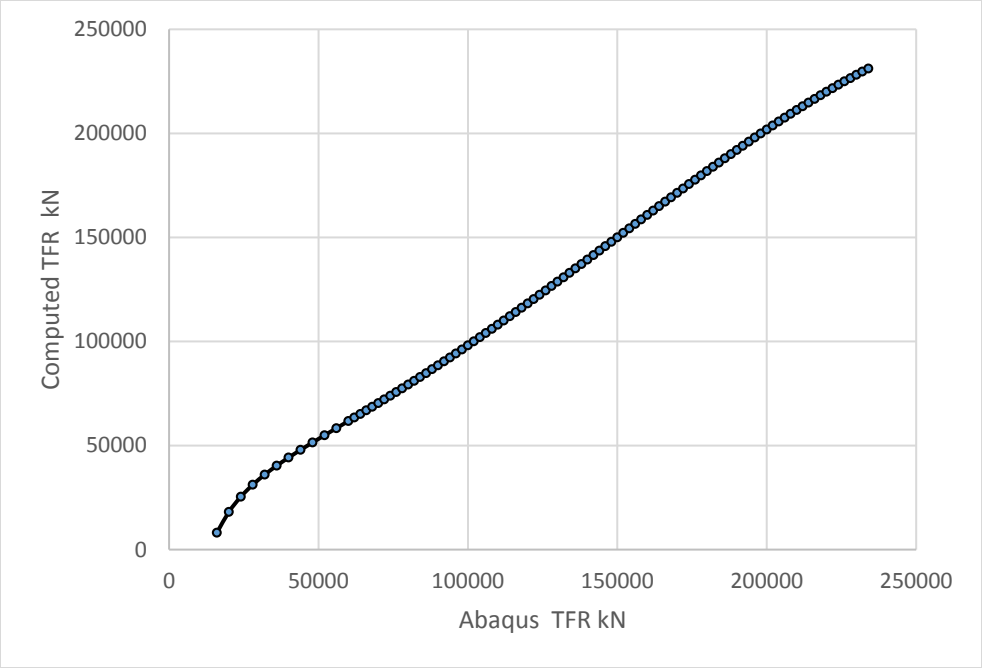

Figure 5.22 Comparison between TFR from Abaqus and TFR fromEquation 5.40 for zero suction

5.7.7 Validation of the Model

The model proposed in Equation 5.40 was compared to the outputs of the parametric study conducted by DeSanctis (2006) for its specific case 13. Soil properties and constitutive models used in DeSanctis study and Equation 5.40 are listed in Table 5.6. Table 5.7 shows the results from both models. TFR of PR in the model proposed in Equation 5.40 was about 41 % of that reported by DeSanctis. The difference could be related to the soil properties used in the models. It can be noticed that modules of elasticity in Eq. 5.40 was 50 % of that used by DeSanctus. The outputs of numerical analyses are governed by stiffness properties rather than strength properties according to Reul (2004).

Table 5.6 Soil properties and models used by DeSanctis (2006)

Model	*E* (kPa)	ν	Cohesion (kPa)	Friction angle (φ)	Constitutive Model	Contact modeling
DeSanctis (2006), Case 13	400 C_u, $E' = 5/6\ E_u$*	0.25	0	30	*M-C*	Thin soil element (0.1*d*)
Equation 5.40	200 C_u	0.49	45	11	*D-P-C*	Master-Slave

* E_u is the undrained modulus of elasticity

Table 5.7 Comparison between the outputs from DeSanctis (2006) model and Equation 5.40

Model	*L/d*	*s/d*	*δ (m)*	*TFR (kN)*	$R_{PRF}/URF (= \alpha_{UR}$, Eq. *5.18)*
DeSanctis (2006), Case 13	20	4	0.05	40,800	0.66
Equation 5.40	20	4	0.05	17,100	0.35

The ratio of load carried by the raft (R_{PRF}) in PRF to the load resisted by URF was 0.66 in DeSanctis model and was 0.35 when calculated using Equation 5.18. It is believed that the difference between the two ratios is attributed to the soil properties and particularly the stiffness of the soil under the raft.

The model was also compared to the model suggested by Sinha (2013) for predicting PRF resistance or maximum settlement of PRF model with zero suction. Soil properties used by Sinha were reported by Maharaj (2003) as shown in Table 5.8.

Table 5.8 Piled raft data (Maharaj, 2003)

Soil		Pile		Raft		Dimensionless Group	
E_s	25 Mpa	E_p	$2x10^3$ - $2x10^6$MPa	E_r	$2x10^3$ - $2x10^6$MPa	$K_p = E_p/E_s$	80-80000
v_s	0.45	v_p	0.3	v_r	0.3		
		d_p	0.5 m	t_r	4.0 m	L_p/d_p	96
		L_p	48 m	L_r	16 m	S_p/d_p	8
		s_p	4 m	B_r	16 m	n	16

Values in Table 5.8 are entered into Equation 5.40 for given settlements, and the corresponding *TFR* values were obtained. The load-settlement curves are plotted in Figure 5.23, in which UDL (uniform distributed load) is the load per unit area and computed as (TFR/A_{raft}) . The proposed model exhibits relatively stiffer load-settlement curve compared to that in Sinha model. It is worth mentioning that Sinha used seven parameters which implies there were four additional parameters in his model (raft thickness, cohesion, friction angle, pile diameter). The model proposed by Sinha was based on thirteen observations only, while the proposed model is based on 99 observations.

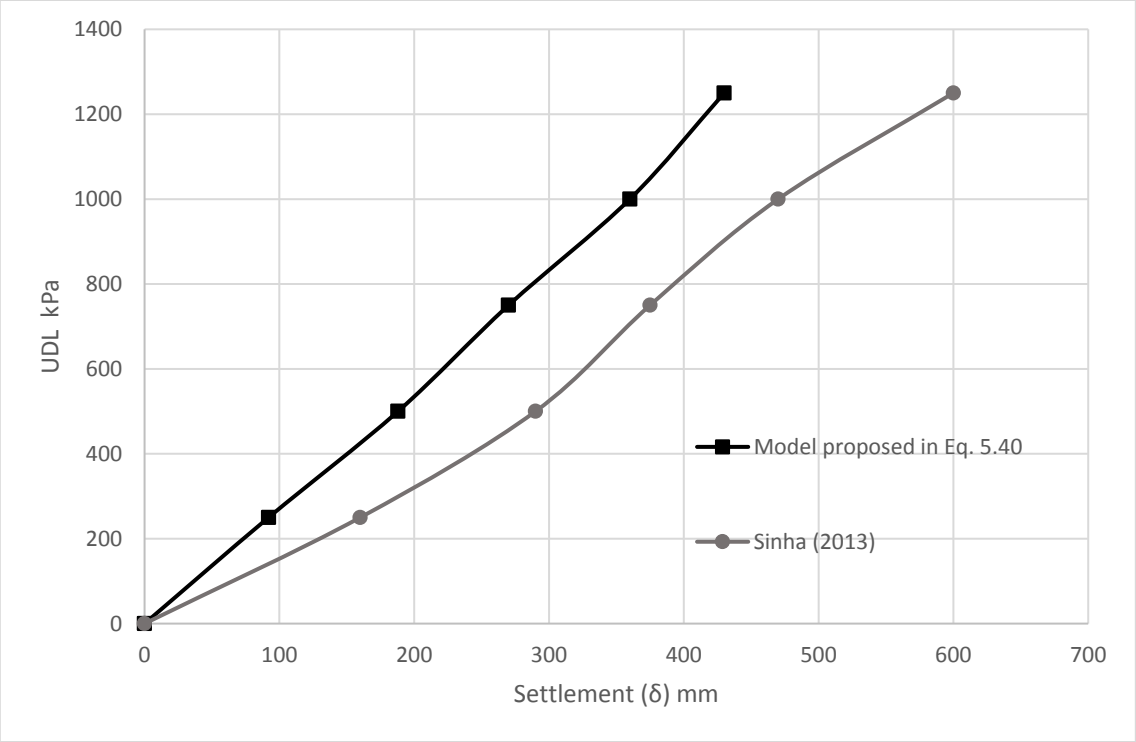

Figure 5.23 Comparision between the proposed model with Sinha (2013) model for zero suction

5.7.8 Numerical Expressions for Estimating TFR for PRF in Partially Saturated Soils

Multi regression analysis were conducted for partially saturated soil of 55 and 200 kPa suctions. Tables 5.9 and 5.10 show samples of the data sets used in the analyses. Output summaries of each analysis are shown in Tables 5.11 to 5.13. Similar observations noticed in the multi-regression analysis of zero suction were noticed as well in 55 and 200 kPa suctions analyses. The models cover a wide range of settlement (δ), pile spacing (S), and pile length/ diameter ratios *(L/d)*.

Table 5.9 Sample of data set generated for conducting multi-regression analysis with 55 kPa suction

Suction = 55 kPa			
TPR	$\delta = 5 * 10^{-11}(TFR)^{2.388}$	$S = 40261(TFR)^{-0.881}$	$\frac{L}{d} = 9 * 10^{-23}(TFR)^{4.65}$
kN	**mm**	**m**	
78000	24.09	1.97	5.08
80000	25.59	1.93	5.72
82000	27.14	1.89	6.41
84000	28.75	1.85	7.17
86000	30.41	1.81	8.00
88000	32.13	1.77	8.90
90000	33.90	1.74	9.88
92000	35.73	1.71	10.95
94000	37.61	1.67	12.10
96000	39.55	1.64	13.34
98000	41.54	1.61	14.69
100000	43.60	1.58	16.13

Table 5.10 Sample data set generated for conducting multi-regression analysis with 200 kPa suction

Suction = 200 kPa			
	$\delta = 2 * 10^{-10}(TFR)^{2.18}$	$S = 29772(TFR)^{-0.813}$	$\frac{L}{d} = 6 * 10^{-30}\ (TFR)^{5.785}$
TPR	δ	S	L/d
kN	**mm**	**m**	
148000	3.81	1.84	5.32
150000	3.92	1.82	5.74
152000	4.04	1.80	6.20
154000	4.15	1.79	6.68
156000	4.27	1.77	7.19
158000	4.39	1.75	7.73
160000	4.51	1.73	8.31
162000	4.63	1.71	8.92
164000	4.76	1.70	9.56
166000	4.88	1.68	10.25
168000	5.01	1.67	10.98
170000	5.14	1.65	11.75
172000	5.27	1.63	12.56

Table 5.11 Regression statics of 55 and 200 kPa suction soil

Regression Statistics		
	Uw = 55 kPa	Uw = 200 kPa
Multiple R	1	1
R Square	1	1
Adjusted R Square	1	1
Standard Error	3544	3492
Observations	99	99

Table 5.12 Analysis of variables (ANOVA) of multi-regression analysis of 55 kPa suction soil

ANOVA					
	df	*SS*	*MS*	*F*	*Significance F*
Regression	3	3.48167E+11	1.16056E+11	9238.361	5.442E-117
Residual	95	1193423297	12562350.5		
Total	98	3.4936E+11			
	Coefficients	*Standard Error*	*t Stat*	*P-value*	
Intercept	77464.46488	1669.912361	46.38834151	4.60216E-67	
X Variable 1	851.3939502	18.59923049	45.77576211	1.54233E-66	
X Variable 2	-9592.626587	458.6106655	-20.91671064	2.48306E-37	
X Variable 3	-148.8869739	7.055976444	-21.10083205	1.24965E-37	

Table 5.13 Analysis of variables (ANOVA) of multi-regression analysis of 200 kPa suction soil

ANOVA					
	df	*SS*	*MS*	*F*	*Significance F*
Regression	3	3.48201E+11	1.161E+11	9513.374	1.357E-117
Residual	95	1159038223	12200402		
Total	98	3.4936E+11			
	Coefficients	*Standard Error*	*t Stat*	*P-value*	
Intercept	79547.47318	1736.173065	45.81771	1.41908E-66	
X Variable 1	22818.47056	434.9836482	52.458226	6.00609E-72	
X Variable 2	-6900.833128	321.960412	-21.433794	3.64601E-38	
X Variable 3	-1034.377621	59.74755503	-17.312468	3.87588E-31	

Equations 5.41 and 5.42 were generatred for estimating TFR in piled raft foundation in soil with average suction values of 55 and 200 kPa, respectively. TFR values obtained from Abaqus simulation for fixed S and L/d values and those computed from Equations 5.41 and 5.42 were plotted against each other in Figures 5.24 for both 55 and 200 kPa suctions. It is noted that the two curves gave the same TFR for 55 kPa and 200 kPa suctions.

For $U_w = 55\ kPa$

$$TFR = 77464.46 + 851.39\ (\delta) - 9592.62\ (S) - 148.88\ \left(\frac{L}{d}\right) \quad 5.41$$

For $U_w = 200\ kPa$

$$TFR = 79547.47 + 22818.47\ (\delta) - 6900.83\ (S) - 1034.37\ \left(\frac{L}{d}\right) \quad 5.42$$

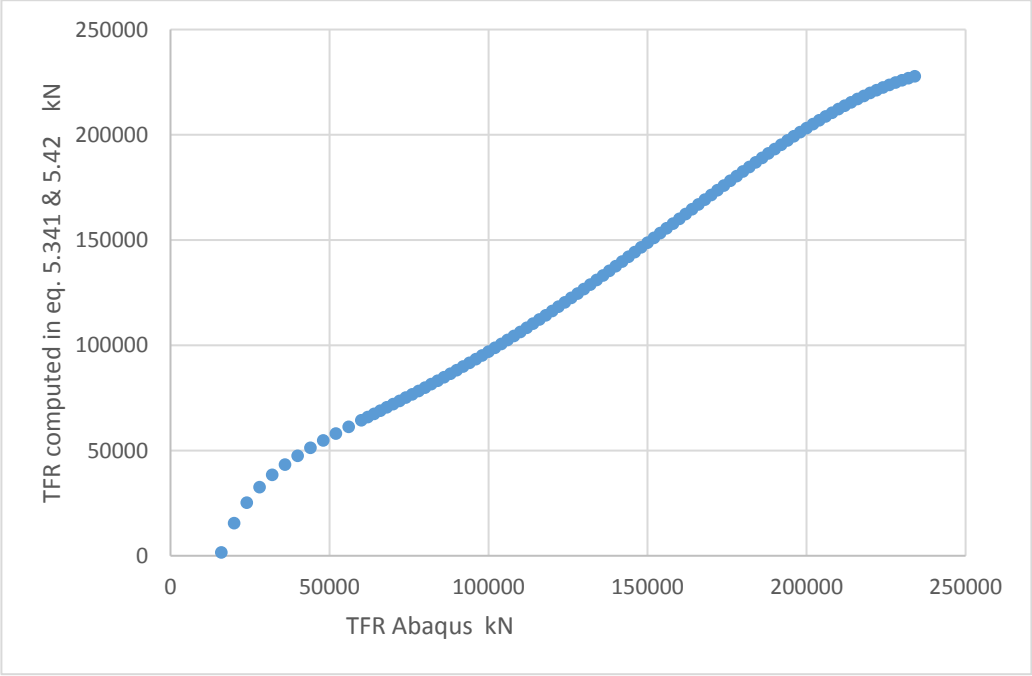

Figure 5.24 Comparison between TFR from Abaqus and TFR from Equations 5.41 & 5.42

CHAPTER 6

CONCLUSIONS AND RECOMMENDATIONS

6.1 Introduction

Piled Raft Foundation (PRF) is a composite structure of shallow and deep foundations. The distribution of stress is complex and it interacts with the soil around. The behavior of SPF and PRF in fully and partially saturated soil was studied experimentally and numerically. The following sections summarize the observations and conclusions noticed in this study as well as some recommendations for future developments.

6.2 Observations and Conclusions

Air Entry Value (AEV) suction is the pivot point when it comes to describing the behavior of any foundation in partially saturated soils. The following observations were made about the role of AEV in the shear strength of the soil and the performance of tested foundations:

For shear strength of the soil used in this study:

- For partially saturated soil samples with suction values higher than the AEV tested in CU and CUW the stress-strain curves of these samples showed a peak pattern failure shape.
- At suction values beyond AEV, the effect of confining pressure became less effective in increasing the shear strength of the soil sample.
- The variation of apparent cohesion with suction was highly noticeable. The cohesion increased linearly from zero to AEV suction region. However it showed less increment beyond the AEV and insignificant variation at high suction values.

- The angle of internal friction did not show considerable changes over a wide range of suction.

For Single Pile Foundation:

- Skin Friction Resistance (SFR) was increased with suction in the soil and reached the peak around AEV suction. SFR decreased beyond this suction up to 2AEV and then reached a constant level.
- The increment in End Bearing Resistance was less noticeable than SFR at suctions below the AEV. However, EBR increased continually beyond AEV and up to the highest suction used in this study (600 kPa).
- At high settlement values, the pile plunged suddenly when tested at suctions below the AEV. As the suction increased, the load settlement curve showed flatter slope and a less noticeable plunging shape at the same settlement values.

For Piled Raft Foundation

- The resistance of PRF increased with suction. The highest rate of increment was around AEV suction in the soil.
- The behavior of piles in PRF was different from that shown in SPF due to the nature of complex interaction factors in PRF.
- The resistance of PRF was less than the combined resistance of the pile group and unpiled raft foundation due to the interaction between the components of PRF.
- In PRF, piles have a higher interaction effect on the raft than the raft interaction effect on the piles.
- For 3x3 grouped pile with concentrated load, central piles carried higher load than side and corner piles.

- The raft in PRF has insignificant contribution to the total load when the state of the fully saturated soil was soft to medium in this study. The highest rate of increment in the load carried by the raft in PRF was around AEV suction. The percentage of load taken by the raft kept increasing with suction and reached minor increment at high suction levels in the soil (600 kPa).
- Measured Suction values decreased when increasing the load in PRF. The reduction was about 10% in all models.

For the conducted parametric study based on Abaqus numerical analysis, the following conclusions were obtained

- There was little effect for the selected range of raft thicknesses on the total resistance of PRF as well as the percentage of load carried by the raft in PRF.
- The capacity of PRF decreased when increasing the spacing in the group. However, the capacity of (24x24x0.8) m PRF with 7d piled spacing was about two times the capacity of unpiled raft foundation in all suctions.
- The percentage of load carried by the raft in PRF increased with increasing pile spacing in the foundation.
- The total foundation resistance was increased with increasing L/d ratio in a linear fashion. However, the load carried by the raft slightly decreased with larger L/d ratios.

For all piled foundations (PRF, PGF)

- The contribution of suction to SFR was more noticeable than EBR at suctions below the AEV. SFR declined beyond the AEV while EBR increased up to 2AEV suction and then leveled off.
- SFR was highly influenced by the effects of interaction between the components of PRF and PGF. Interaction effects on EBR of the piles in PRF and PGF were negligible or even higher than the EBR of SPF at suctions beyond the AEV.

Numerical expressions for determining the bearing capacity of PRF at different suctions and configurations were developed as shown in Equations 5. 27, 5. 40, 5. 41, and 5.42.

6.3 Recommendations for Future Works

- Developing the models for layered soil.
- Conducting large scale model tests in the laboratory or making full scale field tests.
- Considering the variation in suction value along the soil profile.
- Investigating the variation of stress distribution under the raft as well as considering the variation of skin friction resistance along the pile shaft.
- Including different types of loading such as horizontal and dynamic loads.
- Studying the interaction effect between the variables of the multiple regression Models, that is, the relation between the variables themselves.

References

Alonso, E.E., Gens, A. and Josa, A. (1990). A constitutive model for partially saturated soils. Géotechnique , Vol. 40 (3), 405-430.

Anup Sinha (2013). 3-D Modeling of Piled Raft Foundation. M.Sc. Thesis, The Department of Building Civil and Environmental Engineering, Concordia University, Montreal, Quebec, Canada.

Bejamin, L., & Khalilli, N. (2000). A three-phase model for unsaturated soils. *Numerical and Analytical Methods in Geomechanics*, 893–927.

Blight, G.E., & Donald, I.B. (1960). Factors controlling the shear strength of partly saturated cohesive soils. In Proceedings of the American Society of Civil Engineers Research Conference on Shear Strength of Cohesive Soils, Boulder, Colorado, 505-532

Brooks, R.H. and Corey, A.T. (1964). Hydraulic Properties of Porous Media. Hydrology Paper No. 3, Colorado State University, Fort Collins, 1-27.

Burland, J.B. (1965). Some aspects of the mechanical behavior of partly saturated soils. In Moisture equilibria and moisture changes in soils beneath covered areas. Butterworths, Sydney, Australia, pp. 270-278.

Butterfield, R. B. (1971). The Elastic Analysis of Compressible Piles and Pile Groups",. *Géotechnique*, 43-60.

Clancy, P., and Randolph, M.F., (1993). An Approximate Analysis Procedure for Piled Raft Foundations. Int. J.Numer. and Analytical Methods in Geomech., London, 17(12), 849-869.

Clancy, P,. and Randolph, M.F., (1996). Simple Design Tools for Piled Raft Foundations, Géotechnique 46(2), 313-328.

Chow H.S.W. (1987). Iterative Analysis of Pile-Soil-Pile Interaction. Geotechnique 37, No. – 3, 321 - 333.

Coleman J.D. (1962). Stress-Strain relations for partially saturated soils. Géotechnique12 (4), 348-350.

DARMSTAD, T. U. Combined Piled Raft Foundtions. *International Society for Soil Mechanics and geotechnical Engineering*

Decagon Inc. (2016). *Measurements of water potential* . Retrieved from Decagon Devices: https://www.decagon.com/en/soils/water-potential/MPS-6-calibrated-water-potential-sensor.

Desai, C. S., Zaman, M. M., Lighter, J. G., and Siriwardane, H. J.(1984). Thin-layer element for interface and joints. International Journal of Numerical Analys is Methods in Geomechanics, Vol. 8, 19-43

Nguyen, D.D.C. Jo S.B., Kim.D.S. (2013). Design method of piled-raft foundations under vertical load considering interaction effects Computing Geotech, 47 (3), 16-27

Donggyu Park, Junhwan, L. (2015). Interaction effects on load-carrying behavior of piled rafts embedded in clay from centrifuge tests Canadian Geotechnical Journal, 52(10): 1550-1561

Fredlund, D. G. (1989). *Soil suction monitering for roads and airfields.* Hanover: Corps of Engineers.

Fredlund, M. D., Fredlund, D., & Wilson, G. (1997b). Prediction of the Soil-Water Characteristic Curve from. *Third Brazilian Symposium on Unsaturated Soils*, (pp. 13-23). Rio de Janerio.

GCTS Testing Systems. *Fredlund Soil Water Characterstics Curve*. Retrieved from GCTS Testing Systems: https://www.gcts.com/?s=prod_ver&p=products&ID=204

Fredlund, D. G., Rahardjo, H., & Fredlund, M. (2012). *Unsaturated Soil Mechanics in Engineering Practice.* New York: John Wiley & Sons.

Goodman, R.L. Taylor, T. Brekke L. (1968), A model for the mechanics of jointed rock J.S.M.F.D., ASCE., 94 (SM3), pp. 637-659 1968

Guan, Y, Fredlund, D. G., (1997). Direct measurement of high soil suction. In: Simpóosio solos não saturados brasileiro, 3, Rio de Janeiro, 2:543–550

Harvey, E. N., Barnes, D., McElroy,, A., Whitday, , A., Pease, D., & Cooper, K. (1944). Bubble formation in animals. *Journal of cellular and Comparaive Phsycology* , pp. 1-22.

Hassen G., Buhan P. (2006). Elasto-plastic Multiphase Model for Simulating the Response of Piled Raft Foundations Subject to Combined Loadings. Int. J. Numer. Anal. Meth. Geomech. 2006; 30:843–864.

Helwany, S. (2007). *Applied Soil Mechanics with ABAQUS Applications by Sam Helwany.* New York: Wiley.

Hilf, J.W. (1956). An investigation of pore-water pressure in compacted cohesive soils. PhD Thesis. Technical Memo No.654, United States Bureau of Reclamation, Denver

Ho DYF, Fredlund D.G, (1982). Increase in shear strength due to suction for two Hong Kong soils. In: Proc ASCE Geotech Conf, Engineering and Construction on Tropical and residual soils. Honolulu, Hawai, U.S.A., January 11–15, 263–295

Hooper, J.A. (1973). Observations on the Behavior of a Piled-Raft Systems. Geotechnique, 28 (1): 65-83.

Horikoshi, K. and Randolph, M. F. (1997). Optimum Design of Piled Raft Foundations, Proceed. XIV ICSMFE, Hamburg, vol. 2, 1073 - 1076.

Horikoshi, K. and Randolph, M. F. (1998). A Contribution to Optimum Design of Piled Rafts", Geotechnique, 48 (3): 301-317.

Houston, S. L., Perez-Garcia, N., & Houston, W. (2008). Shear Strength and Shear-Induced Volume Change Behavior of Unsaturated Soils from a Triaxial Test Program. *ASCE*, 1619-1632.

Jennings,J.E.B.,and Burland,J.B. (1962). Limitations to the use of effective stresses in partly saturated soils." Géotechnique ,12(2),125 – 144 .

Josa A, Balmaceda A, Gens A, Alonso EE. (1992). An elastoplastic model for partially saturated soil exhibiting a maximum of collapse. In: Owen DRJ, Onate E, Hinton E, editors. Computational plasticity III, vol. 1. Swansea: Pineridge Press; 815–26.

Katzenbach, R., Arslan, U., Gutwald, J., Holzhauser, J., Quick, H. (1997a), Soil-Structure Interaction of the 300 m High Commerzback tower in Frankfurt am Main. Measurements and Numerical Studies. Proc. XIV ICSMFE, Vol. 2, 1081-1084, Rotterdam: Balkema.

Khalili, N., F. Geiser, *and* G. E. Blight, *(*2004). Effective stress in unsaturated soils: Review with new evidence, Int. J. Geomech., 4*(2),* 115–126.

Krahn, J., Fredlund, D. G. *and* Klassen M. J. (1989), Effect of soil suction on slope stability at North Hill, Can. Geotech. J., 26, 269–278.

Kohgo, Y., nakano, m., & Miazaki, T. (1993). Theoritical aspects of constitutive modeling for unsaturated soils. *Soil and Foundation*, 49-63.

Langfelder, L.J, Chen, C.F. Justice J.A. (1968). Air Permeability of Compacted Cohesive Soils.

Li, L., & Zhang. X .(2014). Developement of New High Suction Tensimeters. *Soil Behavior and Geomechanics*, 416-425.

Li, J. (2008). Unsaturated soils: From constitutive modelling to numerical algorithm, by Daichao Sheng, Anto-nio Gens, Delwyn G. Fredlund and Scott W. Sloan, Computers and Geotechnics 35(6) 810–824.

McClelland, Bramlette, Focht, Jr. and John A., (1958), Soil Modulus of Laterally Loaded Piles, Transactions, American Society of Civil Engineers, Vol 123, 1049-1063

Meilani I., Rahardjo H., Leong E.C., and Fredlund D .G. (2002). Mini suction probe for matric suction measurements. Canadian Geotechnical Journal 39 . 1427-1432

Miller GA, Hamid TB. *(*2007). Interfaces direct shear testing of unsaturated soil. Geotechnical Testing Journal. 30*(*3*):*182–191.

Navayogarajah N. *(*1990). Constitutive modeling of static and cyclic behavior of interfaces and implementation in boundary value problems. Ph.D. Dissertation, Department of Civil and Engineering Mechanics, University of Arizona, Tucson, U.S.A.

Ottaviani, M. (1975). Three Dimensional Finite Element Analysis of Vertically Loaded Pile Groups. Geotechnique 25, no.- 2, 159-174.

Poulos, H. G. (2001). Piled raft foundation: design and applications. *Geotechnique*, 95-113.

Poulos, H.G., Small, J.C. Ta, L.D., Sinha, J. & Chen, L. (1997). Comparison of Some Methods for Analysis of Piled Rafts. Proc. 14th Int. Conf. Soil Mech. Found. Eng, Hamburg 2, 1119-1124, Rotterdam: Balkema

Randolph, M.F. and Wroth C. P. (1979). Analysis of Deformation of Vertically Loaded Pile Groups. Géotechnique, 29(4): 423-439.

Randolph, M.F. (1983). Design of Piled Raft Foundations. Proc. Int. Symp. on Recent Developments in Laboratory and Field Tests and Analysis of Geotechnical Problems, Bangkok, 525-537.

Randolph, M. F. (1994). Design methods for pile groups and piled rafts. *State of the Art Report, XIII ICSMFE*, (pp. 61-82). New Delhi.

Reese L.C., Wang S.T., Reuss R. (1993), Test of Auger Piles for Design of Pile Supported Rafts, International Journal of Analytical and Numerical methods in Geomechanics, 22(6), 477-493.

Reul, O & Randolph, M F. (2003). Piled rafts in Over-consolidated Clay- Comparison of In-situ Measurements and Numerical Analyses. Géotechnique, 2003, Vol. 1

Russo, G. (1998). Numerical Analysis of Piled Rafts. Int. Journ. Analytical and Numerical Methods in Geomechanics, 22(6): 477-493.

Rutqvist J, Wu Y S, Tsang C F, Bodvarsson G. *(*2002). A modelling approach for analysis of coupled multiphase fluid flow, heat transfer, and deformation in fractured porous rock. International Journal of Rock Mechanics and Mining Sciences*;* 39*:*429–442

Saez, J. (1986). The shear strength od partially saturated soils. *Geotechnique*, 453-456.

Saez, J. (1989). Shear strength and deformation of partially saturated soils. *Geotechnique,* 43-46.

Sanctis, L., Mandolini, A., Russo, G., & Viggiani, C. (2002). Some remarks on the optimum design of piled rafts. *ASCE Geotechnical Spec*.

Sanctis, L D., Mandolini, A. (2006). Bearing Capacity of Piled Raft on Soft Clay Soil. Journal of Geotechnical and Geo-environmental Engineering, ASCE, vol. 132, no.-12, pp.1600-1610

Sánchez M, Gens A, Guimarães L, Olivella S. (2005). A double structure generalized plasticity model for expansive materials. Int J Numer Anal Meth Geomech 29:751–87.

SIMULIA, Abaqus. (2013). *Analysis of Geotechnical Problems with Abaqus.* Ohio: 3DS Academy.

Sivakumar, V. (1995). An elasto-plastic critical state framework for unsaturated soil . *Geotechnique,* 35-53.

Sheng D, Fredlund, DG, Gens, A. (2008). A new modelling approach for unsaturated soils using independent stress variables. Can Geotech J;45:511–34.

Small, J.C. Poulos, H.G. (2007). Non-linear analysis of piled raft foundations. Contemporary Issues in Deep Foundations, 1-9

SoilMoisture. *2100F Remote Tensiometers*. Retrieved from SOIL MOISTURE: http://www.soilmoisture.com/2100F-REMOTE-TENSIOMETERS

Soonkie, N, Marte, G, Panayiotis, D. (2011). Determination of the shear strength of unsaturated soils using the multistage direct shear test. Eng Geol 122:272 – 280

Sweeney, D. J. (1982). Some in situe soil suction measurements in Hong Kong' s residual soil slopes. *Seventh Southeast Asia Geotechnical Report*, pp. 91-101.

Tripathy, S., Al-Khyat, S., Cleall, P., Baille, W., & Schanz, T. (2016). Soil Suction Measurement of Unsaturated Soils with a Sensor Using Fixed-Matrix Porous Ceramic Discs. *Indian Geotechnical Journal*, 252–260.

Thu, T.M Rahardjo, .H. Leong. E.H. (2007). Soil-water characteristic curve and consolidation behavior for a compacted silt. Canadian Geotechnical Journal, 44 (3) 266-275

Vanapalli, S.K., Fredlund, D.G., and Pufahl, D.E., and Clifton, A.W. (1996). Model for the Prediction of Shear Strength with Respect to Soil Suction.

Vanapalli, S.K., Fredlund, D.G., and Pufahl, D.E., and Clifton, A.W. (1996). Model for the Prediction of Shear Strength with Respect to Soil Suction.

Van Genuchten M.T. (1980). A closed-form equation for predicting the hydraulic conductivity of unsaturated soils, Soil Sci. Soc. Am. J. 44(5):892-898.

Wriggers, P. (1995). Finite Element Algorithms for Contact Problems . Archives of Computational Methods in Engineering, Vol. 2, 4, 1-49.

Zienkiewicz, O.C. B. Best, C. Dullage, K.C. (1970). Stagg Analysis of non-linear problems with particular reference to jointed rock systems, Proc. 2nd Int. Conf. Society of Rock Mech., 8-14

VITA

Salman F. Rubaye

Department of Civil and Environmental Engineering

135 Kaufman hall, Old Dominion University, Norfolk Virginia 23529

Salman Rubaye was born in Iraq on January 7, 1977 to Mr. Fadhel S. Rubaye and Mrs. Khairia A. Alobaidy. He attended Alsharqia high school in Baghdad, Iraq.

He hold a bachelor degree in Highways and Bridges from Building and Construction department in the University of Technology, Baghdad, Iraq.

He earned a Master of Science degree in geotechnical Engineering (2007) from the University of Technology in Baghdad Iraq also.

Salman has also worked with Corps of Engineers as a project engineer as well as with Pernix-Serka joint venture in building some of US embassy annexes in Baghdad, Iraq.

He joined a local university in Wassit, Iraq as a lecturer teaching soil mechanics and traffic engineering before starting his Ph. D program in Old Dominion University in July 2013.